

**DECOY SYSTEMS SIMULATING JET AIRCRAFT PLUME EMISSIONS
AND
STRATEGIES FOR SUPPRESSION OF EMISSIONS
FROM MISSILE PLUMES**



BY

JOHAN FRANCOIS LOMBARD

**DISSERTATION PRESENTED FOR THE DEGREE OF
DOCTOR OF PHILOSOPHY (POLYMER SCIENCE)
AT THE UNIVERSITY OF STELLENBOSCH**

PROMOTERS

PROF. W.J. ENGELBRECHT

PROF. R.D. SANDERSON

STELLENBOSCH

MARCH 1997

DECLARATION

I the undersigned hereby declare that the work contained in this dissertation is my own original work and has not previously in its entirety or in part been submitted at any university for a degree.

20/01/97

Date

**DECOY SYSTEMS SIMULATING JET AIRCRAFT PLUME EMISSIONS
AND
STRATEGIES FOR SUPPRESSION OF EMISSIONS
FROM MISSILE PLUMES**

BY

J.F. LOMBARD

APPROVED:

PROF. W.J. ENGELBRECHT
PROFESSOR OF PHYSICAL CHEMISTRY
INTERNAL EXAMINER

PROF. R.D. SANDERSON
PROFESSOR OF POLYMER SCIENCE
INTERNAL EXAMINER

DR. P.I. BEKKER
EXTERNAL EXAMINER

DR. G.U.B. BROZIO
EXTERNAL EXAMINER

ABSTRACT

This study covers the development of technology to be able to manufacture a flare that can lure a modern state-of-the-art heat-seeking missile. Consequently it was necessary to characterize the exhaust plumes of certain fighter aircraft. This characterization involved the spectral analyses of the aircraft plume emission over the entire infrared region. The important influence that shock heating of CO₂ and N₂ in the Mach discs of the plume has on the infrared spectral emission, has been realised. Since shock heating is absent in normal flare designs, the effect of shock heating was simulated by chemical manipulations of the flare composition. This resulted in a flare which simulated the infrared emission spectrum of a jet aircraft plume.

The inadequacy of the existing operational flare has been demonstrated by spectral analysis. It has also been established that the pyrotechnical composition of this flare is such that it cannot be manipulated to successfully simulate an aircraft plume.

Secondly, the plumes of rocket motors were characterized. The propellant samples of these motors were specially selected to be representative of currently used and nearly qualified propulsion systems. This study not only involved the infrared and ultraviolet emissions of the plumes, but also at 3GHz in the RADAR region regarding transmission and RADAR cross-section measurements.

The results of this study can be applied in the stealth environments of modern rockets and missiles. This technology can also be used in an in-flight identifying (friend or foe) role with respect to aircraft and missiles.

OPSOMMING

Hierdie studie behels die daarstelling van tegnologie wat dit moontlik maak om 'n fakkelt te vervaardig wat oor die vermoë beskik om 'n moderne hittegeleide missiel te kan mislei. Dit was gevolglik nodig om die plume van sekere vliegtuie te karakteriseer. Hierdie karakterisering behels die spektraalanalise van die vliegtuigpluimemissie en strek oor die hele infrarooi gebied van die spektrum. Die skokverhitting van CO_2 en N_2 in die Machskywe van 'n vliegtuigpluim speel 'n belangrike rol tydens die spektrale infrarooi emissie. Hierdie aspek is egter vroeg besef. Aangesien skokverhitting, en dus ook die effek daarvan in die pluim, afwesig is tydens normale fakkelonbranding, was dit genoodsaak om die effek deur chemiese manipulasie te simuleer.

Deur die emissiespektrum van die huidige operasionele fakkelt te analiseer kon die onvermoë daarvan vasgestel word. Dit was ook bepaal dat, weens die chemiese samestelling van die fakkelt, dit nie moontlik is vir hierdie fakkelt om 'n vliegtuigpluim suksesvol te simuleer nie.

Ten tweede was die plume van vuurpilmotors ook gekarakteriseer. Die samestelling van die dryfmiddelkeuse was sodanig dat dit goed verteenwoordigend is van dryfmiddels reeds in gebruik asook in byna gekwalifiseerde stelsels. Tydens hierdie ondersoek was daar nie net gekyk na die infrarooi en ultraviolet emissies nie, maar ook na die 3GHz radargebied. Daar is uitsluitlik gekonsentreer op die radardeursnit en die radardeurlating van plume.

Die resultate wat verkry is kan aangewend word in die sluiptomgewing van moderne vuurpyle en missiele, veral rakende die aandrywingstelsels. Hierdie tegnologie kan ook uitgebou en verder ontwikkel word om in vlug identifikasie (vriend of vyand) van vliegtuie en missiele te kan doen.

ACKNOWLEDGEMENTS

The author wishes to extend his sincere thanks and appreciation to:

Prof. W.J. Engelbrecht, for his able guidance, enthusiastic assistance and personal involvement throughout this study;

Somchem, a division of Denel (Pty) Ltd, and management for financial assistance and allocated project time;

Prof. R.D. Sanderson for his assistance by critical reviewing the investigations and the technical content of this thesis;

Messrs. W.T. Foxcroft and D. Strydom, Armscor Programme Managers, for their managerial assistance and permission for the use of the data;

Messrs. C. Bothma and I.I.J. Krynauw, for their continual technical assistance and personal involvement regarding sample preparations and test range discipline;

Mr Basson, from Survival Electronics CC, for his able guidance regarding SAAF operations and personal enthusiastic involvement with the project;

Messrs. J. Roodt, F. Collin and M.J. Rossouw from the CSIR (Aerotek), for their technical assistance regarding data acquisition and processing in the IR, UV and RADAR regions;

Mr J. Kotze from Avitronics, for his technical involvement with the UV data acquisition;

Mr M. de Bruin, from Swartklip Products, Dr. F. van der Walt, from Mechem, both divisions of Denel (Pty) Ltd, for providing and packaging certain samples;

Mmes. H. Priem, E. Visagie and S. Dockrall, for valued documentational assistance.

This document contains information related to the defence of the Republic of South Africa. The provisions of Section 118 of the Defence Act, Act No 44 of 1957, as well as the provisions of the Act on the Protection of Information, Act No 84 of 1982, are applicable to this document.

When no longer required for authorised purposes, this document must be returned to Configuration Management, Somchem.

LIST OF CONTENTS

1.	INTRODUCTION	16
2.	BACKGROUND AND THEORY	20
	2.1 SPECTRORADIOMETRIC DEFINITIONS, QUANTITIES AND UNITS	20
	2.1.1 Plane Angle and Solid Angle	20
	2.1.2 Radiometric Quantities	21
	2.1.3 Conservation of Energy	22
	2.1.4 Emissivity	22
	2.1.5 Blackbody Radiation (Planck's Law)	23
	2.1.6 The Irradiance (E_{λ}) Falling on a Detector	24
	2.1.7 Stefan-Boltzmann Law	24
	2.1.8 Wien's Displacement Law	25
	2.1.9 Atmospheric Transmittance	25
2.2	APPARATUS AND PROCEDURE FOR OBSERVATIONS	28
	2.2.1 The SR5000 Spectral Radiometer	28
	2.2.2 SR5000 Calibration	29
	2.2.3 The UV Narrow Band Radiometer	30
	2.2.4 UV Radiometer Calibration	33
	2.2.5 AGEMA 900 Imaging Radiometers	33
2.3	WAVE MECHANICS	34
	2.3.1 The Wave Nature of Electrons	35

LIST OF CONTENTS (Cont'd)

2.4	ENERGY LEVELS OF ATOMS	39
2.5	ENERGY LEVELS OF MOLECULES	40
2.5.1	Introduction	40
2.5.2	Rotational Spectra	42
2.5.3	Vibrational Spectrum	49
2.5.4	Vibration-Rotation Spectra	51
2.5.5	Rotational Spectra of Polyatomic Molecules	54
2.5.6	Vibrational Spectra of Polyatomic Molecules	55
2.5.7	Transfer of Vibrational Energy	61
2.5.8	Electronic Spectra	62
2.6	FUNDAMENTALS OF SEMICONDUCTOR PHYSICS	63
2.6.1	Crystal Structure and Energy Bands	63
2.6.2	Group III-V and Group II-VI Semiconductor Alloys	66
2.6.3	Intrinsic and Extrinsic Semiconductors	67
2.6.4	Fundamentals of Optical Electrical Conversion	68
2.6.5	Photoconduction Detectors	72
2.6.6	Photovoltaic Detectors	73
2.6.7	Bolometric Detectors	74
2.6.8	Missile Spectral Bands	75
3.	SPECTRAL PROPERTIES OF AIRCRAFT PLUMES	77
3.1	SPECTRAL MEASUREMENTS	77
3.2	INTERPRETATION OF THE PLUME EMISSION SPECTRUM	80
3.3	FLAME AREA CALCULATIONS	82
3.4	SHOCK HEATING	84

LIST OF CONTENTS (Cont'd)

4.	SPECTRAL PROPERTIES OF FLARE COMPOSITIONS	86
4.1	EXPERIMENTAL SET-UP	86
4.2	ATMOSPHERIC CORRECTIONS	87
4.3	FLARE SPECIFICATION	89
4.4	THE EFFECTIVE FLAME AREA AND TEMPERATURE	89
4.5	IDENTIFICATION OF CHEMICAL SPECIES IN FLAMES OF FLARES	92
4.6	EMISSION OF GRAPHITE	93
4.7	INITIAL FLARE COMPOSITIONS AND MEASUREMENTS	94
4.8	THE ENHANCEMENT OF THE 4.2 AND 4.4 μ m PEAKS	108
4.9	THE CURRENT FLARE	111
4.10	RESULTS OF FURTHER DEVELOPMENT	113
4.11	THE BEST FORMULATION AND POSSIBLE IMPROVEMENTS	120
4.12	CONCLUSION AND RECOMMENDATION	121
5.	SPECTRAL PROPERTIES OF MISSILE PLUMES	125
5.1	PROPELLANT FORMULATIONS	125
5.2	EXPERIMENTAL SET-UP AND SPECTRAL MEASUREMENTS	132
5.3	INTERPRETATION OF SPECTRA	135
5.4	RADAR TRANSMISSION MEASUREMENTS	143
5.4.1	Introduction	143
5.4.2	Measurement Set-up and Equipment	144
5.4.3	Results	145
5.5	RADAR CROSS-SECTION MEASUREMENTS	148
5.5.1	Introduction	148
5.5.2	Measurement Set-up and Equipment	148
5.5.3	Results	152
5.5.4	Discussion of Results	154

LIST OF CONTENTS (Cont'd)

6. CONCLUSIONS AND RECOMMENDATIONS	156
REFERENCES	159

LIST OF APPENDICES

A SPECTRAL RESPONSE OF DETECTORS	162
B UV REFERENCE GRAPHS	168
C MIRAGE F1 PLUME SPECTRUM BETWEEN 0.4 AND 2.5 μ m	171
D DETAIL SPECTRAL EMISSIONS OF SOME ELEMENTS	173
E RESULTS OF FLARE MEASUREMENTS	179
F ADDITIONAL FLARE DATA	186
G SPECTRAL OUTPUTS OF FLARE COMPOSITIONS	190
H PICTORIAL FLARE COMPARISON	209
I CHEMICAL COMPOSITIONS OF THE PLUMES	211
J APPARATUS USED FOR THE MEASUREMENTS	213
K PHOTOGRAPHIC MATERIAL OF THE ROCKET MOTOR PLUMES	216
L RADAR TRANSMISSION DATA	222
M RADAR CROSS-SECTION DATA	233

LIST OF TABLES

2.1	INFRARED BANDS OF H ₂ O VAPOUR	58
2.2	INFRARED ABSORPTION BANDS FOR VARIOUS FUNCTIONAL GROUPS (IN WAVE NUMBERS, cm ⁻¹)	60
4.1	STANDARD SWARTKLIP FLARE COMPOSITION	95
4.2	MECHEM FLARE COMPOSITIONS	95
4.3	SOMCHEM FLARE COMPOSITIONS	97
4.4	COMPARATIVE RESULTS FROM INITIAL MEASUREMENTS	100
4.5	FLARE COMPOSITIONS	114
4.6	PLUME COMPOSITIONS OF HTPB VS GAP AS BINDER	124
5.1	PROPELLANT FORMULATIONS	126

LIST OF FIGURES

2.1	TRANSMITTANCE OF 30m HORIZONTAL AIR PATH AT SEA LEVEL	27
2.2	UV RADIOMETER NORMALIZED FILTER BANDS	31
2.3	THE ENERGY LEVEL DIAGRAM OF A PARTICLE IN A ONE-DIMENSIONAL BOX	37
2.4	ROTATION OF A DIATOMIC MOLECULE	43
2.5	ENERGY LEVEL DIAGRAM	45
2.6	PURE ROTATIONAL ENERGY LEVEL DIAGRAM OF A LINEAR ROTOR	46
2.7	ATMOSPHERIC ABSORPTION OF MILLIMETRE WAVES	48
2.8	VIBRATIONAL ENERGY DIAGRAM FOR A DIATOMIC MOLECULE	50
2.9	THE VIBRATIONAL AND ROTATIONAL ENERGY LEVEL DIAGRAM FOR A DIATOMIC MOLECULE AND THE TRANSITIONS OBSERVED IN THE VIBRATION-ROTATION SPECTRUM	53
2.10	NORMAL MODES OF VIBRATION OF A SYMMETRICAL LINEAR AND NONLINEAR TRIATOMIC MOLECULES	57
2.11	THE VIBRATIONAL ENERGY LEVELS OF N ₂ AND CO ₂	61
2.12	ENERGY BANDING OF ALLOWED LEVELS IN DIAMOND AS FUNCTIONS OF SPACING BETWEEN ATOMS	64
2.13	UNIT CELL OF THE DIAMOND LATTICE STRUCTURE (C, Si, Ge)	65
2.14	UNIT CELL OF THE ZINC BLENDE STRUCTURE (GaAs, InSb)	65
2.15	ENERGY BAND DIAGRAMS FOR (a) SEMIMETALS, (b) METAL, (c) INSULATOR AND (d) SEMICONDUCTORS	66
2.16	ENERGY BANDGAP AND LATTICE CONSTANT FOR GROUP III-V COMPOUNDS AND ALLOYS	66
2.17	CHART OF THE ELECTROMAGNETIC SPECTRUM	69
2.18	BASIC TRANSITIONS IN A SEMICONDUCTOR	70
2.19	THE ENERGY BAND DIAGRAM OF GaAs AND Si AS A FUNCTION OF MOMENTUM	71
2.20	DETECTIVITY (D*) AS A FUNCTION OF WAVELENGTH FOR VARIOUS PHOTOCONDUCTORS AND PHOTODIODES	73

LIST OF FIGURES (Cont'd)

2.21	THE ABSORPTION COEFFICIENT OF Ge, Si AND GaAs AS A FUNCTION OF PHOTON ENERGY	74
2.22	MEASURED THERMAL CONDUCTIVITY FOR SOME PURE SEMICONDUCTORS	75
2.23	MISSILE SPECTRAL BANDS	76
3.1	MODELLING THE F1 AZ PLUME ON MINI-GATE SETTING	78
3.2	RADIANCE OF F1 AZ PLUME WITH ATMOSPHERIC CORRECTIONS	78
3.3	F1 AZ PLUME RADIANCE WITHOUT ATMOSPHERIC CORRECTIONS	79
3.4	PLUME MODEL FOR AREA ESTIMATION	83
3.5	TYPICAL SHOCK WAVE PATTERNS IN EXHAUST PLUMES	84
4.1	FLARE ASSEMBLY	86
4.2	EXPERIMENTAL TEST SET-UP	87
4.3	ATMOSPHERIC CORRECTION OVER THE CALIBRATION AND MEASUREMENT PATHS	88
4.4	THE EXITANCE CURVE FOR INCREASING BLACKBODY TEMPERATURES AT A SPECIFIC WAVELENGTH	90
4.5	THE MEDIAN TEMPERATURE AND CORRESPONDING AREA	91
4.6	F1 AZ PLUME (MINI-GATE) IN RELATIVE STERANCE UNITS	102
4.7	SPECTRAL OUTPUT OF THE MTV FLARE COMPOSITION	103
4.8	SPECTRAL OUTPUT OF SF DBRAL FLARE COMPOSITION	104
4.9	SPECTRAL OUTPUT OF SF289 FLARE COMPOSITION	105
4.10	SPECTRAL OUTPUT OF SF914 FLARE COMPOSITION	106
4.11	SPECTRAL OUTPUT OF MF06 FLARE COMPOSITION	106
4.12	STRUCTURE OF CYANURIC ACID INDICATING THREE HNCO DECOMPOSITION FRAGMENTS	109
4.13	SPECTRAL OUTPUT OF THE IR M1A1 MTV FLARE	112

LIST OF FIGURES (Cont'd)

4.14	INTEGRATED RADIANCE IN THE RANGE 0.4 - 1.0 μm	115
4.15	INTEGRATED RADIANCE IN THE RANGE 1.0 - 2.0 μm	116
4.16	INTEGRATED RADIANCE IN THE RANGE 3.5 - 4.0 μm	117
4.17	RADIANCE VALUES (1st SET)	118
4.18	RADIANCE VALUES (2nd SET)	118
4.19	VISUAL-NEAR IR INTEGRAL (0.4 - 2.0 μm)	120
4.20	PEAK RATIOS IN THE RANGE 4.4 μm - 2.9 μm	121
5.1	TYPICAL TEST SET-UP	132
5.2	B61 TEST MOTOR ASSEMBLY	133
5.3	TEST PLATFORM FOR THE B61 TEST MOTORS	135
5.4	IR DATA IN THE RANGE 0.45 - 1.15 μm	137
5.5	IR DATA IN THE RANGE 1.3 - 2.4 μm	139
5.6	IR DATA IN THE RANGE 2.5 - 5 μm	139
5.7	IR DATA IN THE RANGE 8 - 12 μm	140
5.8	DATA FROM THE WHOLE IR SPECTRUM	141
5.9	UV DATA BETWEEN 230 AND 280nm	142
5.10	SET-UP FOR RADAR TRANSMISSION MEASUREMENTS	145
5.11	RADAR CROSS-SECTION MEASUREMENT OF ROCKET PLUMES	150

LIST OF PLATES

1	VIBRATION-ROTATION SPECTRUM OF HCl	54(i)
2	VIBRATION-ROTATION SPECTRUM OF CO	54(ii)
3	VIBRATION-ROTATION BAND OF H ₂ O BENDING VIBRATION	59(i)
4	VIBRATION-ROTATION BANDS OF H ₂ O STRETCHES	59(ii)
5	VIBRATION-ROTATION SPECTRUM OF CO ₂	59(iii)
6	ABSORPTION SPECTRA OF CO ₂ AND CO	82(i)

SECTION 1 INTRODUCTION

Many of the guided weapons systems belong to a certain group of missiles with heat-seeking target-tracking capabilities. This means that a potential target has to reach a certain minimum heat emittance threshold to be distinguished (locked-on) and followed (tracked) against the background. The heat source of a target is primarily caused by the exothermic combustion process of its own propulsion system. Aerodynamic heating may only come into effect for targets operating at high velocities.

The seeker head of a heat-seeking missile consists of an outer transparent dome that houses the moveable optical platform which collects and focuses the incoming heat waves on a sensor. The output signal of the sensor is fed to the autopilot for signal processing. The sensors normally operate in the 2 to 5 μ m electromagnetic wavelength range. This is also known as the middle infrared (IR) range.

In the event of the target being a fighter aircraft the exhaust plume of the jet engine would be the obvious heat source for an incoming missile to lock onto.

From an IR-following missile point of view it is thus important that the missile should "see" the aircraft plume and once locked onto it, must not be distracted from its mission path. An understanding and applying of distracting mechanisms opens the field of anti-missile/counter measures and decoy systems. One such decoy system is a flare being deployed by the threatened aircraft. The effectiveness of the decoy (flare) would be a direct measure of the capability of the flare to distract the incoming missile from the initially targeted aircraft. To succeed the decoy must, first, be attractive enough for the missile to lock on the flare and, second, the flare must move far enough away from the aircraft to

mislead the missile from its original flight path. This also ensures that the aircraft is removed from the field of view of the seeker as the seeker would by default resume a tracking mode after the flare is burnt out.

Years ago this method of luring an incoming missile was performed successfully by deploying a brute display of white hot combustibles. This approach would cover the total visible, ultraviolet (UV) and IR wavelength regions and subsequently the seeker heads of that era would lock onto virtually any object that is brighter and radiates more energy than the aircraft plume.

This is not the situation with later seeker versions, in which modern technologies are used in order to counter the effect of being decoyed by a robust point flame alone. Today the seekers are programmed to recognize the aircraft plume. This is done by analysing the electromagnetic spectrum of the plume. It is a very powerful tool and/or capability as the seeker can actually determine some chemical characteristics of the plume. If a flare is deployed it must have the same spectral characteristics as the aircraft plume, in order to be attractive enough for the homing missile. Modern seekers are also equipped with filter systems so that only certain band widths are used for detection. These filters also attenuate the effect of the background noise such as sunlight and cloud linings.

The IR flares that are currently employed by the South African Air Force (SAAF) are inadequate with respect to their ability to simulate successfully a jet aircraft plume. The situation worsens dramatically when the afterburner of the fighter aircraft is activated. It is customary to assume a scenario under which flares are deployed by fighter aircraft with afterburner(s) activated.

This study is firstly directed to establish the capability to manufacture a flare that, when deployed, must simulate a fighter aircraft plume. This means that the flame of the flare must have certain electromagnetic characteristics that would be attractive enough for a modern seeker to lock on to, and to remain locked, for long enough for the flare to operate successfully as a decoy.

To obtain such a capability it was necessary to measure, analyse and study the characteristics of the aircraft plume. Consequently strategies to simulate the characteristics of the plume by a flare, had to be developed.

The second part of this study is directed towards the characterisation of rocket motor plumes. Modern rocket motors have a tendency towards longer burn times. This holds specially for the sustainer propulsion units that could easily burn until impact. For such missile systems that are not fully autonomous after launch, or where a signal link from the weapon to a ground command centre is needed, it is important that the plume emission does not interfere with the data links. It would be of great value to the propellant scientist to be able to prescribe the correct propellant formulation for a specific weapon system i.e. without adverse affects on command and data signals.

For this reason the plumes of solid rocket motors were studied. A representative range of propellant formulations was selected and test fired in order to do the plume measurements. Initially the characterization of the plumes was done with respect to the different chemical species present. By characterizing the plumes originating from the different propellant formulations it would be possible to derive the effect of the plume's emission on the electromagnetic frequencies. By introducing this as a further parameter of consideration it would be possible to prescribe a more appropriate propellant formulation for a certain weapon system.

During these studies it was shown that certain propellant plumes can cause a total blockage or screening off of signal linkages, hence making positive communication virtually impossible.

A third aspect that was investigated was the detectability of missile plumes. This was achieved by applying heat-sensitive sensors to assist in early warning devices. One such application would be to detect a plume of a launched or incoming missile. This part of the study deals with the stealth aspects of a rocket plume. Again, if a missile must have good stealth properties, it must be known which chemical species are responsible for the specific electromagnetic behaviour in the plume.

SECTION 2 BACKGROUND AND THEORY

This study - which is of an interdisciplinary kind - required knowledge and the integration of knowledge of largely diverging fields of science. Hence a brief summary of background theory with regard to spectroradiometry, wave mechanics, energy levels and spectroscopy of molecules and solid phase materials, is given. Only those aspects relevant to this study are emphasized.

2.1 SPECTRORADIOMETRIC DEFINITIONS, QUANTITIES AND UNITS

The eventual engineering application of flares required a substantial recalculation of raw spectral data. The following spectrometric fundamentals and definitions were used [Leuschner, Section 2, 1989];

2.1.1 Plane Angle and Solid Angle

Plane angle (two dimensional)

$$\theta = \frac{S}{r}$$

with S = projected arc length and
r = radius. Units = radians (rad).

Solid angle (Three dimensional)

$$\omega = \frac{A}{r^2}$$

with A = projected arc length and $r^2 = \text{radius}^2$. Units = steradians (sr).

2.1.2 Radiometric Quantities

Radiant Energy

$$Q_e = \int \Phi_e dt \quad (\text{W.s})$$

with Φ_e = radiant flux (W) and
dt = time interval (s).

Radiant Flux

$$\Phi_e = \frac{dQ_e}{dt} \quad (\text{W})$$

= Flow or radiant energy per time interval.

Radiant Intensity

$$I_e = \frac{dQ_e}{d\omega} \quad (\text{W.sr}^{-1})$$

= Radiant flux per unit solid angle.

Radiant Flux Density

Exitance

$$M_e = \frac{d\Phi_e}{dA} \quad (\text{W.m}^{-2})$$

= Radiant flux leaving unit area.

Irradiance

$$E_e = \frac{d\Phi_e}{dA} \quad (\text{W.m}^{-2})$$

= Radiant flux falling on unit area.

Radiance

$$L_e = \frac{d^2\Phi_e}{d\omega \cdot dA \cdot \cos\theta} \quad (\text{W.sr}^{-1}.\text{m}^{-2})$$

with $dA \cdot \cos\theta =$ projected area.

2.1.3 Conservation of Energy

The sum of absorbed, reflected and transmitted flux must equal the incident flux
i.e.

$$\alpha_e + \rho_e + \tau_e = 1$$

2.1.4 Emissivity

$$\varepsilon = \frac{Q_e}{Q_{Be}}$$

with; $Q_e =$ Flux emitted by body at temp T,

$Q_{Be} =$ Flux emitted by blackbody at same temp T and a

Blackbody = Perfect radiator and perfect absorber.

2.1.5 Blackbody Radiation (Planck's Law)

The spectral radiant exitance for a blackbody is given by;

$$M(T, \lambda) = \frac{2\pi hc^2}{\lambda^5 (\exp(hc / \lambda kT) - 1)}$$

with; λ = wavelength (m)

h = Planck's constant
= 6.626196×10^{-34} (W.s² or J.s)

c = velocity of light
= 2.9979×10^8 (m.s⁻¹)

k = Boltzmann's constant
= 1.380622×10^{-23} (W.s.K⁻¹ or J.K⁻¹)

T = absolute temperature of the surface
= temp (°C) + 273.16.

2.1.6 The Irradiance (E_I) Falling on a Detector

The irradiance is given by the following equation;

$$E_\lambda = \frac{A}{\pi r^2} \int_{\lambda_1}^{\lambda_2} M(T, \lambda) \cdot \varepsilon(\lambda) \cdot \tau(\lambda) \cdot d\lambda$$

with;

A = area of source

r = distance between the source and detector

$M(T, \lambda)$ = spectral radiant exitance

ε = emissivity

τ = atmospheric transmittance

λ_1 and λ_2 refers to the integration over the operative wavelengths of the specific detector used.

2.1.7 Stefan-Boltzmann Law

The total radiant exitance over the whole wavelength band is;

$$M_e = \int_0^{\infty} M_{e\lambda} d\lambda = \sigma T^4 \quad (\text{W}\cdot\text{m}^{-2})$$

where σ = Stefan-Boltzmann constant

$$= 5.6686 \times 10^{-8} \quad (\text{W}\cdot\text{m}^{-2}\cdot\text{K}^{-4}).$$

2.1.8 Wien's Displacement Law

The wavelength at which maximum spectral radiant exitance occurs can be obtained by differentiating Planck's Law and setting it equal to zero. The following is obtained;

$$\lambda_{\max} = \frac{2897.8 \times 10^{-6}}{T} \quad (\text{m})$$

$$= \frac{2897.8}{T} \quad (\mu\text{m}).$$

2.1.9 Atmospheric Transmittance

[RCA, Electro-Optic Handbook, 1974]

When a source emits radiation having an intensity I , and its path is through a vacuum, the irradiance E at some distance R from the source may be calculated according to the inverse square law. Thus

$$E = \frac{I}{R^2} \quad (\text{W} \cdot \text{sr}^{-1} \cdot \text{m}^{-2})$$

If, however, the path is through a gaseous atmosphere, some of the radiation is lost by scattering and some by absorption. Therefore;

$$E = T_a \frac{I}{R^2} \quad (\text{W} \cdot \text{sr}^{-1} \cdot \text{m}^{-2})$$

where;

T_a = the atmospheric transmittance over a designated path (T_a has a value of less than unity).

Atmospheric transmittance T_a is a function of many variables: wavelength, path length, pressure, temperature, humidity, and the composition of the atmosphere. The factor T_a defines the decrease in radiant intensity due to absorption and scattering losses along the atmospheric path.

The horizontal path transmittance of the atmosphere T_a over a path length R for radiation of wavelength λ may be expressed by;

$$T_a = \exp(-\sigma R)$$

where σ is the spectral attenuation coefficient.

Figure 2.1 shows the atmospheric transmittance (%) for a horizontal path of approximately 30m at sea level. The complicated structure of this Figure is due to the vibration-rotation spectral properties of the CO_2 and H_2O molecules in the atmosphere. Understanding of these properties as well as of the spectral properties of vibrationally excited CO_2 and H_2O molecules, was crucial in the development of new lasers.

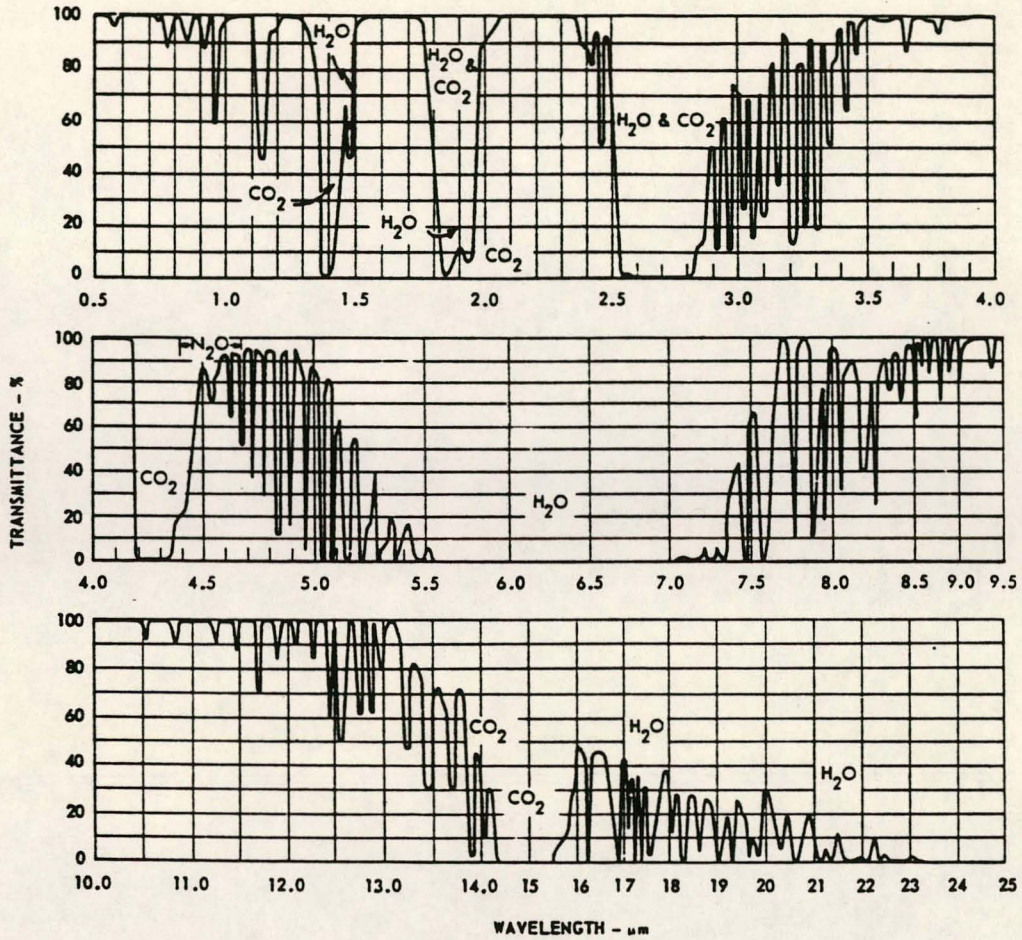


FIGURE 2.1 TRANSMITTANCE OF 30m HORIZONTAL AIR PATH AT SEA LEVEL [RCA]
 (Containing 5.7mm precipitable water at room temperature).

2.2 APPARATUS AND PROCEDURE FOR OBSERVATIONS

Very little information was available from the literature on spectral characteristics of jet aircraft, rocket plumes and flames of decoy systems. Characterisation of these over the ultraviolet, visible and infrared regions was a very demanding task. This was done in conjunction with the Aerotek division of the CSIR. As a result a valuable bank of spectral data was acquired.

A SR5000 spectral radiometer and a ultraviolet (UV) radiometer (a custom built three channel radiometer) were used for measurements. Thermal imaging cameras (AGEMA 900) were used for source area and temperature estimations in the infrared bands, while an imaging UV radiometer and a video camera were used in the ultraviolet and visible range.

2.2.1 The SR5000 Spectral Radiometer

This apparatus was extensively used throughout this investigation. Measurements were made in the $0.4\mu\text{m}$ to $2.5\mu\text{m}$ range (with a silicon and lead sulphide, Si/PbS detector set) and the $2.5\mu\text{m}$ to $14.5\mu\text{m}$ range (indium antimonide and cadmium mercury telluride, InSb/CMT detector set). Appendix A contains the spectral response of the detectors used for the infrared measurements.

The distances between the SR5000 and the test point were measured. Normally these ranges were 200 to 500m. This distance was used in atmospheric transmission calculations. The same detector field of view (FOV) was used for experiments and calibration in the case of the Si/PbS set, while appropriate FOV's were chosen for the InSb/CMT region.

Adequate time was allowed for the detectors to cool down in the case of the Si/PbS detectors, while the InSb/CMT wafer detector was cooled down by means of liquid nitrogen (77K).

Time allowed for one filter wheel scan was set to 0.5 seconds at an internal chopper frequency of 200Hz for the Si/PbS detector. In the case of the faster InSb/CMT detector, the scan speed was set to one scan per 0.5 seconds at an internal chopper frequency of 750Hz.

Atmospheric measurements were made regularly of temperature, humidity and air pressure during the tests. It was found that the temperature at night varied only by a few degrees (19°C - 22°C). The humidity changed from approximately 70% - 80%, while the air pressure was almost constant at 1015mbar.

The very high absorption in the band between 2 μ m and 3 μ m is due mainly to H₂O and some CO₂ absorption. Water is the dominant absorption species at 6 μ m. For spectral SR5000 measurements the minimum absorption in these bands was limited to 1%, thus preventing division by numbers close to zero and resultant emissivities larger than unity or too large temperature predictions.

2.2.2 SR5000 Calibration

The SR5000 radiometer was calibrated in the laboratory using a calibrated blackbody placed 3m away. This distance was used in the atmospheric calculation for the calibration path transmittance.

The radiometer was calibrated for all the field of view (FOV) settings used during the tests. It was found that a temperature of 700°C had to be used on the 6 mrad FOV setting to prevent saturation of the radiometer InSb/CMT detector set. The

measured voltages were exported in ASCII format and used as the voltage output for irradiance by blackbody calibration. Theoretical radiance values were calculated at the two different temperatures and those values were used as the theoretical blackbody calibration output values. The atmospheric parameters (humidity, air pressure and temperature) that were recorded during measurements, were used to generate a number of atmospheric transmission files. These were used during calculation to correct for the path transmittance during measurement.

During the first attempt to do these measurements with the SR5000 the blackbody temperature was set to 1173K for calibration of the first detector set (Si/PbS) and to 773K for that of the second detector set (InSb/CMT).

2.2.3

The UV Narrow Band Radiometer

A custom-built three channel ultraviolet (UV) radiometer was used for the UV photon count measurements and the UV data obtained was used mainly for the missile propellant plume studies. The three UV channels were;

channel 0 - wide band: 230 to 280nm,

channel 1 - narrow band: 258 to 262nm and

channel 2 - narrow band: 251 to 256nm.

These filter bands are graphically presented in Figure 2.2 [Roodt, 1992].

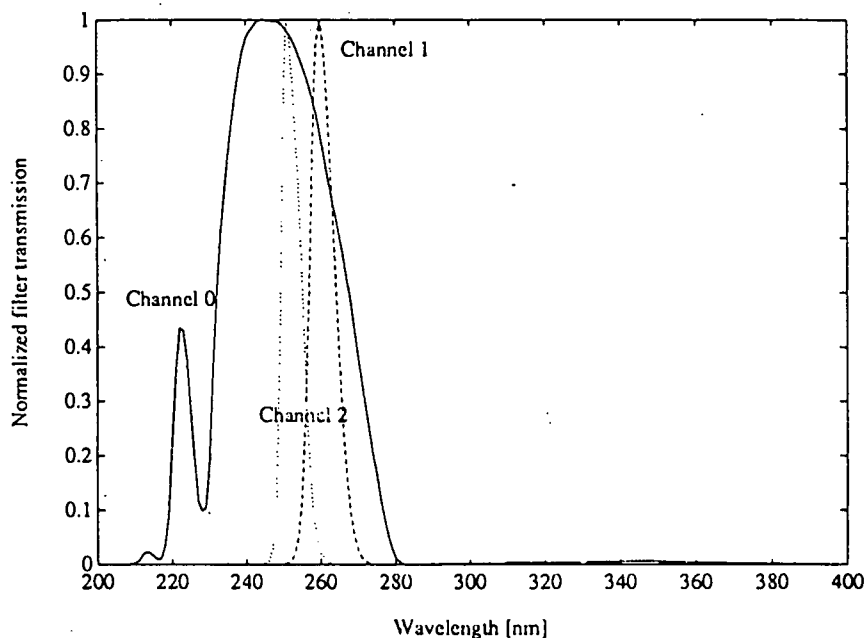


FIGURE 2.2 UV RADIOMETER NORMALIZED FILTER BANDS

It was safe to assume that the UV radiation incident from the background was negligible and it was therefore not necessary to make any subsequent corrections during data processing.

On the Y-axis a photon incidence level higher than that capable of causing saturation of the equipment was selected as an upper limit for the graphical representation of the data, and one at the same level as the background radiation was selected as the lower limit. The X-axis of all the graphs was labelled in seconds with a range of 15s. In this way it was ensured that all the graphs could be plotted on a similar set of axes, allowing the different events to be compared.

In order to determine the average photon flux per 8ms during the combustion, it was decided that the part of the combustion best representing the average would

be chosen for events with a well-defined single-stage characteristic. For those events where the flame spluttered and seemed to burn in two distinctly different stages, the higher stage was chosen, unless it appeared that one of the other stages lasted for a significantly longer period than the higher one.

Reference graphs were generated (refer to Appendix B) for each of the three channels on all three days. These graphs were created by fitting a blackbody curve to the same Y-axis scale as the data. By so doing, a suitable range of temperatures was selected. Once the temperature range was selected for the X-axis, a range of greybodies was plotted, ranging in emissivity from 0.1 to 1.0 in units of 0.1.

For each event, three processed UV data graphs were obtained, one for each channel. The average photon flux value obtained from such a graph was then read off the Y-axis of the corresponding reference graph for the particular channel and date. The value was then read across onto the plotted greybody curves. A minimum temperature value was then read off the X-axis for the emissivity value of 0.1.

Three sets of temperature ranges were obtained for every event. In order to determine a suitable temperature value for each event, the lowest minimum temperature value for the event was chosen. The maximum temperature corresponding to it was chosen to represent the event, and an emissivity of 0.1 allocated to it. The same temperature value on the other channels cross-referenced to the photon count rate yielded emissivity values below 1.0. Although different temperatures and emissivities could have been chosen to represent each event, the use of this method guaranteed consistent results which can be compared with each other.

2.2.4 UV Radiometer Calibration

The UV Radiometer was calibrated by measuring the count rate from a known source at specified distances, namely 10m, 20m, 30m, 40m and 50m. The known source used was a calibrated quartz lamp. Measurements were made with all three channels of the UV Radiometer.

These calibration measurements were then duplicated by calculating the theoretical number of photons incident upon each of the three apertures every 8ms, from the known source, taking into consideration all the different factors such as the atmospheric transmittance on the day of calibration, the filter and photomultiplier tube attached to the specific channel, and the size of the aperture used for the specific channel.

The calculated photon count values, and the measured count rates were then tabulated, and a regression program was then run on the two sets of data.

Three regression equations were thus obtained, one for each channel. These equations could then be applied to the data measured in counts per 8ms, allowing the data to be converted into incident photons per 8ms.

Proper stability of the photomultiplier tubes in the UV radiometer was ensured by running the system on dark current setting (tubes closed) for approximately 45 minutes.

2.2.5 AGEMA 900 Imaging Radiometers

Two Thermovision 900 Series imaging radiometers by AGEMA Infrared Systems were used for plume image recordings in the 3 to 5 μ m and 8 to 12 μ m ranges. A

radiometer consists of a scanner, microprocessor, keyboard and video monitor. Each scanner has two lens systems namely, 10° and 2.5° field of view (FOV) for the short-wave instrument and a 10° and 5° FOV lens for the long-wave scanner. These scanners can be fitted with the following standard filters;

- | | |
|-------------------------------|---|
| Flame (FLM) | - used when measuring hot objects through flames, e.g. furnaces. |
| Atmospheric (ATM) | - used when measuring objects hotter than 200°C from a distance. |
| Sun Reflex (SRX) | - used for suppressing reflected short-wave radiation below 3.4µm, e.g. from the sun. |
| High Temperature Filter (HT1) | - used when measuring objects up to 2000°C. |

Note: The abbreviations for the different filters are given in brackets and are used as such where applicable.

2.3

WAVE MECHANICS

The energy levels - and transitions between energy levels - of the species (atomic and molecular), in the plumes of aircraft and missiles as well as in the flames of flares, play an important part in their characteristics. Energy levels in matter are explained by the vast subject of wave (quantum) mechanics. In order to explain which energy levels exist in the species relevant to this study a very short introduction to wave mechanics is given. This leads to the discussion of the relevant spectroscopic properties.

2.3.1 The Wave Nature of Electrons

[Blinder, 1996, Hutchison, 1968]

Electromagnetic radiation cannot be regarded as a smooth continuous wave but as a shower of discrete packets of energy, each named a photon. The essential feature of this hypothesis is that the radiation can exchange energy with a system only in discrete units of a definite size. Energy changes smaller than that corresponding to one quantum are not permitted. Planck proposed that the energy E of a single quantum should be related linearly to the frequency ν of the radiation by the equation

$$E = h \nu$$

where h is Planck's constant = 6.6256×10^{-34} Joule sec.

The proposal found almost immediate application and support in the photoelectric effect. It is sufficient to say here that the evidence was that an electron in a solid could gain energy from a monochromatic light beam only in definite amounts, and that this quantity of energy depended linearly on the frequency of the light.

The properties of a particle should be represented by those of the de Broglie wave, which can be represented in a one-dimensional space, generally by the wave function.

$$\Psi = A \cdot \cos(Kx - \omega t) + B \cdot \sin(Kx - \omega t)$$

with $K = \frac{2\pi}{\lambda}$ = wave number,

$\omega = 2\pi\nu$ and A and B are constants.

$|\Psi|^2 dx dy dz =$ probability of finding the particle in a specific volume and

Total Energy = Kinetic energy + Potential Energy (V).

With this as a basis and the incorporation of a certain number of postulates the Schrödinger time-independent equation can be derived, namely;

$$\frac{\partial^2 \Psi}{\partial x^2} + \frac{8\pi^2 m}{h^2} (E - V) \Psi = 0$$

By solving the Schrödinger equation for the boundary conditions;

$$x = 0, \quad \Psi = 0 = A \quad \text{and}$$

$$x = a, \quad \Psi = 0 = B \sin \alpha a$$

$$\text{with,} \quad \alpha^2 = \frac{8\pi^2 m}{h^2} E$$

and A and B the constants of the space-dependent part of the solution;

$$\Psi = A \cos \alpha x + B \sin \alpha x$$

These conditions are met only if $\alpha a = n\pi$, where n is an integer, $n = 1, 2, 3, \dots$

Thus solutions of the Schrödinger equation exist only if E is confined to the magnitudes;

$$E_n = \frac{n^2 h^2}{8ma^2} \quad (n = 1, 2, 3, \dots)$$

This demonstrates that the bound electron may only have certain energies or energy levels. The levels for this particular problem are shown in the following Figure. This concept of energy levels in general plays a dominating role in the

study of the electronic properties of matter, the essential feature being that the solution for Ψ will exist only if the energy of the electron has one of a number of definite values. These values are represented by the following energy level diagram (Figure 2.3):

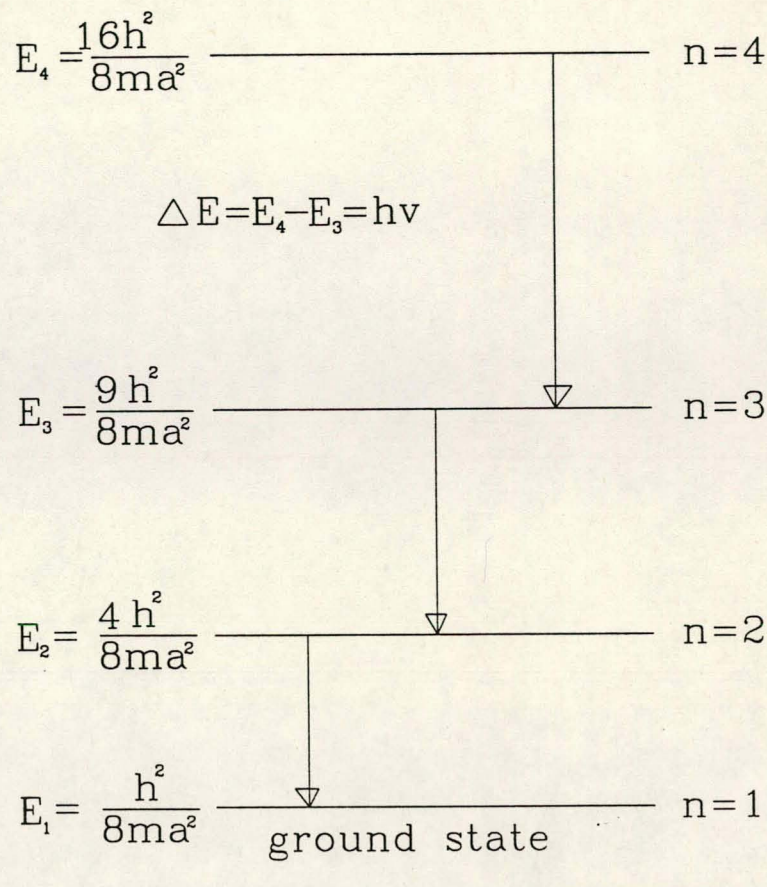


FIGURE 2.3 THE ENERGY LEVEL DIAGRAM OF A PARTICLE IN A ONE-DIMENSIONAL BOX

Since the electron can exist only in certain energy levels, the energy that is emitted from or absorbed by the system can have only certain discrete values indicated by the arrows in the diagram. This uniqueness of transition energy is one of the most striking features of atomic physics. It is also conveniently consistent with Planck's quantum postulate concerning radiation since the quanta correspond to the energy changes between levels.

The model of a particle in an one-dimensional box can easily be extended to a three-dimensional box where the translations of a particle in the x, y and z directions are considered. Solving the Schrödinger equation for this model is achieved by separating the three variables. This leads to an energy equation involving three independent quantum numbers. This equation is also applicable to molecular systems and is an expression of the translation energy of molecules.

2.4

ENERGY LEVELS OF ATOMS

[Alberty, 1987, Daniels, 1962, Daniels, 1966]

The electronic energy levels for atoms are obtained by solving the relevant Schrödinger equation. This is a severe mathematical problem and can be solved exactly only for the hydrogen atom and leads to the orbital energies of this atom. For more complicated atoms approximate methods have to be employed e.g. the self-consistent field (SCF) methods. This results in atomic orbital energies. However, in order to explain the fine structure of atomic emission and absorption spectra the quantum mechanics of orbital and spin angular momenta and their coupling must be invoked.

In general a specific state of an atom is characterized by a so-called term symbol. This term symbol has the form $2S+1L_J$ and is preceded by the electronic configuration i.e. the occupancy of the atomic orbitals. S is the quantum number for the total spin angular momenta of the electrons, L is the quantum number for the total orbital angular momentum and J is the quantum number for the total angular momentum of the electrons. The energies of a vast number of excited electronic states of atoms and free ions have been determined and compiled [Moore, 1958].

Transitions between electronic states are governed by the selection rules;

for $\Delta n \geq 1$, $\Delta S = 0$, $\Delta L = 0, \pm 1$ but $L = 0$ cannot combine with $L = 0$ and $\Delta J = 0, \pm 1$ but $J=0$ cannot combine with $J=0$.

Emissions by atomic species in excited electronic states are relevant to this investigation, since chemical reactions in, for example flares, may result in atoms (especially metal atoms) in such states.

2.5 ENERGY LEVELS OF MOLECULES

[Alberty, 1987, Barrow, 1966, Blinder, 1969, Daniels, 1962, Daniels 1966]

2.5.1 Introduction

Energy level diagrams of molecules can be extremely complicated due to the various contributions to the internal energy.

The internal energy of a molecule in a certain state may be considered, according to the Born-Oppenheimer approximation, to be made up of contributions from rotational energy E_{rot} , vibrational energy, E_{vib} , and electronic energy, E_{el} ,

$$E = E_{\text{rot}} + E_{\text{vib}} + E_{\text{el}}$$

Actually this division into separate contributions is not exact; for example, the rotational energy depends somewhat on the amount of vibrational energy because the mean internuclear distance, and hence the moment of inertia, depends on the vibrational energy.

The state of an isolated molecule may be specified by using a series of quantum numbers, one for the rotational level, one for the vibrational level and one for the electronic level. In the process of absorption or emission there is a change in this set of quantum numbers. For example, if a molecule is in the ground electronic level and the zero-point vibrational level has some particular amount of rotational energy, absorption of a photon may raise the molecule to higher electronic, vibrational, or rotational levels.

There are many transitions which might give rise to absorption or emission, but only those satisfying certain selection rules are allowed.

Electronic, vibrational, and rotational changes may all occur upon the absorption or emission of a single photon, and so the equation $E = h\nu$ may be written

$$h\nu = (E_{el}^I - E_{el}^{II}) + (E_{vib}^I - E_{vib}^{II}) + (E_{rot}^I - E_{rot}^{II}),$$

where the upper state is represented by a single prime, and the lower state by a double prime. A fact which considerably simplifies the interpretation of spectra is that, in general,

$$(E_{el}^I - E_{el}^{II}) \gg (E_{vib}^I - E_{vib}^{II}) \gg (E_{rot}^I - E_{rot}^{II})$$

if all three types of changes are involved in a certain transition. Consequently, rotational, vibrational, and electronic transitions occur in different regions of the electromagnetic spectrum. Since only small quanta of energy are required to change from one rotational energy level to another, these changes may be studied by themselves in the far-infrared and microwave regions of the electromagnetic spectrum ($\lambda > 30\mu\text{m}$). Vibrational changes result from absorption in the near-infrared region. For each vibrational level, however, there are many rotational levels, and so bands of closely spaced lines are obtained.

Electronic changes produce absorption and emission in the visible and ultraviolet regions. Bands of closely spaced lines or even an apparent continuum of absorption may be obtained because of the closely-spaced lines due to the numerous vibrational and rotational changes.

In order to get clearer ideas of the various energy level diagrams, their origins are described under the headings: Rotational, Vibrational and Electronic Spectra.

2.5.2 Rotational Spectra

The kinetic energy of a point mass is

$$E = \frac{1}{2} mv^2$$

but if the point mass is rotating about a point it is more useful to express the kinetic energy in terms of the angular velocity ω in number of radians per second. For a particle moving in a circle with radius r and having a velocity v the particle makes $v/2\pi r$ revolutions per second or $2\pi(v/2\pi r) = v/r = \omega$, in radians per second. Substituting $v = r\omega$ in the first equation yields

$$E = \frac{1}{2} mr^2\omega^2 = \frac{1}{2} I\omega^2$$

where the moment of inertia I is given by mr^2 . For rotational motion I takes the place of m in the equation for translation motion and ω takes the place of v .

A rigid diatomic molecule rotates about the centre of mass of the molecule, and if the distances of the two atoms (of mass m_1 and m_2) from the centre of mass are represented by r_1 and r_2 the rotational energy is given by

$$E_{\text{rot}} = \frac{1}{2} \omega^2 (m_1 r_1^2 + m_2 r_2^2) = \frac{1}{2} I \omega^2$$

Thus the moment of inertia for a diatomic molecule is given by

$$I = m_1 r_1^2 + m_2 r_2^2$$

It is more convenient to express the moment of inertia in terms of the distance between the two atoms $r = r_1 + r_2$. As illustrated in Figure 2.4, the centre of mass is located so that

$$r_1 m_1 = r_2 m_2$$

Combining this equation with $r = r_1 + r_2$ yields

$$r_1 = \frac{m_2}{m_1 + m_2} r$$

$$r_2 = \frac{m_1}{m_1 + m_2} r$$

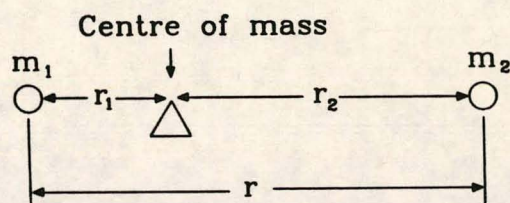


FIGURE 2.4 ROTATION OF A DIATOMIC MOLECULE

By substitution the following is obtained

$$I = \frac{r^2}{\frac{1}{m_1} + \frac{1}{m_2}} = \mu r^2$$

where μ , the reduced mass, is defined by

$$\mu = \frac{m_1 m_2}{m_1 + m_2}$$

or

$$\frac{1}{\mu} = \frac{1}{m_1} + \frac{1}{m_2}$$

Thus the moment of inertia of a diatomic molecule is equivalent to that of the reduced mass revolving at a distance r from the axis.

Classically, a rotating object can have any rotational energy, but according to quantum mechanics the angular momentum J is quantized in units of $h / 2\pi$, as from the Bohr theory of the hydrogen atom. Solution of the Schrödinger equation for the rigid rotator shows that the possible angular momentum $I\omega$ of a diatomic molecule is given by

$$I\omega = \frac{h}{2\pi} \sqrt{J(J+1)} \quad J = 0, 1, 2, \dots$$

where J is the angular momentum quantum number. Substitution of the equation for the rotational energy yields

$$E_{\text{rot}} = \frac{1}{2} I\omega^2 = \frac{(I\omega)^2}{2I} = \frac{h^2}{8\pi^2 I} J(J+1)$$

The rotational energy is normally expressed in terms of the rotational constant B of the molecule and as defined by the following equation has the dimensions of a wavenumber and is expressed in m^{-1} or cm^{-1} . The energy of a rotational state is thus obtained by division by hc . This yields;

$$E_{\text{rot}} = BJ(J+1) \quad \text{with } B = \frac{h}{8\pi^2 cI}$$

The corresponding energy level diagram is given in Figure 2.5:

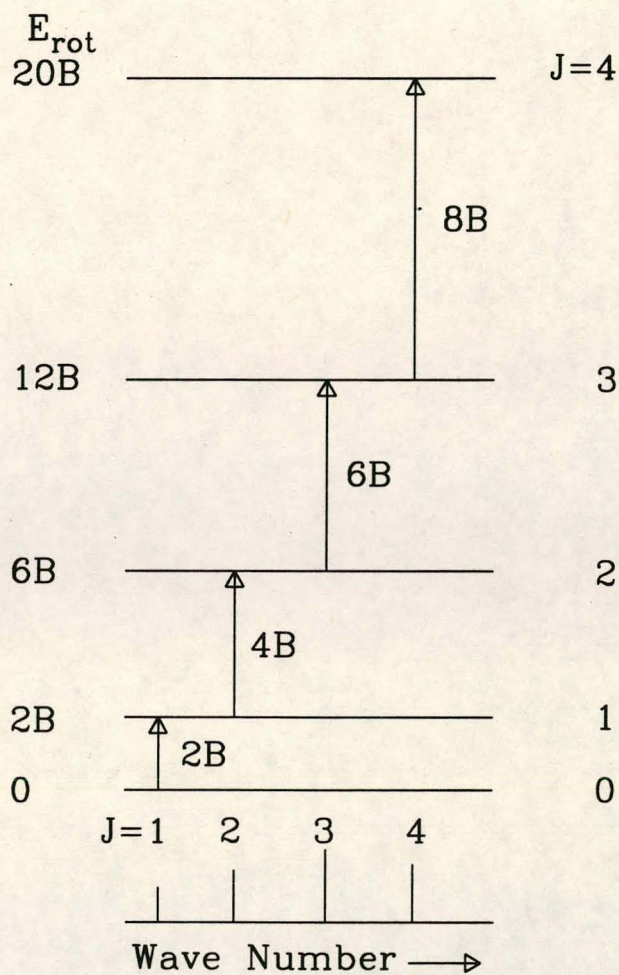


FIGURE 2.5 ENERGY LEVEL DIAGRAM

It can be shown that the only transitions which are allowed between the rotational levels are those for which $\Delta J = \pm 1$. That is, $+1$ for absorption, and -1 for emission. The frequency in wave numbers for a transition from a level with quantum number $J-1$ to the level J is given by;

$$\bar{\nu} = E^J - E^{J-1} = B\{J(J+1) - J(J-1)\} = 2BJ$$

where J , the quantum number for the upper level, can only have values of 1,2,3, Thus the frequency of the radiation absorbed is directly proportional to the quantum number of the rotational level to which the molecule is excited by the absorption of a quantum of radiation. As a result we find a series of equally spaced lines in the far-infrared and microwave spectra of diatomic molecules. This is illustrated by Atkins, 1990, in Figure 2.6:

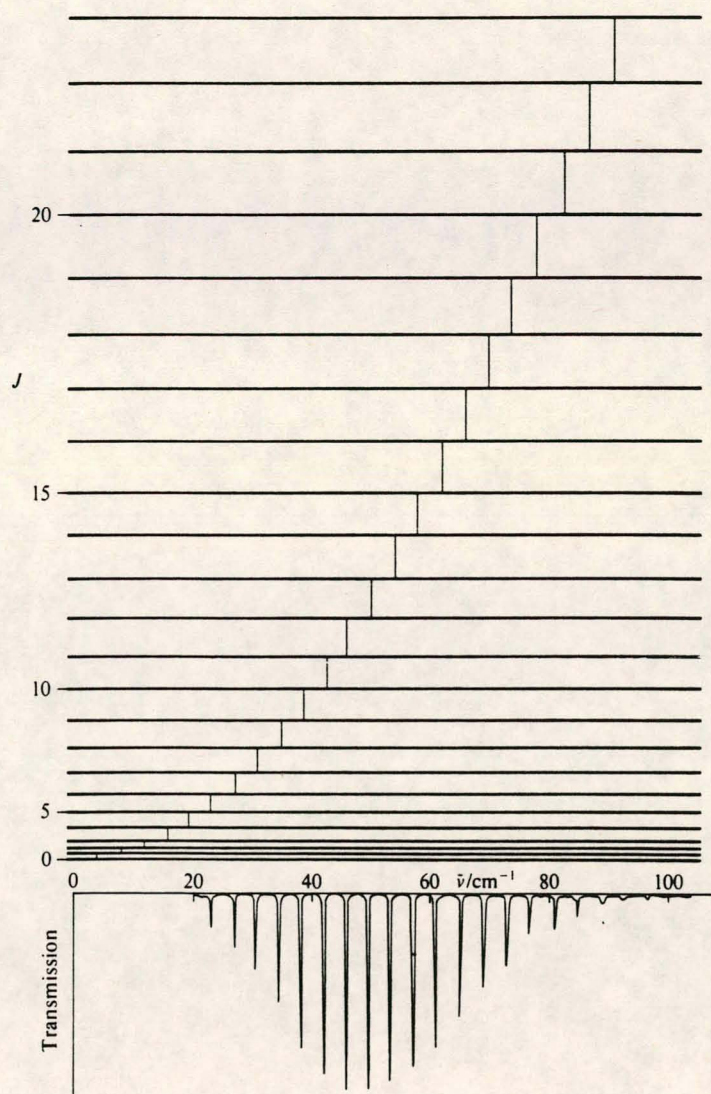


FIGURE 2.6 PURE ROTATIONAL ENERGY LEVEL DIAGRAM OF A LINEAR ROTOR

The moments of inertia of isotopically substituted molecules are appreciably different, and therefore a separate series of lines is found for each isotopically different species of a given molecule.

A molecule may be changed from one rotational level to a higher one by the absorption of a photon of electromagnetic radiation only if the molecule has a permanent dipole moment. Classically, electromagnetic radiation may be produced by a rotating dipole, since this rotation produces an alternating electric field. Since molecules such as N_2 and CO_2 do not have electric dipole moments, they do not interact with the electric field of electromagnetic radiation and thus do not show pure rotational spectra as do molecules like HCl and H_2O , which have electric dipole moments. Whether or not a molecule may have a dipole moment depends on its symmetry.

The O_2 molecule, which has no electric dipole moment, is an important exception. This molecule has two unpaired electrons, and consequently a magnetic dipole moment. The magnetic dipole moment can interact with the magnetic field of electromagnetic radiation. Therefore, O_2 has a rotational spectrum.

The rotational spectroscopic inactivity of N_2 and CO_2 , and the activity of O_2 and H_2O have very important implications for the attenuation of radar waves in the atmosphere. This can clearly be seen in Figure 2.7. Since the water molecule has three different rotational axes with three different rotational constants, it will absorb in three different regions. Each peak consists of closely spaced lines as in Figure 2.6, but only the outer contour is observed.

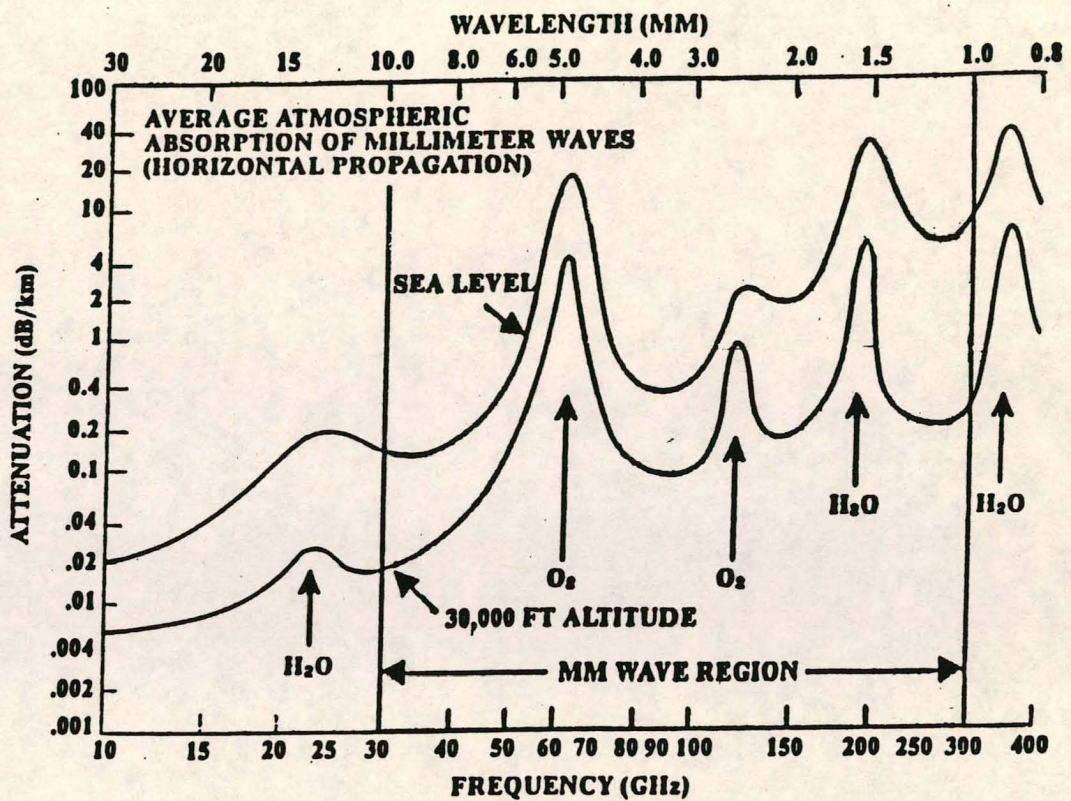


FIGURE 2.7 ATMOSPHERIC ABSORPTION OF MILLIMETRE WAVES

Radicals and ions of diatomic and polyatomic species present in missile plumes as a result of incomplete combustion have magnetic dipoles and can absorb radar waves of correct wave length.

The relative intensities of rotational lines are also dependent on the relative populations of the levels in the initial state. The relative populations must, under thermal equilibrium conditions, adhere to the Boltzmann distribution law i.e.

$$\frac{N_J}{N_0} = (2J + 1) \exp\left(-\frac{\Delta E_J}{k_B T}\right),$$

where N_J = population of rotational level J and

N_0 = population of rotational level J=0

$\Delta E_J = BJ(J+1)$

k_B = Boltzmann constant

= 1.380622×10^{-23} (J.K⁻¹)

T = equilibrium temperature.

Thermal equilibrium cannot prevail in the plumes of aircraft and missiles because of the shock heating that occurs when the products of combustion pass through the shock fronts. Refer to figure 3.5 and photographic material in Appendix K. Consequently the relative intensities of rotational lines must change for species present in these plumes.

2.5.3

Vibrational Spectrum

Vibrational spectra originate from changes in vibrational energy levels. Absorption and emission spectra of this type, however, are shown only by molecules for which a change in dipole moment accompanies the vibrational motion. A fluctuating dipole moment offers a mechanism for interaction between the molecule and electromagnetic radiation. Homonuclear diatomic molecules such as H₂ and N₂ have zero dipole moment for all bond lengths and therefore do not show vibrational spectra. In general, heteronuclear diatomic molecules have dipole moments which depend on internuclear distance, and so they have vibrational spectra. For molecules with more than two atoms it is not necessary for the molecule to have a permanent dipole moment, since certain vibrations may involve the oscillation of a dipole moment about zero.

The vibrational energy levels are given by;

$$E_{\text{vib}} = (v + \frac{1}{2})h\nu_0 \quad (\nu_0 = \frac{\pi}{2} \sqrt{\frac{k}{m}})$$

where v is the vibrational quantum number, ν_0 the fundamental vibration frequency and k is the force constant. This equation is obtained by solving the Schrödinger equation for the harmonic oscillator, assuming that a diatomic molecule's vibrational motion can be approximated by a harmonic motion.

With this equation the difference in vibrational energy between two levels with vibrational quantum numbers v and v' is given by

$$\Delta E = E_{\text{vib}} - E'_{\text{vib}} = (v + \frac{1}{2})h\nu_0 - (v' + \frac{1}{2})h\nu_0 = (v - v')h\nu_0$$

The vibrational energy diagram for a diatomic molecule is given in Figure 2.8:

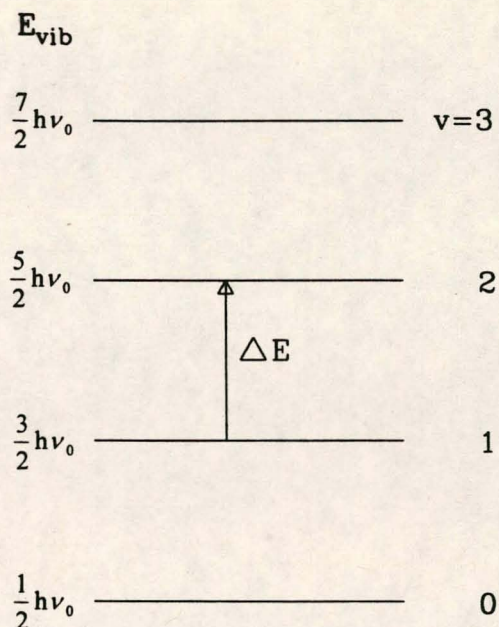


FIGURE 2.8 VIBRATIONAL ENERGY DIAGRAM FOR A DIATOMIC MOLECULE

The selection rule for a transition between energy levels for a harmonic oscillator is $\Delta v = \pm 1$. That is, +1 for absorption and -1 for emission. Since most molecules are in the ground vibrational state at room temperature, absorption will result in the transition $v = 0 \rightarrow 1$. This is the only transition expected on absorption for a quantum mechanical harmonic oscillator. Molecules are anharmonic oscillators and additional transitions are observed, but at lower intensities. These additional transitions violate the selection rule $\Delta v = \pm 1$ and are said to be forbidden. Larger changes in vibrational quantum number are not forbidden for anharmonic oscillators.

These transitions are referred to as overtones and play a very important part in, for example, the transmittance of a horizontal air path (refer to Figure 2.1).

2.5.4 Vibration-Rotation Spectra

A diatomic molecule can be approximated by a combination of a harmonic oscillator and a rigid rotor. This results in a complicated vibrational rotational energy level diagram (refer to Figure 2.9).

A diatomic molecule in a specific vibrational level may be in one of several rotational levels. The populations of the various rotational levels at equilibrium are determined by the Boltzmann distribution. When a diatomic molecule in the $v=0$ level absorbs a quantum of radiation which is sufficiently large to raise it to a higher vibration level, the molecule has to go to a different rotational sublevel of the higher vibrational state because the selection rule for the rotational quantum number J is $\Delta J = \pm 1$. The possible transitions are shown in Figure 2.9 where the lower group of rotational levels all belong to the $v = 0$ vibrational level and the upper group of rotational levels all belong to the $v = 1$ vibrational level.

The energy, in wave number (by division by hc), before absorption of a quantum is given by;

$$E = \bar{\nu}_0 \left(v + \frac{1}{2} \right) + BJ(J+1) \quad \text{with } \bar{\nu}_0 = \frac{\nu_0}{c}$$

and similarly the energy after absorption of a quantum is given by;

$$E^1 = \bar{\nu}_0 \left(v^1 + \frac{1}{2} \right) + BJ^1(J^1 + 1)$$

The frequency of an absorption line in wave numbers is given by;

$$\bar{\nu} = E^1 - E$$

The transitions for which $\Delta J = -1$ produce the lines in the so-called P branch of the spectrum. By substitution and with $v = 0$, $v^1 = 1$, and $J^1 = J - 1$, the wave numbers of the lines in the P branch of the spectrum are obtained.

$$\bar{\nu}_p = \bar{\nu}_0 - 2BJ$$

where J is the rotational quantum number of the initial state and may have values of 1,2,3.....

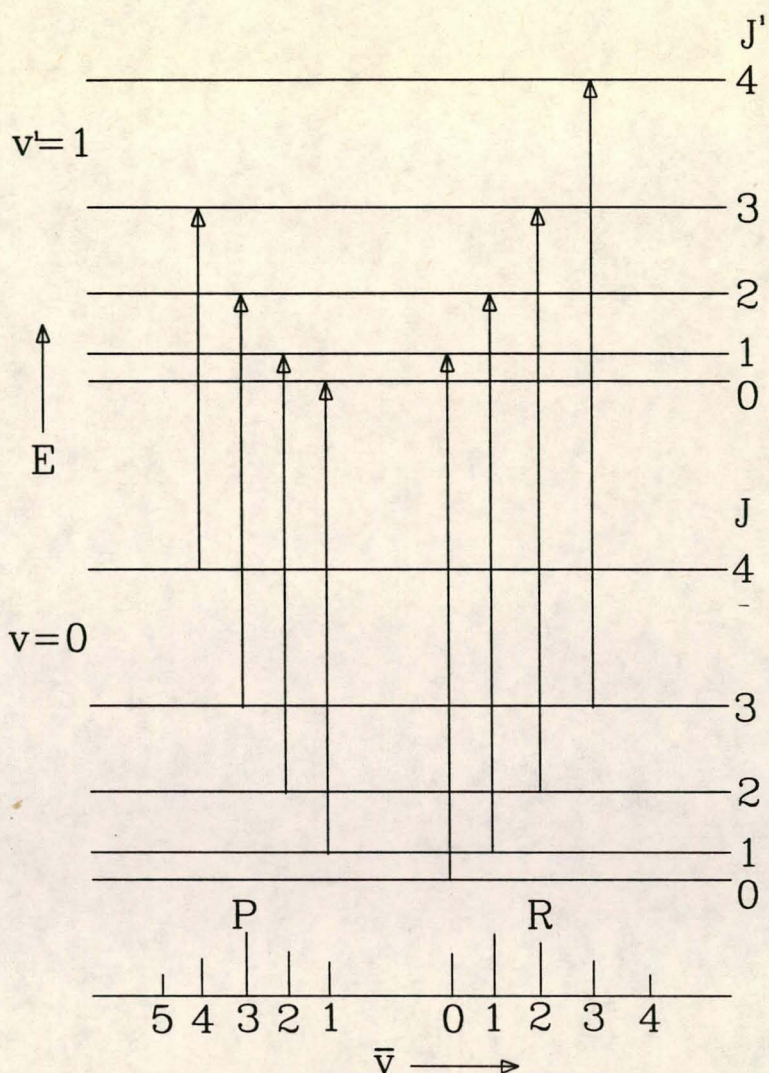


FIGURE 2.9 THE VIBRATIONAL AND ROTATIONAL ENERGY LEVEL DIAGRAM FOR A DIATOMIC MOLECULE AND THE TRANSITIONS OBSERVED IN THE VIBRATION-ROTATION SPECTRUM

The transitions for which $\Delta J = +1$ produce the lines in the so-called R branch of the spectrum. Again by substitution, and with $v = 0$, $v^1 = 1$, and $J^1 = J + 1$, the wave numbers of the lines in the R branch are obtained.

$$\bar{\nu}_R = \bar{\nu}_0 + 2B + 2BJ$$

where J is the rotational quantum number of the initial state and may have values of 0,1,2, It is evident that there will not be a line with a frequency of ν_0 , since the transition $J=0$ to $J=0$ is forbidden.

Examples are given of the vibration-rotation absorption spectra of HCl and CO (refer to Plates 1 and 2). The so-called fine structure in the case of HCl is clearly observable [also refer to Halliday, 1970]. This is due to the small moment of inertia (large rotational constant B) of HCl. The CO molecule has a larger moment of inertia (smaller rotational constant) therefore the individual rotational lines are barely observed. The band contours of the P and R branches are observed.

When one is also observing emission of vibrational excited molecules - as in this investigation - the reverse of the processes depicted in Figure 2.9 apply resulting in spectra of radiance vs frequency.

2.5.5 Rotational Spectra of Polyatomic Molecules

For a polyatomic molecule the moment of inertia about a particular axis is given by;

$$I = \sum_i m_i r_i^2$$

where r_i is the perpendicular distance of the nucleus of mass m_i from the axis.

It simplifies the treatment of the rotational motion of a nonlinear (rigid) molecule to use three axes, the principal axes, which are fixed in the molecule and rotate with it. In symmetrical molecules the principal axes of inertia coincide with the symmetry axes of the molecule. A plane of symmetry in a molecule must contain two of the principal axes of inertia and be perpendicular to the third. The

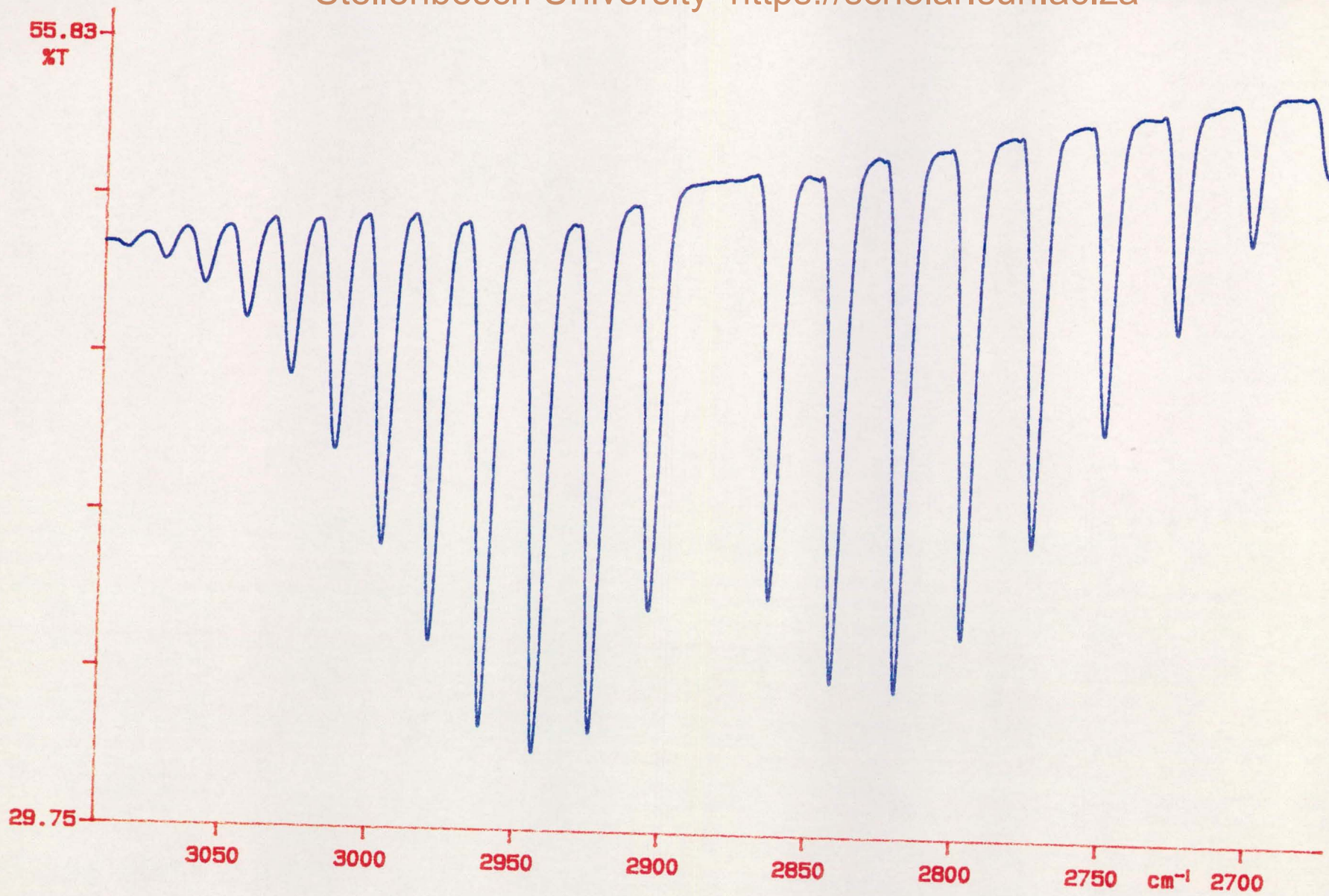


Plate 1. Vibration-rotation Spectrum of HCl

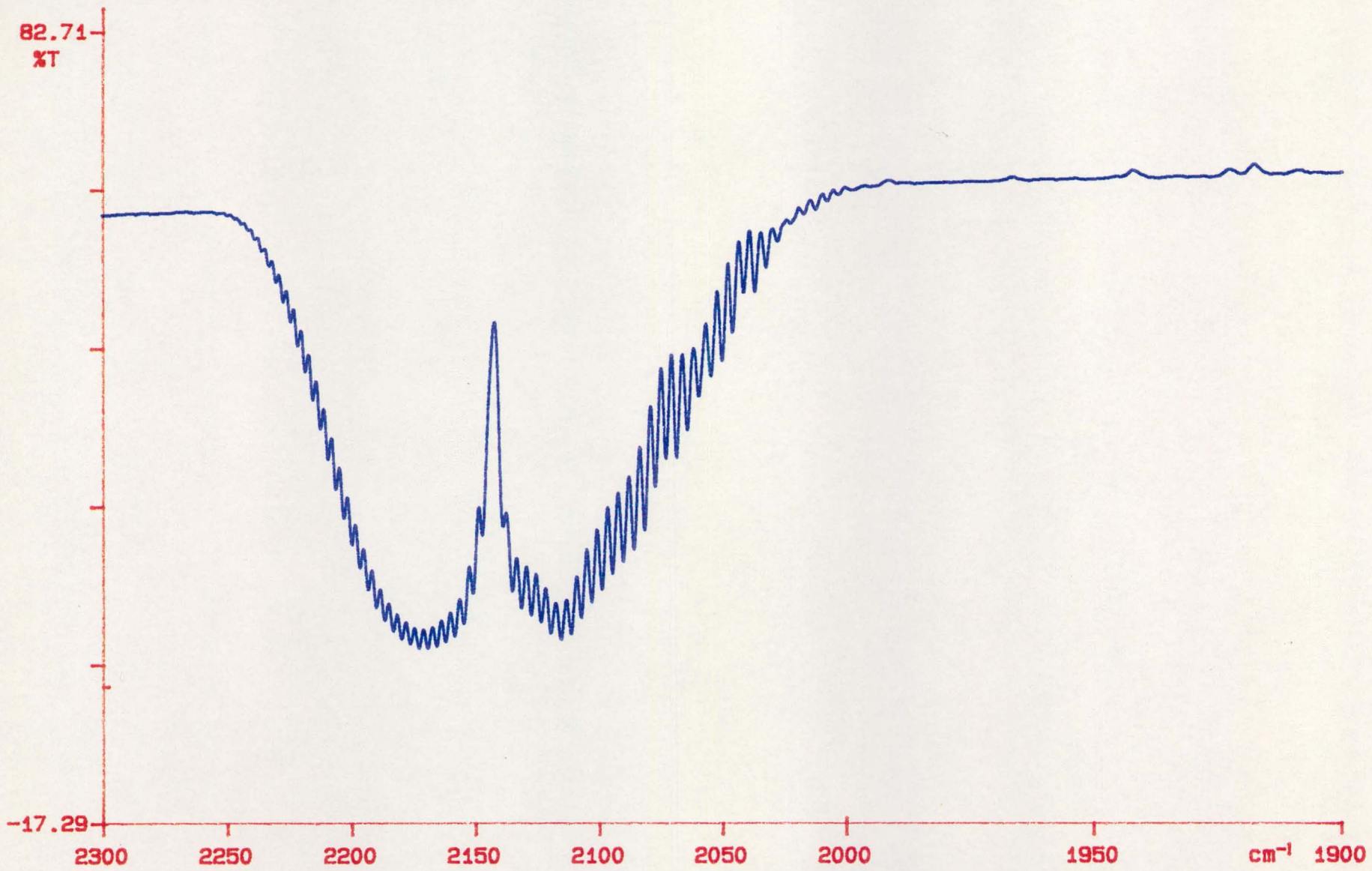


Plate 2. Vibration-rotation spectrum of CO

principal axes rotate with respect to a set of axes fixed in space with their origin also at the centre of mass.

The moments I around the principal axes are called the principal moments and are defined by equations of the form described above.

2.5.6 Vibrational Spectra of Polyatomic Molecules

The vibratory motion of a polyatomic molecule may be very complicated, but all the possible motions may be described in terms of simple motions, called the normal modes of vibration.

In the normal modes of vibration, the nuclei move in straight lines and in phase. The vibrational motions are said to be in phase when the nuclei pass through the extremes of their motion simultaneously. The motions of the nuclei in the normal modes are such that the centre of mass does not move and the molecule does not acquire any angular momentum. Each normal mode has a characteristic vibration frequency. Any vibratory motion of a molecule may be expressed as a sum of displacements in the various normal modes.

The number of normal modes depends upon the number N of atoms in the molecule. There are $3N - 5$ normal modes of vibration for a linear molecule, and $3N - 6$ normal modes for a nonlinear molecule. These relations may be obtained by considering the number of degrees of freedom for molecules. The degrees of freedom of a molecule are the independent co-ordinates required to locate a molecule in space and specify the position of each nucleus with respect to a co-ordinate system. For a molecule having N nuclei, $3N$ Cartesian co-ordinates are required to describe the position of each atom in space, so that the total number of degrees of freedom is $3N$. These degrees of freedom may be distributed between

translational degrees of freedom, rotational degrees of freedom, and vibrational degrees of freedom. All molecules have three degrees of translational freedom; that is, the position of the centre of mass of the molecule may be specified by giving three Cartesian co-ordinates.

The number of rotational degrees of freedom is the number of angles which must be specified to describe the orientation of a rigid molecule in space. The orientation of a linear molecule can be described by giving two angles with respect to a co-ordinate system. To describe the orientation of a nonlinear molecule, three angles are required.

The number of internal degrees of freedom of a molecule may be obtained by subtracting the sum of the translational and rotational degrees of freedom from N , yielding $3N - 5$ for linear molecules and $3N - 6$ for nonlinear molecules. Internal degrees of freedom include vibrations and internal rotations. If there is an appreciable potential energy for an internal rotation about some bond, there will be an oscillation about a mean position.

For any diatomic molecule $3N - 5 = 1$, that is, a single vibrational degree of freedom. In other words a single coordinate is required to specify the internuclear distance. For a linear triatomic molecule like CO_2 , $3N - 5 = 4$, that is, four vibrational degrees of freedom. The corresponding motions of the atoms for these vibrations for CO_2 are shown in Figure 2.10. The two on the left are symmetrical and asymmetrical stretching vibrations. The two on the right are bending motions which differ only in that they are in mutually perpendicular planes. Such vibrations which have the same frequency are called degenerate vibrations. It may be noted in this Figure that stretching vibrations have higher frequencies than bending vibrations. This is often true and is a result of the fact that a larger force is required to stretch a molecule than to bend it.

For a nonlinear triatomic molecule, such as H_2O ($3N - 6 = 3$), there are three normal modes of vibration. These normal modes are shown in Figure 2.10.

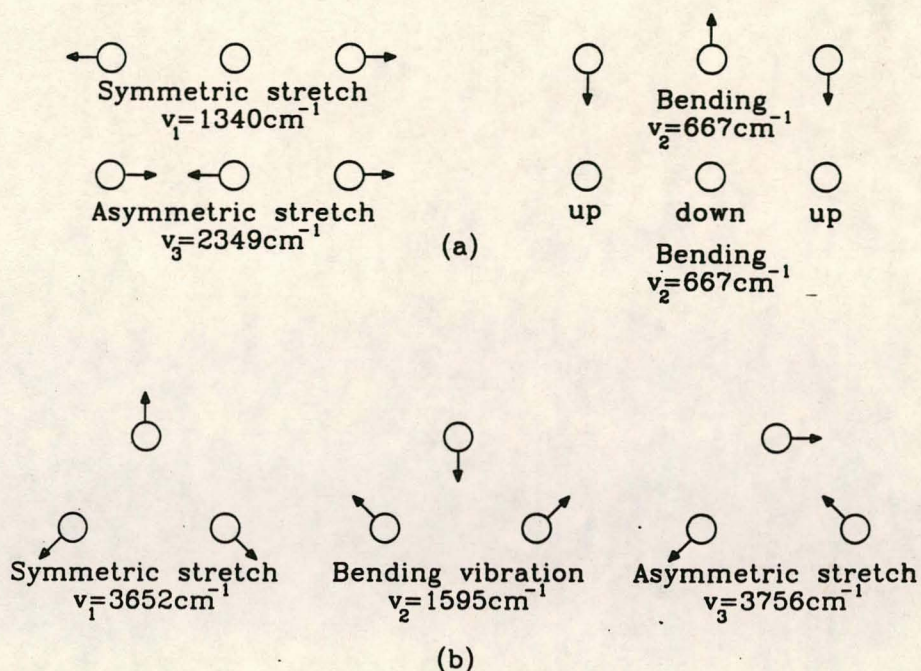


FIGURE 2.10 NORMAL MODES OF VIBRATION OF A SYMMETRICAL LINEAR AND NONLINEAR TRIATOMIC MOLECULES

(a) and (b) refer to a symmetrical linear triatomic molecule e.g. CO_2 and a nonlinear triatomic molecule e.g. H_2O .

It should be noted that the symmetric stretch vibration of CO_2 does not introduce an oscillating dipole moment, so that this vibration is inactive with respect to absorption and emission.

The three vibrations of the H_2O molecule each introduce an oscillating dipole and each is active with respect to absorption and emission.

TABLE 2.1 INFRARED BANDS OF H₂O VAPOUR

$\bar{\nu}$ (cm ⁻¹)	Intensity	Interpretation
1595.0	very strong	ν_2
3151.4	medium	$2\nu_2$
3651.7	strong	ν_1
3755.8	very strong	ν_3^-
5332.0	medium	$\nu_2 + \nu_3$
6874.0	weak	$2\nu_2 + \nu_3$

The infrared spectrum of a gas is more complicated than one would at first expect from the normal mode analysis. This is because the infrared spectrum contains fundamental transitions (i.e. normal vibration frequencies), overtones (i.e. multiples of normal frequencies), and combination tones (i.e. combinations of normal frequencies). For a polyatomic molecule it may be very difficult to identify the normal frequencies.

The frequencies, in wave numbers, of the strongest bands for H₂O vapour are summarized in Table 2.1. By use of more advanced theory it is possible to identify the normal modes as shown in Figure 2.10. The weaker bands in the spectrum are the overtones and combination tones shown in the Table. The vibrations are not strictly harmonic and so the overtones are not exact multiples and the combination tones are not exact sums as shown in the Table.

A further complication in the infrared spectra of polyatomic molecules in the gas phase is the rotational transitions which will simultaneously take place. This gives rise to P and R branches in the absorption bands of fundamental transitions,

overtones and combination tones. For some transitions a central so-called Q branch may be observed. Depending on the moments of inertia with respect to the principal axis of rotation - and the resolution of the spectrometer - some bands may show a fine structure; otherwise only the band contour can be observed.

The H₂O molecule has small moments of inertia, so that its absorption bands will have a fine structure. This is evident in Plates 3 and 4. The CO₂ molecule has a relative large moment of inertia, therefore only the band contour can be observed (refer to Plate 5).

The effect of these absorptions on the transmittance of infrared radiation on a horizontal air path can clearly be seen in Figure 2.1. The strong absorption at 15μm (667cm⁻¹) is due to the bending vibration of CO₂. The fine structure surrounding this absorption is due to pure rotational transitions of the H₂O. The strong absorption with fine structure around 6.3μm (1595cm⁻¹) is due to the bending vibration of H₂O. The fearely sharp and strong absorption at 4.3μm (2349cm⁻¹) is due to asymmetric stretching vibration of CO₂. The sharp triple peak at 3.25μm (3077cm⁻¹) is due to an overtone (2x1594cm⁻¹) of the H₂O bending vibration. The broad peak at 2.55 to 2.80μm is mainly due to the asymmetric and symmetric stretching vibrations of H₂O plus a combination tone of CO₂ ($2\nu_2 + \nu_3$). The double peak in the region of 1.9μm (5263cm⁻¹) is made up by a combination tone of H₂O ($\nu_1 + \nu_2$) and a combination tone of CO₂. The peak at 1.4μm (7143cm⁻¹) is again an overtone of CO₂.

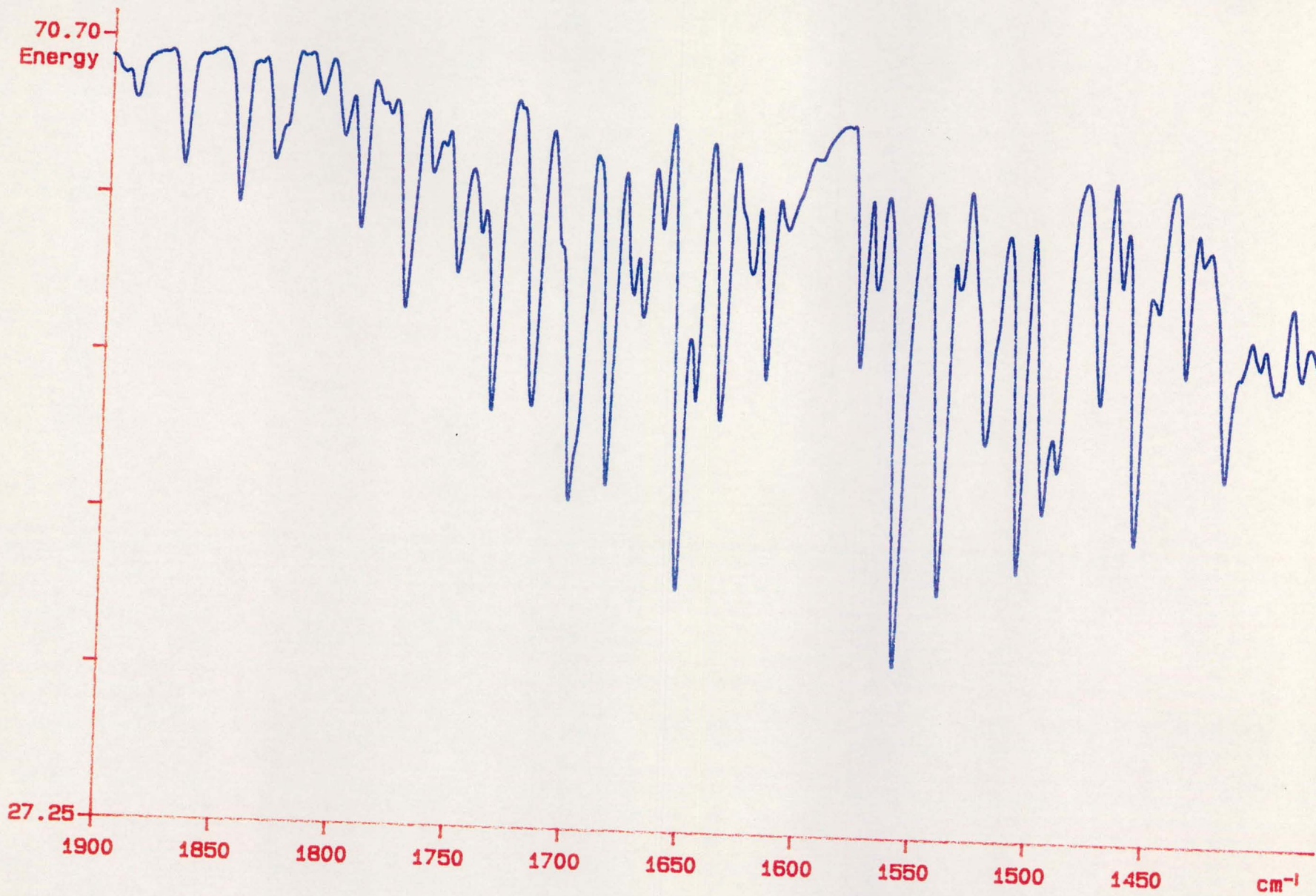


Plate3.Vibration-rotation band of H2O bending vibr

PERKIN ELMER

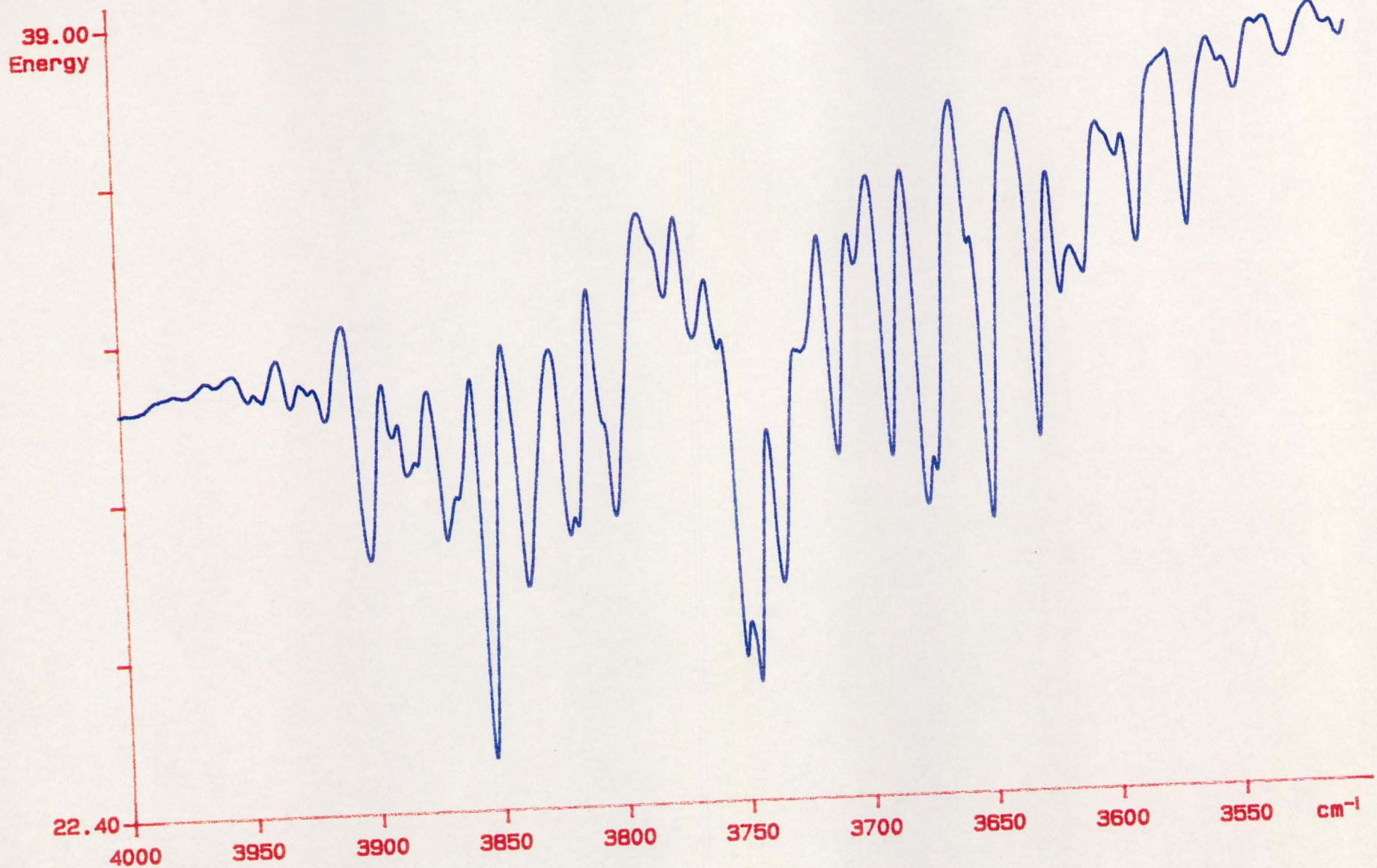


Plate 4. Vibration-rotation bands of H₂O stretches

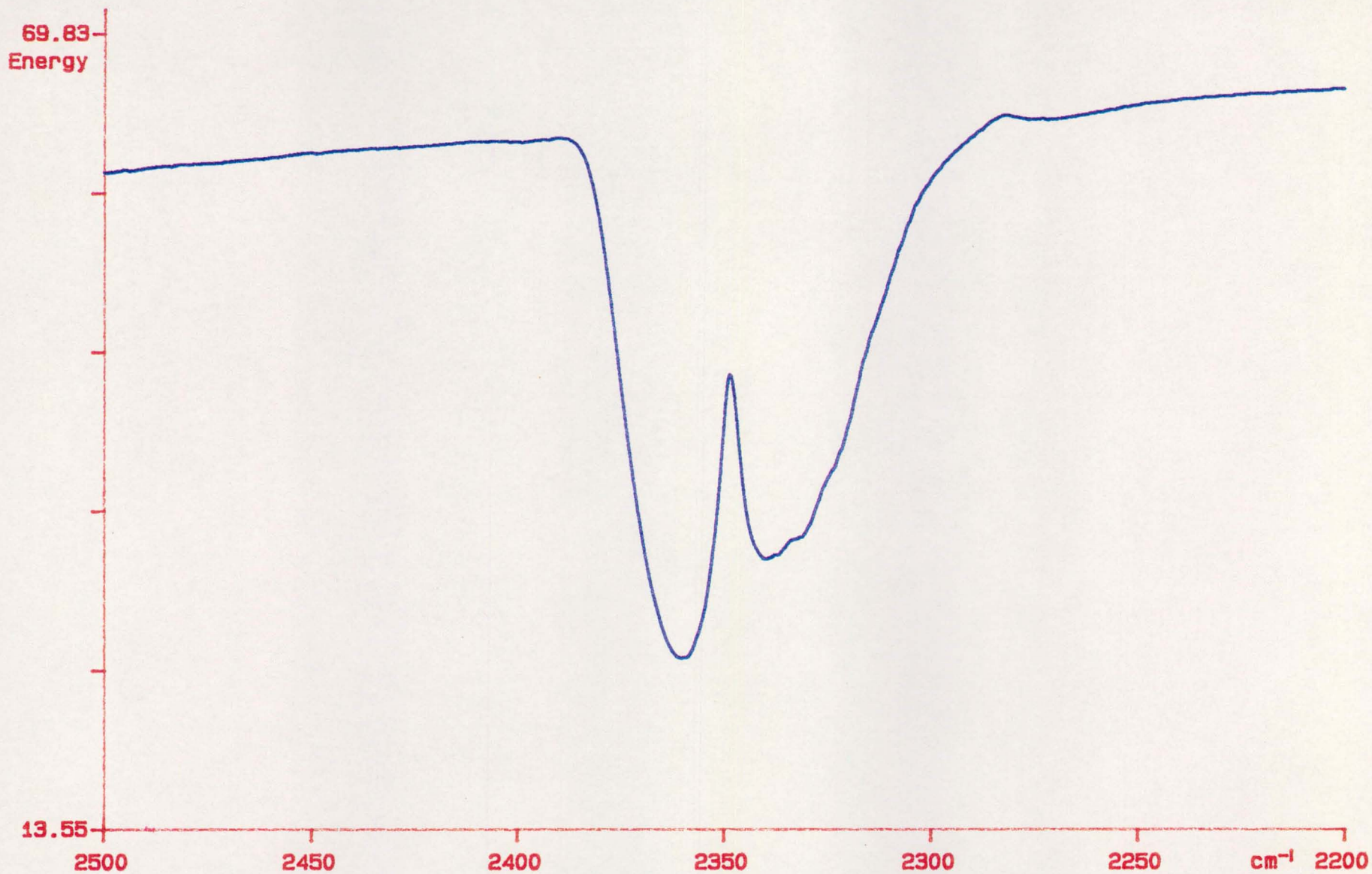


Plate 5.Vibration-rotation spectrum of CO2

TABLE 2.2 INFRARED ABSORPTION BANDS FOR VARIOUS FUNCTIONAL GROUPS (IN WAVE NUMBERS, cm^{-1})

O-H st	3800-3000
N-H st	3500-3100
C-H st	3100-2750
S-H st	2600-2500
C=O (ketone) st	1725-1650
N-H bend	1650-1550
C-H bend	1475-1375
C=C st	1675-1575
C-C (aromatic) st	1650-1550
C-O st	1300-1100

with, st = stretching frequency and
bend = bending frequency.

The vibrational spectra of polyatomic molecules are very useful in identifying them and serve as criteria of purity. For such practical applications the infrared spectra for a large number of compounds have been catalogued and are used as "fingerprints". Functional groups within the molecule have quite characteristic absorption bands and are shown in the Table above. The wavelengths at which a certain group absorbs vary slightly, depending on the structure of the rest of the molecule. The principal functional groups within the molecule may frequently be determined and such information can be used to positively identify compounds where chemical evidence permits relatively few possible structures.

In this study Tables such as Table 2.2 were used to predict which frequencies will be emitted when vibrationally excited molecules, with specific functional groups, are present in flames of flare compositions.

2.5.7 Transfer of Vibrational Energy

[Atkins, 1990, Kirk-Othmer, 1981]

The transfer of vibrational energy during intermolecular collisions is of particular importance in this investigation. It is well known that this transfer is very effective if there is a resonance between the vibrational energy levels of the colliding species. This transfer of vibrational energy will enhance the infrared emission of the species which are activated as a result of the collisions. The CO₂ laser is a device where this phenomenon is used and is of particular relevance to this study.

The mixture of gases for the CO₂ laser consists of N₂, CO₂ and He. The vibrational energy levels of N₂ and CO₂ are depicted in Figure 2.11:

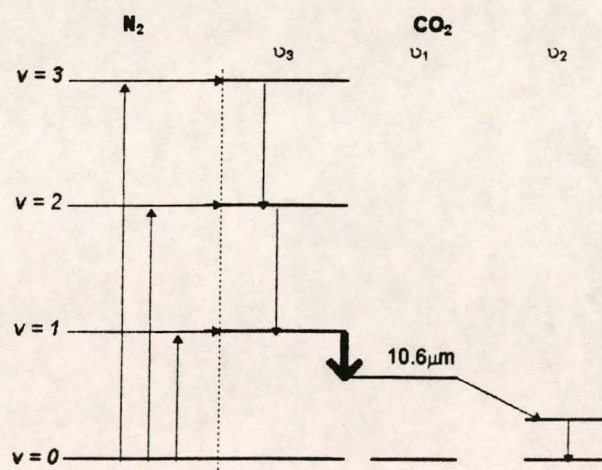


FIGURE 2.11 THE VIBRATIONAL ENERGY LEVELS OF N₂ AND CO₂

with; ν_1 = symmetric stretching vibration

ν_2 = bending vibration

ν_3 = asymmetric stretching vibration.

The N_2 molecules are vibrationally excited by an electronic discharge through the lasing medium. By an accidental matching of the vibrational energy levels of N_2 and the asymmetric stretching vibration of CO_2 , vibrational energy can be transferred by a single collision from N_2 to CO_2 . This results in a so-called population inversion with respect to the $v=1$ level of the symmetric stretching vibration. When this activated CO_2 molecule is stimulated in a resonant cavity, laser emission at $10.6\mu\text{m}$ is obtained.

In the absence of a resonant cavity spontaneous emission at the frequency of the asymmetric stretching vibration will occur. This will result in a double peak at 4.2 and $4.4\mu\text{m}$ which can be correlated with the double peak in Plate 5.

2.5.8

Electronic Spectra

Transitions between electronic levels of molecules lead to absorption and emission in the visible and ultraviolet parts of the spectrum. For some molecules the changes in energy accompanying changes in electronic excitation are so great that absorption occurs only in the vacuum ultraviolet. Since the absorption and emission frequencies depend on the differences in energy between the ground state and various excited states, molecules with similar ground states may have very different spectra. Since vibrational and rotational changes accompany electronic changes, bands instead of sharp lines are seen in these spectra. For larger molecules there are so many lines that broad absorption bands are obtained.

2.6

FUNDAMENTALS OF SEMICONDUCTOR PHYSICS

[Leuschner, Section 4, 1989]

As indicated in section one, sensors for infrared radiation at specific wavelengths are employed in the seeker head of heat-seeking missiles. These sensors are invariably of the semiconductor type. In order to understand the so-called spectral bands at which the different combinations of sensors in seeker heads can operate, the fundamentals of semiconductor physics are briefly discussed.

2.6.1

Crystal Structure and Energy Bands

To understand the nature of semiconductors one must consider what happens when similar atoms are brought together to form a crystalline solid. An atom comprises a positively charged nucleus which is surrounded by negatively charged electrons. The latter overlap, forming a band of energy states instead of the discrete energy states of isolated atoms. The energy distribution of the states depends strongly on the interatomic distance. This is illustrated in Figure 2.12 for an assembly of carbon (C) atoms, which crystallizes in a diamond lattice structure, the same structure as for silicon (Si) and germanium (Ge). The unit cell of the diamond structure, repeated in three-dimensional space to form the lattice is shown in Figure 2.13, where a is the lattice constant mentioned in Figure 2.13. Semiconductors compounded from elements of Group III and IV of the Periodic Table (III-IV compounds), for example gallium-arsenide (GaAs) or indium-antimonide (InSb), usually crystallize in the Zincblende structure. The unit cell of this structure is shown in Figure 2.14, with a the crystal lattice.

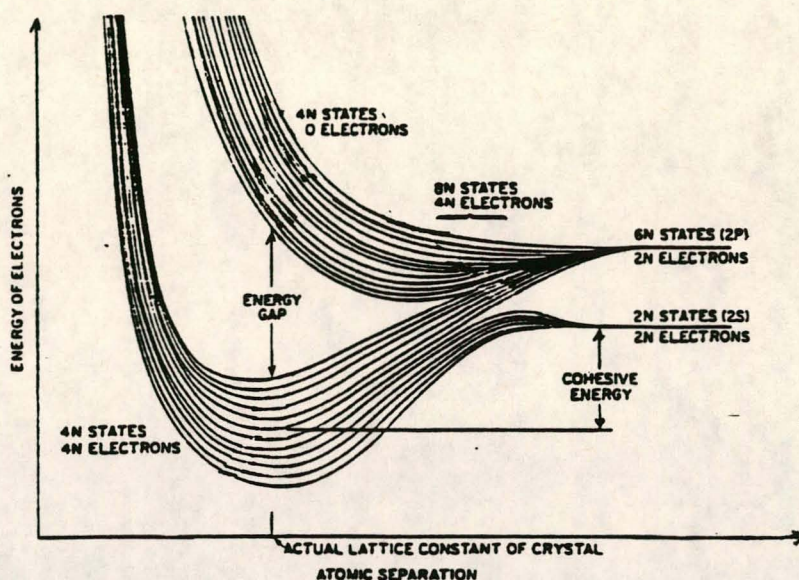


Figure 2.12 ENERGY BANDING OF ALLOWED LEVELS IN DIAMOND AS FUNCTIONS OF SPACING BETWEEN ATOMS

When a cut of Figure 2.12 is made at the position shown as the actual lattice constant of the crystal, a simplified energy band diagram can be drawn. The band of lower energies is called the valence band, while the band of higher energies is called the conduction band. Figure 2.15 shows the energy band diagrams of various materials. In semimetals, the conduction band is only partially filled with electrons (Figure 2.15a), while for metals the two bands can be seen to overlap (Figure 2.15b). For insulators and semiconductors there is a forbidden gap of energies (Figure 2.15c, d) where an electron cannot be found. In this case all the states in the valence band are filled, while all the states in the conduction band are empty, thus there is no contribution to current flow. In a semiconductor the forbidden energy gap is not too large for energy added thermally or by an externally applied field, to cause an electron to jump from the valence band to the conduction band in order to produce current flow. When an electron has jumped

to the conduction band, a net positive charge known as a hole, remains in the valence band that also contributes to current flow.

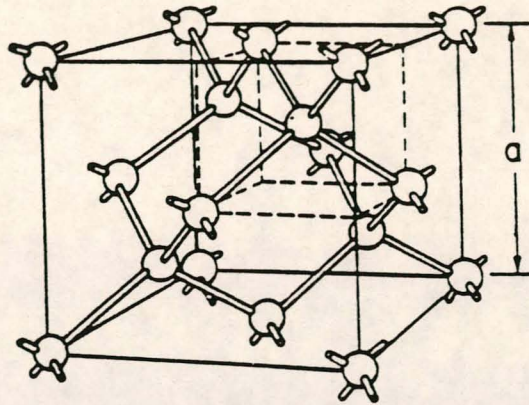


FIGURE 2.13 UNIT CELL OF THE DIAMOND LATTICE STRUCTURE (C, Si, Ge)

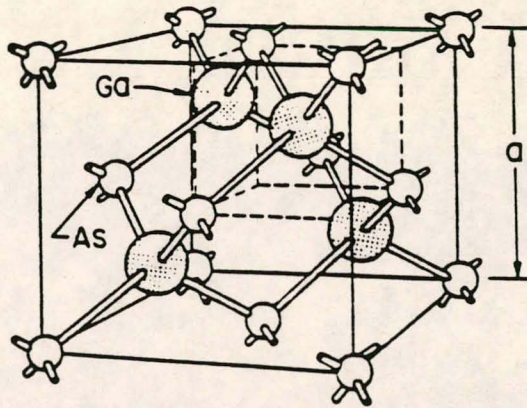


FIGURE 2.14 UNIT CELL OF THE ZINCBLLENDE STRUCTURE (GaAs, InSb)

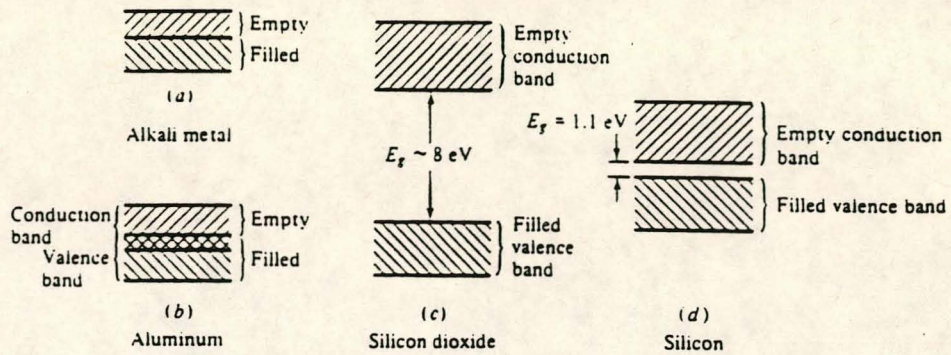


FIGURE 2.15 ENERGY BAND DIAGRAMS FOR (a) SEMIMETALS, (b) METAL, (c) INSULATOR AND (d) SEMICONDUCTORS

2.6.2

Group III-V and Group II-VI Semiconductor Alloys

The bandgaps of Group IV semiconductors are fixed and of a limited range (there are not many Group IV semiconductors), and thus it becomes necessary to manufacture semiconductors by compounding Group III (Ga, In, Al) and V (P, As, Sb) or Group II (Hg, Cd, Zn) and VI (Te, Se, S) elements. Figure 2.16 contains a plot of the energy bandgap (E_g) and the lattice parameter (a) for the major III-V compounds.

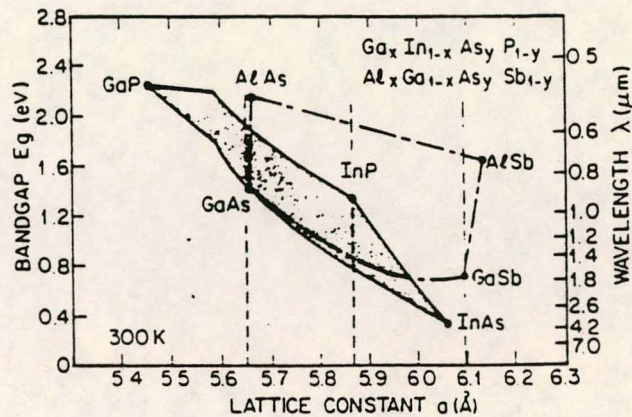


FIGURE 2.16 ENERGY BANDGAP AND LATTICE CONSTANT FOR GROUP III-V COMPOUNDS AND ALLOYS

Elements and binary compounds are indicated by points, with fixed bandgap energy and lattice constant. Ternary alloys are obtained when two III-V (or II-VI) compounds with the same group V (or VI) element are alloyed. The notation frequently used is $A_xB_{1-x}C$, with A and B Group III or II elements and C a Group V or VI element. The two elements from the same group are sometimes placed alphabetically, but usually according to their atomic numbers. Ternary alloys are denoted by lines between the binaries (Figure 2.16), giving them one degree of freedom in that both bandgap and lattice vary with composition. However when one is fixed, the other is as well. Quaternary alloys are obtained when four binary III-V or II-VI compounds (combinations of the quaternary constituent elements) are alloyed. The notation for quaternary alloys is $A_xB_{1-x}C_yD_{1-y}$. In the bandgap-lattice constant space they are denoted by areas bounded by the four binary alloys (Figure 2.16). Quaternary alloys have two degrees of freedom since a range of lattice parameters are available for each bandgap and conversely, a range of bandgaps are available for each lattice constant.

2.6.3 Intrinsic and Extrinsic Semiconductors

In a pure and perfect semiconductor, concentration of electrons in the conduction band create holes in the valence band. This concentration is called the intrinsic concentration. The crystal conductivity can be controlled by introducing impurities. The impurity is called a dopant and the semiconductor is said to be extrinsic.

If a Group V element is introduced in a Group IV semiconductor, the dopant substitutional atom has one more electron than is necessary for the covalent bonds. The excess electrons are loosely bound to their constituent atoms and thus little energy is needed to place them in the conduction band. The free electron leaves behind a fixed positive charge, and the atom is said to be ionized. The

ionization energy is small, and is situated near the conduction band edge and inside the band gap. At room temperature the thermal energy is sufficient to ionize all impurity atoms, so that the number of excess electrons equals the number of impurity atoms. Since these dopant atoms readily donate electrons, they are called donors, and the type of extrinsic semiconductor is called “n type”. Electrons acting as carriers in an n type semiconductor are known as majority carriers, while holes are called minority carriers. The donor impurities necessary to create n type III-V compound semiconductors are found in Group VI of the Periodic Table.

When a Group III element is used as impurity for a Group IV semiconductor, one electron is missing from the bonding configuration. A hole is thus produced in the valence band with a fixed negative charge remaining with the impurity atom. The ionization energy is small and situated near the valence band edge and inside the bandgap. With this type of dopant, called an acceptor, a “p type” extrinsic semiconductor is created. In a p type semiconductor holes are the majority carriers, while electrons are the minority carriers.

2.6.4 Fundamentals of Optical-Electrical Conversion

Photonic devices are those in which the basic particle of light, the photon, plays a major role. Photonic devices can be divided into two groups: (1) devices that convert electrical energy into optical radiation and (2) devices that convert optical radiation into electrical energy. Both mechanisms can be explained by electron transitions between energy states - by radiative recombination for electrical to optical conversion, and by carrier generation through absorption for optical to electrical conversion. The energy differences between states and the optical frequency are related to each other. Figure 2.17 is a chart of the electromagnetic

spectrum where the frequency of the wave and the equivalent energy are indicated.

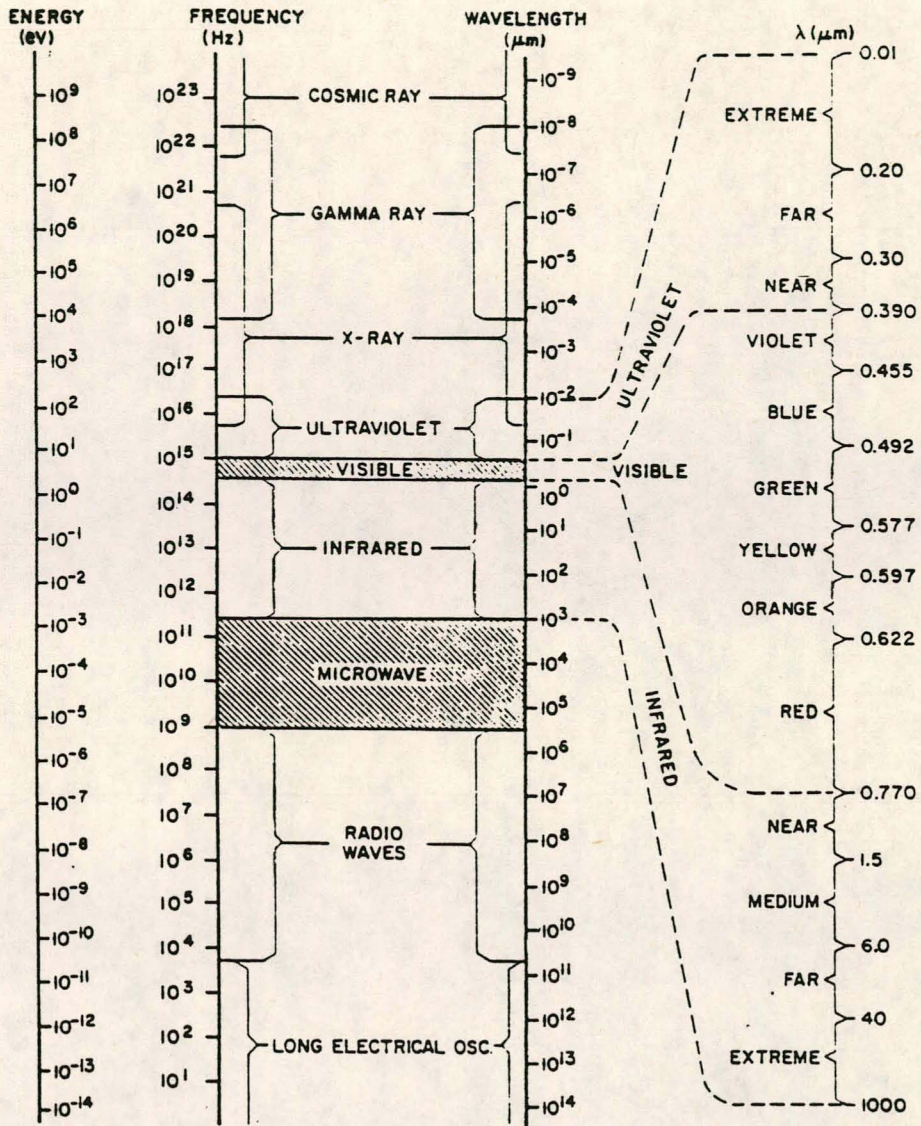


FIGURE 2.17 CHART OF THE ELECTROMAGNETIC SPECTRUM

Figure 2.18 shows the basic transitions in a semiconductor. The first classification is of interband transitions: (a) intrinsic absorption/ emission corresponding closely in energy to bandgap (b) higher energy absorption/emission involving energetic carriers. The second classification is the transitions involving chemical impurities or defects: (a) conduction band to acceptor (b) donor to

valence band (c) donor to acceptor and (d) deep levels. The third is the intraband transitions involving energetic carriers.

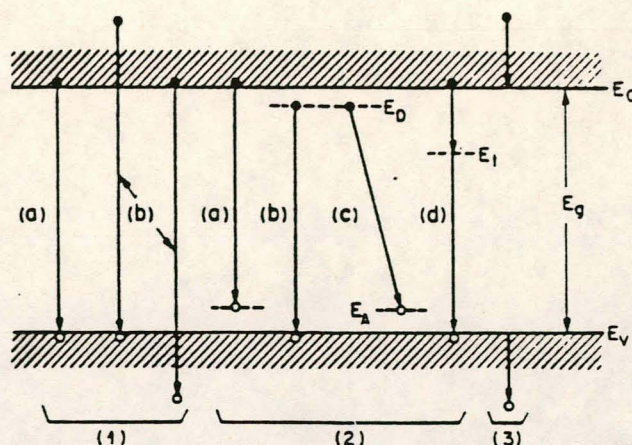


FIGURE 2.18 BASIC TRANSITIONS IN A SEMICONDUCTOR

Both the absorption curve and the emission curve can be found by the product of the density of filled initial states of the transition, the density of empty target states of the transition and the probability that the transition will take place. When absorbing optical energy many of these transitions occur, though in a certain material under specified conditions some transitions dominate. The fact that more than one transition can occur during photon absorption causes a wide spectral response absorption curve. When optical radiation is emitted, not all of these transitions occur and not all of these transitions are radiative, often causing a very narrow spectral response emission curve. The radiative transition is in direct competition with nonradiative recombination transition, and for radiation to be possible the radiative transition has to be the dominant one.

The hitherto ignored fact that the energy band diagram is also a function of crystal momentum starts to play an important role, especially when emission mechanisms are examined. The energy band diagrams as functions of momentum for GaAs and Si are shown in Figure 2.19. The maximum energy of the valence band and

the minimum energy of the conduction band occur at the same momentum for GaAs. Materials exhibiting this characteristic are known as direct band gap semiconductors. An indirect band gap material has the characteristic that the maximum energy of the valence band does not occur at the same momentum as the minimum energy of the conduction band. The top of the valence band is usually defined as having zero momentum.

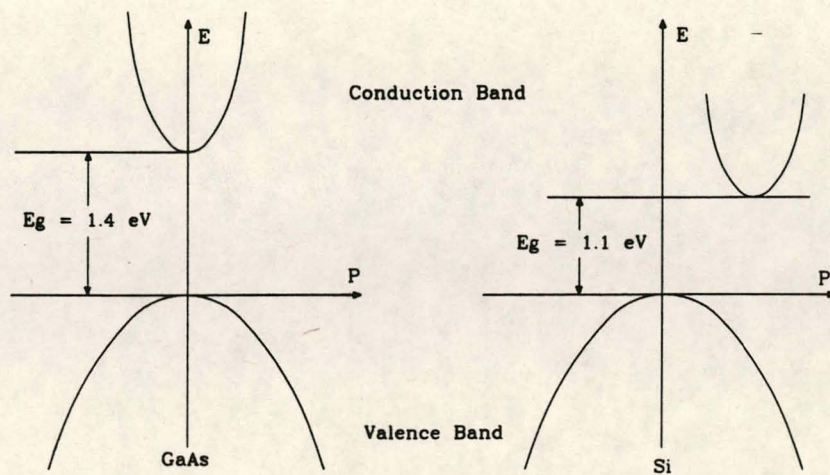


FIGURE 2.19 THE ENERGY BAND DIAGRAM OF GaAs AND Si AS A FUNCTION OF MOMENTUM

An interband transition in a direct band gap material can take place with momentum automatically conserved. In contrast, for an interband transition in an indirect bandgap material, momentum conservation must be ensured with the cooperation of a momentum particle called a phonon. A phonon reveals itself through displacement of an atom. The other classes of transitions shown in Figure 2.18 can all be phonon-assisted. In the absorption spectrum direct and indirect transitions are probable, but the probability that an indirect radiative transition will take place is several orders of magnitude less than the probability for a direct radiative transition to take place. Optical radiation is thus mostly found in direct energy bandgap materials.

Nonradiative recombination processes do not result in the external emission of a photon. In the Auger effect, the energy released by the recombining electron is immediately absorbed by another electron which then dissipates the energy by emitting phonons. Another important nonradiative recombination process is by surface recombination states or through crystal defects and inclusions. All these cause a local continuum of energy states, and all electrons and holes within a diffusion length from the surface, defect or inclusion will be drawn to the trap, where they will recombine nonradiatively by the continuum of states.

2.6.5 Photoconduction Detectors

A photoconductor consists simply of a slab of semiconducting material with ohmic contacts affixed to opposite ends. When incident light falls on the surface of the semiconductor, electron-hole pairs are generated, resulting in an increase in conductivity. When an electric field is applied across the semiconductor, the generated carriers drift in the field causing a photon current to flow in the external circuit. The detectivity of various photoconductors as a function of the wavelength of the incident light is shown in Figure 2.11. Specifically notice the wide range of far-infrared wavelengths obtainable with HgCdTe.

The detectivity $[D^*(\lambda, f)]$ is defined by Wolfe and Zissis as a normalization of the spectral detectivity $[D(\lambda)]$ to take into account the detector area (A_d) and electrical bandwidth (Δf) dependence. The spectral detectivity is the reciprocal of the spectral noise equivalent power $[\text{NEP}]$. The detectivity is represented by:

$$D^*(\lambda, f) = \sqrt{A_d \cdot \Delta f} \cdot D(\lambda) \quad [\text{cm} \cdot \text{Hz}^{0.5} \cdot \text{W}^{-1}]$$

and with
$$D(\lambda) = \frac{1}{(\text{NEP})_\lambda} \quad [\text{W}^{-1}]$$

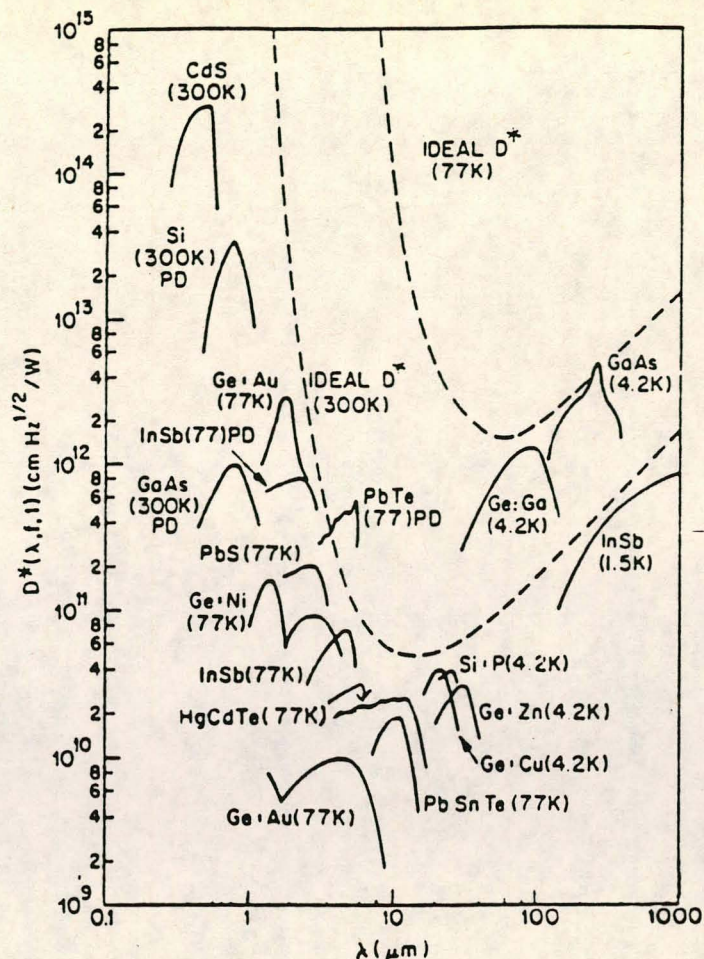


FIGURE 2.20 DETECTIVITY (D^*) AS A FUNCTION OF WAVELENGTH FOR VARIOUS PHOTOCONDUCTORS AND PHOTODIODES

The dashed curves are the ideal theoretical D^* at 77K and 300K viewing and angle of 2π steradians. Photodiodes are indicated with PD.

2.6.6 Photovoltaic Detectors

Photovoltaic effects constitute a class of phenomena in which light generates a voltage across a portion of the semiconductor. Actually, the light produces only an excess of free carriers, which move in response to local fields to accumulate in regions where they produce a net space charge. It is this deviation from thermal equilibrium that is responsible for the photovoltage. The photo-generated carriers can be driven by a variety of local fields, like those discussed for p-n and metal-

semiconductor junctions, as well as heterojunctions. The carriers can be generated by any of the absorption transitions between energy states as described previously, with one or other mechanism dominating for a specific material under certain circumstances. As examples the absorption coefficients of Ge, Si and GaAs are shown in Figure 2.21.

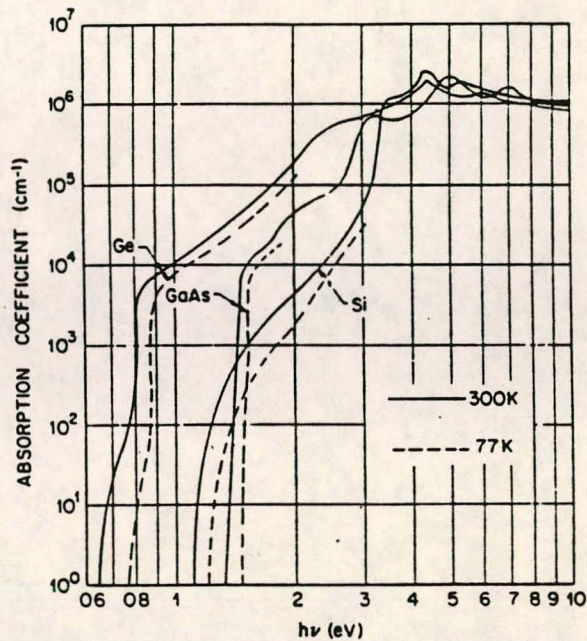


FIGURE 2.21 THE ABSORPTION COEFFICIENT OF Ge, Si AND GaAs AS A FUNCTION OF PHOTON ENERGY

2.6.7

Bolometric Detectors

Bolometers are devices that respond to heating produced by absorbed radiation. The thermal conductivities of various semiconductors as functions of temperature are shown in Figure 2.22. The three essential parts of a bolometric detector are the thermally absorbing surface, a thermometer and a thermal link to a heat sink. A metal film (Bi or Ni-Cr alloy) at liquid He temperature is usually used as thermal absorber, while a doped semiconductor (typically Ga-doped Ge) is used as a thermometric element. The main application of bolometers is for long

wavelength infrared detection ($100\mu\text{m}$) where no sensitive photon detectors currently exist.

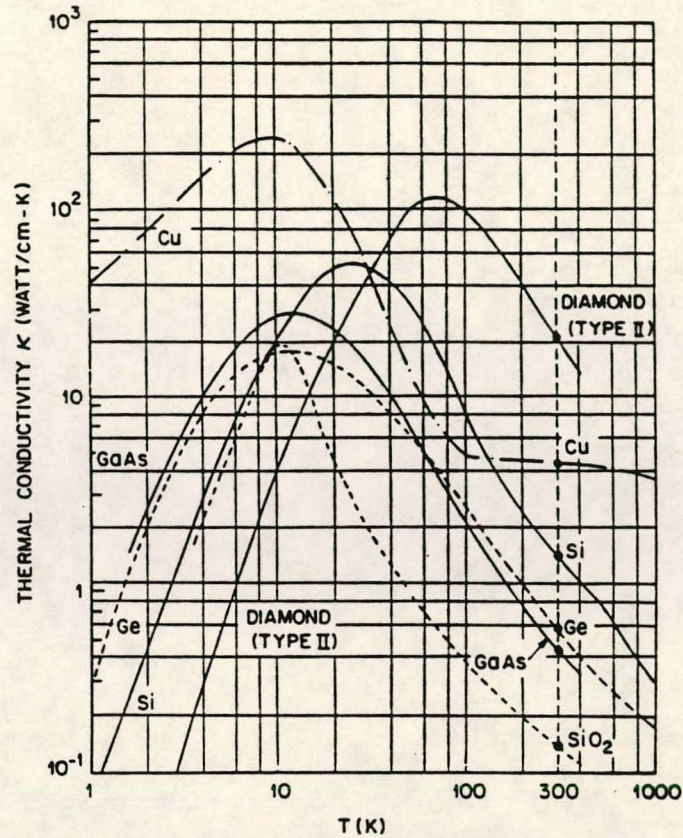


FIGURE 2.22 MEASURED THERMAL CONDUCTIVITY FOR SOME PURE SEMICONDUCTORS

2.6.8 Missile Spectral Bands

The sensors employed in seeker heads have undergone some changes through the years. Earlier models employed a PbS sensor; limiting the spectral band to a narrow shorter wavelength region (2 to $3\mu\text{m}$). Later models used sensors operating at a wider and shorter wavelength region (0.5 to $3\mu\text{m}$). Some of the newer models operate at the longer wavelength region (4 to $5\mu\text{m}$). Some models operate in both the 0.5 to $3\mu\text{m}$ and 4 to $5\mu\text{m}$ wavelength regions.

For this investigation the spectral bands of the ground-to-air missiles that are likely to be encountered by the SAAF were required. This information was supplied by the Aerotek division of the CSIR [Infrared Technology Workshop Proceedings, 1994] and is depicted in Figure 2.23.

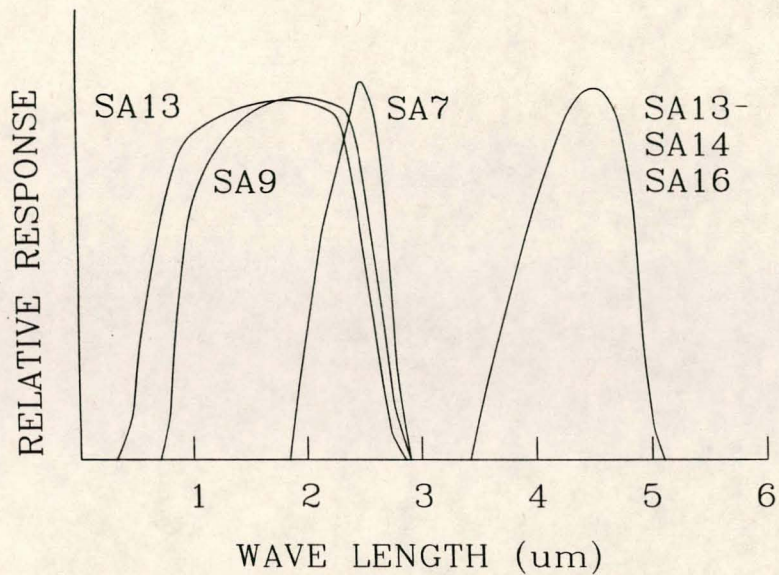


FIGURE 2.23 MISSILE SPECTRAL BANDS

The SA7, 14 & 16 are shoulder launch missiles while the SA9 & 13 are vehicle launched systems. Note that the SA13 has a dual band width detection capability.

SECTION 3 SPECTRAL PROPERTIES OF AIRCRAFT PLUMES

3.1 **SPECTRAL MEASUREMENTS**

The spectral data of the aircraft's plume were captured and processed in the 0.4 to 5 μ m IR band width. The aircraft used was the Mirage F1 AZ burning standard Jet A1 fuel and the plume was measured at a 90° side-on view with the mini-gate (afterburner) activated. This specific IR wavelength range was used as all the heat-seeking anti-aircraft missiles of interest operate in this band width (refer to Figure 2.23).

Although it was expected that the spectral characteristics of the plumes might change with the afterburner fully activated, it was impossible to keep the aircraft stationary under these conditions. For practical reasons measurements were thus restricted to the so-called mini-gate afterburning.

It was also expected that the spectral characteristics might change when the aircraft was operating at high altitudes. Current technology, however, does not allow measurements under these conditions and therefore sea level conditions are assumed.

The plume of the Cheetah aircraft was also evaluated. Since the same fuel was used by both aircraft no differences were spectrally detected.

The following Figures represent the spectral outputs of a F1 AZ plume on different occasions in the 2.5 to 5 μ m region. Note that the relative sterance units (see later) represent the case of zero atmospheric corrections.

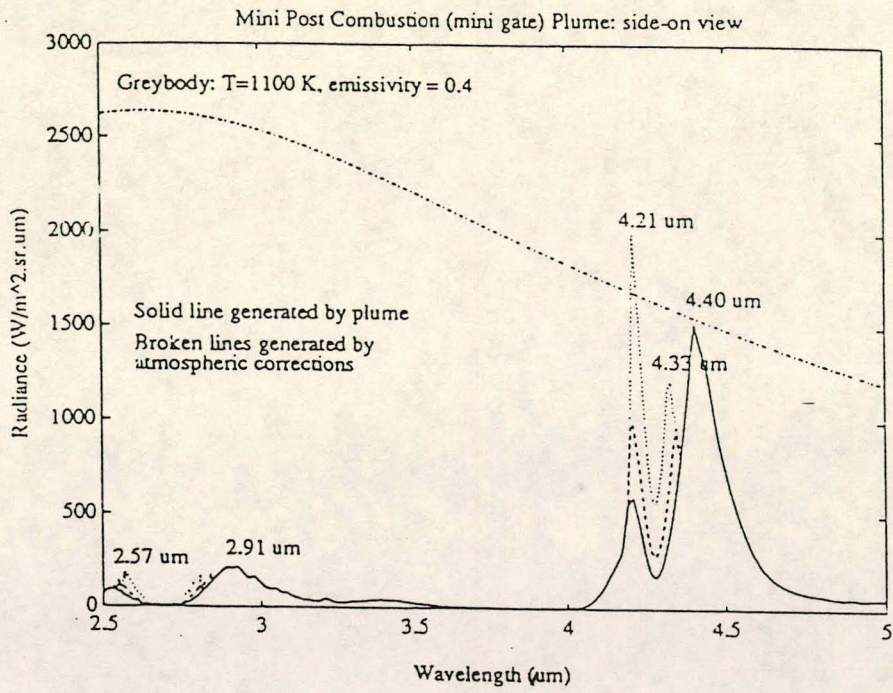


FIGURE 3.1 MODELLING THE F1 AZ PLUME ON MINI GATE SETTING

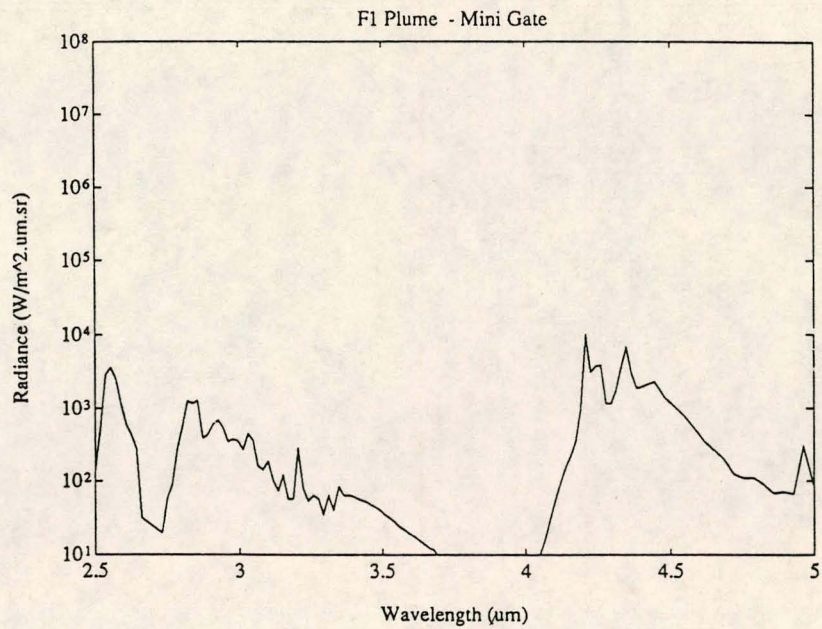


FIGURE 3.2 RADIANCE OF F1 AZ PLUME WITH ATMOSPHERIC CORRECTIONS

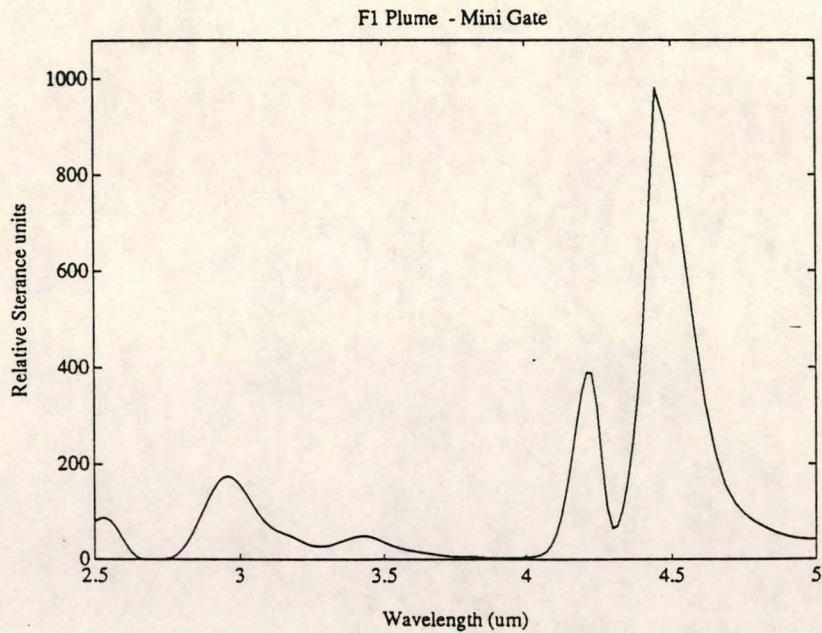


FIGURE 3.3 F1 AZ PLUME RADIANCE WITHOUT ATMOSPHERIC CORRECTIONS

Note that the peak at $4.4\mu\text{m}$ (see Figure 3.1) is remarkable less sensitive to atmospheric changes than the $4.2\mu\text{m}$ peak. This is ascribed to the lesser attenuation capability of the atmosphere at $4.4\mu\text{m}$.

The spectra in Figures 3.2 and 3.3 were chosen as those to be simulated by the spectra of the decoy flares.

Appendix C contains a spectrum of the plume measured in the 0.4 to $2.5\mu\text{m}$ range.

3.2 INTERPRETATION OF THE PLUME EMISSION SPECTRUM

With reference to the Figures in paragraph 3.1 the points of interest are;

- 2.57 μm
- * 2.7 μm
- 2.9 μm
- 4.2 μm
- * 4.3 μm
- 4.4 μm

with * representing minimum levels and the others are all peaks.

The minimum values are caused by the cold atmospheric absorption of H_2O and CO_2 at 2.6 to 2.8 μm and of CO_2 at 4.2 to 4.35 μm . Refer to Figure 2.1.

In the case of Jet A1 fuel being oxidized the combustion products are mainly carbon dioxide (CO_2) and water (H_2O). The plume of the aircraft thus consists mainly of CO_2 and H_2O both at various stages of excitation. According to Silverstein, 1967, (see also Figure 3.3) the fundamental vibrational frequencies are at the following wavelengths;

for H_2O ;

3652 cm^{-1} (2.74 μm) - symmetrical stretching

3756 cm^{-1} (2.66 μm) - asymmetrical stretching

1596 cm^{-1} (6.27 μm) - bending

and for CO₂

1340 cm⁻¹ (7.46μm) - symmetrical stretching (inactive)

2350 cm⁻¹ (4.26μm) - asymmetrical stretching

666 cm⁻¹ (15.0μm) - two modes of bending.

From these fundamental vibrational values alone it is not possible to describe the plume emission spectrum satisfactorily. The asymmetrical stretching vibration of CO₂ fundamentally has the centre of its double peak at 4.26μm and with its P and R branches extending to both sides (see Plate 5). However, with the gaseous CO₂ molecules at the elevated temperature of a jet plume as well as the contributing effects of shock heating (see later) these species are at various stages of rotational excitation resulting also in the population of higher rotational levels. This causes a much wider band of emissions than atmospheric CO₂ can absorb. The double peaks at 4.2 and 4.4μm were consequently assigned mainly to the outer edges of the P and R branches of the emission spectrum of vibrationally and rotationally excited CO₂ molecules in the plume. It is precisely this double peak that is the main identifier of a Jet A1 aircraft plume. The peak at 4.4μm is also the least affected by atmospheric attenuation (Figure 2.1). It should be noted that the SA 13, 14 and 16 all exhibit pronounced detection capabilities in this region.

The double peak in the 2.5 to 3μm as well as the fine spectral structure between and 3μm and 3.5μm are assigned to the emission of the vibrationally and rotationally excited water molecules. Again these peaks have been influenced by the attenuation of cold atmospheric H₂O.

It must also be noted that in the case of the SA 13, where two IR regions are monitored, the relation of intensities observed in these two regions are important.

It should therefore always be the aim to maintain this ratio and to enhance the 4.2 - 4.4 μm double peak with respect to the 2.5 - 3.0 μm double peak if necessary, when simulating the aircraft plume spectrally with a decoy flare.

An important question arose whether the presence of CO should have been observed in the spectrum of the jet plume. In order to resolve this question the absorption spectra of CO₂ and CO were compared under similar conditions (Plate 6). This comparison shows that their absorptions are well separated. Accordingly their emissions should be well separated and the emission of CO be observable - which is not the case. An explanation for this lack of emission would be that CO formed during the combustion process was in the $v = 0$ vibrational state, which cannot emit.

3.3

FLAME AREA CALCULATIONS

Initially only the plumes of the aircraft and the missile motors were measured. The area calculations were at that stage done by using video data from the AGEMA, visible video and UV images. The projected plume area (side view) was modelled [Roodt, 1992] by means of an isosceles triangle starting at the nozzle with base $2v$ and height $(1-k)L$. Onto the base of the triangle a parabola is fitted with the rounded end forming the tail of the plume. The width of the parabola is obviously $2v$ and the height is set at kL , measured from the base of the triangle along the axis of the plume to the origin of the parabola. L is the total length of the plume measured from nozzle to tail-end, while $2v$ is the height measured at the widest area of the plume. At this point the fraction of the length of the plume contained in the parabola is measured as k . The total plume area may then be calculated as:

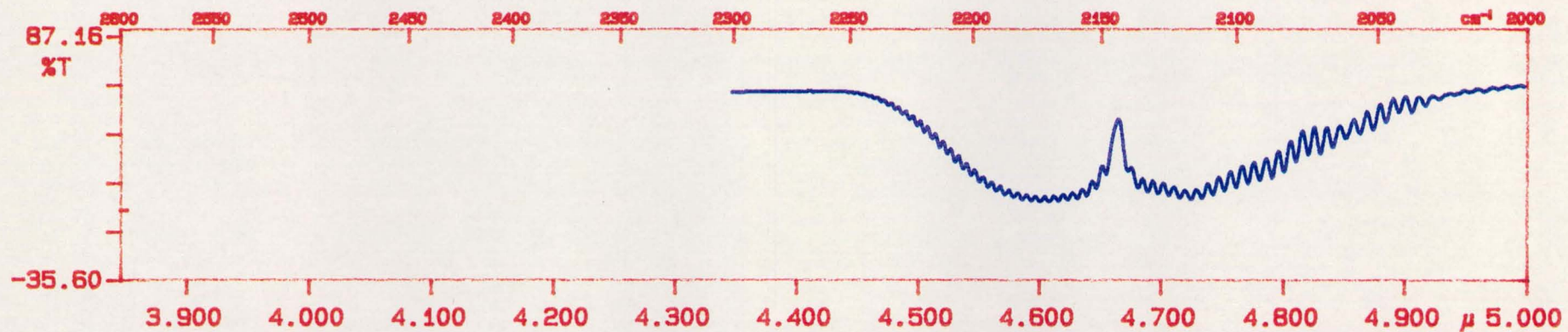
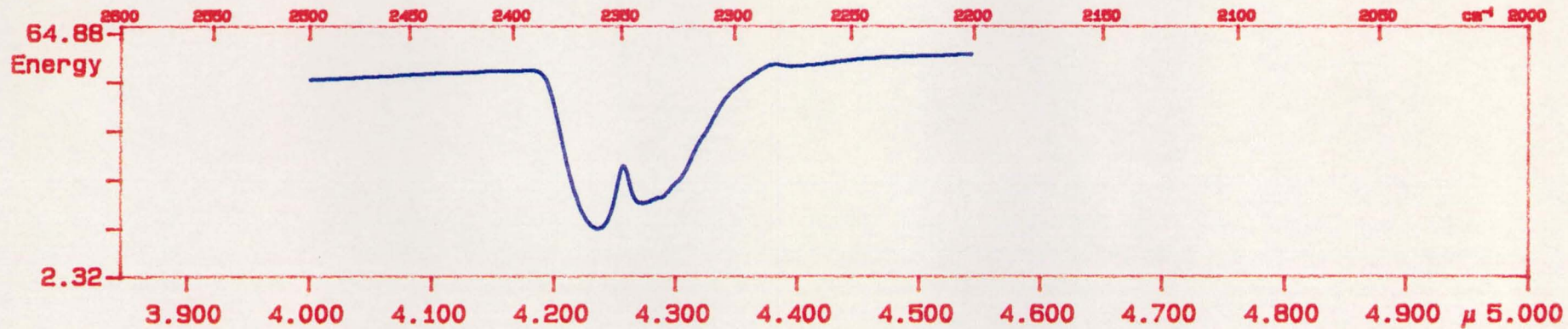


Plate6. Absorption spectrum of CO₂ (hi) and CO (lo)

$$\begin{aligned}
 \text{Area} &= 0.5 \times (\text{area of parabola}) + 2 \times (\text{area of triangle}) \\
 &= 0.5 \times (2.667kLv) + 2 \times ((1-k)Lv \times 0.5) \\
 &= 1.333kLv + (1-k)Lv \\
 &= Lv(1.333k + 1 - k) \\
 &= Lv(0.333k + 1)
 \end{aligned}$$

The model is depicted in the following diagram:

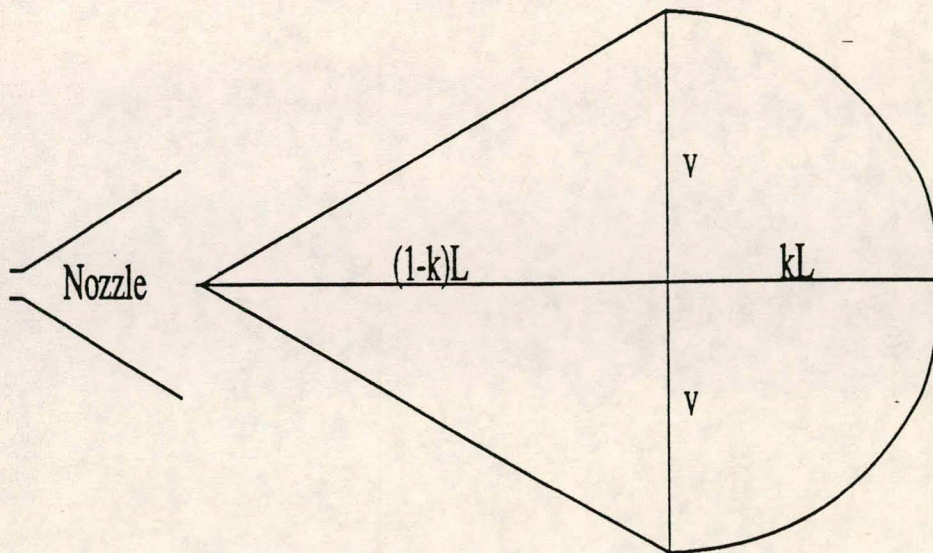


FIGURE 3.4 PLUME MODEL FOR AREA ESTIMATION

The video material was calibrated for width and height aspects so that the plume parameters could be measured directly on the images.

During later development and mathematical refinement all the plume areas were determined as described in paragraph 4.4.

3.4

SHOCK HEATING

Both Sutton, 1976, and Shapiro, 1953, describe the occurrence of supersonic shock patterns in rocket plumes. In conical and contour-type nozzles, shock waves are often visible in the exhaust jet. Certain propellants have relatively non-luminous flames and therefore they show a clean shock wave pattern. With other propellants, such as certain solid propellants, the exhaust jet is incandescently luminous or cloudy, and this phenomenon obscures the shock wave pattern.

The shock waves are a series of expansion and compression waves forming a diamond pattern. The first visible shock wave usually commences at the exit of the nozzle.

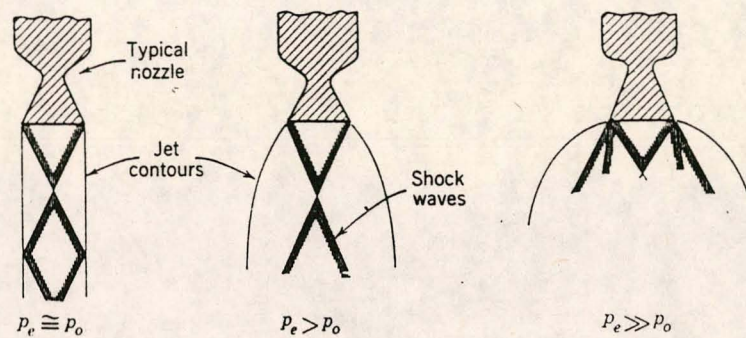


FIGURE 3.5 TYPICAL SHOCK WAVE PATTERNS IN EXHAUST PLUMES

Zucrow, 1976, and Shapiro, 1953, describe a normal shock wave as an instance where the pressure increases five-fold across a front, while the velocity decreases by a factor of three. Theoretical calculations and experimental measurements show that the thickness of a normal shock is sub-micron and is comparable with the mean free path of the molecules.

The theoretical calculations are based on formulae which require lengthy derivations that are beyond the scope of this study. It is sufficient to give a qualitative explanation of the molecular level of some events at the shock front.

When a molecule, e.g. CO₂, H₂O, or partially combusted species, passes the shock front a large part of its translational energy is converted into vibrational and rotational energy through intermolecular collisions.

A sudden increase of pressure, density as well as temperature will occur. This further excites the gaseous molecules that pass through the shock wave. These excited molecules cause spectral emissions in the UV, visible and IR regions and form the observable shock fronts, or shock disks (also refer to as Mach disks, or shock diamonds) in a jet plume. It is such emissions that render these shock disks visible to the human eye under favourable conditions.

These shock disks are present only in situations where gas velocities are equal or above Mach 1 and therefore are applicable only to the aircraft plume and rocket nozzles. *Such conditions are not present during the combustion of a normal flare. This should be realized, and presents the most important consideration in the development of decoy flares.*

It is thus important to note that the presence of multiple shock disks in the aircraft plume will enhance specifically the excitation of the gaseous combustion products H₂O and CO₂. This causes an enhancement in intensity and band broadening of the emission in the 2.5 to 3µm and especially in the 4.2 to 4.4µm regions.

SECTION 4 SPECTRAL PROPERTIES OF FLARE COMPOSITIONS

4.1 EXPERIMENTAL SET-UP

Due to the lack of published data, the characterisation of the jet plume emissions, their analysis and the development of suitable flares had to be undertaken concurrently. The characterisation of the emission of missile plumes was added at a later stage. This was convenient since the experimental set-up and the logistics for conducting field measurements were similar.

The first IR and UV measurements on flare compounds were done during December 1993 and all observations were done after sunset. This was done to ensure a negligible atmospheric background count.

The flare compounds were manufactured by casting the composition in wafer shapes with a single flare comprising two mating wafers with ignition compound between. Ignition was done electronically by positioning a standard bridge wire initiator between the sandwiched flare wafers. Every flare was positioned on a stand with a metal grid 1.5m above the ground.

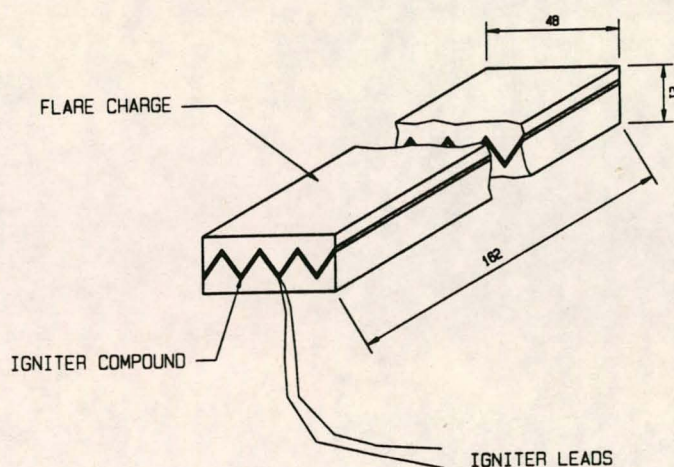


FIGURE 4.1 FLARE ASSEMBLY

The SR5000 spectroradiometer was placed 200m from the flare stand. A second measurement position was situated approximately 50m from the flare stand. At this station area information was captured using the AGEMA 900 imaging radiometer operating in the 3-5 μ m band. Ultraviolet measurements were done by using the UV radiometer as described previously in paragraph 2.2.3. A video camera, with engaged electronic shutter, was used for visual recording. Temperature, humidity and air pressure were recorded for calibration and modelling purposes. The layout of the test site is shown in Figure 4.2.

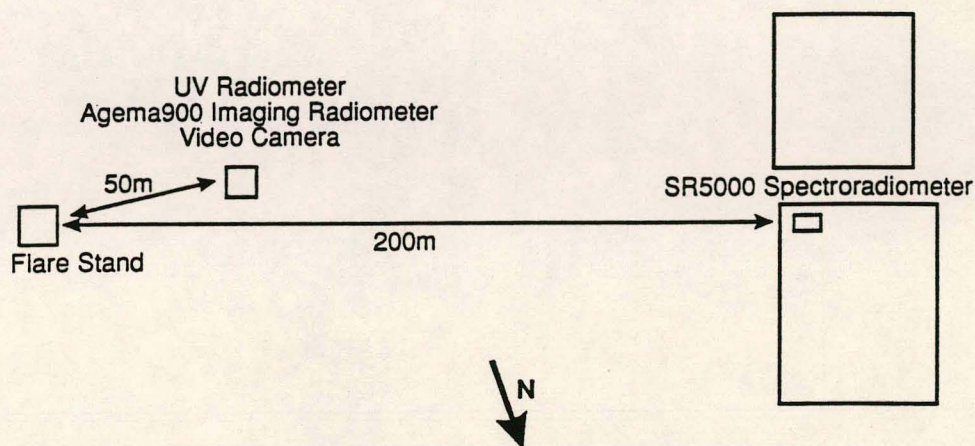


FIGURE 4.2 EXPERIMENTAL TEST SET-UP

The calculations involved the correction for the atmosphere, calibration and data reduction on all three radiometric instruments used. From the imager area effective blackbody temperatures were calculated. Several ways existed therefore to compare the compounds.

4.2

ATMOSPHERIC CORRECTIONS

To correct for the atmosphere, atmospheric simulations were run using the LOWTRAN 7 code. Transmission was calculated over 3m, 10m, 20m, 30m, 40m,

50m and 200m for use with the calibration of the UV radiometer and the spectroradiometer and for path correction during the measurements.

The following Figure shows the difference between the measurement and calibration path transmittances.

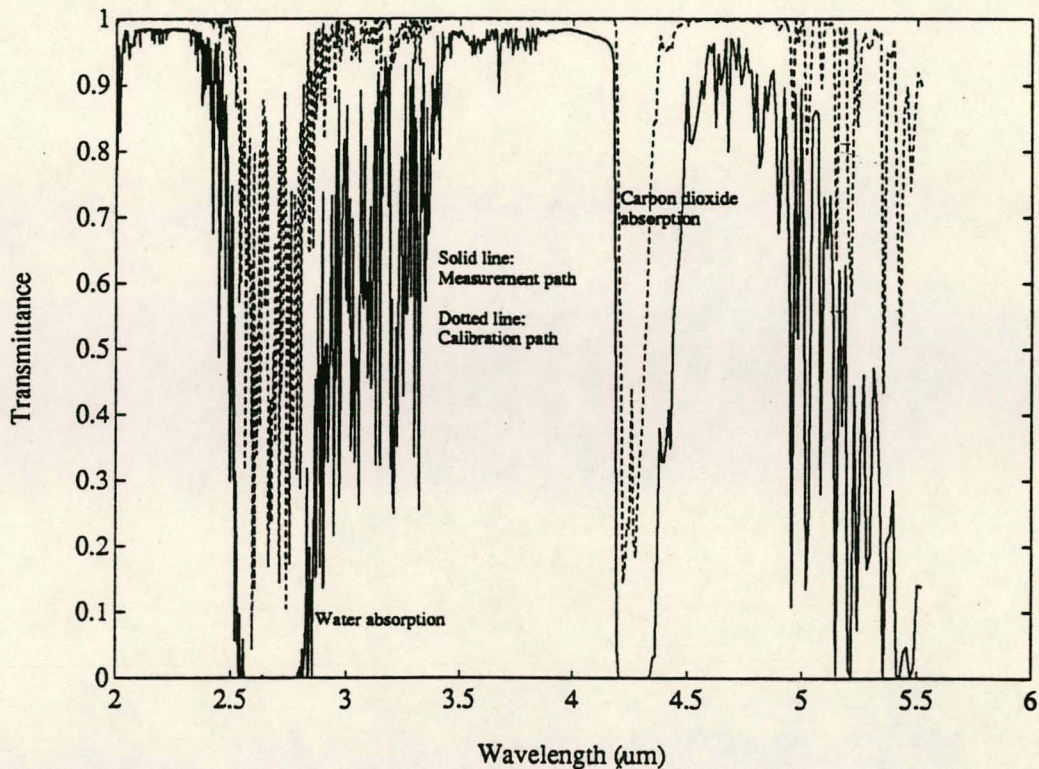


FIGURE 4.3 ATMOSPHERIC CORRECTION OVER THE CALIBRATION AND MEASUREMENT PATHS

From this picture evidently the path transmittance approaches zero for the major absorption bands over the IR band width. This will push up the calculated radiance to excessively high values which will dwarf the rest of the useful spectrum. It was decided to limit the minimum transmission to 2% to overcome this potential problem. This technique was used to process all captured data with the SR5000 spectral radiometer.

4.3

FLARE SPECIFICATION

After initial evaluation of the plume of the aircraft involved, the following preliminary specifications were accepted as guidelines for a new generation flare;

- a) The current flare M1A1 to be replaced with a flare charge with dimensions: 25 x 50 x 205mm.
- b) Static projected flame area: $> 6\text{m}^2$.
- c) Emissivity at $4.4\mu\text{m} > 0.5$.
- d) Radiance between 3 and $5\mu\text{m} < 2.0\text{kW}\cdot\text{m}^{-2}\cdot\text{sr}^{-1}$.
- e) Effective flame temperature: 1200 to 1400K.
- f) A relationship greater than 200 between radiance in the 3 to $5\mu\text{m}$ and the UV bands.
- g) Total burn time $> 3\text{s}$.
- h) Rise time to 0.66 of maximum radiance = 250ms.
- i) After 2s, output > 0.2 of maximum intensity.
- j) Launch velocity from aircraft $> 15\text{m}\cdot\text{s}^{-1}$.
- k) Electrical ignition of flare is required.

4.4

THE EFFECTIVE FLAME AREA AND TEMPERATURE

To determine the area of radiance of a thermal image for any flame or gaseous fire by merely looking at the IR image and trying to establish where the actual energy is situated using the temperature scale provided with the image, is not a trivial problem. A mathematically sound method was developed [Roodt, 1994] and used in order to assist in computing this projected area accurately. The object is to calculate which portion of the image contains 80% of the radiance and to use this information to determine the projected area, assuming that 20% of the image represents smoke and hot air around the flame.

To determine the projected area, one is interested in the radiance as a function of temperature only. The wavelength is determined by the narrow band filter used in the thermal imager. The spectral distribution of the radiation emitted by a blackbody is described by Planck's radiation law (refer to paragraph 2.1.5) which produces an exponential curve with a moderate slope at low temperatures and a rapid increase in the slope as the temperature increases, as shown in Figure 4.4.

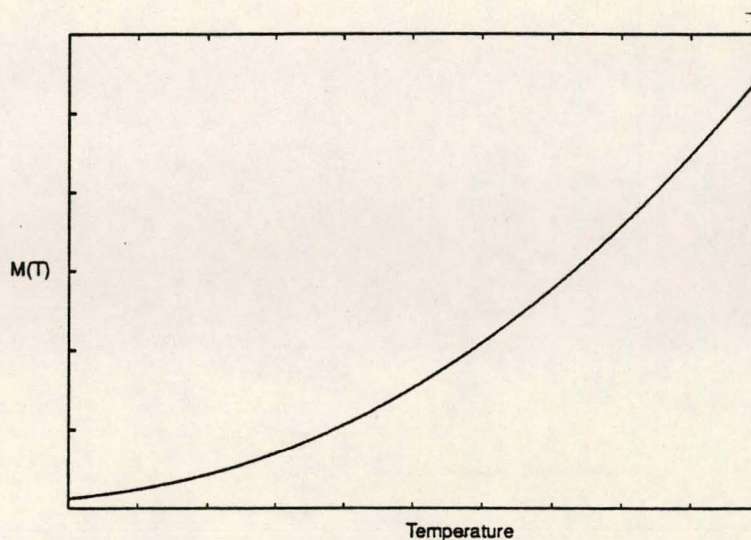


FIGURE 4.4 THE EXITANCE CURVE FOR INCREASING BLACKBODY TEMPERATURES AT A SPECIFIC WAVELENGTH

The next step is to integrate the temperature distribution between the minimum temperature (T_{\min}) on the edge of the image and the maximum temperature (T_{\max}) in the centre of the image as given by the thermal imager. This value would then represent the radiance by the source as observed through the projected area.

The next step will be to divide the area under the graph between (T_{\min}) and (T_{\max}) into five equal areas, each representing 20% of the total radiance from the source, as illustrated by the next graph.

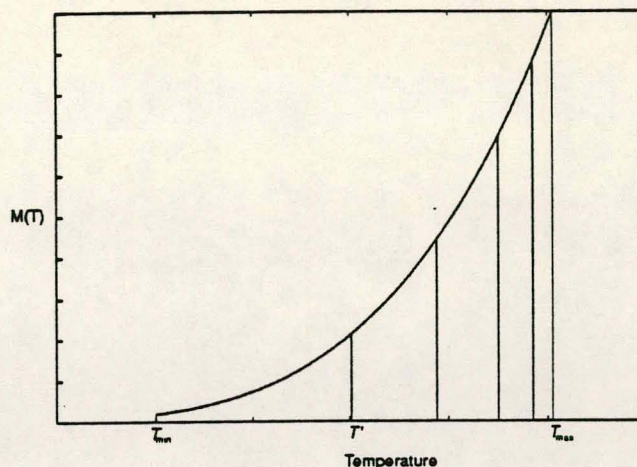


FIGURE 4.5 THE MEDIAN TEMPERATURE AND CORRESPONDING AREA

If the total exitance is thus divided by 5, the result would yield the integrated radiance for each of the five areas. Knowing the required integrated radiance for each of the five areas, it is now possible to calculate the five temperatures representing the 20% intervals of integrated radiance from the source. It is also now possible to determine T' , the temperature above which 80% of the integrated radiance of the source lies. Using an isotherm set at T' , the projected flame area covering 80% of the radiance from the source can be determined and this is then used as the area of the source.

The flame temperature of the source is subsequently determined. This is done by calculating the median temperature between T' , now used as a minimum temperature, and T_{\max} . All temperatures were determined at an emissivity equal to unity.

For the UV measurements the same technique of determining the flame areas and temperatures was employed. The centre line of the filterset of each channel was chosen as the wavelength to calculate the radiance at. As the temperatures were calculated in the infrared band, the area estimation may yield conservative values in the ultraviolet bands.

4.5 IDENTIFICATION OF CHEMICAL SPECIES IN FLAMES OF FLARES

The identification of the chemical species with respect to the electromagnetic spectrum were treated in two groups, namely, the atoms on an elemental basis and polyatomic molecules. Spectral characterization was considered only from the UV (200nm), through the visible spectrum to the far-infrared region (14 μ m). As stated previously the elements do not emit in the rotational and vibrational regions. Their spectral emissions occur mainly in the electronic transitional regions that emit in the UV band. *It is therefore important to note that the metals mainly fall in this category and should be eliminated from the formulations where no UV emission is wanted.* Appendix D contains the detail emission spectra of some relevant elements.

In asymmetrical polyatomic molecules, where changes in dipole moments do exist, combinations of vibrational (bending & stretching) and rotational transitions occur. This causes various identifiable emission bands in the visible and IR regions. In these regions, which stretch from 0.5 μ m (green) to 2.4 μ m (end of the near IR band), water and carbon dioxide, and mixtures thereof in the flame, manifest themselves as small peaks that are well suppressed by cold atmospheric water and carbon dioxide. (see e.g. sf930 in Appendix G and also Figure 2.1) This suppression takes place at 1.15 μ m, 1.4 μ m (CO₂) and at 1.9 μ m by the mixture of atmospheric H₂O and CO₂. A broad band of H₂O and CO₂ emission exists between 2.2 and 3.5 μ m with a very well established atmospheric block-out

by cold H₂O and CO₂ at 2.6 to 2.7 μ m. The fine structure of water emission from the flame is visible between 3.0 and 3.5 μ m. A similar situation exists in the range 4.0 to 5.0 μ m, in which the flame emits a broad band consisting of excited CO₂. Again the cold atmospheric CO₂ suppresses the flame emission strongly at 4.3 μ m. This causes the broad-band emission of the excited CO₂ to appear as a double peak.

Transmittance reaches zero between 5.5 and 7.5 μ m as this region is totally suppressed by atmospheric water. The far IR region ranges from 7.5 to 14 μ m. Total transmittance blockage is caused by cold atmospheric H₂O and CO₂ beyond 14 μ m.

4.6

EMISSION OF GRAPHITE

[Gaydon, 1970]

Small particles are formed in many flames, and they may profoundly affect the radiation. Soot particles may form in organic flames and particles of metallic oxides such as MgO or Al₂O₃ are formed in other flames. The spectrum is then always mainly continuous, instead of consisting of discrete bands, and is more like that from a black body. However, it is wrong to assume that it is identical to that of a black, or even a grey body, at the flame temperature. There are two reasons for this. First, the emissivity of the material of the particle may vary with wavelength; this is particularly true for metallic oxides. The second reason is associated with the scattering of light by small particles; Mie, 1908, has shown that particles which are smaller than a wavelength of light will not only scatter according to the well-known law that the intensity of the scattered light is proportional to the inverse fourth power of the wavelength, but will absorb with an absorption coefficient that also depends on wavelength, even if the material of the particle is black or grey. Thus, by Kirchhoff's law, the emissivity of small

particles will also vary with wavelength. The emissivity may be calculated from Mie's equations if the complex refractive index is known. For very small particles the Rayleigh fourthpower scattering law dominates; for large particles it will approach that for the material of the particle, and for particles comparable in size to the wavelength, the emissivity will change with wavelength in a more complex manner.

4.7 INITIAL FLARE COMPOSITIONS AND MEASUREMENTS

The first flares were obtained from three Denel companies, namely, Swartklip Products, Somchem and Mechem. To date Swartklip is the manufacturer and supplier of the standard flare currently used by the South African Air Force [SAAF]. Mechem and Somchem were the suppliers of experimental flare compounds. The nomenclature chosen for the flare tests is;

SPF - Swartklip Products Flare
MF - Mechem Flare
SF - Somchem Flare

Any characters after the mentioned source designators are related to the compound and the scan (frame) number. The scan numbers are separated by using the characters decimal point or underscore.

For the first test trails various compositions were prepared. These compositions are listed in the following Tables:

TABLE 4.1 STANDARD SWARTKLIP FLARE COMPOSITION

NAME	COMPOSITION	PERCENTAGE
spf	Magnesium	54
	Teflon	30
	Viton	16

TABLE 4.2 MECHEM FLARE COMPOSITIONS

NAME	COMPOSITION	PERCENTAGE
mf01	PE	20
	APC	80
mf02	PE	13
	APC	67
	RDX	20
mf03	PE	13
	APC	67
	TNT	20

NAME	COMPOSITION	PERCENTAGE
mf04	PE	13
	APC	67
	RDX	10
	TNT	10
mf05	PE	13
	APC	67
	NTO	20
mf06	PE	13
	APC	67
	Hex	20
mf07	PE	14
	APC	74
	Cyanuric Acid	10

With; PE - Polyester resin system
 APC - Ammonium perchlorate
 RDX - Trinitrotrimethylene trinitramine
 TNT - Trinitrotoluene
 NTO - Nitro-tri-azo-5-one
 Hex - Hexamine.

TABLE 4.3 SOMCHEM FLARE COMPOSITIONS

NAME	COMPOSITION	PERCENTAGE
sf2515	HTPB	14.0
	APC	70.0
	Al	16.0
sf2524	HTPB	13.8
	APC	86.2
	SiC	1.0
sfdbral (sf265)	HTPB	16.4
	NG/TA	35.6
	MP200	25.0
	RDX	18.0
	Al	5.0
sf280	HTPB	15.0
	APC	68.0
	Al	15.0
	PrBI	2.0
sf289	HTPB	25.0
	APC	73.0
	C	2.0

NAME	COMPOSITION	PERCENTAGE
sf298	HTPB	14.0
	APC	68.0
	Al	16.0
	Fe ₂ O ₃	2.0
sf913	HTPB	15.0
	APC	67.0
	Al	5.0
	Oxa	13.0
sf914	HTPB	15.0
	APC	67.0
	Al	5.0
	Hex	13.0
sf916	HTPB	14.0
	APC	76.0
	Al	5.0
	SrCO ₃	5.0
sf917	HTPB	12.8
	APC	81.2
	SrCO ₃	5.0
	SiC	1.0

NAME	COMPOSITION	PERCENTAGE
sf263	HTPB	16.4
	NG/TA	43.0
	MP200	40.6

With;	HTPB	- Polyurethane binder system
	APC	- Ammonium perchlorate
	Al	- Aluminium
	PrBl	- Prussian Blue
	C	- Carbon black
	Fe ₂ O ₃	- Ferric oxide
	Oxa	- Oxamide
	Hex	- Hexamine
	SiC	- Silicon Carbide
	SrCO ₃	- Strontium Carbonate
	NG/TA	- Nitroglycerine/tri-acetine solution
	MP200	- Ball powder.

During the combustion of these flare compositions the IR and UV data were recorded. Only the IR data ranging between 2.5 and 5µm were processed while the UV data for the three channels 0, 1 and 2 were recorded. All the data sets as well as the calculated flame areas, flame temperatures, filters used and emissivities are tabulated in Appendix E.

The results of these initial measurements, and for comparative purposes the best data sets, were extracted from Appendix E and tabulated as follows;

TABLE 4.4 COMPARATIVE RESULTS FROM INITIAL MEASUREMENTS

Composition Name	Integrated IR Radiance 3-5 μ m (W.m ⁻² .sr ⁻¹)	Integrated IR Radiance 3.5-4 μ m (W.m ⁻² .sr ⁻¹)	Integrated UV Radiance 250-400nm (W.m ⁻² .sr ⁻¹)	Effective Temperature from UV (K)	Effective Blackbody Temperature from AGEMA (K)	Peak Radiance at 4.4 μ m (W.m ⁻² .sr ⁻¹ . $\Delta\lambda$ ⁻¹)
Swartklip 5	52 300	10 900	48.4	2 275	1 824	15 700
F1AZ MG	1 100	5	-	-	-	1 940
Somchem 914	56 200	2 930	1.1	1 860	962	78 000
Mechem 6	57 600	3 440	0.4	1 775	990	73 300

With;

Swartklip 5 = spf 5 = standard MTV flare

F1 AZ MG = Mirage F1 AZ plume with mini afterburner activated

Somchem 914 = sf914

Mechem 6 = mf6

Both compositions sf914 and mf6 contained hexamine (13% and 20%, respectively) as an additive.

The integrated IR value over the 3 to 5 μ m range indicates a strong radiance which makes the flare more "visible" with respect to the luminosity of the aircraft plume. A low integrated value between 3.5 to 4 μ m is wanted as this renders the peaks at 2.5 to 3 μ m and 4.2 to 4.4 μ m more prominent.

The low UV values obtained for the two experimental flare compositions (sf914 and mf6) are caused by the absence of magnesium in the flare plumes. The electronic spectra of metals as explained manifest themselves largely in the UV regions.

The enhancement of the peak at $4.4\mu\text{m}$ in the case of the experimental compositions with respect to the low value obtained from the standard MTV spf5 flare rendered these compositions worthy of further investigation.

These initial results obtained can also be illustrated by expressing the y-axes as "Relative Sterance Units".

This was done merely to show the different effects in the spectral outputs of the flames caused by the various additives. By using this scale the points of concern become more prominent in that Relative Sterance Units are not suppressed by atmospheric conditions.

This is the same as Radiance ($\text{W}\cdot\text{m}^{-2}\cdot\text{sr}^{-1}$) except that the influence of the atmospheric absorption was mathematically removed. In other words it can be seen as a path length of 200m though a vacuum (no attenuation) with all other parameters such as instrument calibration setting, filter and optic corrections, background energy and reflections remaining unchanged.

Figure 4.6 shows the output in "Relative Sterance Units" of the F1 plume with the mini-afterburner activated (mini-gate). When the jet engine is operating on 100% power, but without any afterburner on (100% dry combustion) the spectral output curve remains the same but at an overall lower magnitude. The change from 100% dry combustion to mini gate setting is approximately ten-fold.

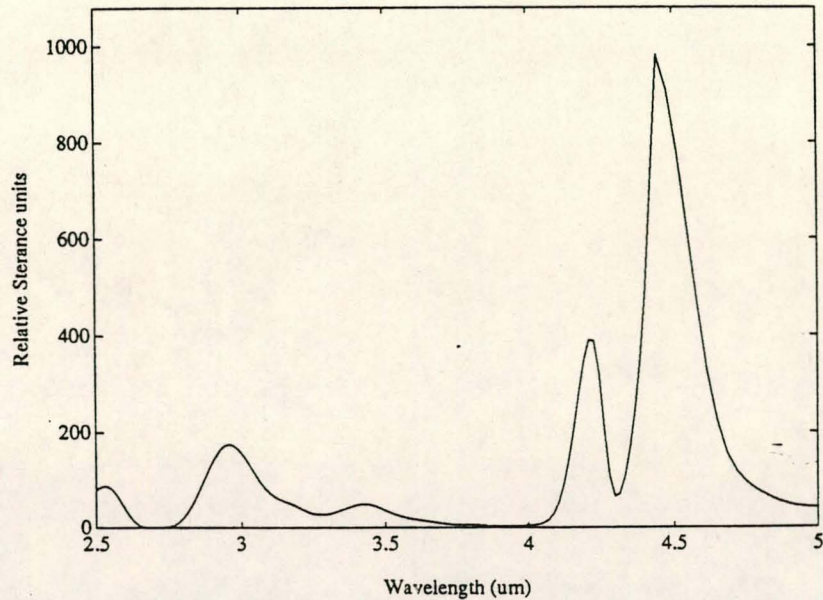


FIGURE 4.6 F1 AZ PLUME (MINI GATE) IN RELATIVE STERANCE UNITS

Spectrally this is also the required spectrum of a possible flare composition.

As stated previously there are certain spectral peaks at specific wavelengths and relative magnitude that are important and must be simulated in decoy flares. In the F1 AZ spectral picture the important peaks are at $2.6\mu\text{m}$, $2.9\mu\text{m}$, $4.2\mu\text{m}$ and $4.4\mu\text{m}$ (refer to paragraph 3.2) and with discrete lows at $2.7\mu\text{m}$, the 3.5 to $4\mu\text{m}$ range and at $4.3\mu\text{m}$. By using the relative sterance units the peak heights also become more noticeable. It can be seen that the peak at $4.4\mu\text{m}$ is much higher than the $4.2\mu\text{m}$ peak and the ratios of the $4.4\mu\text{m}$ peak to the peak at $2.9\mu\text{m}$ and $2.6\mu\text{m}$ are approximately 5 and 10 times, respectively.

If the spectral output of the F1 AZ plume is compared with that of the current Swartklip (MTV) flare it is evident that the MTV composition is spectrally incorrect.

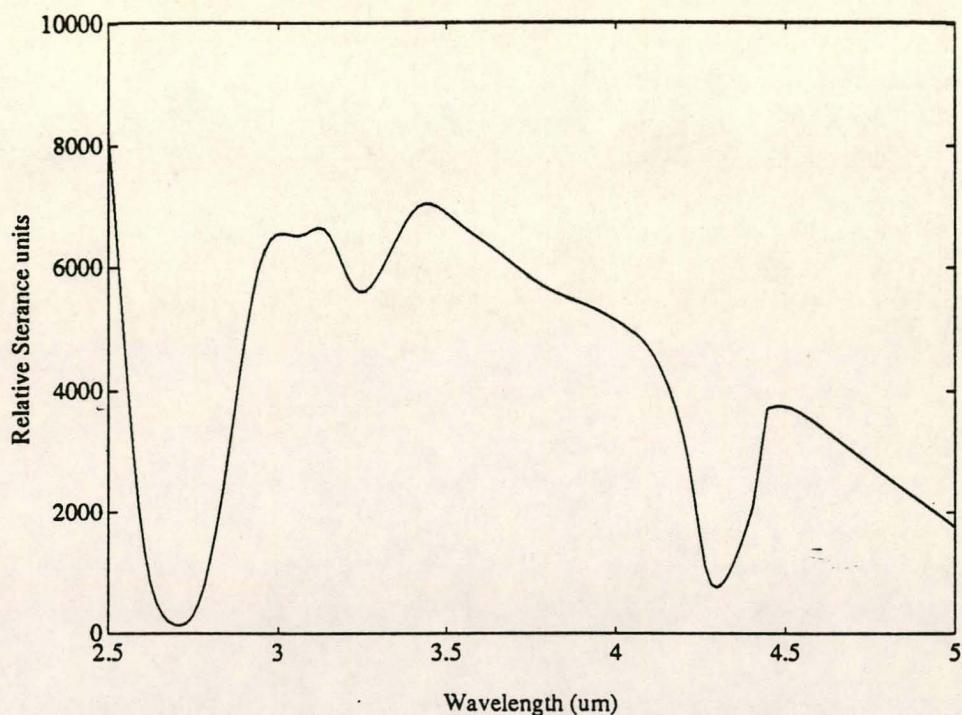


FIGURE 4.7 SPECTRAL OUTPUT OF THE MTV FLARE COMPOSITION

It can be seen that the important peaks are all of the wrong magnitude if compared relatively with each other, also, the distinct enhancement of the integral between 3.5 and 4 μ m is evident. This, as discussed previously, is caused by the broad band emission of the hot metal atoms (magnesium) and soot particles in the MTV flare flame. Refer to sections 4.5 and 4.6.

The same effect is obtained by using a different metal powder. Refer to the flare composition sfdbral that contains 5% aluminium.

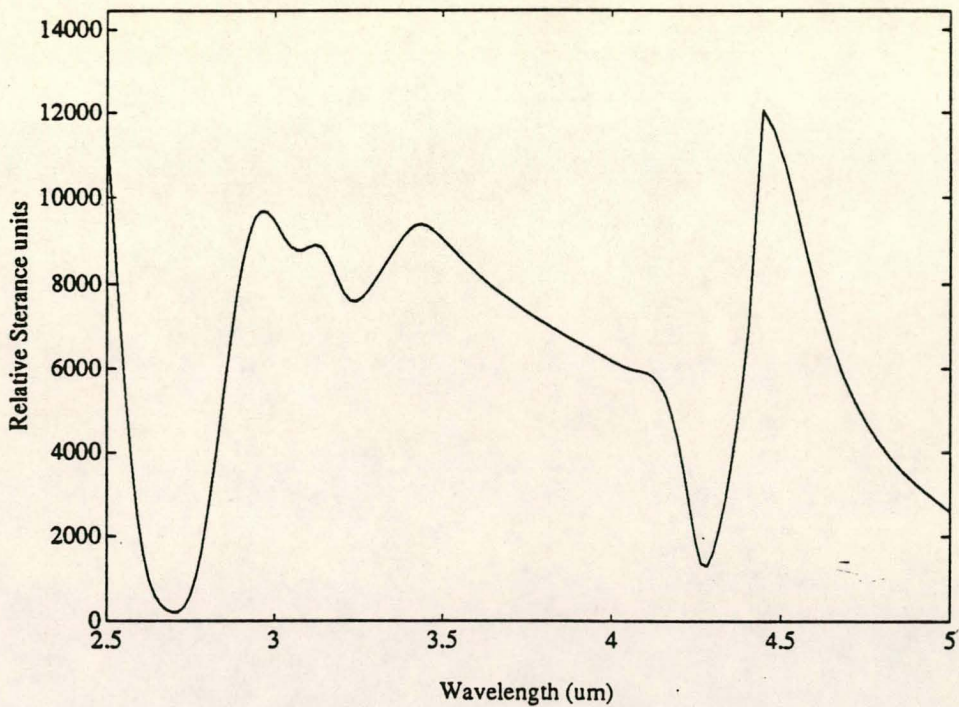


FIGURE 4.8 SPECTRAL OUTPUT OF SF DBRAL FLARE COMPOSITION

Again the metal oxide, Al_2O_3 in this case, causes the marked increase in the 3.5 to $4\mu m$ integral region.

Figure 4.9 shows the effect of doping the flare composition with additional carbon (2% carbon-black). The effect is also clearly visible by the enhancement of the 3.5 to $4\mu m$ integral.

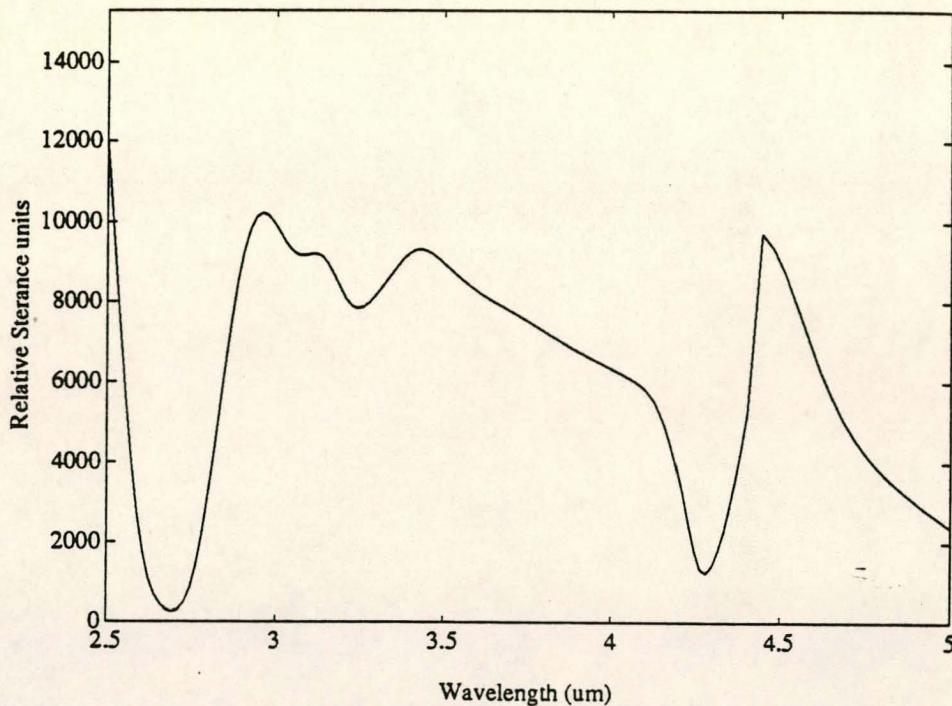


FIGURE 4.9 SPECTRAL OUTPUT OF SF289 FLARE COMPOSITION

For the output signal from a flare composition to be spectrally correct, a high IR emission, along the shape of the aircraft plume, is desirable. An additional increase at the 2.9 to 3.0 μm region would also be welcome. A high UV output, on the other hand, is unwanted. For all the compositions studied the following two curves fitted the wanted description the best.

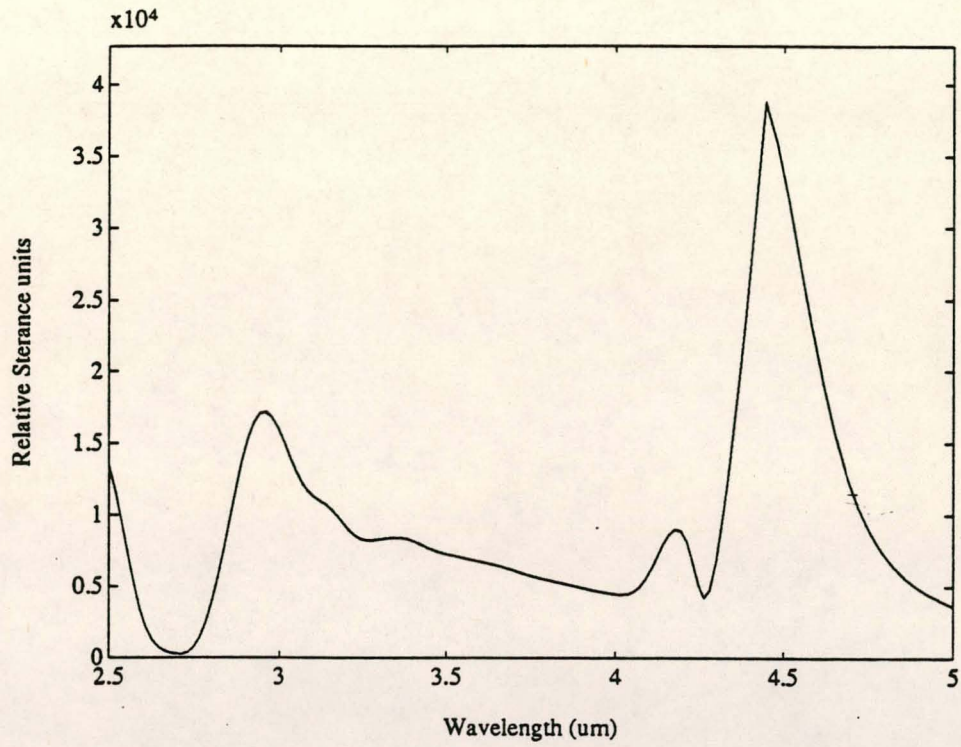


FIGURE 4.10 SPECTRAL OUTPUT OF SF914 FLARE COMPOSITION

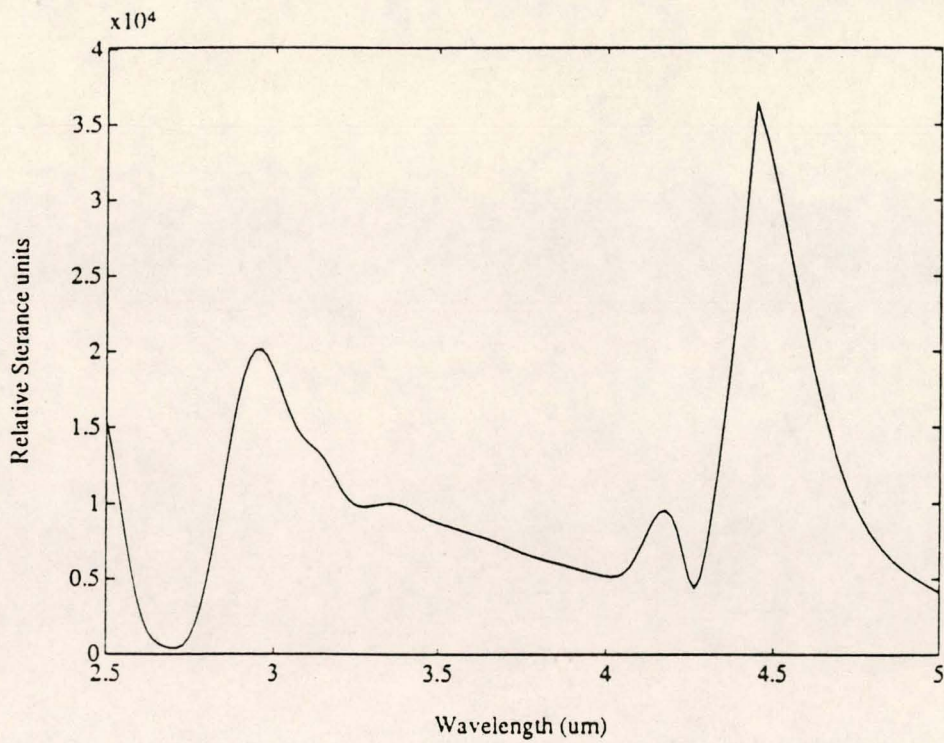


FIGURE 4.11 SPECTRAL OUTPUT OF MF06 FLARE COMPOSITION

In both formulations hexamine was used as the functional additive. These compositions gave very good results with respect to the wanted spectral description of a successful flare. It was this basic flare composition that qualified for further investigations (see later).

Not noted in Table 4.3 is a flare composition of foreign origin. The exact source is not known and the formulation had to be altered slightly to be able to produce a sample of this flare composition for testing. This alteration only entailed a resin system change. The original formulation used a polyester resin as a binder system. The ratios of the constituents remained unchanged. The composition is as follows;

HTPB resin system	17.2%
Boron powder	3.0%
Potassium nitrate	52.9%
Cesium nitrate	6.4%
Ferric oxide	0.5%
Hexamine	15.4%
Silicon	4.6%

This formulation produced generally poor results. The manufacturing, processability, flammability and burn rate at atmospheric conditions all behaved unsatisfactorily. The few frames of data that were captured revealed poor radiation values as well as the expected interference of the metal content (boron, potassium, cesium, iron and silicon) in the formulation. These metals caused an enhancement of the 3.5 to 4 μ m region and an unwanted contribution to UV emission. With this poor performance it was decided not to include this formulation in future investigations. It is notable that hexamine was used in the formulation together with two nitrates as the oxidising agent. The one good point

was the relatively strong peak enhancement that was observed at $4.4\mu\text{m}$ that provided a wanted positive peak ratio. This $4.4\mu\text{m}$ peak increase is strongly coupled to the utilization of hexamine as additive.

4.8 THE ENHANCEMENT OF THE 4.2 AND $4.4\mu\text{m}$ PEAKS

A decoy system that simulates the aircraft plume must be spectrally correct. As stated earlier (see paragraph 3.2) the aircraft plume represents a complete oxidation state of the JET A1 fuel at elevated temperature as well as the additional excitation by shock fronts. This condition causes the discrete broadened spectral peaks for the excited water and carbon dioxide molecules at the two ranges 2.5 to $3\mu\text{m}$ and 4.2 to $4.4\mu\text{m}$. It must be noted that for the aircraft plume the ratio of the 4.2 to $4.4\mu\text{m}$ range to that of the 2.5 to $3\mu\text{m}$ range is of the order of 10:1 with respect to the measured radiance values. It is thus important to incorporate this feature into the decoy system as well. This enhancement of the 4.2 to $4.4\mu\text{m}$ range over the 2.5 to $3\mu\text{m}$ range renders the radiance output spectrally more correct.

In the case of the combustion of a normal flare there are no gas velocities near sonic conditions in the flame. The enhancement of the 4.2 to $4.4\mu\text{m}$ range would be impaired since no additionally excited CO_2 through shock heating would be present in the flare flame, as in the case of the aircraft plume.

One way of enhancing the spectral output at $4.4\mu\text{m}$ would be to do it chemically. This is achieved by incorporating chemical compositions in the flare formulations that would cause spectral radiance at $4.4\mu\text{m}$. The $4.4\mu\text{m}$ peak needs to be addressed more than the $4.2\mu\text{m}$ peak, but both are caused by the fundamental asymmetrical stretching of the CO_2 . CO_2 is a combustion product of any

hydrocarbon system being used as a fuel. This is therefore present in all flare compositions investigated.

From infrared handbooks and tables [Silverstein, p97, 1967] the only chemical species that show spectral activity at 4.4 μm is the asymmetrical stretching of the isocyanate group (-N=C=O). Chemical compounds that could cause fragments of this species when oxidized during combustion, would be the obvious choices to include in the formulation. The gaseous compound isocyanic acid (HNCO) was an obvious choice. It is a decomposition product of solid cyanuric acid with the structural formula as shown in the following Figure.

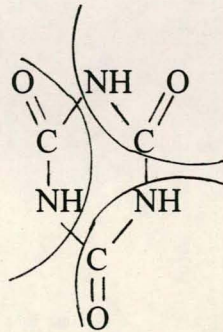
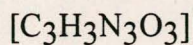


FIGURE 4.12 STRUCTURE OF CYANURIC ACID INDICATING THREE HNCO DECOMPOSITION FRAGMENTS

It was hoped that some HNCO would survive in the flame to emit at 4.4 μm . For this reason cyanuric acid was included in composition mf07. This strategy actually led to an enhancement of the 4.4 μm peak.

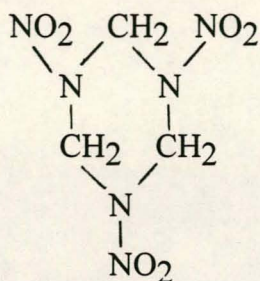
Another strategy which was implemented was to include energetic compounds in the formulation. This was based on the idea that the extra energy in the flame will provide more vibrationally excited CO_2 as well as combustion fragments containing -N=C=O groups. These compounds are listed in the initial flare

formulations (see Tables 4.2 & 4.3). The structural formulae of compounds investigated were;

TRINITRO-TRIMETHYLENE-TRIAMINE

RDX

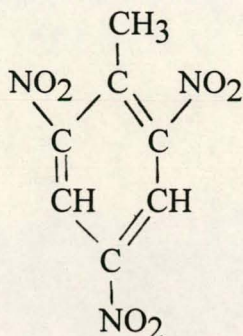
[C₃H₆N₆O₆]



TRINITROTOLUENE

TNT

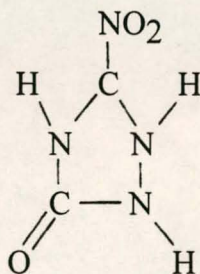
[C₇H₅N₃O₆]



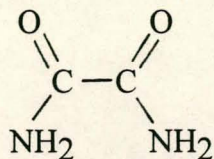
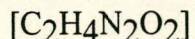
NITRO-TRI-AZO-5-ONE

NTO

[C₂H₃N₄O₃]

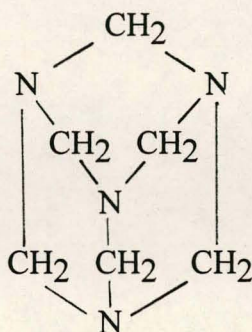
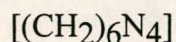


OXAMIDE



HEXAMETHYLENETETRAMINE

HEXAMINE



All these compounds as well as other nitrogen-containing compounds such as nitroglycerine and ball powder MP200 were tested during the initial trails. The MP200 powder is used as a propellant in small-calibre fire arms.

The results of these tests are presented in Appendix E with the most promising candidates being shaded (highlighted) in the Tables. An important fact to note is that the formulation with the best performance was obtained by using hexamine as an additive.

4.9

THE CURRENT FLARE

The qualified IR flare being used by the SAAF is the 25 X 50mm INFRA RED M1A1 flare. Upon activation the flare is ejected from a metal canister and ignited once safely separated from the aircraft. The main charge consists of a

Magnesium-Teflon-Viton (MTV) composition pressing. The Teflon and Viton both serve as oxidizing agents of magnesium as well as internal lubricants during manufacture. These polymers are thermoplastics and serve also as the binder system. Its hydrocarbon polymeric structure together with the magnesium act as the fuel for combustion. The inclusion of magnesium powder is mainly for its pyrophoric ability and enhancement of the combustion temperature.

The spectral output of this flare is presented in the following Figure.

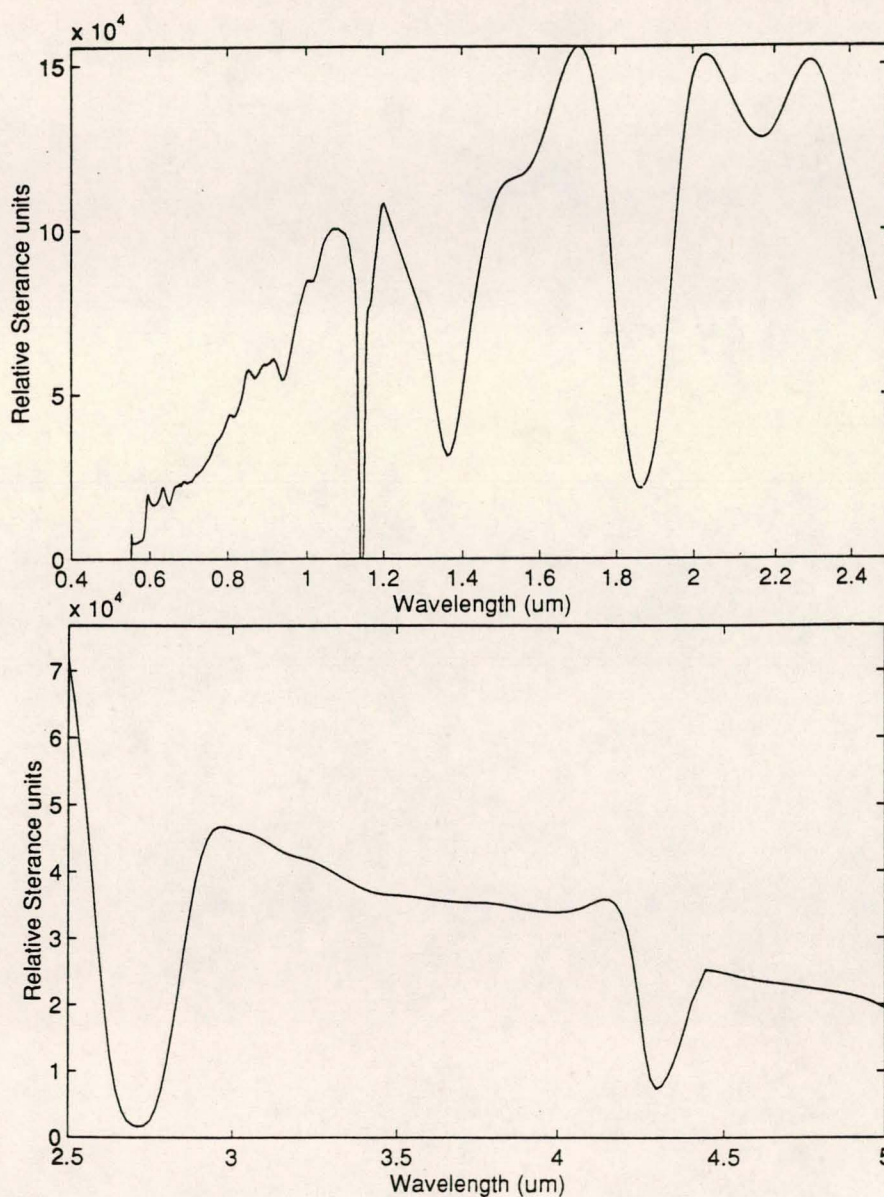


FIGURE 4.13 SPECTRAL OUTPUT OF THE IR M1A1 MTV FLARE

Obviously a large part of the radiant energy available is emitted in the visible and very-near infrared regions. This is due to the combustion of the magnesium in the composition. The relatively high emission between 3.5 and 4 μm when compared to that of the aircraft plume is also caused by the presence of the metal fuel (magnesium in this case). When oxidized, the magnesium forms a mixture of MgF_2 and MgO . Both species are solid particles at the apparent flame temperature. Being at elevated temperatures these particles will emit in the middle infrared region as a broad band. It is also important to note that the peak at 4.4 μm , relative to what is wanted, diminishes greatly.

Apart from the total brightness as a point in the sky, when activated, the aforesaid aspects all add up to a flare that is spectrally incorrect and thus renders itself insufficient to function reliably against modern seeker heads.

4.10

RESULTS OF FURTHER DEVELOPMENT

The initial flare tests were done to establish the chemical compounds that would give the best results with respect to the spectral correctness of the flare flame. These early trials were discussed in previous sections. As stated earlier the formulations containing the hexamine performed best and were chosen for further investigation. This development entailed 1) the determination of the effect of different levels of hexamine content in the flare formulation 2) flare charge packing for more effective deployment and 3) improvement of the manufacturing process to ensure better processability and homogeneity of the composition. Only item 1 will be dealt with in this study.

The hexamine content was varied from 1 to 15%. It is also notable that the particulate matter can be introduced at various particle sizes. This is done to ensure certain advantageous properties such as rate of combustion and the

rheological properties of the mixture. In these flare compositions only two particle sizes were considered. These were designated coarse (200 μm) and fine (20 μm) respectively.

The only particulate matter (solids) in this formulation are the ammonium perchlorate oxidizer and the hexamine. The total solids content was also investigated at two levels, namely, 80 and 85%. This was done to study the effect of a higher oxidizer content as this will increase the rate of combustion as well as the flame temperature. The ignition and overall combustibility properties are also improved by utilising an oxidizer enriched formulation, which is particularly advantageous at high altitudes. The mixtures that were investigated are presented in Table 4.5:

TABLE 4.5 FLARE COMPOSITIONS

Name	% Solids	% Hexamine	APC C/F
sf930	85	5 C	68/32
sf931	85	15 C	64/36
sf932	80	10 F	80/20
sf933	80	1 F	71/29
sf935	80	3 C	70/30
sf937	80	7 C	70/30
sf938	75 AN	10 C	70/30
sf939	polyester binder system		

With;

% solids - the total solid content

C - coarse (200 μ m)

F - fine (20 μ m)

HTPB was used as the binder system.

Only data for the IR range 0.4 to 5 μ m were recorded and processed for these flare tests. No UV data were processed as it was determined during earlier tests (see Appendix E) that the UV radiation, for the basic formulation containing only hexamine as additive, is negligible.

The IR data obtained is presented in the following discussion and Figures.

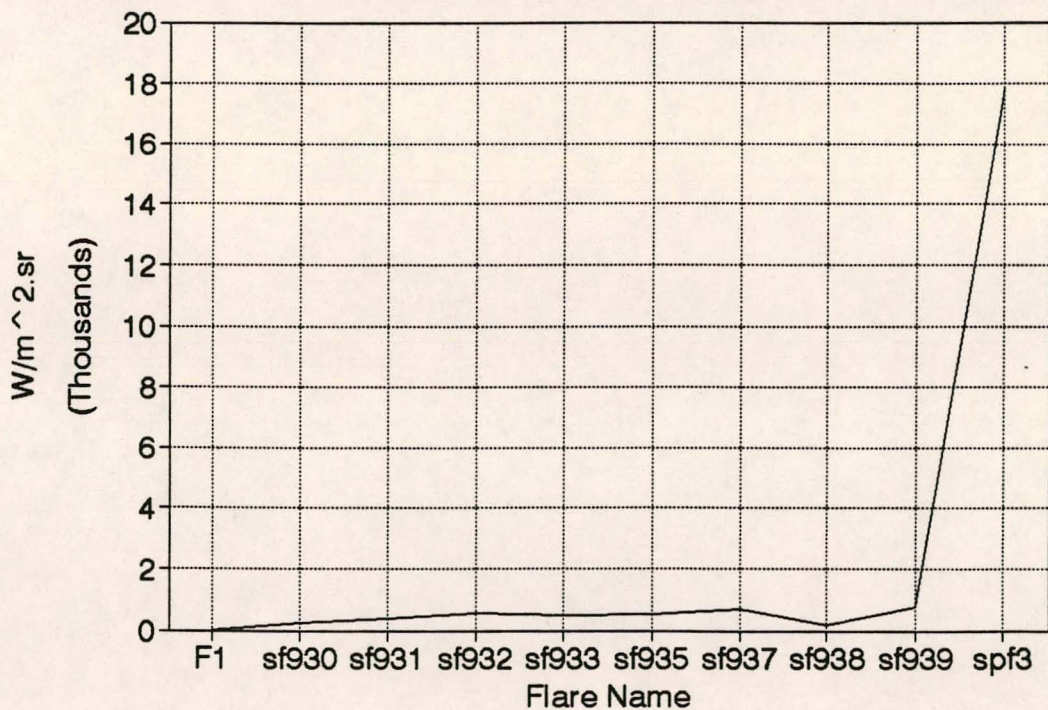


FIGURE 4.14 INTEGRATED RADIANCE IN THE RANGE 0.4 - 1.0 μ m

When compared with the electromagnetic spectrum (see Figure 2.17) it can be seen that this radiation includes the visible (human eye) region. This is the region from $0.4\mu\text{m}$ (green) to $0.77\mu\text{m}$ (dark red). From 0.77 to $1.0\mu\text{m}$, is in the very-near IR region. From this Figure it is evident that the F1 plume is dramatically less active with respect to radiation than the current MTV flare (spf3). The sf-series of flares are all also relatively non-radiative in this region.

Consider the IR region between 1 and $2\mu\text{m}$.

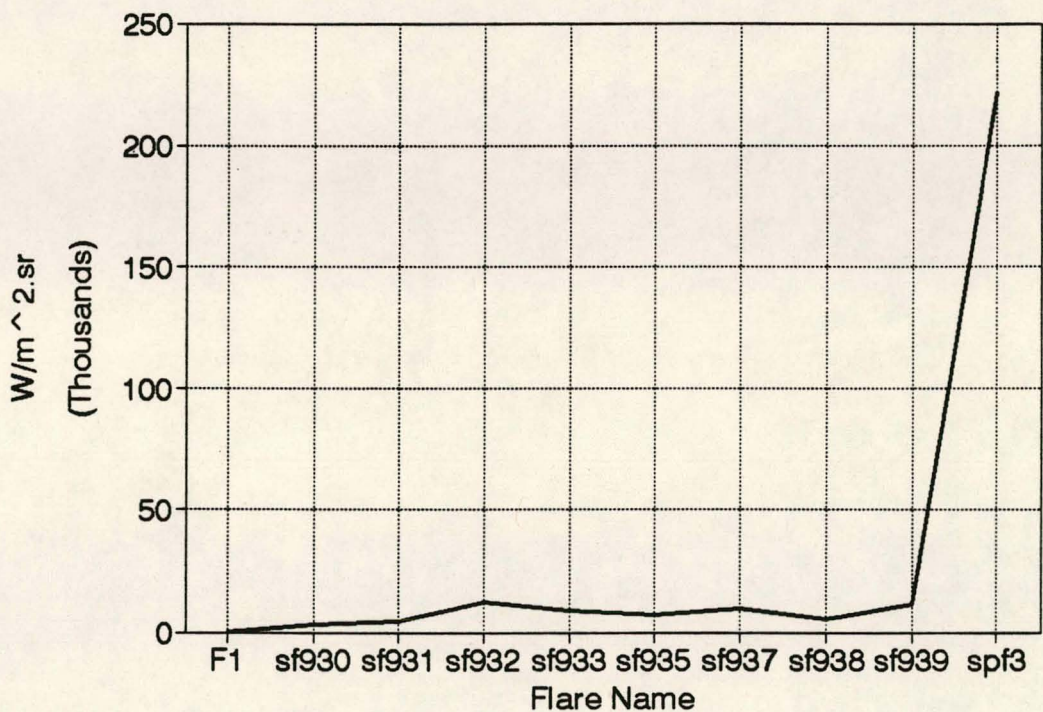


FIGURE 4.15 INTEGRATED RADIANCE IN THE RANGE $1.0 - 2.0\mu\text{m}$

This is similar to the findings of the previous graph. This shows that the current MTV flare (spf3) radiates also excessively in this near-to-middle IR region.

An important region is the total radiation level 3.5 to 4.0 μm . Here again the MTV flare (spf3) radiates excessively. As previously discussed this is due to the hot metallic and soot present in the flame of this flare composition. The flare formulations ranging from sp930 to sp938, excluding sp932, performed much better.

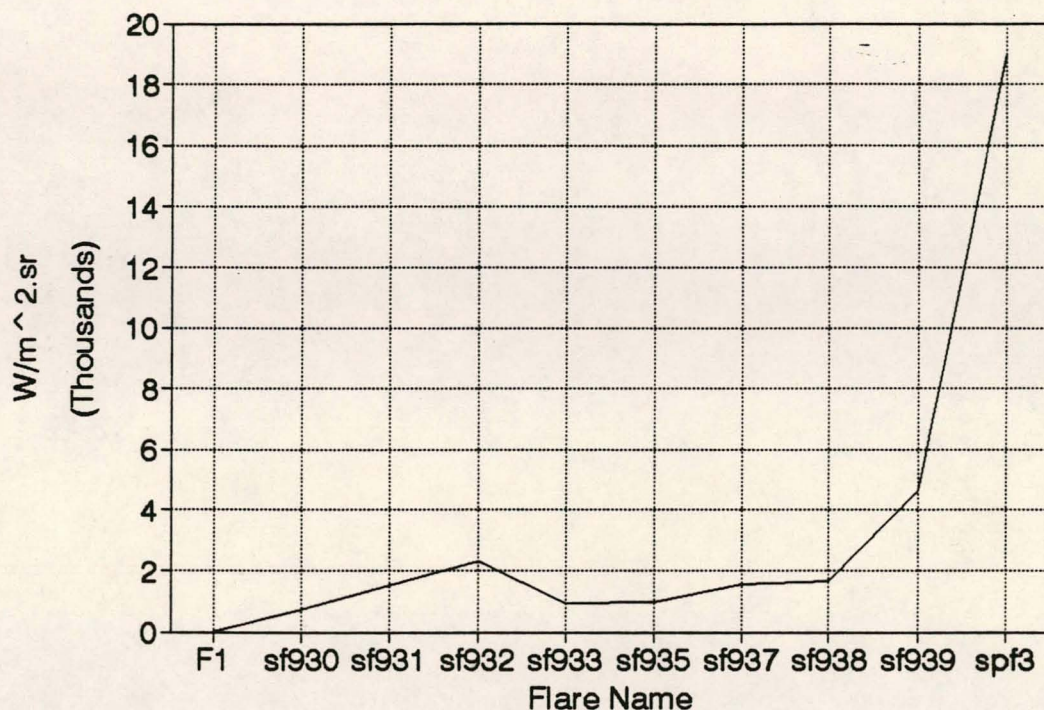


FIGURE 4.16 INTEGRATED RADIANCE IN THE RANGE 3.5 - 4.0 μm

A further important feature of this processed data set is not only the integrated values between certain wavelengths, but also the order of magnitude at specific wavelengths. Figures 4.17 and 4.18 show the radiance at specific wavelengths as selected previously.

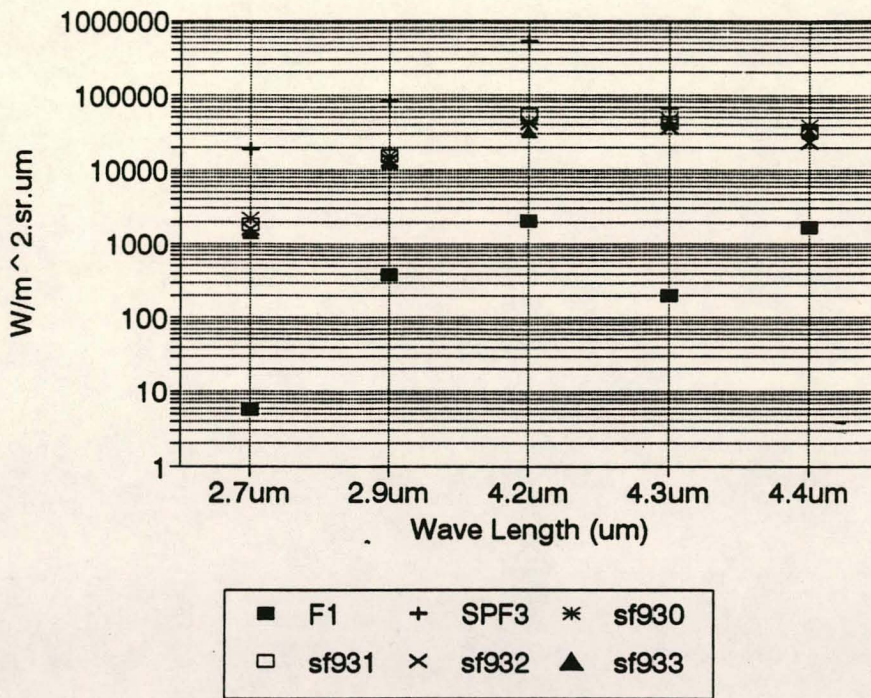


FIGURE 4.17 RADIANCE VALUES (1st SET)

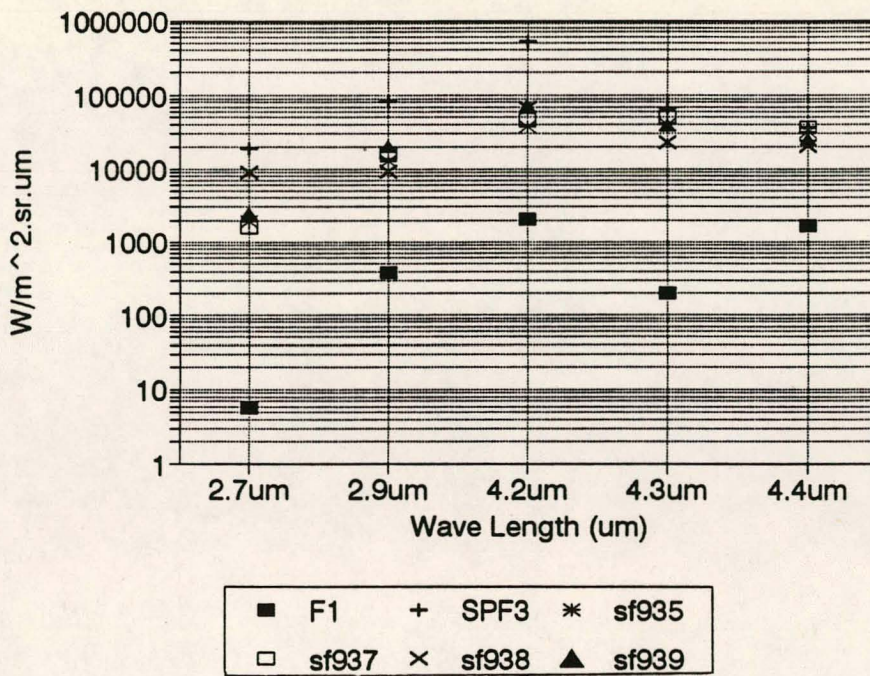


FIGURE 4.18 RADIANCE VALUES (2nd SET)

From these pictures it is evident that the MTV flare (spf3) radiates significantly stronger at wavelengths 2.7, 2.9 and 4.2 μm , but falls back if compared with the population of the sf-series of flares at wavelengths 4.3 and 4.4 μm . It can also be seen that the sf-series of flares follow the curvature of the F1 fairly well except that the F1 emission is much lower for all the measured wavelengths. This is an advantageous characteristic as this renders the flare more visible and attractive than the aircraft plume.

The most important feature of the last two graphs (Figures 4.17 and 4.18) is the ratio of the peak values at wavelengths 4.4 μm and 2.9 μm . It shows that for the aircraft plume (F1) this ratio is approximately 4.4 and for the sf930 flare approximately 2.5. The same ratio calculated for the current MTV flare (spf3) is 0.43. This ratio shows a negative slope with respect to the wavelength ratio. This means that for the measured high value at 2.9 μm for the MTV flare the peak obtained at 4.4 μm is totally underdeveloped. For this flare thus to be spectrally more correct it should have a radiance output at 4.4 μm of at least $210\text{kW}\cdot\text{m}^{-2}\cdot\text{sr}^{-1}\cdot\mu\text{m}^{-1}$. A value of $38\text{kW}\cdot\text{m}^{-2}\cdot\text{sr}^{-1}\cdot\mu\text{m}^{-1}$ was actually measured.

Additional measured data of these flare are given in Appendix F.

The continuous output graphs of the processed data for all the compositions are presented in Appendix G for the wavelengths 0.4 to 5 μm . This is presented for both instances, namely, radiance and relative sterance units.

4.11 THE BEST FORMULATION AND POSSIBLE IMPROVEMENTS

From the aforesaid processed data over the IR range 0.4 to 5 μ m the following deductions are relevant to select the best flare formulation. The following Figure shows the total radiance in the visual to near IR region (0.4 μ m to 2.0 μ m).

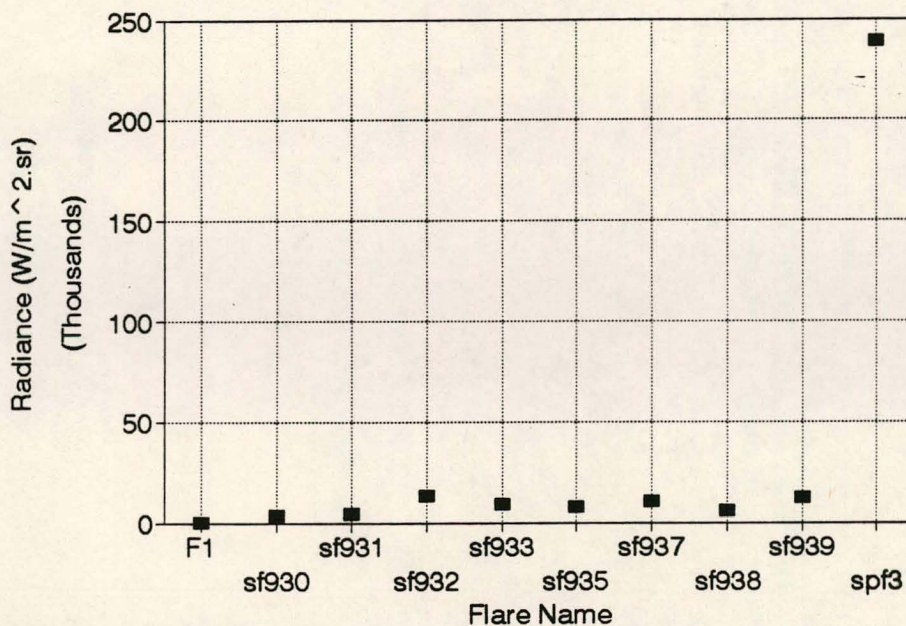


FIGURE 4.19 VISUAL-NEAR IR INTEGRAL (0.4 - 2.0 μ m)

From this Figure it is evident that the F1 aircraft plume is emitting very little and that the best sf composition is sf930.

The same holds for the total radiance between 3.5 and 4.0 μ m. This is also a region where the aircraft plume is emitting virtually nothing and the sf930 composition again performed the best against this minimum radiance output (Refer to Figure 4.16 of the previous section).

A further aspect that was discussed in the previous section was the ratio of the $4.4\mu\text{m}$ peak with respect to the $2.9\mu\text{m}$ peak.

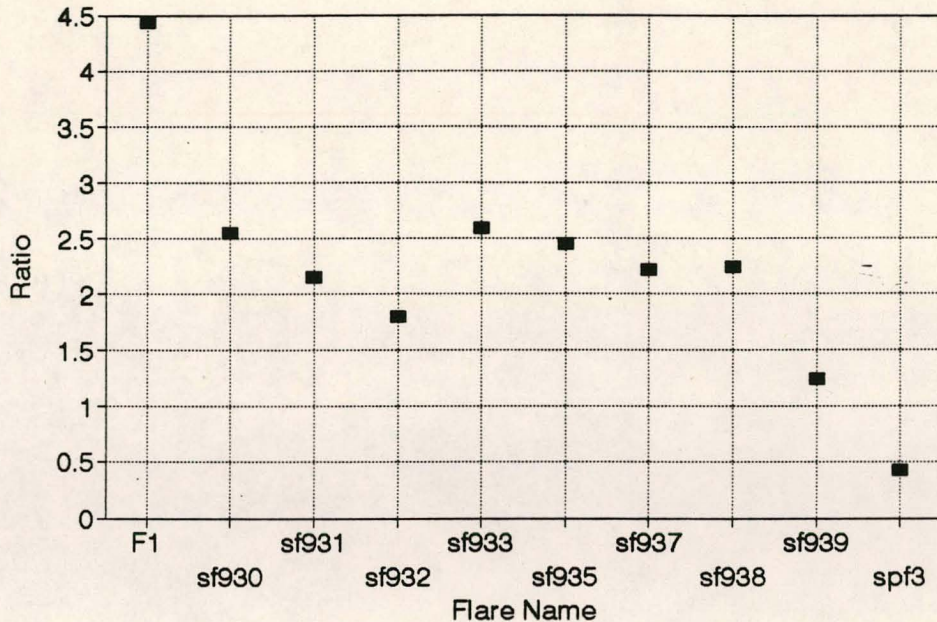


FIGURE 4.20 PEAK RATIO'S - $4.4\mu\text{m}$ TO $2.9\mu\text{m}$

The aircraft plume shows a high ratio (strong positive slope) and the sf930 composition still remains a good candidate especially when compared with the MTV flare (spf3) which in fact produced a negative slope.

Appendix F also shows the absolute values of radiation at $4.4\mu\text{m}$. This value needs to be a maximum relative to the rest of the electromagnetic emission. Although the emission of the aircraft plume is relatively low the $4.4\mu\text{m}$ peak remains an apparent feature of this emission. Again the sf930 composition produced a prominent peak at $4.4\mu\text{m}$.

CONCLUSION AND RECOMMENDATIONS

With this in mind it can be stated that the sf930 performed the best with respect to the chosen parameters. Appendix H shows the difference between the MTV flare and the spectrally corrected flare when statically tested.

One way to improve this flare composition would be to enhance the double peak radiance at 4.2 and 4.4 μm even further. This can be accomplished by considering the following three options;

1. Provide additional carbon for the production of CO_2 .
2. To intervene in the mechanism of the combustion process to produce more vibrationally excited CO_2 and
3. To provide vibrationally excited N_2 as combustion product.

When the first option is considered it must be kept in mind that any additional carbon added to the formulation must be converted completely to CO_2 and not to just hot glowing soot particles. This would defeat the object as hot particulate matter will increase the total radiance in the 3.5 to 4.0 μm region.

The second option is not easily accomplished as combustion mechanisms are complex and therefore not predictable and not easily controlled.

With respect to the third option it must be realized that vibrationally excited N_2 cannot rid itself of its excitation energy through emission. This energy must be transferred to other species through intermolecular collisions. The collision transfer of energy from vibrationally excited N_2 in the first vibrational state to the

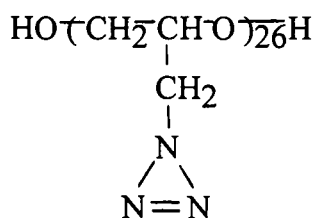
asymmetrical stretching vibration of CO₂ is a very efficient process. This transfer will provide rotationally excited CO₂ molecules in the first vibrational state of the asymmetrical stretching vibration. These aspects were discussed in detail in section 2.5.7 (Transfer of Vibrational Energy). *Since this process occurs in the product gas mixture surrounding the flare, this could also be an important mechanism by which to increase the static flame area of a flare.*

These considerations could be used to explain why the addition of the energetic compounds to the flare compositions in general led to the enhancement of the 4.2 and 4.4 μm double peaks. On combustion these compounds yield vibrationally excited N₂.

One compound that can probably provide even more vibrationally excited N₂ upon combustion is glycidylazide polymer (GAP). It has been established that this compound releases vibrationally excited N₂ early in its combustion. This polymer can also be employed as the binder system together with ammonium perchlorate as oxidizer.

As a theoretical comparison the formulation sf930 was compared with a fictitious composition similar to sf930, but the HTPB chemically substituted with GAP.

The chemical structure of GAP is;



Molecular mass = 2500 to 3000 g.mole⁻¹.

The simulation was done at atmospheric pressure and a flame temperature of 800K (527°C). The plume compositions (as mole fractions) are:

TABLE 4.6 PLUME COMPOSITIONS OF HTPB VS GAP AS BINDER

Species	sf930	sfGAP	Change
CH ₄	0.05323	0.00015	-99.7 %
CO	0.04611	0.00722	-84.3 %
CO ₂	0.21540	0.19105	-11.3 %
HCl	0.17059	0.18460	+ 8.2 %
H ₂	0.19292	0.06239	-67.7 %
H ₂ O	0.21271	0.38957	+83.1 %
N ₂	0.10474	0.16500	+57.5 %
C (gr)	0.00421	0.00000	-100. %

With; gr = graphite.

It can be seen that by replacing the HTPB with GAP the methane (CH₄), carbon monoxide (CO), hydrogen (H₂) and carbon (as graphite) content dropped considerably while there was a marked increase of nitrogen (N₂) and water (H₂O). These species are all evidence of better and more complete combustion and with the additional N₂ prominent.

A flare based on a composition containing GAP should be considered in future for upgrading of the flare developed in this investigation.

SECTION 5 SPECTRAL PROPERTIES OF MISSILE PLUMES

5.1 **PROPELLANT FORMULATIONS**

In order to characterize and analyse the spectral properties of missile plumes the first task was to establish the sample basis. For this reason a range of propellant formulations were selected to be representative of the spectrum of propellant formulations for the relevant weapon products. This range of formulation includes currently qualified items as well as nearly qualified (in development) items. It also contains formulations with propellant constituents to be utilized in future missiles. The selected group of formulations contain both composite and double base formulations which constitute the two major solid rocket propellant families. Each group can be subdivided in two sections. The composite group is subdivided into the conventional smoky and reduced smoke propellant formulations. The double base group is subdivided into the extruded and the cast double base propellants.

It is in the reduced smoke composite propellant group and their derivatives where the most attention is focused upon for future use. Certain additives to the extruded double base formulations also show promising results regarding their use in tactical high volume rate missiles and rockets.

Table 5.1 contains the formulations of the selected range of propellant formulations studied:

TABLE 5.1 PROPELLANT FORMULATIONS

NAME	COMPOSITION	PERCENTAGE
V3C (V3std)	AP	70.0
	Al	16.0
	HTPB	14.0
V3KS	AP	68.0
	Al	16.0
	KS	2.0
	HTPB	14.0
V3FO	AP	68.0
	Al	16.0
	Fe ₂ O ₃	2.0
	HTPB	14.0
V4 (V4std)	AP	86.0
	SiC	1.0
	HTPB	13.0

NAME	COMPOSITION	PERCENTAGE
V4KS	AP	84.0
	SiC	1.0
	KS	2.0
	HTPB	13.0
V4SC	AP	84.0
	SiC	1.0
	SC	2.0
	HTPB	13.0
VLAP	AP	82.0
	Al	4.0
	HTPB	14.0
GG	AN	78.0
	HTPB	22.0

NAME	COMPOSITION	PERCENTAGE
DBR	NC	42.8
	NG	30.0
	EC	2.2
	Pbst	0.5
	TiO ₂	0.6
	C	0.1
	RDX	20.0
	Compound 7	3.8
DBKNKAF	NC	42.8
	NG	30.0
	EC	2.2
	Pbst	0.5
	TiO ₂	0.6
	C	0.1
	KN	6.0
	RDX	10.0
	Compound 7	3.8
	KAIF	4.0

NAME	COMPOSITION	PERCENTAGE
DBNQKN	NC	42.8
	NG	30.0
	EC	2.2
	Pbst	0.5
	TiO ₂	0.6
	C	0.1
	KN	6.0
	NQ	14.0
	Compound 7	3.8
GDBB (GDBR)	NC	32.6
	NG	32.8
	EC	1.3
	Cusal	1.0
	Pbst	1.2
	C	0.3
	RDX	20.1
	Compound 7	1.5
	CuO	0.3
TA	8.9	

NAME	COMPOSITION	PERCENTAGE
GDBRKN	NC	35.98
	NG	30.56
	EC	1.25
	Pbst	0.90
	Cusal	0.75
	C	0.25
	CuO	0.25
	RDX	15.00
	TA	8.91
	KN	4.5
	Compound 7	1.65
GDBSK	NC	55.85
	NG	24.63
	DOP	3.46
	EC	2.10
	TA	9.67
	Pbst	3.79
	C	0.51

With;

- AP - Ammonium perchlorate
- Al - Aluminium

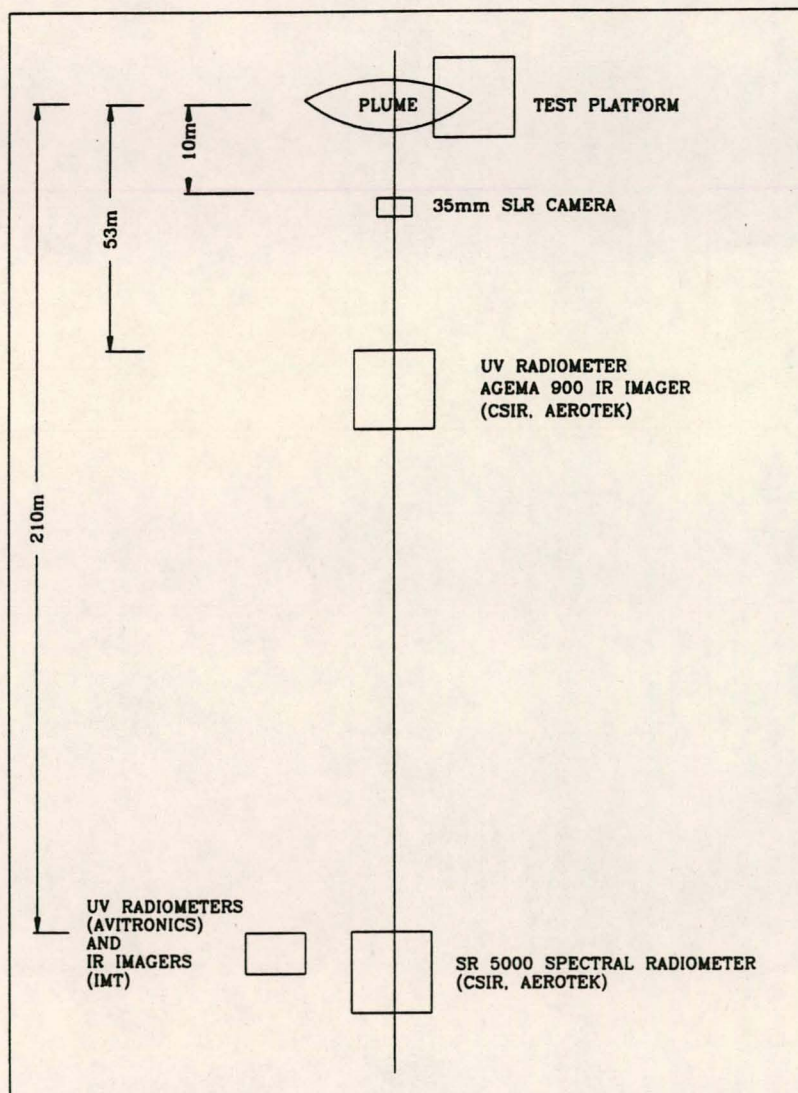
HTPB	-	Urethane binder system
KS	-	Potassium sulfate
SC	-	Strontium carbonate
Fe ₂ O ₃	-	Ferric oxide
SiC	-	Silicon carbide
AN	-	Ammonium nitrate
NC	-	Nitrocellulose
NG	-	Nitroglycerine
EC	-	Ethylcentralite
Pbst	-	Lead stearate
TiO ₂	-	Titanium di-oxide
C	-	Carbon black
RDX	-	Trinitro-trimethylene-triamide
Compound 7	-	Stabilizer
KN	-	Potassium nitrate
KAIF	-	Potassium aluminium fluoride
NQ	-	Nitroguanidine
Cusal	-	Copper salicilate
CuO	-	Copper oxide
TA	-	Tri-acetine
DOP	-	Di-octylphthalate.

Appendix I lists the theoretical mole fractions of the chemical species present in the plumes for the tabulated formulations above.

5.2

EXPERIMENTAL SET-UP AND SPECTRAL MEASUREMENTS

The experimental set-up for the measurements of the missile plumes was similar to that for the flares. All the measurements were also performed well after sunset to ensure a cool and even background. The rocket motors were affixed in such a position that the atmosphere formed the background. The following picture shows schematically a typical test set-up.

FIGURE 5.1 TYPICAL TEST SET-UP

Appendix J shows photographs of the apparatus used.

All the propellant formulations were prepared under well-established and qualified propellant manufacturing procedures at Somchem. The final propellant samples were all evaluated by test firings in the B61 test motor. This is a standard test motor configuration which contains approximately 0.5kg of propellant and resembles a real static rocket motor firing and evokes a plume very true and representative of a real missile firing.

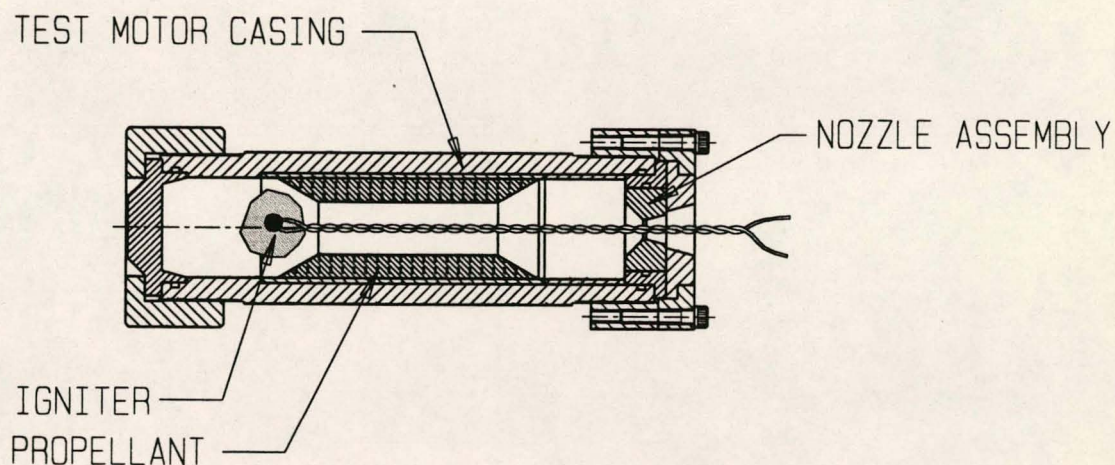


FIGURE 5.2 B61 TEST MOTOR ASSEMBLY

The propellant is geometrically arranged to provide a near-neutral thrust profile and the burn time of a motor was designed to be between 1.0 and 1.5s. In order to accomplish this it was necessary to burn the composite group of propellant at 6 to 8 MPa while the double base group was operating at 10 to 12 MPa. This is also an advantageous feature as the real missile propulsion systems tend to operate in similar pressure ranges. This provided a mass flow rate for all the samples of between 0.3 and 0.5 kg.s⁻¹, making the plumes equivalent in "size" for comparison purposes. By using this test-motor concept the propellant sample could be manufactured easily in multiple quantities for evaluation. All the tests were done at ambient temperature.

The major components of the B61 test motor are the propellant charge, motor casing, bulkhead with igniter and the nozzle assembly. The igniter consists of 10g MTV granules and 10g G12 black powder. It must be noted that during the measurements sampling took place after total dissipation of the igniter combustion products.

After assembly the B61 test motor was strapped down on the test platform from where the tests were commenced. The following picture shows the installation that served as the test platform.



FIGURE 5.3 TEST PLATFORM FOR THE B61 TEST MOTORS

5.3

INTERPRETATION OF SPECTRA

The spectra obtained from the propellant samples will be discussed in their different groups as the results for each group are unique for that propellant group.

The groups are as follow;

V3 Series - Smoky composite propellant

- V3STD
- V3FO
- V3KS

V4 Series - Reduced smoke composite propellant;

- V4STD
- V4KS
- V4SC
- VLAP
- GG

DB Series - Extruded double base propellant;

- DBR
- DBKNKAF
- DBNQKN

GDB Series - Cast double base propellant;

- GDBR
- GDBRKN
- GDBSK

For these propellant samples, data were recorded over the full IR- and UV spectrum. This includes the following;

- 0.45 - 1.15 μ m - visual and very near IR
- 1.3 - 2.4 μ m - near IR
- 2.5 - 5 μ m - middle IR
- 8 - 12 μ m - far IR

- 230 - 280nm - wide band UV.

Figure 5.4 shows the data for the IR range between 0.45 and 1.15 μm .

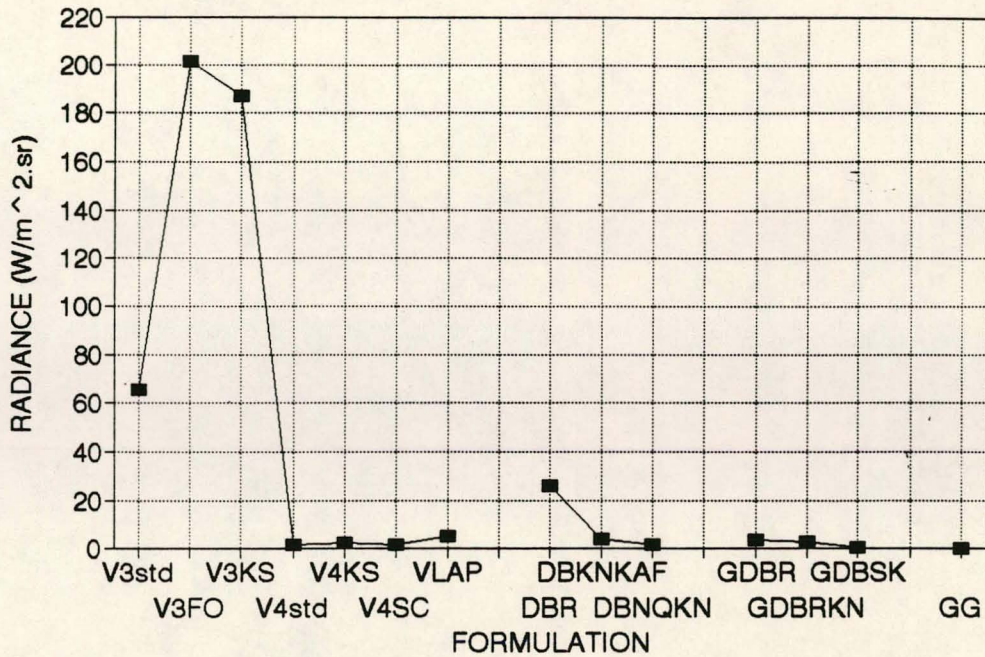


FIGURE 5.4 IR DATA BETWEEN 0.45 AND 1.15 μm

This range covers the visual range (human eye) and obviously the V3-series of propellants are the most prominent with the formulation containing the ferric oxide being the worst. Photographs of these plumes are presented in Appendix K. It is clear, because of the metal content, that these formulations distinctly exhibit primary smoke formation. The VLAP formulation contains 4% aluminium which contributes to the visibility of the plume when compared with the other formulations of the V4-series. The plume is also slightly larger with a more diffuse appearance of the flame (see photo). The rest of the group (V4-series) has

a favourable appearance with respect to this wavelength. The V4SC shows the typical coloration of the plume caused by the strontium ion in the formulation.

The DBR formulation reveals a prominent flame in the plume caused by afterburning of the combustion products. This effect is greatly eliminated by the addition of the potassium ion. DBKNKAF and DBNQKN both contain the element potassium the effect of which is clearly visible. It must be noted that the presence of the potassium (K) ion in the composite formulations does not improve matters at all; in fact it worsens the situation (Refer to propellant samples V3KS and V4KS).

The GBD-series as a whole show very little activity in this visible region except GDBB which shows some distinct afterburning. Very good suppression of the afterburning was again obtained by the addition of the potassium ion in the form of potassium aluminium fluoride and/or potassium nitrate. An interesting observation is that this suppression allows the observation of the shock fronts in the plumes (Refer to the photographs of DBKNKAF, DBNQKN, GDBRKN and GDBSK in Appendix K). The shock heating causes re-ignition of combustible products in these cases.

The GG formulation revealed no traces of visibility and could not be detected in any of the other electromagnetic regions.

The following graphs show the spectral contributions of the propellant samples over the rest of the IR regions.

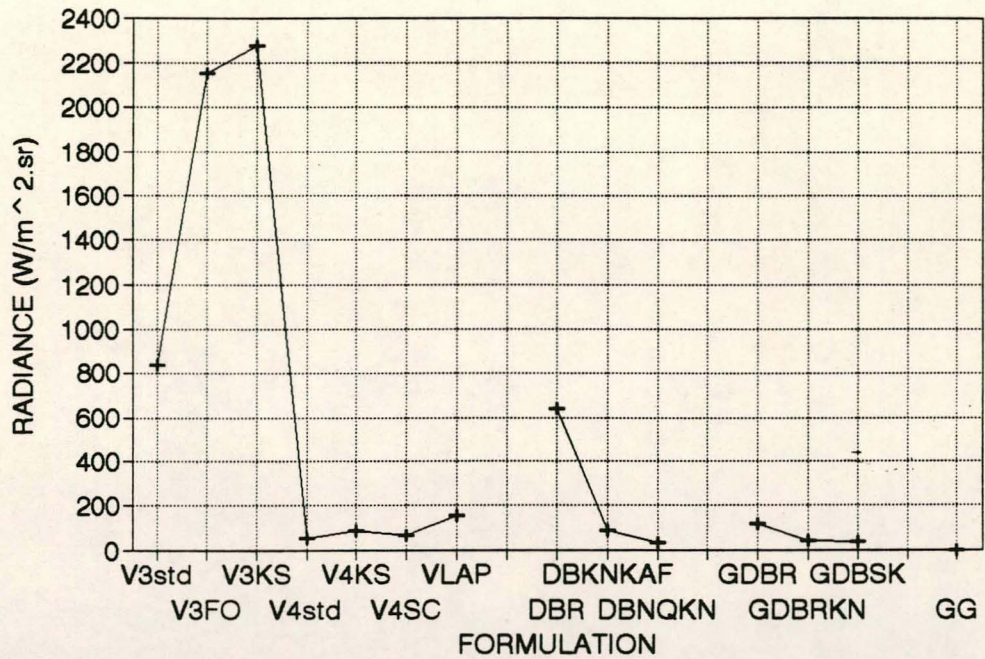


FIGURE 5.5 IR DATA BETWEEN 1.3 AND 2.4 μm

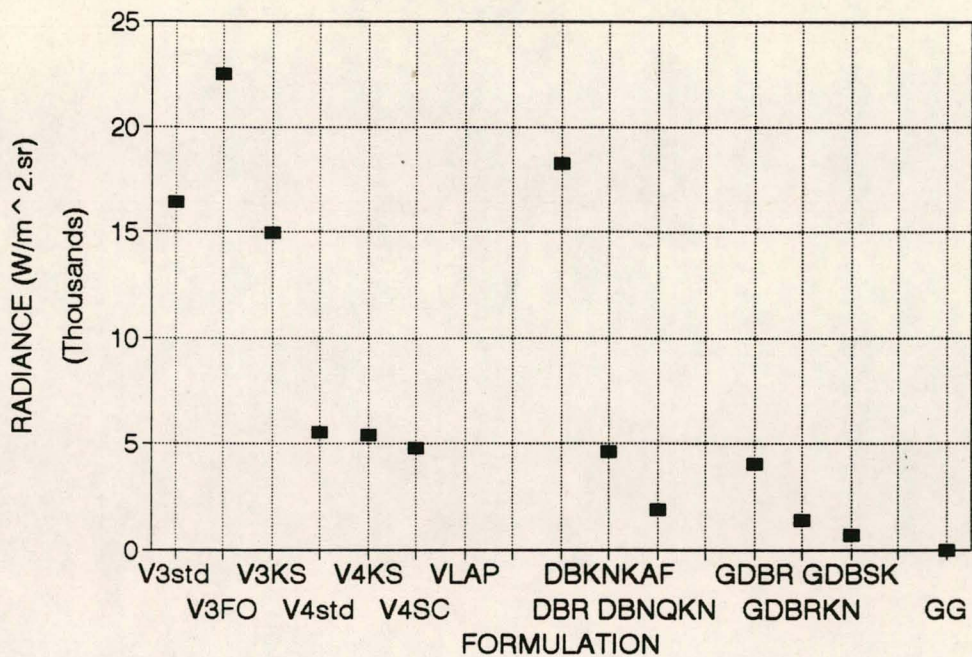


FIGURE 5.6 IR DATA BETWEEN 2.5 AND 5 μm

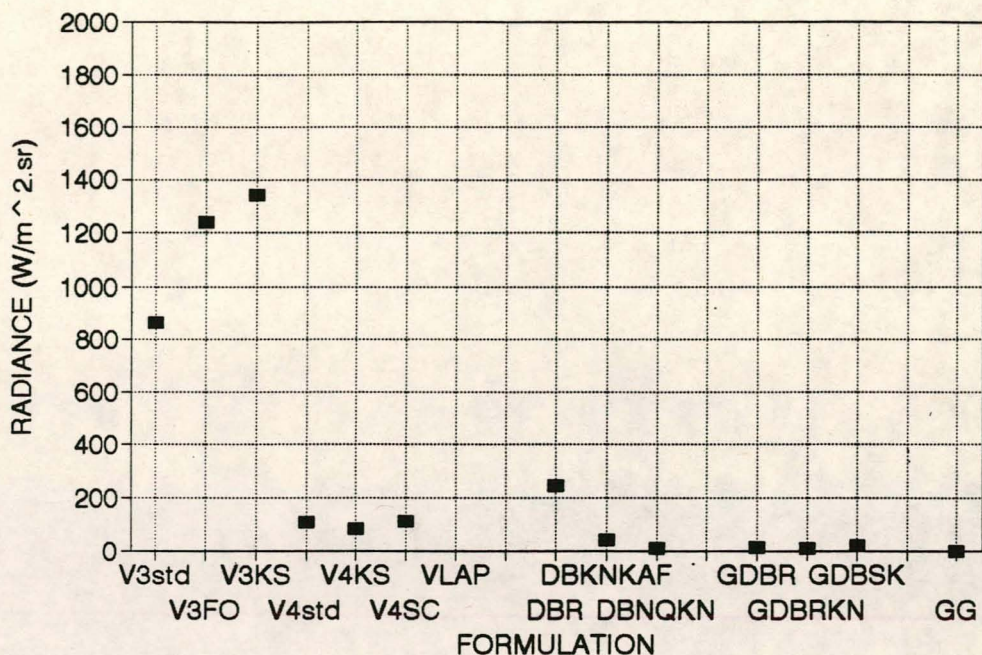


FIGURE 5.7 IR DATA BETWEEN 8 AND 12 μ m

All these graphs reveal a similar pattern as discussed earlier for the visual range. A notable measurement was made for the DBR sample in the middle IR region. (2.5 to 5 μ m). Here the IR emission is of the same order as for the V3-series of propellants.

The explanation for the DBR sample being out of line with the other members of this group is possibly its high (20%) RDX content. This will produce a high radiance in the 4.2 to 4.4 μ m region for similar reasons as in the case of flares i.e. the production of vibrationally excited N₂ which can transfer its vibrational energy to the asymmetrical stretching vibration of the CO₂ molecule.

The next Figure is an aggregate of the previous graphs on the same axis.

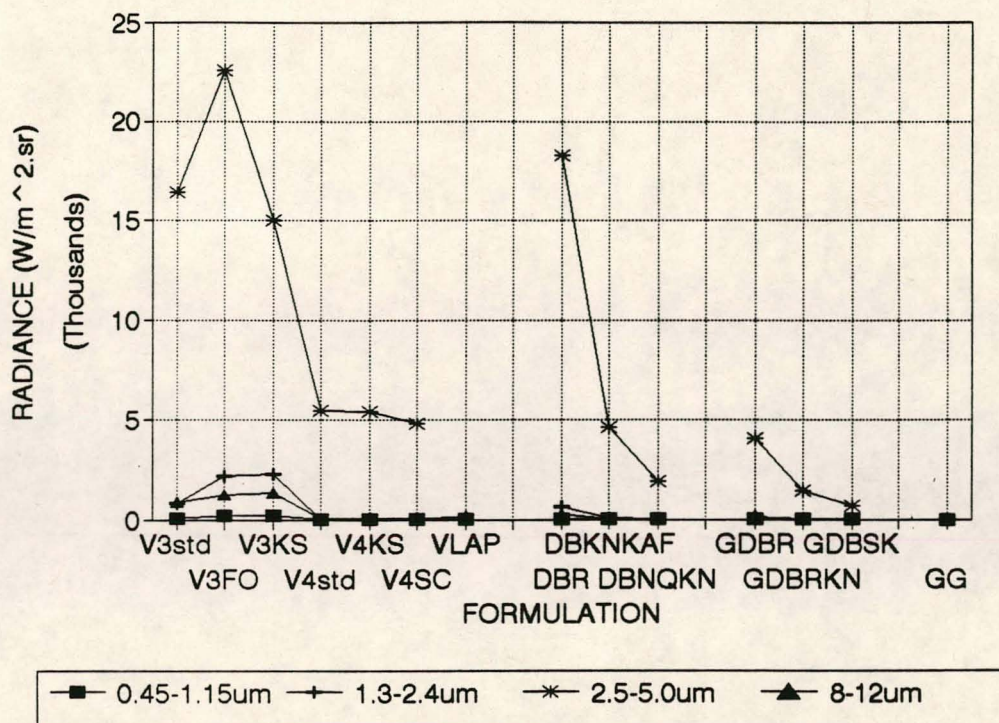


FIGURE 5.8 DATA FROM THE WHOLE IR SPECTRUM

From this picture it is clear which IR region contributes the most to the total spectral output for a specific propellant formulation. Obviously the middle infrared region (2.5 to 5 μ m) contributes the most for virtually all the samples tested. It is also clear that the IR emissions in the visual and near IR region (0.45 - 1.15 μ m) are very small when compared with those in other regions. It must also be noted that the VLAP formulation was evaluated only in the visual and near-IR regions.

The following graph shows the wide band UV data.

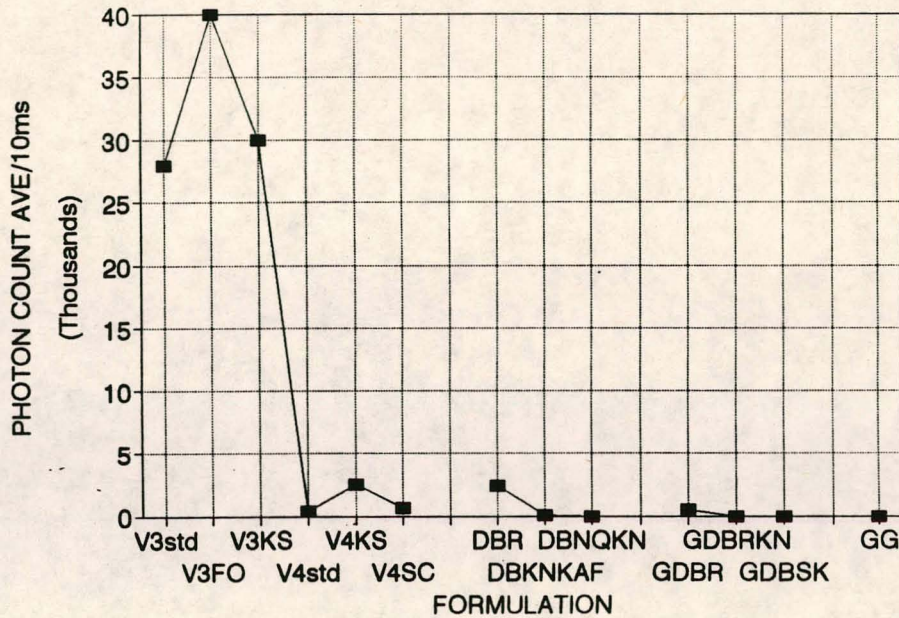


FIGURE 5.9 UV DATA BETWEEN 230 AND 280nm

Again a very similar pattern is evident for the UV range. These data are an important feature with respect to early warning and missile-tracking systems as many of these systems rely on a measurable UV output. Clearly the metal-containing composites (V3-series) emit the most UV radiation. This is largely due to the solid particulate matter in the plume that causes scattering and reflection making the UV emission prominent virtually from any direction. It must be noted that zero measurements were assigned to DBNQKN, GDBRKN, GDBSK and GG propellant formulations. Values of only 5 and 300 photon count average/10ms were measured for DBKNKAF and V4std, respectively. In real terms, such low values render these propellants virtually invisible (not traceable) with respect to

UV detection systems. Again, no UV data could be obtained for the VLAP formulation.

Another significant observation must be added which pertains to both flare compositions and missile propellants containing ammonium perchlorate i.e. sf937, V3C, V3FO, V3KS, V4, V4KS and VLAP. The product analysis (see Table in Appendix I) indicates that a substantial amount of hydrochloric acid is present in gaseous form. One would expect emission in the 3.3 to 3.7 μ m region (refer to Plate 1, The Spectrum of HCl), but there is no indication of such an emission using the existing apparatus. This could be ascribed to complete absorption of the HCl on particulates, the dissociation of the HCl in the water, or that HCl is formed in the $v=0$ vibrational state which cannot emit.

5.4 RADAR TRANSMISSION MEASUREMENTS

5.4.1 Introduction

As indicated in the section discussing the rotational spectra of molecules, water, CO, HCl and polyatomic ions and radicals which might occur in missile plumes can absorb radar waves depending on the frequency employed.

Communication with a rocket often occurs by radar from the rear, through the plume of hot, ionized gases. The frequency and type of signal propagating through the plume have to be chosen such that signal loss and distortion are a minimum. Information transferred using, for instance, phase modulation radar would be adversely affected by phase distortion in the plume.

5.4.2 Measurement Set-up and Equipment [Rossouw, 1995]

Measurements taken during initial tests indicated high levels of phase distortion and attenuation through the plumes, measured at 8GHz with two horn antennas. Several measurements displayed an increase in signal propagating through the plume, which was attributed to a multipath effect. To reduce the possibility of multipath effects, a parabolic reflector antenna was used as the transmitter, due to its highly directive pattern, with a main beamwidth of 6° at 3GHz. The reflector was a 910mm dish fed by a log periodic array. Operation in the near zone of the antenna would render a transmitted beam roughly the size of the aperture, not unlike that of a flashlight. Since the transmission and radar cross-section (RCS) measurements were also done, with these antennas, the choice of operating frequency was determined by the RCS equipment, which had an operating bandwidth of 0.5-3GHz. It was therefore decided to do transmission measurements at 3GHz, using horizontal polarisation. Figure 5.10 shows a schematic of the measurement set-up. A horn antenna mounted on a wooden beam and suspended above the rocket motor was used as the receiver. The transmitter reflector antenna was mounted on an aluminium plate and placed on the ground 14m behind the nozzle and pointing approximately 10° upwards, through the plume, towards the horn.

Two synthesised sweepers, phase-locked for coherency of the received signal, were used as transmitter and local oscillator. The received signal was mixed down and was captured by a storage oscilloscope. Transmission measurements

commenced approximately 2s before the plume was generated and continued for 10s.

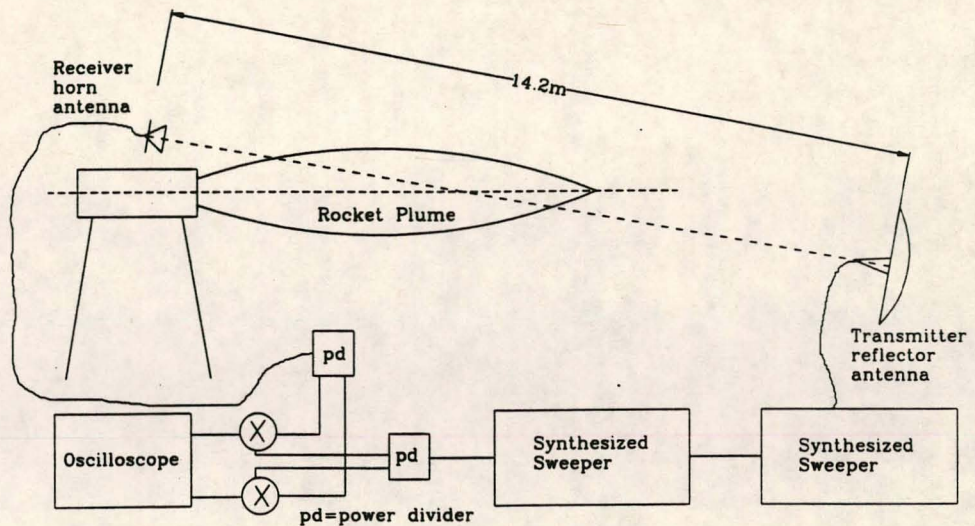


FIGURE 5.10 SET-UP FOR RADAR TRANSMISSION MEASUREMENTS

5.4.3 Results

Refer to Appendix L for pictorial results. Excluding plume GG, all the plumes showed a spike in the transmission measurements at ignition. This serves as a good ignition time index. It is also pleasing to note that no increases in measured levels were observed, so that it seems that the multipath problem had been successfully addressed.

Plume V3STD displayed high levels of attenuation initially, with the attenuation linearly decreasing during the course of 2s. The received signal level dropped

from 5.35mV to 5.2mV, or by 2.8%. After the initial 2.5° spike from -148.8° to -146.3° and back to -147.5° when the rocket was ignited, the jump in phase decreased linearly to -148° while the plume was burning, followed by a sharp decline once the plume died.

For plume VLAP the attenuation was 0.9%, staying relatively constant for the duration of the plume. Attenuation ends 2s after ignition. The constant phase of the plume during the first second after ignition at -144.7°, up from the rest value of -145.5° before ignition, is followed by a higher phase excursion at -144°, lasting for 0.8s, which also ends 2s after ignition. A last spike in the phase occurs 5s after ignition ($t = 6.8s$).

Plume GG introduced no amplitude effects to the transmitted signal. Phase effects were also absent.

DBKNKAF produced an increasing amount of attenuation from 5.3mV signal received to 5.2mV measured 2s after ignition, an attenuation of 1.9%. Two attenuation spikes in the transmission occur, one at ignition and one exactly 2s after ignition. A measure of attenuation was present after the plume had died, probably due to smoke in the range. The phase jumped from -137.3° before ignition to -136.8°, rising to a sharp peak 2s after ignition, corresponding to the attenuation spike observed. A -136.4° phase level continued after the spike occurring at $t = 4s$ (2s after ignition), also caused by the smoke that led to the continued attenuation.

DBNQKN also displayed increasing attenuation as the plume continued. Ignition was marked by an attenuation spike ($t = 2.1\text{s}$) and the signal received was attenuated from 5.33mV to an eventual 5.25mV , or by 1.5% . Approximately 1.8s after ignition the received signal started returning to the original level. No appreciable change in the phase occurred once the plume was burning, but after $t = 4\text{s}$, the phase dropped from -137.5° to -138° .

GDBSK had the spike occurring at ignition, but no attenuation of the transmitted signal was observed. No remarkable phase difference was found.

GDBKN produced an attenuation of the signal from 5.45mV to 5.4mV , or 0.9% . The attenuated level continued for the duration of the measurement, slowly returning to the initial level towards the end of the measurement. No significant phase distortion occurred.

GDBB initially attenuated the signal from 5.4mV to 5.15mV (4.6%) with the level of attenuation decreasing to 5.2mV (3.7%) 1.8s after ignition, before returning to the level it had before the plume was fired. Phase changes were insignificant.

Plume V4std attenuated transmission from 5.17mV to 5.12mV initially and progressively further to 5.10mV . This represents a 1% to 1.4% attenuation over the period of 2.3s when the plume was active. A slight increase in the phase was noted towards the end of the cycle, but is of the level of the noise in the phase graph and thus inconclusive.

5.5 RADAR CROSS-SECTION MEASUREMENTS

5.5.1 Introduction

Detection of a rocket can be influenced by the RADAR Cross-Section (RCS) of its plume, which forms a plasma of hot, ionized gases that may interact with electromagnetic waves, for instance by reflecting the incident waves from a RADAR, or by attenuating them to so reduce the RCS of the plume.

5.5.2 Measurement Set-up and Equipment [Rossouw, 1995]

A pulse RADAR attachment was added to a HP 8510 vector network analyser, to avoid the problems experienced when continuous wave (CW) RADAR measurements were made in previous measurements. CW measurements require that once calibration of the measurement range was performed, using a known reference target such as a sphere, no object in the range may be moved without violating the calibration. CW measurements are also vulnerable to reflections from objects behind the target which can swamp the measured effect. Using a pulse RADAR, the transmitted and received signals are gated to eliminate spurious reflections from outside the target zone. A calibration measurement is done, before experiments commence and with single frequency operation the measured RCS values are simply scaled to agree with theoretical values for the calibration target.

Two 910mm parabolic reflectors were used as transmitter and receiver antennas, respectively (a bistatic RADAR). Both were mounted on a plate and placed on the ground, 10m behind the rocket motor, which was approximately 2.5m above the ground. The antennas were aimed at the rocket nozzle at an angle of 11° from its axis. Horizontal polarisation was used with enough squint in the look direction of the antennas to ensure that both look directly at the rocket. An operating frequency of 3GHz was used.

The transmittance pulse was made 40ns (12m) long; with the motor 10m away, the transmitter was off by the time the pulse returned to the receiver. The receiver gate was set 20ns (6m) wide and placed over the centre portion of the return from the rocket. This ensured that only the portion of the return when the whole target was illuminated uniformly, was measured. Delay between the pulses was adjusted to capture only the return of the rocket and its plume and not from other reflectors further downrange. A high pulse repetition frequency 900kHz was used to ensure maximum average power received. Transmitted power level was varied up to 29dB.m^2 (800 mW).

A trihedral corner reflector was used to test the extent of the target range and to ensure that the best possible alignment of the antennas was achieved.

A 750mm sphere was used as a known target for calibration and compared with the theoretical result to perform scaling of the measurements.

Figure 5.11 shows the RCS measurement set-up, remotely controlled with a PC, as the equipment had to be near the antennas, which were located directly behind the rockets.

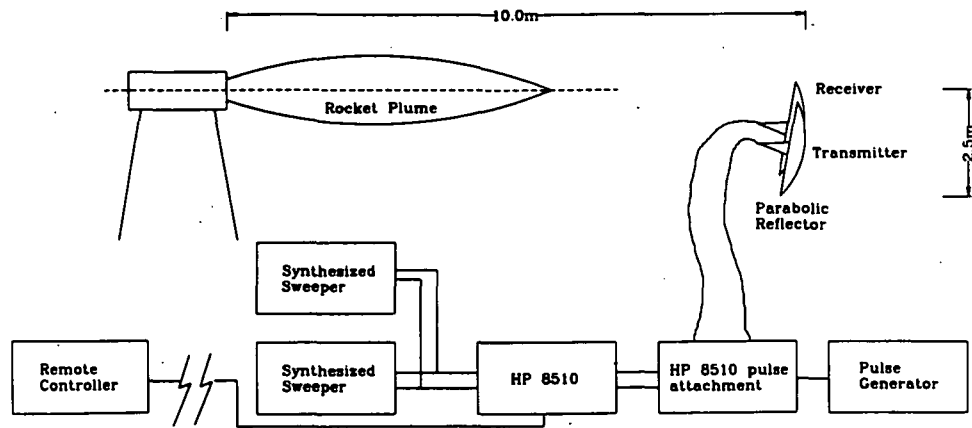


FIGURE 5.11 RADAR CROSS-SECTION MEASUREMENT OF ROCKET PLUMES

RCS values were measured over a period of 12s, starting approximately 2s before ignition of the plumes.

The RADAR cross-section, as function of aspect angle, of a circular disk of the same diameter as the rocket motor was calculated to verify that the RCS measurements were not taken from an angle where a steep slope exists in the RCS of the disk. This may adversely affect the measurements if the motor should vibrate when the rocket motors are fired, by causing rapid variations in the RCS of the motor.

The disk was used to model the rocket motor outlet and one can assume that the RCS beamwidth of the motor outlet will be similar to or broader than that for a disk of the same diameter.

The RCS of a known sphere was measured on an empty range for calibration purposes.

The trihedral corner reflector used to align the parabolic reflectors and adjust the receiving gate of the pulse RADAR was also measured on the empty range. To verify the calibration level, the measured RCS of the corner reflector, at 7.63 dB.m² was compared with the theoretical maximum RCS of 10.66 dB.m².

Measurements of the plumes were done in a target containing the rocket motor, its plume as well as part of the mounting structure, as the antennas have a beamwidth of approximately 1m at that range. Range length was determined by the receiver gate width and was set to 6m from the motor nozzle towards the antennas, to include as much of the plume as possible in the measurement. The RCS of the range prior to ignition of the plume can be seen in the first 1 to 2s of each RCS measurement and should be used as the reference value of each rocket plume, as this value is seen to vary from one rocket to the next. These variations may be attributed to differences in alignment between the antennas and rocket motor from one measurement to the other. The contribution of the plume to the total RCS appears as a step in the measurement.

5.5.3 Results

The absolute value of the RCS of the range (rocket and stand) varied between measurements from -2.8 dB.m^2 and -5.5 dB.m^2 , and should be borne in mind if the absolute RCS of the plumes are compared. The drift in the RCS of the rocket motor assembly (motor and stand) is caused by variations in alignment between the rocket and the two antennas. The structure will have an RCS with much more complex behaviour from different angles of incidence than the disk and may vary by the differences encountered for even small variations in angle of measurement. Slight differences in the position of the rocket motor stand, or in the position of the RADAR antennas will cause enough difference in angle of incidence to be noticeable.

Results show that certain compounds produce significant increases in measured RCS, while others influenced it only moderately and some not at all (Refer to Appendix M for pictorial presentations of the following results).

Two V3STD plumes were fired. Measured RCS over an interval starting 1.5s before ignition show a 2 dB.m^2 step in measured RCS due to the plumes raising the level to -2.3 dB.m^2 or 0.589 m^2 . The plume burned for 2s after which the RCS returned to the level before ignition. A high level of correspondence was observed between the two plumes, both in amplitude and duration of the RCS peak.

The V3KS plume caused a 3dB.m^2 increase in RCS to -2dB.m^2 (0.63m^2) which continued for 3s. After the plume had died the RCS remained at -4 dB.m^2 (1 dB.m^2 above the value for the range) until the end of the measurements.

Plume V3FO was the only one where the measured RCS was actually reduced by 2 dB.m^2 to -8 dB.m^2 (0.16m^2) after the rocket was fired and remaining low for the duration of the measurements.

V4STD had no significant effect upon the RCS of the range.

V4KS also did not influence the measured RCS noticeably.

VLAP increased the RCS by 1.9 dB.m^2 from 3.3 dB.m^2 during the first second of ignition, then the RCS decreased gradually to 1 dB.m^2 above the range during the next 1.8s. The RCS remained at this level for the next 4.4s before decreasing again.

A third V3STD plume was fired for instrument testing. Although the absolute value of the RCS differed from that measured earlier, the shape was similar. The increase in RCS due to the plume was 1.3 dB.m^2 , reaching a value of -1.8dB.m^2 . After the plume died the RCS returned to the value before firing.

Plume DBR may have caused a small reduction in RCS, from -2.6 to -2.8 dB.m^2 , but this is of the same magnitude as drift in the RCS level during a measurement and should be regarded as insignificant.

DBKNKAF caused an increase in RCS from -3.6 to -2dB.m^2 during its 3s burn time.

Plume DBNQKN caused a 2.5dB.m^2 increase in RCS to -1.6dB.m^2 , which continued throughout the measurement. After the plume stopped, a dense smoke filled the range, dispersing very slowly.

GDBSK did not influence the RCS measured.

GDBKN and GDBB also did not influence the RCS.

5.5.4 Discussion of Results

Radar transmission and RCS measurements of missile plumes must in principle be effected by two factors i.e. absorption of the microwaves and reflection. The absorption can be caused by molecules with dipole moments (electric and magnetic) and organic radicals (being products of not completely combusted fuel).

A quick calculation using the formulae given in Section 2.5 gives an absorption frequency for HCl in the 620 to 3100GHz region and for CO in the 120 to 610GHz region. The lower frequency region for CO is due to its smaller rotational constant B. B itself is inversely related to the moment of inertia I ($= \mu r^2$).

The frequencies for HCl and CO are well beyond the 3GHz used in the present measurements.

However, if large organic radicals are considered, the moments of inertia could be so large ($5.6 \times 10^{-43} \text{kg.m}^2$) that absorption at 3GHz may be possible. This would be manifested as a decrease in the RCS. The rocket motor V3FO could be such a case.

Clearly, with reference to Figure 2.7 (radar attenuation spectrum of atmosphere) measurements with radars in the 30 to 300GHz region should provide a wealth of additional information with regard to stealth and identification aspects.

The increase in RCS observed at 3GHz for most rocket motors can be attributed to reflection. This is caused by particulates in the plumes. Some motors e.g. GDBSK, V4STD, V4KS and DBR show no increase and can be regarded as clean-burning i.e. without reflecting (back-scattering) particulates.

It is thus clear that the information gathered from a 3GHz radar should not be discarded but be used in conjunction with information from higher-frequency radars.

SECTION 6 CONCLUSIONS AND RECOMMENDATIONS

It was demonstrated that electromagnetic measurements of plumes could be done successfully. In doing this, it was necessary to interface different science disciplines, namely atomic and molecular spectroscopy, radiometry, electro-optics, radar technology and rocket propulsion science. This was the first attempt of its kind regarding this industry. Flame and plumes being hot dynamic gaseous mediums are remarkably difficult to characterize and it is also difficult to quantify certain parameters. It was consequently necessary to test available instrumentation and to develop mathematical software and models from theoretical baselines to ensure the capturing of trustworthy and reliable data.

It can be concluded that a flare composition was developed with a spectral emission that matched the spectral emission of an aircraft plume. Therefore it was first necessary to measure and characterize the aircraft plume. After analyses of the spectral characteristics of aircraft plumes, events that cause these characteristics and the detection capabilities of certain ground launched missiles, the formulating of the flare compositions commenced. The successful behaviour of the flare was achieved by means of chemical modifications and manipulation of additives and other constituents to the formulation. This flare composition is subjected to qualification for manufacturing should the need arise.

A further formulation based on the GAP polymer was proposed for future investigation and upgrading of the flare.

A representative selection of rocket and missile propellant formulations were successfully characterized with respect to their plume signatures. This study was

focused mainly in the visible to far-infrared (0.4 to 14 μ m) and ultraviolet (230 to 280nm) bands of the electromagnetic spectrum. Through this investigation it was established which propellant formulations are susceptible to be located by early-warning tracking systems. This study also made it possible to broadly identify launched rockets and/or missiles by gathering data of their plumes.

Through this study it was demonstrated that the presence of the potassium ion (K) in the combustion products reduces the secondary combustion (afterburn) in the plume remarkably for the double base group of propellant formulations. This is not only true for the visible region, but also holds for the whole of the IR and UV regions. The presence of potassium adversely affects the plumes of all the formulations from the composite group. It was also clearly demonstrated that the inclusion of metals, such as aluminium, which leads to the formation of primary smoke during combustion, in the formulation greatly affect the plume signature in a negative manner regarding stealthiness of a design. This is valid for the total electromagnetic range under discussion.

Since the onset of this investigation many IR characterisation equipment and measuring techniques have developed to such an extent that the usefulness thereof became appropriate. Two such improvements are the newly available Bomem Fourier Transform Spectralradiometer and the modern Raman Spectrometer. It is recommended that certain propellant samples be characterised by these improved techniques to stimulate and facilitate further research in this study.

From the RADAR transmission measurements of the rocket plumes, it can be deduced that where high attenuations were observed, large phase shifts can also be expected. For the propellant formulations which displayed moderate attenuations, negligible phase distortions were reported.

Finally the RADAR cross-sections (RCS) of the rocket plumes were measured with 3GHz radar and from the results obtained it is concluded that the plumes of certain rocket motors caused a notable increase in RCS. Several cases showed increases in RCS of 2dB over that of the rocket itself. This corresponds to a rocket and stand with RCS of 0.2m^2 to a total RCS of 0.63m^2 when measured from an angle 11° from the longitudinal axis of the rocket. Others showed no increase.

It has been shown that RCS measurements on missile plumes with higher frequency radars are needed to provide additional information. This information in conjunction with that obtained from, UV and IR emissions should be used for detection and stealth purposes.

A composite missile detection system capable of switching between UV, IR and low and high frequency radars must be considered.

An important consequence of the characterisation of the emission spectra of jet plumes is the identification of friend or foe. The emission spectra of jet plumes can be manipulated to such an extent that one's own IR-guided missiles can recognise and ignore them. Strategies for this manipulation should be developed.

REFERENCES

Alberty, R.A., Physical Chemistry, pp484-513, John Wiley & Sons, 7th. Ed., 1987.

Atkins, P.W., Physical Chemistry, p480 and p520, Oxford University Press, 4th. Ed., 1990.

Barrow, G.M., Physical Chemistry, pp332-359, McGraw-Hill Book Co., 2nd. Ed., 1966.

Blinder, S.M., Advanced Physical Chemistry, A Survey of Modern Theoretical Principles, pp60-100, The Macmillan Company, 1st print, 1969.

Daniels, F., Alberty, R.A., Physical Chemistry, pp531-553, John Wiley & Sons, Inc., 3rd. Ed., 1966.

Daniels, F., Williams, J.W., Bender, P., Alberty, R.A., Cornwell, C.D., Experimental Physical Chemistry, pp519-520, McGraw-Hill Book Co. Inc., Sixth Ed., 1962.

Gaydon, A.G., Wolfhard, H.G., Flames - Their Structure, Radiation and Temperature, pp211-238, Chapman and Hall LTD, 3rd. Ed., 1970.

Halliday, D., Resnick, R., Fundamentals of Physics, pp770-771, John Wiley & Sons, Inc., International Ed., 1970.

Hutchison, T.S., Baird, D.C., The Physics of Engineering Solids, pp209-288, John Wiley & Sons, Inc., 2nd. Ed., 1968.

Infrared Technology Workshop Proceedings, Aeronautical Systems Technology, CSIR, 23 June 1994.

Kirk-Othmer, Encyclopedia of Chemical Technology, 3rd. Ed., Vol. 14, p 54, John Wiley & Sons, 1981.

Leuschner, F.W., Olckers, P., Introduction to Photonics, pp1-10, Section 2, Radiometric and Photometric Quantities and Units, The Laboratory for Advanced Engineering, UP., Sept. 1989.

Leuschner, F.W., Olckers, P., Introduction to Photonics, pp1-22, Section 4, Fundamentals of Semiconductor Physics, The Laboratory for Advanced Engineering, UP., Sept. 1989.

Mie, G., Ann. Phys. Leipzig, 25, p377, 1908.

Moore, C.E., Atomic Energy Levels, United States Department of Commerce, National Bureau of Standards, Circular 467, Vols. I - III, 1958.

RCA, Electro-Optics Handbook, Technical Series EOH-11, pp35-37, 1974.

Roodt, J.H.S., le Roux, F.P.J., Collin, F.G., Lombard, O.C., Spectral Measurements of Missile Propellant Plumes, Aero 92/054, Aeronautical Systems Technology, CSIR, February 1992.

Roodt, J.H.S., Collin, F.G., Lombard, O.C., Spectral Measurements of Missile Propellant Plumes - January 1993, Aero 93/063, Aeronautical Systems Technology, CSIR, March 1993.

Roodt, J.H.S., Collin, F.G., Lombard, O.C., Denner, B.F., Evaluation of New Generation Flare Compounds, Langebaanweg, December 1993, Aero 94/026, Manufacturing and Aeronautical Systems Technology, CSIR, January 1994.

Rossouw, M.J., Electromagnetic Measurements Of Rocket Plumes, Aero 95/014, Manufacturing and Aeronautical Systems Technology, CSIR, January 1995.

Shapiro, A.H., The Dynamics and Thermodynamics of Compressible Fluid Flow, Vol 1, p112, The Ronald Press Company, 1953.

Silverstein, R.M., Bassler, G.C., Spectrometric Identification of Organic Compounds, 2nd. Ed., p66 and p97, John Wiley & Sons Inc., 1967.

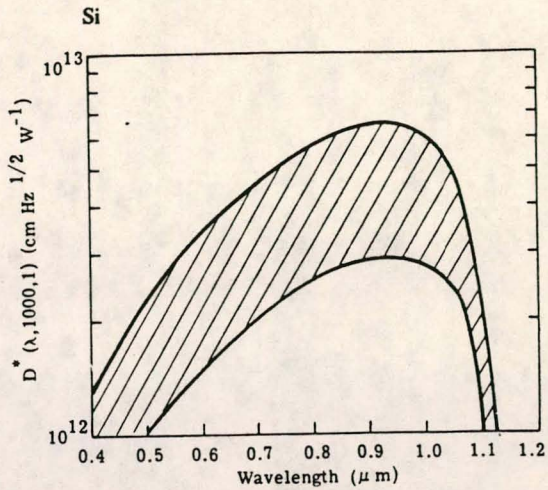
Sutton, G.P., Ross, D.M., Rocket Propulsion Elements, 4th. Ed., pp125-126, John Wiley & Sons Inc., 1976.

Wolfe, W.L., Zissis, G.J., The Infrared Handbook, pp70-89 of Section 11, Environmental Research Institute of Michigan, Revised Ed., 1985, 3rd. Printing 1989.

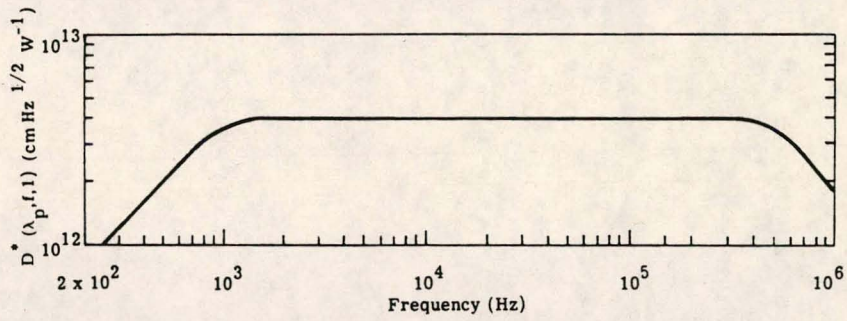
Zucrow, M.J., Hoffman, J.D., Gas Dynamics, Vol 1, pp328-329, John Wiley & Sons, 1976.

APPENDIX A
SPECTRAL RESPONSE OF DETECTORS
[Wolfe, 1985]

$T_d = 300 \text{ K}$
 $A_d = \text{wide range}$
 $R_d = 50 \text{ to } 5 \text{ kilohms}$
 $\tau = 2 \times 10^{-7} \text{ sec}$
 $\mathcal{R}_{\lambda_p} = 650 \text{ mA W}^{-1}$



(a) Spectral response of detector $D^*(\lambda, 1000, 1)$.



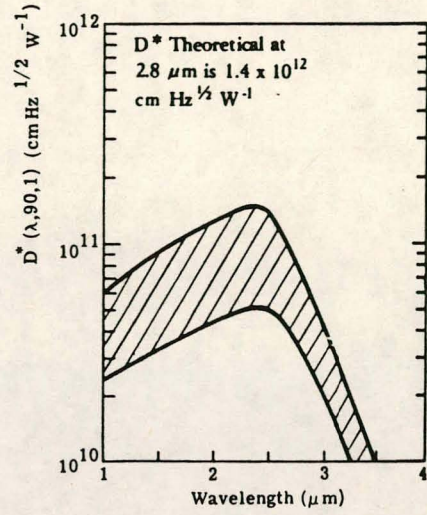
(b) Frequency response of detector $D^*(\lambda_p, f, 1)$.

Note

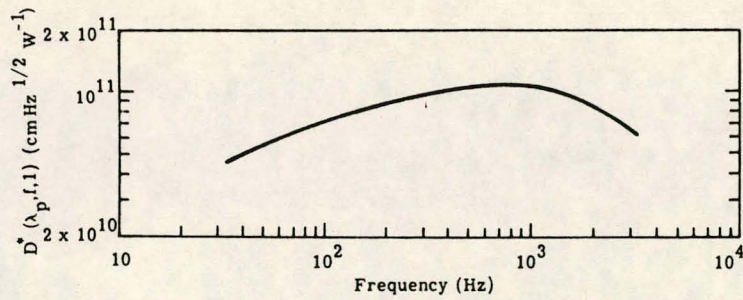
- (1) Small detectors have been made in arrays on 0.6 mm centers or less, and large detectors several centimeters in diameter or more have been made.
- (2) \mathcal{R} depends upon bias voltage.
- (3) Capacitance can vary from 2 to 800 pF, depending on bias.

PbS

$T_d = 300 \text{ K}$
 $A_d = 4 \times 10^{-6} \text{ to } 16 \text{ cm}^2$
 $R_d = 4 \text{ megohms}$
 $\tau = 100 \text{ to } 500 \mu \text{ sec}$
 $\text{FOV} = 180^\circ \text{ or } 2\pi \text{ sr}$
 $\mathcal{R}_{\lambda p} \approx 10^6 \text{ V W}^{-1}$
 $\mathcal{R}_{\lambda p} / \mathcal{R}_{bb} \approx 95$



(a) Spectral response of detector $D^*(\lambda, 90, 1)$.



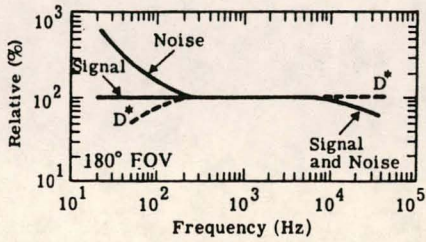
(b) Frequency response of detector $D^*(\lambda_p, f, 1)$.

Note

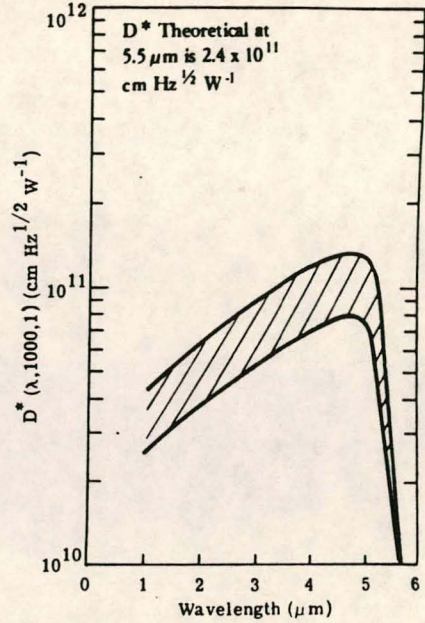
Resistance depends upon the l/w ratio of a responsive element. The values stated above are for a square detector.

InSb PV

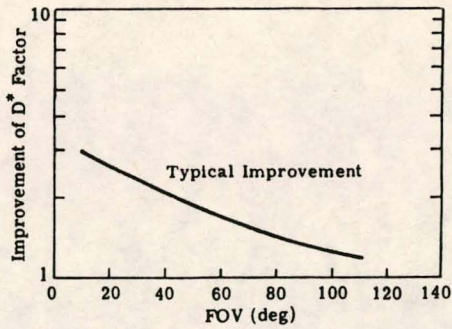
$T_d = 77 \text{ K}$
 $A_d = 10^{-4} \text{ to } 10^{-1} \text{ cm}^2$
 $R_d = 1 \text{ to } 100 \text{ megohms}$
 $\tau < 1 \mu\text{sec}$
 $\text{FOV} = 60^\circ$
 $\text{Background temperature} = 300 \text{ K}$
 $\mathcal{R}_\lambda \approx 10^5 \text{ V W}^{-1}$
 $\mathcal{R}_{\lambda_p} / \mathcal{R}_{bb} \approx 5.0$



(a) Frequency response of detector signal and noise.



(b) Spectral response of detector $D^*(\lambda, 1000, 1)$.



(c) Improvement in D^* versus FOV for typical detectors.

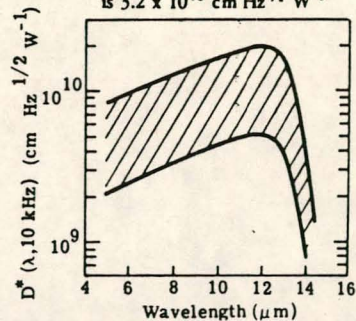
Note

- (1) Resistance is area and bias voltage dependent.
- (2) D^* will increase when the FOV is restricted with cold shields or when the spectral extent is restricted with cold spectral filters.

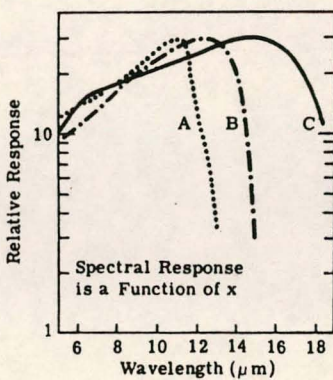
Hg_{1-x}Cd_xTe

$T_d = 77$ K
 $A_d = 4 \times 10^{-6}$ to 4×10^{-2} cm²
 $R_d = 20$ to 600 ohms
 $\tau = 100$ to 800 nsec
 $FOV = 10^\circ$ to 130°
 Background temperature = 300 K
 $\mathcal{R}_\lambda = 10^4$ V W⁻¹
 $\mathcal{R}_{\lambda_p} / \mathcal{R}_{bb} \approx 2$

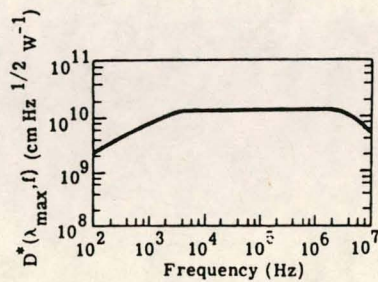
D^* Theoretical at $12.5 \mu\text{m}$
 is 3.2×10^{10} cm Hz^{1/2} W⁻¹



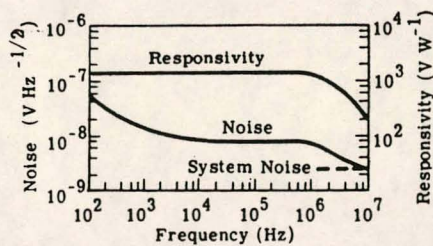
(a) Spectral response of detector $D^*(\lambda, 10 \text{ kHz})$.



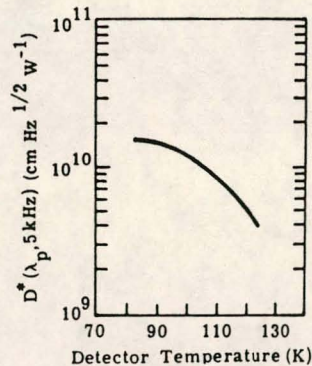
(b) Spectral response of detector responsivity. Curve A: $x = 0.21$; Curve B: $x = 0.20$; Curve C: $x = 0.17$.



(c) Frequency response of detector $D^*(\lambda_p, f)$.



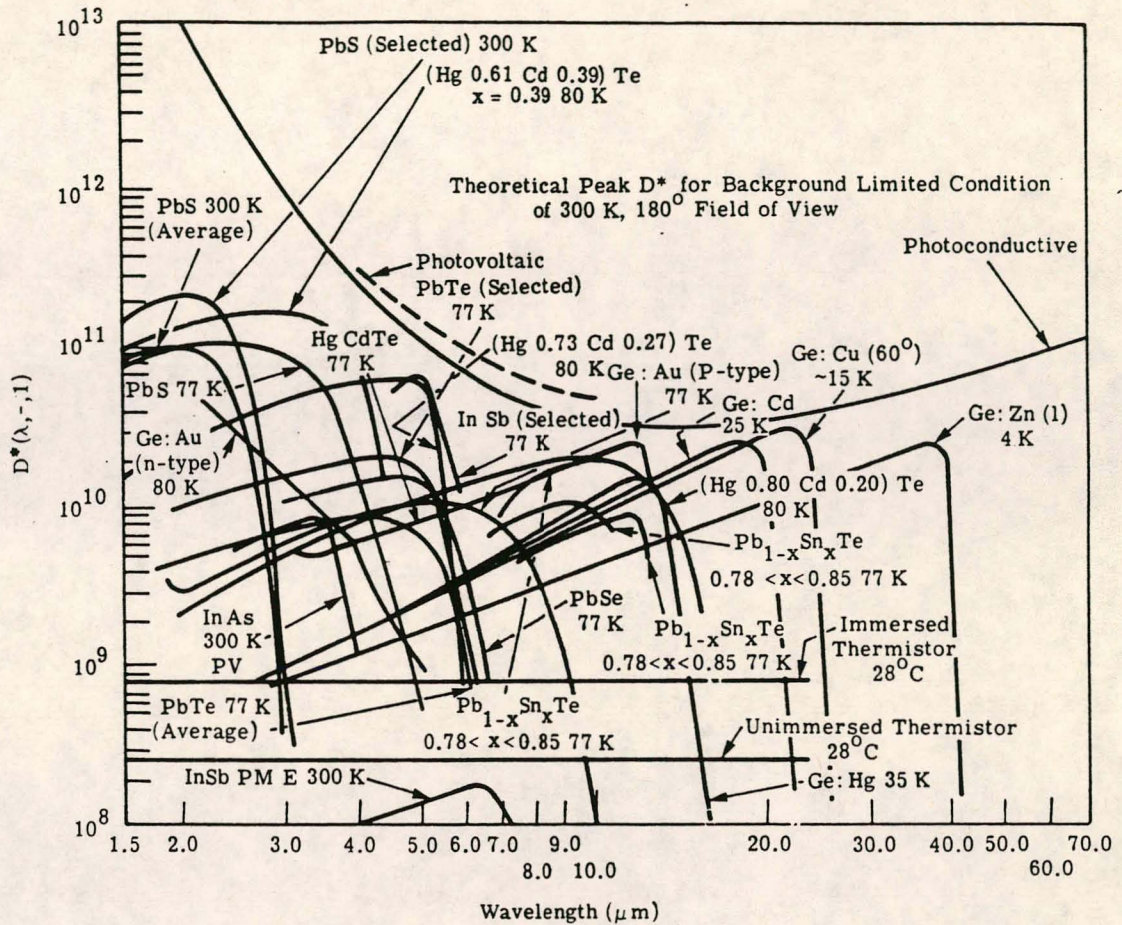
(d) Frequency response of detector noise.



(e) Temperature of detector $D^*(\lambda_p, 5 \text{ kHz})$.

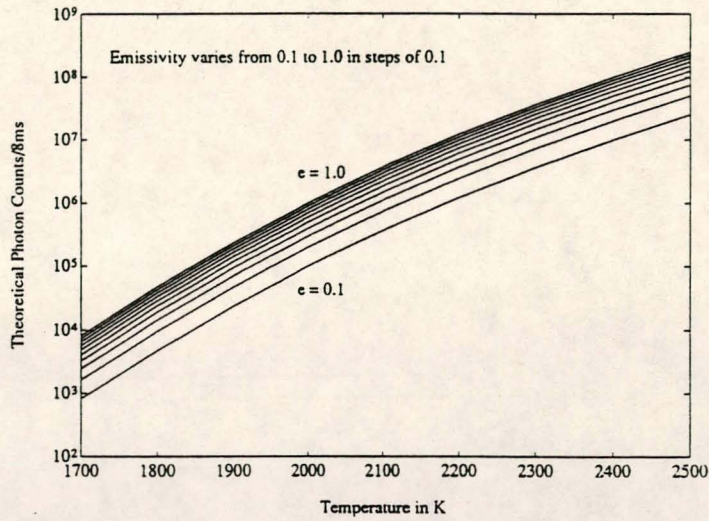
Note

Spectral response is determined by the alloy composition.

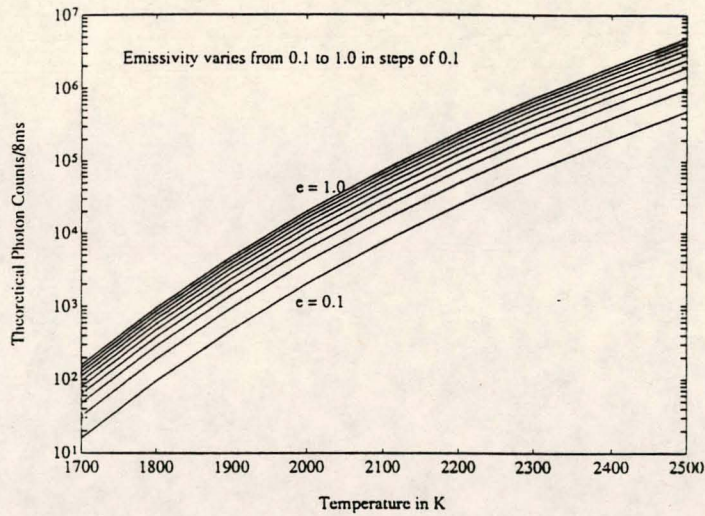


APPENDIX B
UV REFERENCE GRAPHS
[Roodt, 1993]

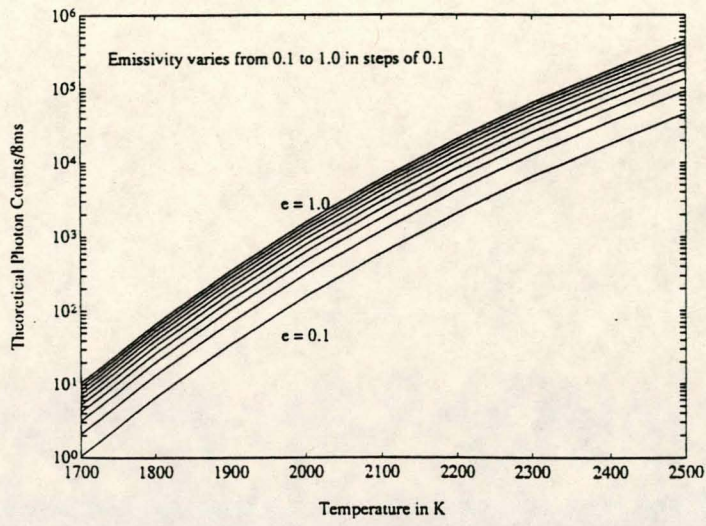
Graphs for effective temperature estimations



Channel 0 Reference Graph (Wide band: 230 - 280nm)



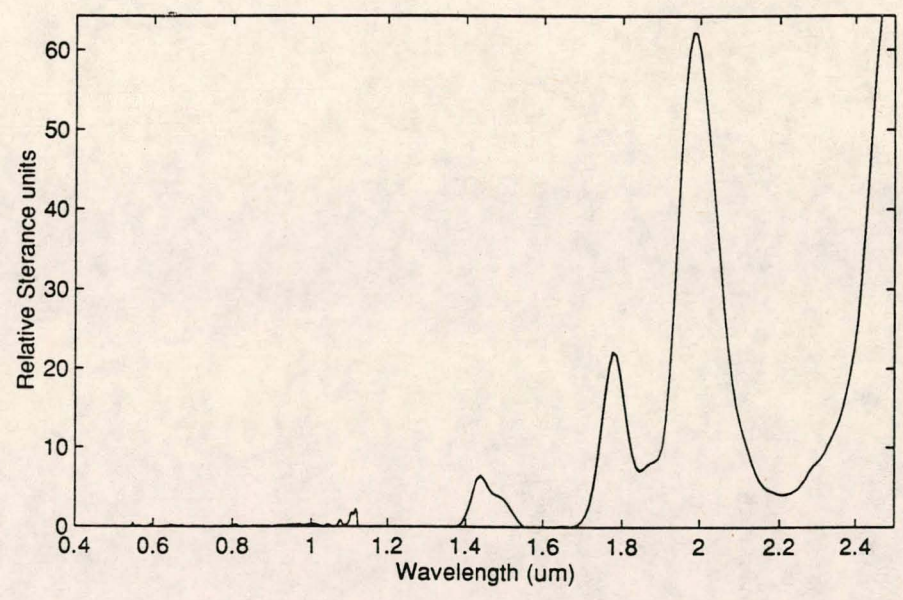
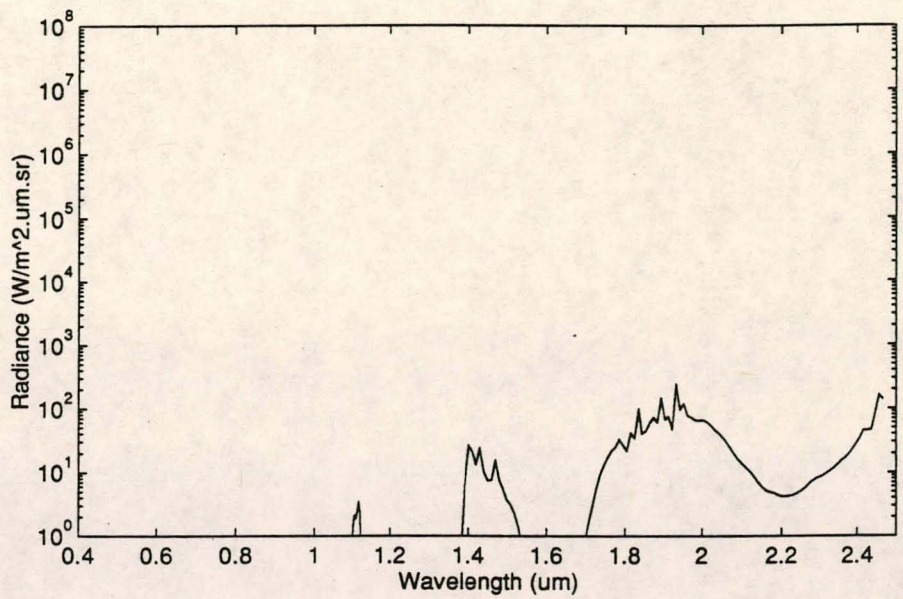
Channel 1 Reference Graph (Narrow band: 258 - 262nm)



Channel 2 Reference Graph (Narrow band: 251 - 256nm)

APPENDIX C

MIRAGE F1 PLUME SPECTRUM BETWEEN 0.4 AND 2.5 μ m



APPENDIX D
DETAIL SPECTRAL EMISSIONS OF SOME ELEMENTS

Elements	Wave Length	Emission	Characteristic
Al (Aluminium)	0.308	m	near UV
	0.309	m	near UV
	0.394	m	near UV
	0.396	m	near UV
B (Boron)	0.250	m	far UV
	0.250	m	far UV
	0.345	w	near UV
C (Carbon)	0.248	w	far UV
	0.427	s	violet
Cl (Chlorine)	0.479	vs	blue
	0.481	s	blue
Cs (Cesium)	0.454	m	blue
	0.455	m	blue
	0.459	w	blue

Elements	Wave Length	Emission	Characteristic
Cu (Copper)	0.214	w	far UV
	0.325	s	near UV
	0.327	s	near UV
	0.511	m	green
	0.515	m	green
	0.522	m	green
	0.578	m	yellow
F (Fluorine)	0.686	s	red
	0.690	vs	red
Fe (Iron)	0.276	w	far UV
	0.358	m	near UV
	0.372	m	near UV
	0.382	m	near UV
	0.388	w	near UV
	0.438	m	violet
	0.527	m	green
	0.533	w	green
H (Hydrogen)	0.122	w	far UV
	0.434	vw	violet
	0.486	vw	blue
	0.656	w	red

Elements	Wave Length	Emission	Characteristic
K (Potassium)	0.404	vw	violet
	0.405	vw	violet
	0.578	vw	yellow
	0.691	vw	red
	0.694	vw	red
	0.766	vw	near IR
	0.769	vw	near IR
N (Nitrogen)	0.120	w	far UV
	0.410	w	violet
	0.411	w	violet
	0.567	w	green
	0.568	vw	green
O (Oxygen)	0.777	w	near IR
Pb (Lead)	0.217	w	far UV
	0.220	vw	far UV
	0.283	s	far UV
	0.357	s	near UV
	0.364	vs	near UV
	0.368	vs	near UV
	0.406	vs	violet
	0.561	vw	green

Elements	Wave Length	Emission	Characteristic
S (Sulfur)	0.182	w	far UV
	0.183	w	far UV
	0.253	vw	far UV
Si (Silicon)	0.251	w	far UV
	0.252	w	far UV
	0.253	w	far UV
	0.288	m	far UV
	0.391	w	violet
Sr (Strontium)	0.346	w	near UV
	0.347	w	near UV
	0.408	vs	violet
	0.422	s	violet
	0.431	w	violet
	0.461	vs	blue
	0.496	m	green
	0.689	m	red

Elements	Wave Length	Emission	Characteristic
Ti (Titanium)	0.335	m	near UV
	0.336	w	near UV
	0.337	m	near UV
	0.364	m	near UV
	0.365	m	near UV
	0.376	m	near UV
	0.376	m	near UV
	0.498	m	green
	0.499	m	green
	0.500	vw	green
	0.501	m	green

With;

vw = very weak

w = weak

m = medium

s = strong

vs = very strong.

APPENDIX E
RESULTS OF FLARE MEASUREMENTS
[Roodt, 1994]

Results for the Mechem compounds.

Compound	Date	Filter	Temperature span [°C]	Transmission (Atmosphere) [%]	Combustion			Half			Notes
					Time	Area [m ²]	Temp [°C]	Time	Area [m ²]	Temp [°C]	
MF01	6/12/93	HT1	500-2000	98.4	21:33:36	0.128	486				
MF01_2	6/12/93	HT1	300-1000	98.4	21:37:57	0.03	485				Flare fell off
MF01_3	7/12/93	HT1	300-1000	98.4	20:52:58	0.078	514				
MF02_1	6/12/93	HT1	300-1000	98.4	21:47:00	0.114	446				
MF02_2	6/12/93	HT1	300-1000	98.4	21:51:51	0.042	542	21:51:52	0.161	391	
MF02_3	7/12/93	ATM	150-500	98.6	20:57:08	0.134	481				
MF03_1	6/12/93	HT1	300-1000	98.4	21:55:54	0.065	463				
MF03_2	7/12/93	ATM	150-500	98.6	21:00:24	0.135	483				
MF04_1	7/12/93	ATM	300-1000	98.6	21:03:57	0.084	701				
MF04_2	6/12/93	FLM	250-1200	98.4	22:14:40	0.045	453	22:14:42	0.127	465	
MF05_1	7/12/93	ATM	300-1000	98.6	21:06:34	0.097	537				Half of flare fell off
MF05_2	6/12/93	FLM	250-1200	98.4	22:32:21	0.069	462				
MF06_1	7/12/93	ATM	300-1000	98.6	21:09:09	0.099	658	22:09:14	0.082	717	
MF06_2	7/12/93	ATM	300-1000	98.6	21:25:42	0.094	435	21:25:48	0.076	618	
MF07_1	7/12/93	ATM	300-1000	98.6	21:12:23	0.143	562				Half of flare fell off
MF07_2	7/12/93	ATM	300-1000	98.6	21:30:15	0.066	505				

Results for the Somchem compounds.

Compound	Date	Filter	Temperature span [°C]	Transmission (Atmosphere) [%]	Combustion			Half			Notes
					Time	Area [m ²]	Temp [°C]	Time	Area [m ²]	Temp [°C]	
SF2515_1	7/12/93	ATM	300-1000	98.6	21:38:02	0.134	690	21:38:04	0.214	789	Half of flare fell off
SF2515_2	7/12/93	ATM	300-1000	98.6	21:44:05	0.058	649	21:44:07	0.117	648	Half of flare fell off
SF2524_1	7/12/93	ATM	300-1000	98.6	21:50:02	0.176	594	21:50:04	0.14	502	Half of flare fell off
SF913_1	7/12/93	HT1	300-1000	98.4	22:05:04	0.079	358				
SF913_2	7/12/93	FLM	150-600	98.4	22:11:29	0.068	438	22:11:34	0.069	557	
SF914_1	7/12/93	FLM	150-600	98.4	22:18:17	0.195	588				
SF914_2	7/12/93	ATM	300-1000	98.6	22:22:50	0.053	415	22:22:58	0.064	689	
SF917_1	7/12/93	ATM	300-1000	98.6	22:28:10	0.167	600	22:28:13	0.185	543	
SF917_2	7/12/93	ATM	300-1000	98.6	22:34:15	0.152	552				
SF916_1	7/12/93	ATM	300-1000	98.6	22:46:59	0.199	461				Flare fell off
SF916_2	7/12/93	ATM	300-1000	98.6	22:51:13	0.155	576				
SF2524_2	7/12/93	ATM	300-1000	98.6	22:55:55	0.157	632				Half of flare fell off
SFDB1	7/12/93	ATM	300-1000	98.6	23:10:03	0.305	851	23:10:06	0.251	835	

Results for the Somchem compounds (continued).

Compound	Date	Filter	Temperature span [°C]	Transmission (Atmosphere) [%]	Combustion			Half			Notes
					Time	Area [m ²]	Temp [°C]	Time	Area [m ²]	Temp [°C]	
GAB_1	8/12/93	HT1	300-1000	98.4	00:19:40	0.033	405				
GAB_2	8/12/93	FLM	150-600	98.4	00:31:38	0.038	440				
SFDBRAL1	7/12/93	ATM	300-1000	98.6	23:36:06	0.115	688				(SFDBRAL1_X.1 MG)
SFDBRAL2	8/12/93	ATM	300-1000	98.5	20:47:20	0.184	812				
SFDBR1	8/12/93	ATM	300-1000	98.5	20:35:20	0.175	803				
SFDBR2	8/12/93	ATM	300-1000	98.5	20:41:20	0.214	768				
SFDB2	8/12/93	ATM	300-1000	98.6	20:24:55	0.16	637				
SFDB3	8/12/93	ATM	300-1000	98.5	20:30:17	0.377	734				
SF913_3	8/12/93	FLM	150-600	98.2	21:00:28	0.093	529				
SF914_3	8/12/93	FLM	150-600	98.2	21:04:56	0.211	588				
SF915_1	7/12/93	ATM	300-1000	98.6	23:41:54	1.23	985				
SF917_3	8/12/93	FLM	150-600	98.2	21:08:24	0.231	524				
SF280_1	7/12/93	ATM	300-1000	98.6	23:50:47	0.315	648				Half of flare fell off, broke up
SF289_1	7/12/93	ATM	300-1000	98.6	23:56:08	0.343	970				
SF289_2	8/12/93	ATM	300-1000	98.6	00:00:23	0.216	970				
SF298_1	8/12/93	HT1	500-2000	98.4	00:06:36	0.308	755				
SF2524_3	8/12/93	ATM	300-1000	98.5	20:53:14	0.244	627				
SF2524_4	8/12/93	ATM	300-1000	98.5	20:56:43	0.205	579				
SF2515_3	9/12/93	ATM	300-1000	98.5	00:10:46	0.184	652				
SF2515_4	9/12/93	ATM	300-1000	98.5	00:16:10	0.232	683				

Results for the Swartklip Products Standard Flares.

Compound	Date	Filter	Temperature span [°C]	Transmission (Atmosphere) [%]	Combustion			Half			Notes
					Time	Area [m ²]	Temp [°C]	Time	Area [m ²]	Temp [°C]	
SPREF1	6/12/93	HT1	500-2000	98.4	21:02:15	0.326	1603				Flare fell off
SPF2	6/12/93	HT1	500-2000	98.4	21:17:29	0.386	1552				
SPF3	6/12/93	HT1	500-2000	98.4	21:22:31	0.252	1651				Flare fell off
SPF4	6/12/93	HT1	500-2000	98.4	21:26:48	0.559	1568				Flare fell off, broke up
SPF5	6/12/93	HT1	500-2000	98.4	22:53:07	0.441	1551				
SPF6	6/12/93	HT1	500-2000	98.4	22:59:01	0.388	1554				Flare fell off, broke up
SPF7	7/12/93	HT1	500-2000	98.4	20:36:22	0.293	1555				
SPF8	7/12/93	HT1	500-2000	98.4	20:45:31	0.397	1546				
SPF9	7/12/93	HT1	500-2000	98.4	20:49:12	0.437	1549				Flare fell off
SPF9	8/12/93	HT1	500-2000	98.4	20:10:17	0.524	1528				Flare fell off, broke up

Calculated radiance values for flare compounds from selected scans.

Composition name	Radiance Integrated from 3-5 μ m	Radiance Integrated from 3.5-4 μ m	Radiance value at 2.7 μ m	Radiance value at 2.9 μ m	Radiance value at 4.2 μ m	Radiance value at 4.3 μ m	Radiance value at 4.4 μ m
gab1.20	1.16E+04	6.09E+02	1.23E+03	4.81E+03	2.56E+04	6.05E+04	1.73E+04
gab2.3	1.02E+04	5.51E+02	5.48E+02	5.18E+03	2.32E+04	4.13E+04	1.96E+04
mf011.16	1.06E+04	3.83E+02	2.06E+03	7.37E+03	3.36E+04	4.33E+04	1.48E+04
mf012.14	2.25E+04	7.19E+02	3.07E+03	1.75E+04	7.45E+04	8.50E+04	2.98E+04
mf013.19	1.36E+04	5.08E+02	2.35E+03	9.48E+03	6.49E+04	5.30E+04	1.83E+04
mf021.13	7.98E+03	1.78E+02	1.40E+03	2.97E+03	3.27E+04	3.34E+04	1.24E+04
mf022.14	1.20E+04	2.69E+02	4.38E+02	5.04E+03	4.49E+04	5.04E+04	2.03E+04
mf023.10	2.84E+04	7.21E+02	3.64E+03	1.87E+04	6.01E+04	1.60E+05	4.22E+04
mf031.18	5.87E+04	1.92E+03	5.09E+03	3.33E+04	2.34E+05	2.31E+05	8.47E+04
mf032.6	3.52E+04	1.42E+03	5.03E+03	2.51E+04	9.12E+04	1.78E+05	4.83E+04
mf041.9	6.85E+04	2.98E+03	9.34E+03	6.24E+04	2.82E+05	2.57E+05	9.05E+04
mf042.9	2.74E+04	8.26E+02	3.02E+03	1.81E+04	1.16E+05	1.01E+05	3.74E+04
mf051.10	3.32E+04	1.22E+03	4.40E+03	2.61E+04	1.32E+05	1.30E+05	4.60E+04
mf052.14	1.77E+04	5.42E+02	1.96E+03	8.74E+03	5.14E+04	8.44E+04	2.87E+04

Calculated radiance values for flare compounds from selected scans (continued).

Composition name	Radiance Integrated from 3-5um	Radiance Integrated from 3.5-4um	Radiance value at 2.7um	Radiance value at 2.9um	Radiance value at 4.2um	Radiance value at 4.3um	Radiance value at 4.4um
mf061.13	5.76E+04	3.44E+03	8.43E+03	4.73E+04	2.10E+05	2.35E+05	7.33E+04
mf062.19	3.11E+04	1.31E+03	4.67E+03	2.09E+04	9.05E+04	1.52E+05	4.48E+04
mf071.8	3.02E+04	1.10E+03	3.38E+03	2.05E+04	9.71E+04	1.34E+05	4.34E+04
mf072.15	2.12E+04	8.88E+02	3.65E+03	1.34E+04	6.59E+04	9.23E+04	3.23E+04
sf25151.15	5.13E+04	2.56E+03	9.52E+03	5.07E+04	1.83E+05	2.20E+05	6.51E+04
sf25152.18	3.01E+04	1.32E+03	2.77E+03	1.86E+04	9.50E+04	1.05E+05	4.22E+04
sf25241.8	3.10E+04	1.34E+03	2.59E+03	1.77E+04	1.40E+05	9.62E+04	3.99E+04
sf25242.13	3.50E+04	1.55E+03	4.97E+03	2.58E+04	1.64E+05	1.09E+05	4.39E+04
sfdbral1.3	2.38E+04	3.74E+03	4.62E+03	2.22E+04	9.14E+04	5.28E+04	1.95E+04
sf280.8	4.81E+03	2.84E+02	1.12E+03	5.87E+03	1.73E+04	1.42E+04	5.20E+03
sf2891.9	2.18E+04	3.79E+03	6.39E+03	2.40E+04	8.34E+04	4.45E+04	1.48E+04
sf2892.11	4.15E+04	6.01E+03	9.22E+03	3.73E+04	2.03E+05	9.31E+04	3.09E+04
sf2981.5	9.64E+03	8.54E+02	2.45E+03	1.27E+04	4.10E+04	1.53E+04	7.12E+03
sf9131.20	4.64E+03	1.09E+02	7.23E+02	1.57E+03	1.53E+04	2.50E+04	8.29E+03
sf9132.15	3.87E+04	1.34E+03	4.67E+03	2.50E+04	9.63E+04	2.08E+05	5.68E+04
sf9141.11	2.38E+04	1.43E+03	2.87E+03	1.92E+04	7.76E+04	1.00E+05	3.14E+04
sf9142.13	5.62E+04	2.93E+03	5.53E+03	3.96E+04	2.10E+05	2.31E+05	7.80E+04
sf9161.19	2.19E+04	5.40E+02	1.88E+03	1.07E+04	4.32E+04	1.20E+05	3.37E+04
sf9162.11	3.75E+04	1.52E+03	4.87E+03	2.58E+04	1.74E+05	1.19E+05	5.02E+04
sf9171.12	2.85E+04	1.30E+03	3.95E+03	2.53E+04	9.85E+04	1.10E+05	3.68E+04
sf9172.10	6.89E+03	2.36E+02	1.26E+03	4.29E+03	1.19E+04	3.96E+04	1.02E+04
sfdb1.7	1.30E+04	2.13E+03	2.05E+03	1.19E+04	4.91E+04	3.05E+04	9.63E+03
spf4.10	1.39E+04	3.13E+03	1.97E+03	1.35E+04	5.86E+04	2.05E+04	5.43E+03
spf5.2	5.23E+04	1.09E+04	8.40E+03	4.27E+04	3.51E+05	5.37E+04	1.57E+04
spf6.3	3.77E+04	7.86E+03	4.52E+03	2.48E+04	2.12E+05	5.13E+04	1.51E+04
spf7.4	4.35E+04	9.61E+03	7.87E+03	3.77E+04	2.64E+05	4.53E+04	1.37E+04
spf8.7	1.44E+04	2.98E+03	2.78E+03	1.28E+04	7.47E+04	2.10E+04	5.89E+03
spf9.2	4.00E+04	9.10E+03	9.00E+03	3.83E+04	2.62E+05	3.64E+04	1.10E+04
F1AZ MG	1.10E+03	5.40E+00	1.90E+01	5.97E+02	1.00E+04	1.76E+03	1.94E+03
F1AZ Dry	1.41E+02	8.06E-01	1.33E+01	1.57E+01	1.42E+03	2.22E+02	2.68E+02

UV results for Swartklip Products standard flares.

Event	Date	Flame Area (m ²)	Temperature (K)	Emissivity Channel 0	Emissivity Channel 1	Emissivity Channel 2	Integrated BB-Radiance (W.m ⁻² .sr ⁻¹) (250-400nm)
spf1	6/12/93	0.08	2270	0.2	0.11	-	46.57
spf2	6/12/93	0.08	2270	0.4	0.12	-	46.57
spf3	6/12/93	0.05	2240	0.2	0.11	0.12	37.07
spf4	6/12/93	0.09	2275	0.3	0.14	0.17	48.35
spf5	6/12/93	0.09	2275	0.45	0.15	0.18	48.35
spf6	6/12/93	0.08	2270	0.25	0.13	0.13	46.57
spf7	7/12/93	0.06	2160	0.45	0.11	0.16	19.58
spf8	7/12/93	0.08	2170	0.24	0.12	0.13	21.26
spf9	7/12/93	0.09	2170	0.15	0.13	0.17	21.26
spf9a	8/12/93	0.1	2115	0.11	0.22	0.13	13.4
spf10	8/12/93	0.08	2140	0.1	0.13	0.14	16.58
spf11	8/12/93	0.08	2165	0.22	0.12	0.11	20.41

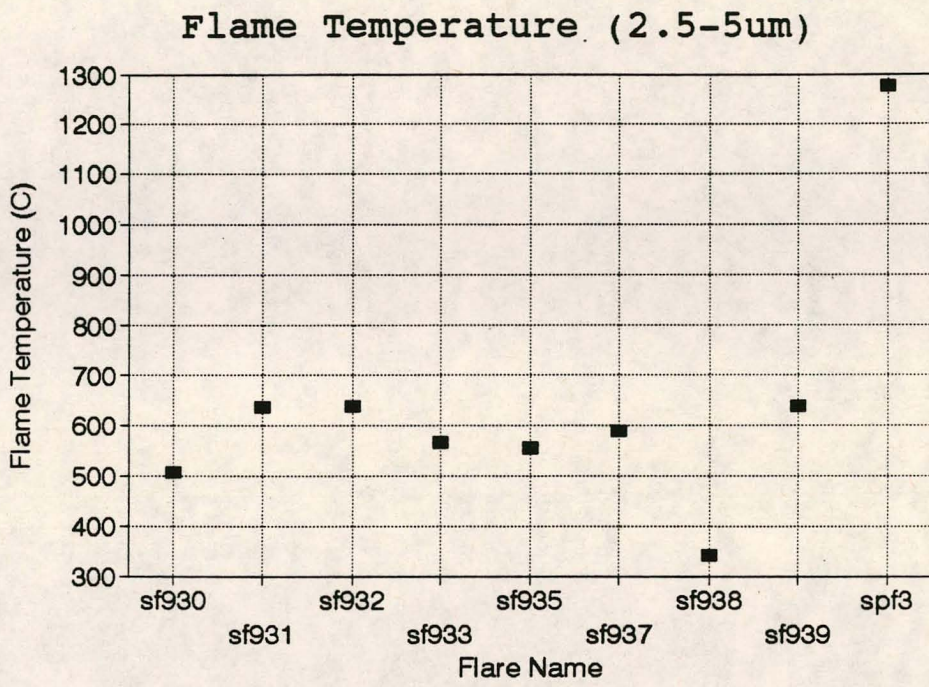
UV results for Mechem flares.

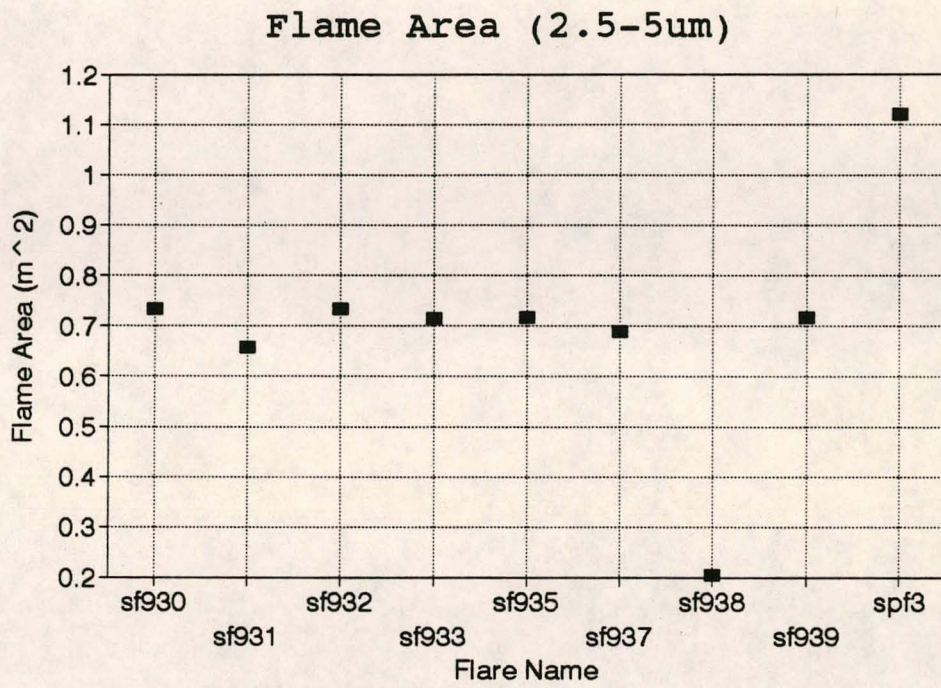
Event Half flare marked with *	Date	Flame Area (m ²)	Temperature (K)	Emissivity Channel 0	Emissivity Channel 1	Emissivity Channel 2	Integrated BB-Radiance (W.m ⁻² .sr ⁻¹) (250-400nm)
*mf01-1	6/12/93	0.03	1985	0.25	0.33	0.12	4.08
*mf01-2	6/12/93	0.03	2020	0.2	0.28	0.10	5.7
*mf01-3	7/12/93	0.03	1925	0.15	0.27	0.1	2.24
*mf02-1	6/12/93	0.02	2065	0.15	0.22	0.1	8.63
*mf02-2	6/12/93	0.03	2075	0.18	0.2	0.11	9.44
*mf02-3	7/12/93	0.03	1950	0.15	0.28	0.16	2.89
*mf03-1	6/12/93	0.02	2010	0.2	0.31	0.1	5.19
mf03-2	7/12/93	0.02	1940	0.15	0.27	0.12	2.61
mf04-1	7/12/93	0.02	1980	0.13	0.19	0.12	3.89
*mf04-2	6/12/93	0.02	2035	0.18	0.2	0.11	6.56
mf05-1	7/12/93	0.02	1935	0.15	0.28	0.10	2.48
*mf05-2	6/12/93	0.02	1965	0.22	0.26	0.10	3.35
mf06-1	7/12/93	0.02	1775	0.1	0.3	0.1	0.42
*mf06-2	7/12/93	0.02	1760	0.10	0.28	0.12	0.35
mf07-1	7/12/93	0.03	1925	0.12	0.3	0.1	2.24
*mf07-2	7/12/93	0.02	1830	0.18	0.37	0.12	0.8

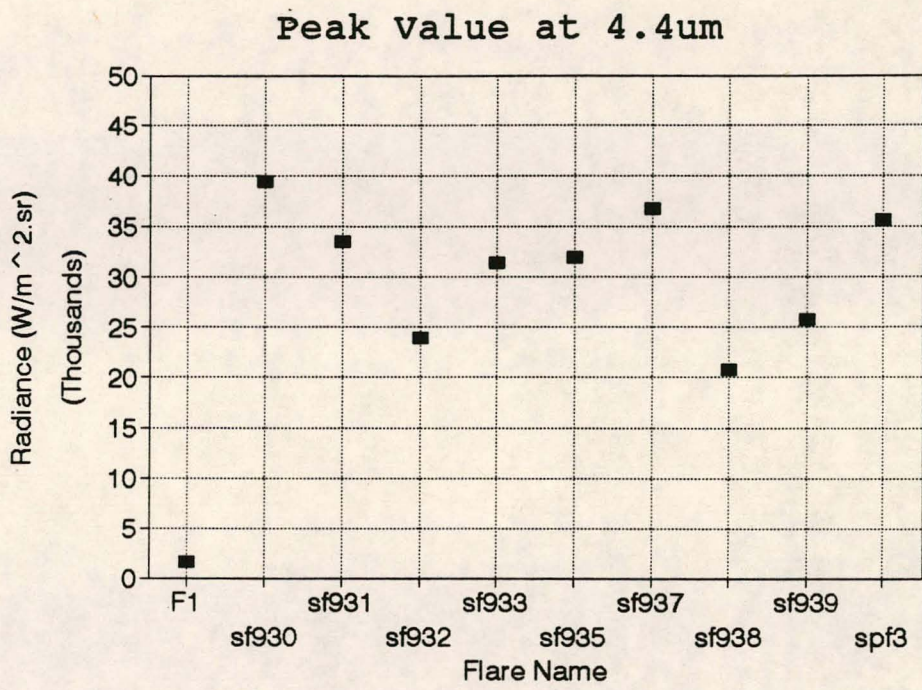
UV results for Somchem flares.

Event	Date	Flame Area (m ²)	Temperature (K)	Emissivity Channel 0	Emissivity Channel 1	Emissivity Channel 2	Integrated BB-Radiance (W.m ² .sr ⁻¹) (250-400nm)
sf2515-1	7/12/93	0.03	2120	0.43	0.10	0.2	13.99
sf2515-2	7/12/93	0.02	2090	0.4	0.10	0.14	10.78
sf2515-3	8/12/93	0.04	2110	0.3	0.1	0.17	12.84
sf2515-4	8/12/93	0.04	2110	0.3	0.11	0.13	12.84
sf2524-1	7/12/93	0.03	2093	0.1	0.1	0.1	11.07
sf2524-2	7/12/93	0.03	2090	0.13	0.1	0.10	10.78
sf2524-3	8/12/93	0.04	2110	0.14	0.1	0.1	12.84
sf2524-4	8/12/93	0.04	2110	0.1	0.10	0.10	12.84
sf280-1	7/12/93	0.06	2100	0.2	0.2	0.1	11.77
sf286-1	8/12/93	0.03	2110	0.12	0.1	0.1	12.84
sf288-1	8/12/93	0.06	2150	0.17	0.1	0.12	18.02
sf289-1	7/12/93	0.06	1825	0.12	0.36	0.13	0.76
sf289-2	7/12/93	0.05	1850	0.10	0.38	0.1	1
sf289-3	8/12/93	0.04	1820	-	0.45	0.10	0.16
sf298-1	7/12/93	0.06	2070	0.3	0.26	0.1	9.03
sf301-1	8/12/93	0.06	2150	0.3	0.12	0.13	18.02
sf302-1	8/12/93	0.03	2100	0.15	0.1	0.12	11.77
sf913-1	7/12/93	0.02	1710	0.1	0.24	0.2	0.19
sf913-2	7/12/93	0.01	1820	0.12	0.22	0.1	0.71
sf913-3	8/12/93	0.02	1850	0.1	0.27	0.13	1
sf914-1	7/12/93	0.03	1900	0.1	0.24	0.11	1.72
sf914-2	7/12/93	0.02	1860	0.1	0.24	0.12	1.12
sf914-3	8/12/93	0.04	1935	0.10	0.22	0.10	2.48
sf915-1	7/12/93	0.25	2275	0.3	0.1	0.1	48.35
sf916-1	7/12/93	0.04	2060	0.35	0.21	0.10	8.25
sf916-2	7/12/93	0.03	2070	0.42	0.15	0.1	9.03
sf916-3	8/12/93	0.03	1960	0.12	0.4	0.15	3.19
sf916-4	8/12/93	0.03	1960	0.1	0.35	0.13	3.19
sf917-1	7/12/93	0.04	2100	0.17	0.1	0.1	11.77
sf917-2	7/12/93	0.03	2090	0.12	0.1	0.1	10.78
sf917-3	8/12/93	0.04	2110	0.13	0.11	0.12	12.84
sf919-1	8/12/93	0.03	2110	0.11	0.10	0.10	12.84
sfdb-2	8/12/93	0.04	1810	0.21	0.52	0.1	0.64
sfdb-3	8/12/93	0.07	1820	0.27	0.6	0.1	0.71
sfdb-1	8/12/93	0.04	1810	0.2	0.55	0.1	0.64
sfdb-2	8/12/93	0.04	1800	0.12	0.35	0.13	0.56
sfdb-1-1	7/12/93	0.03	1660	0.11	0.4	0.4	0.1
sfdb-1-2	8/12/93	0.03	1820	0.12	0.32	0.1	0.71

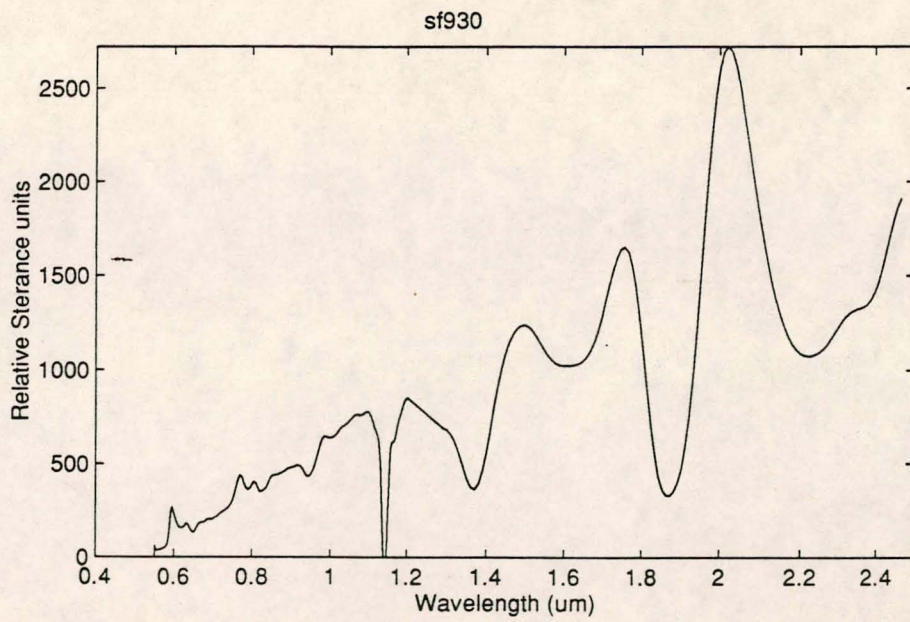
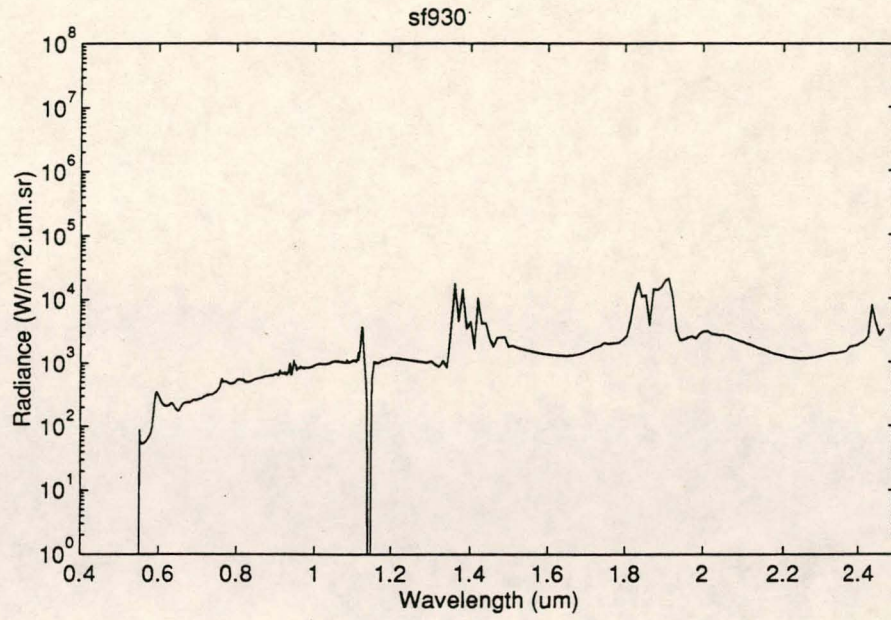
APPENDIX F
ADDITIONAL FLARE DATA

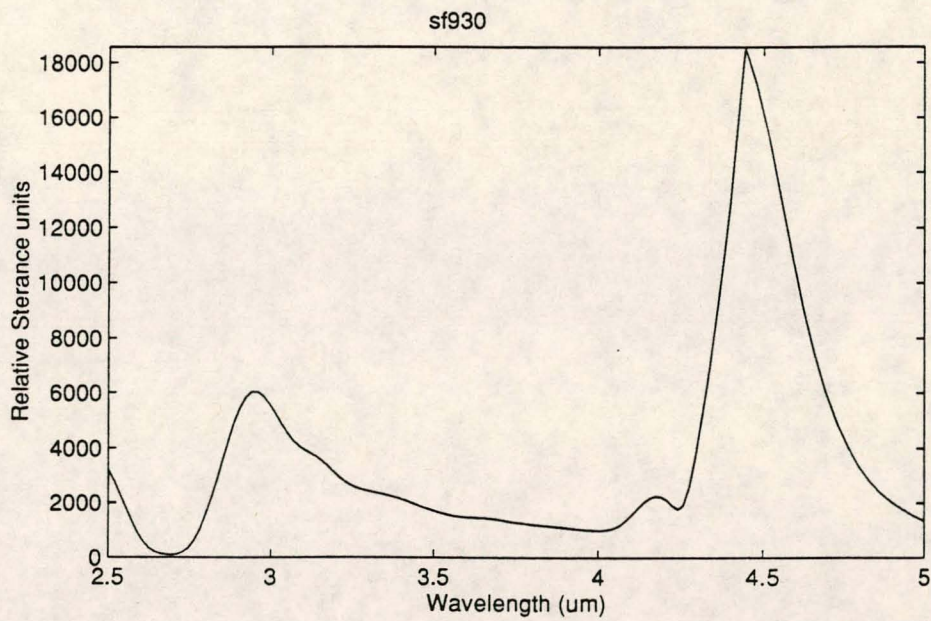
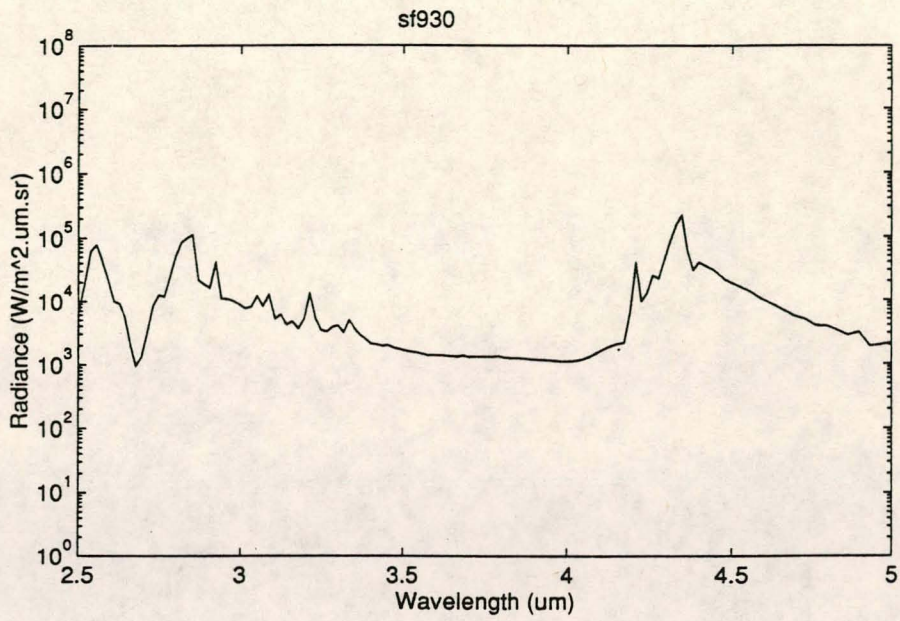


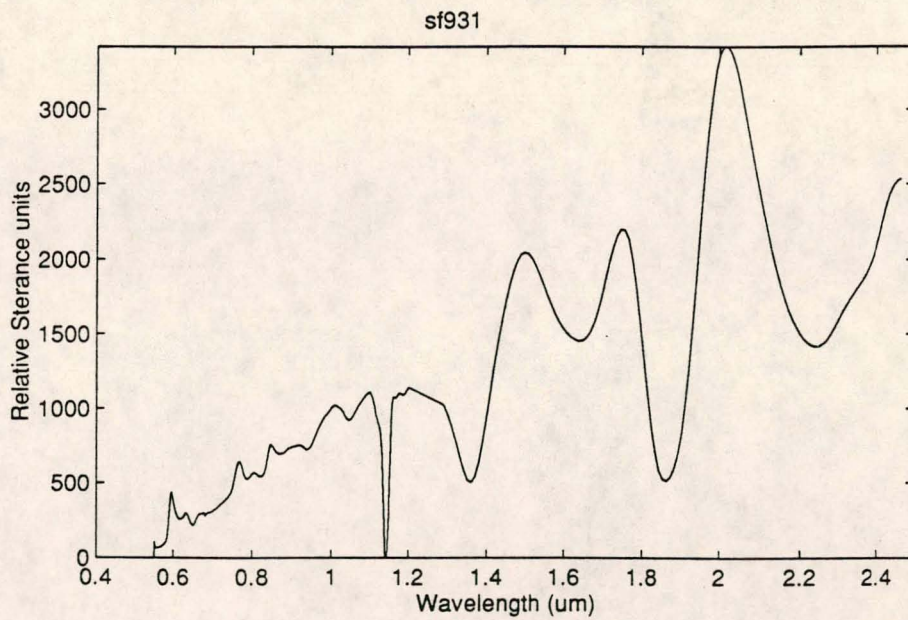
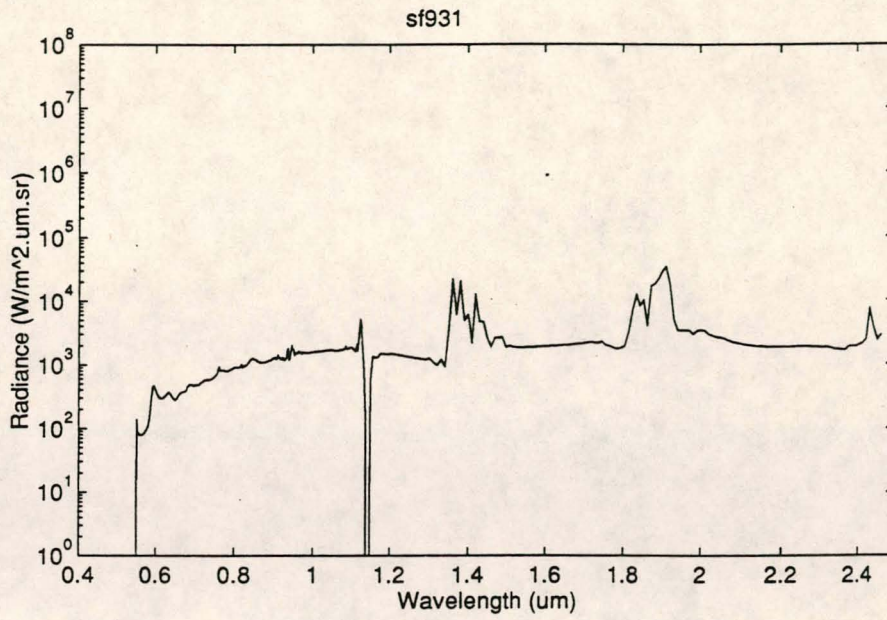


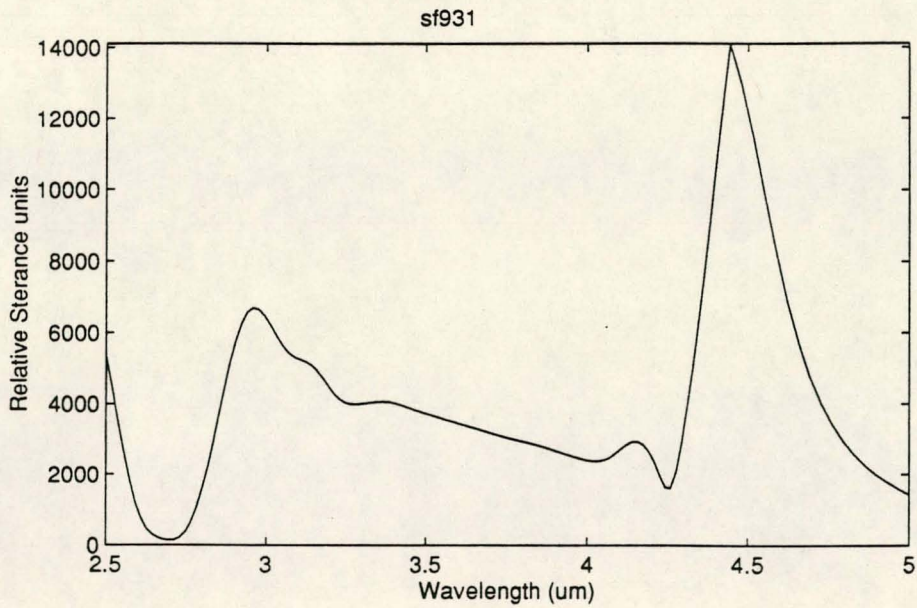
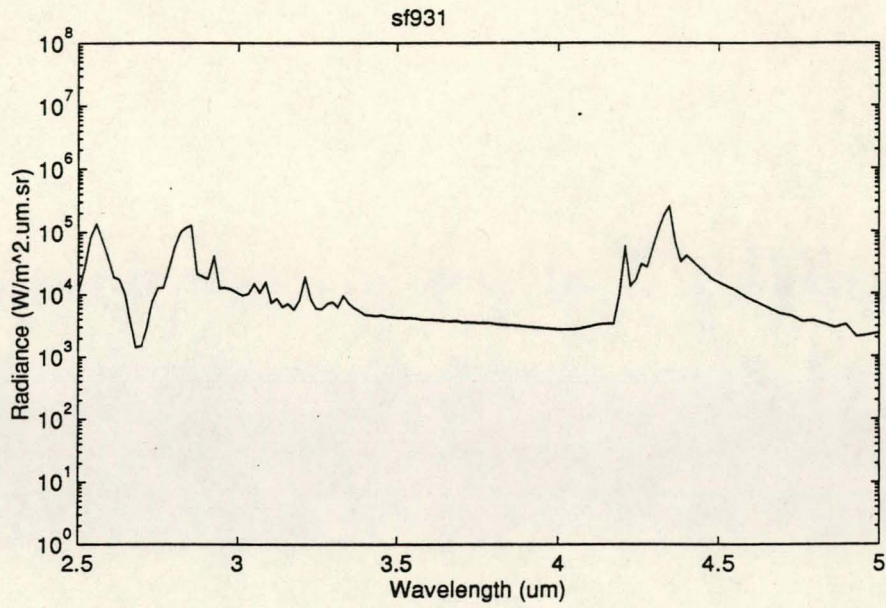


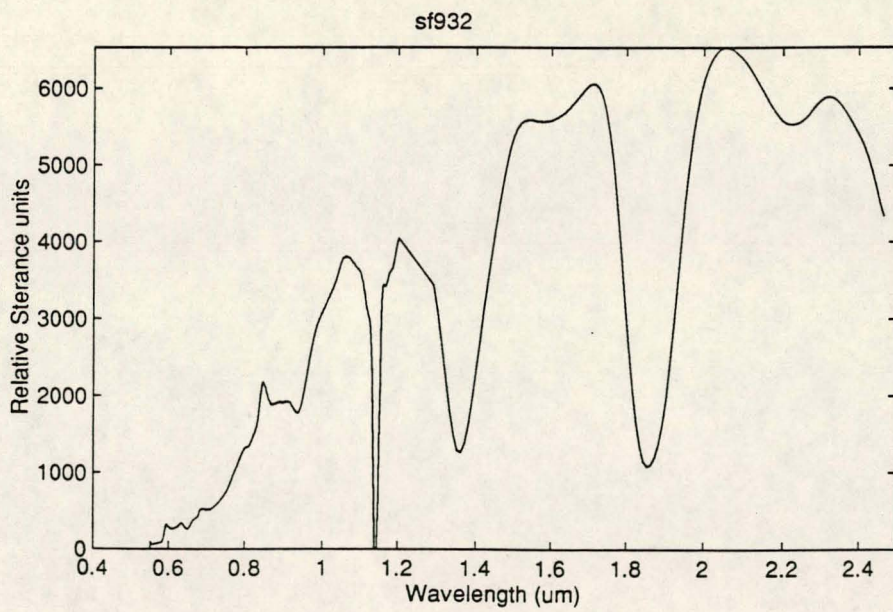
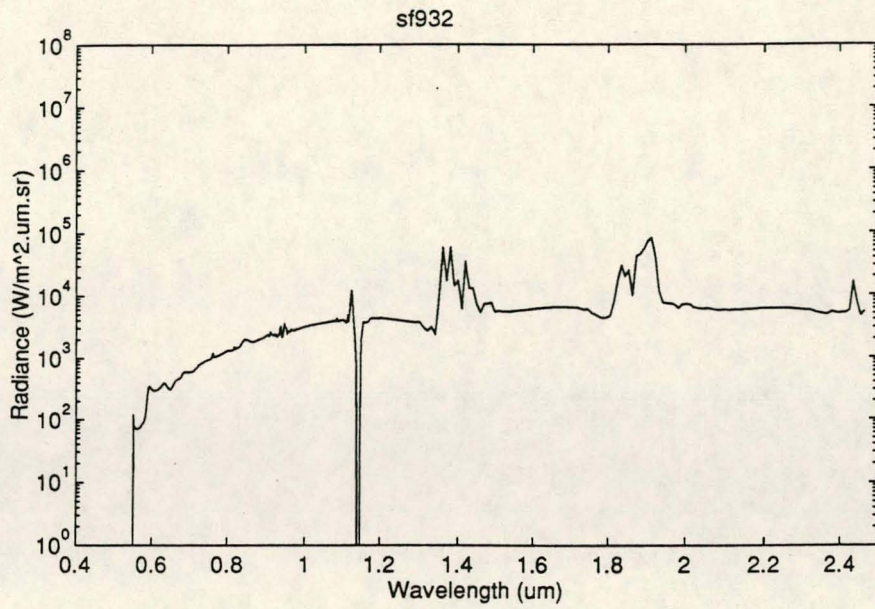
APPENDIX G
SPECTRAL OUTPUTS OF FLARE COMPOSITIONS

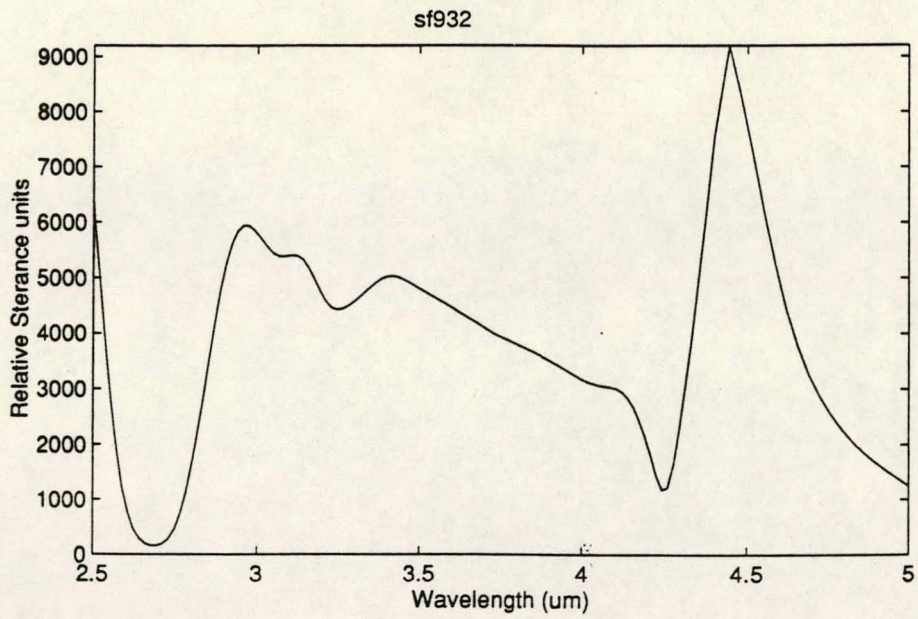
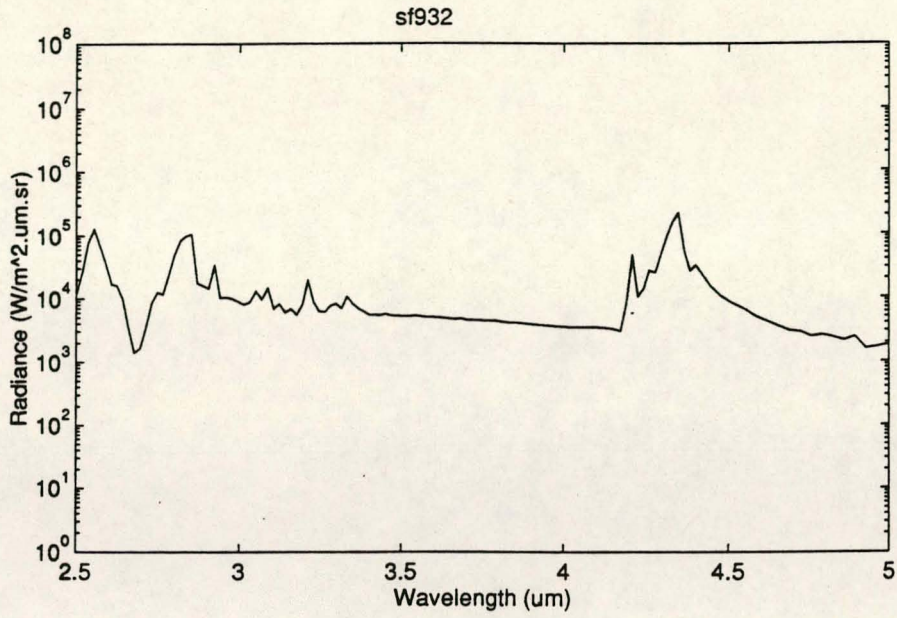


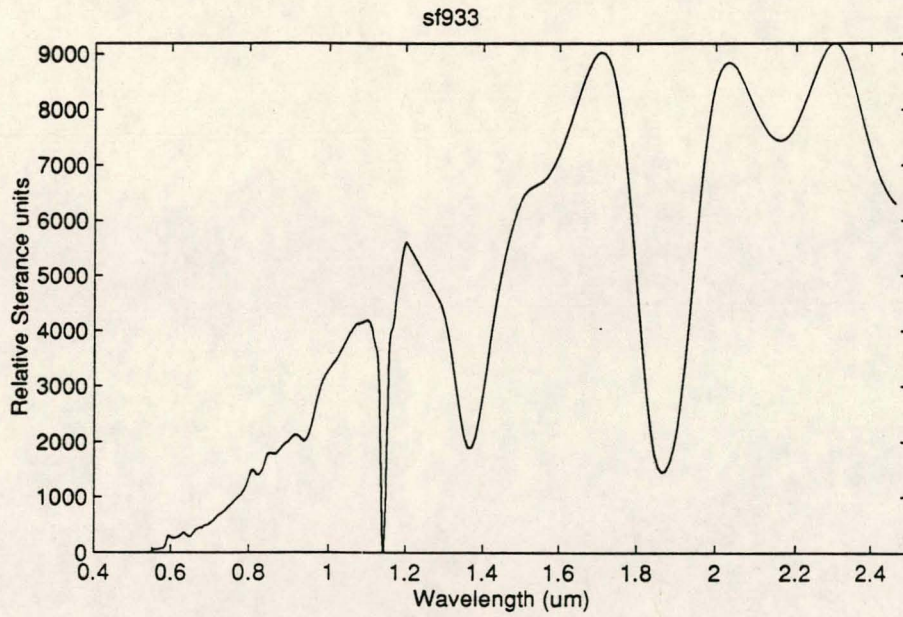
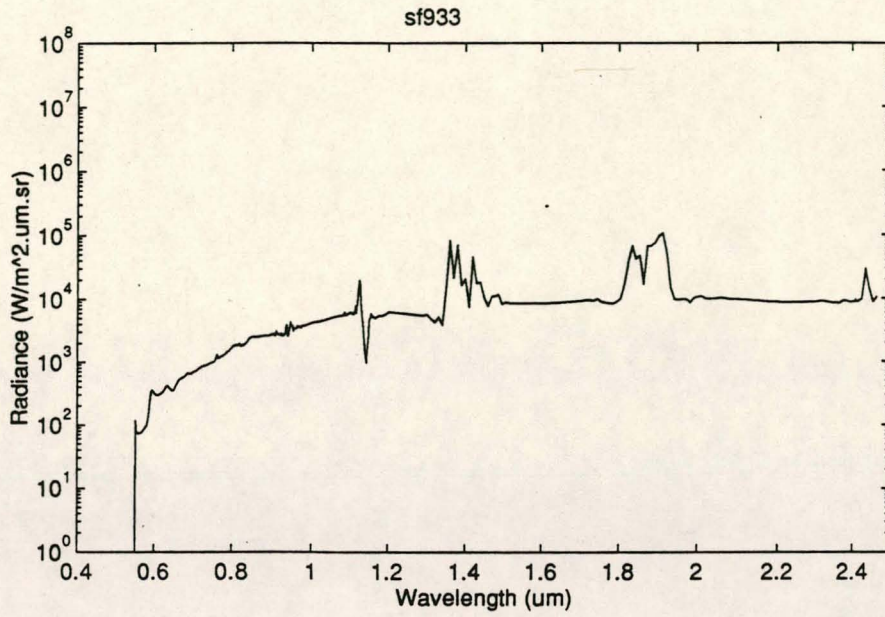


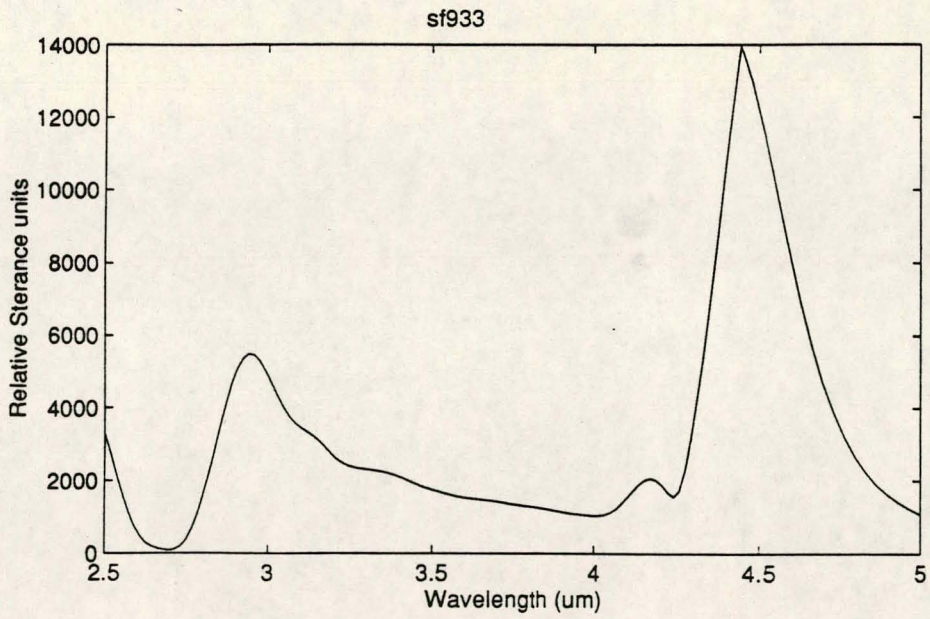
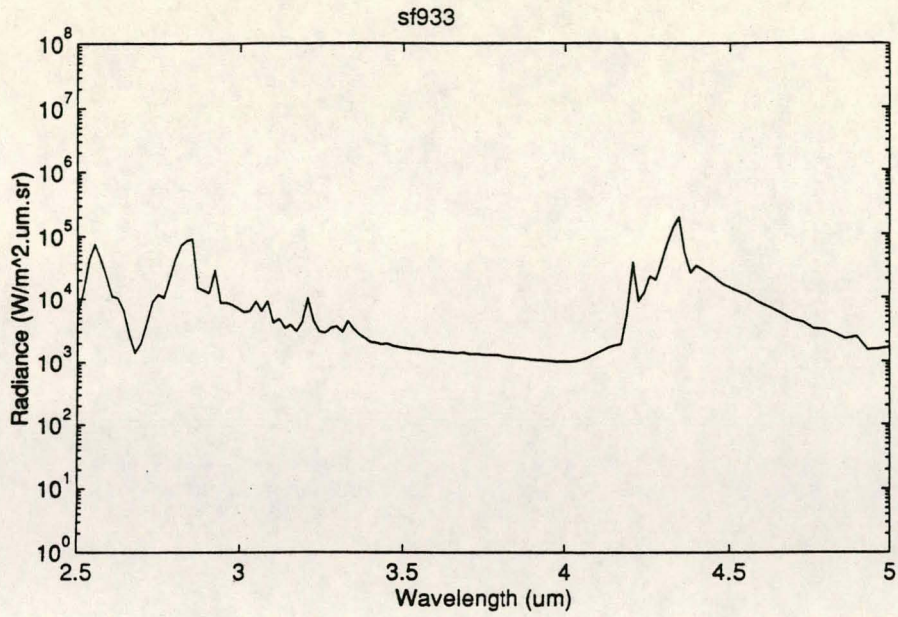


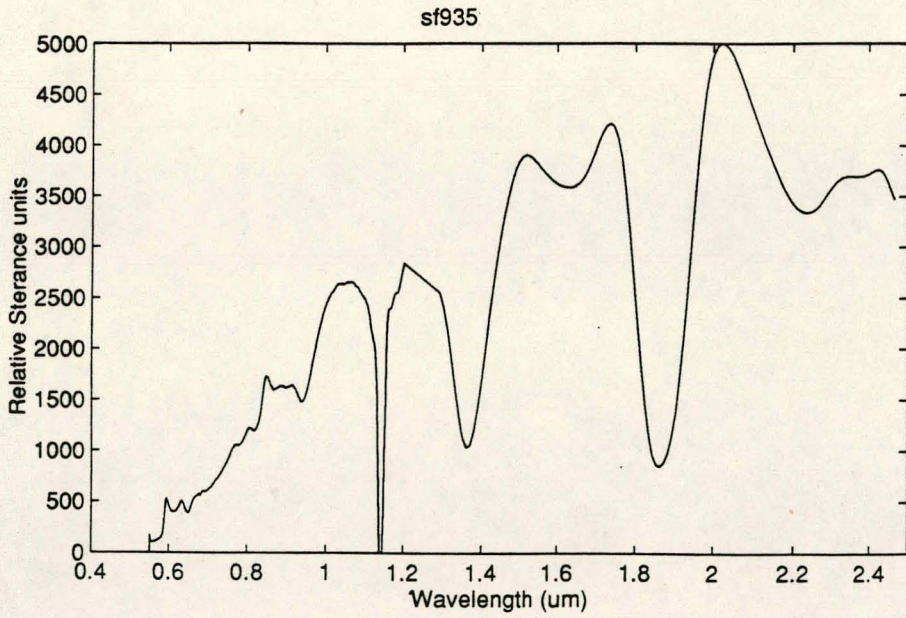
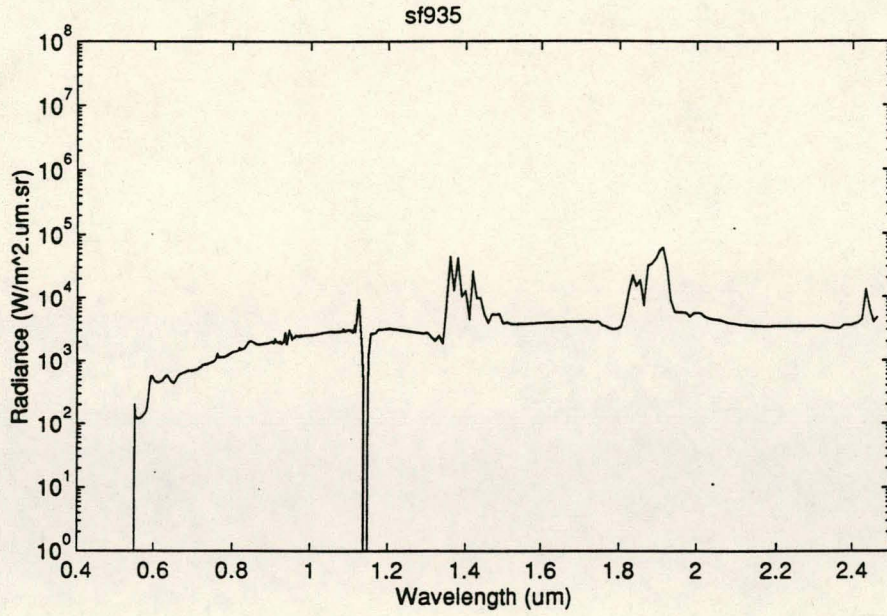


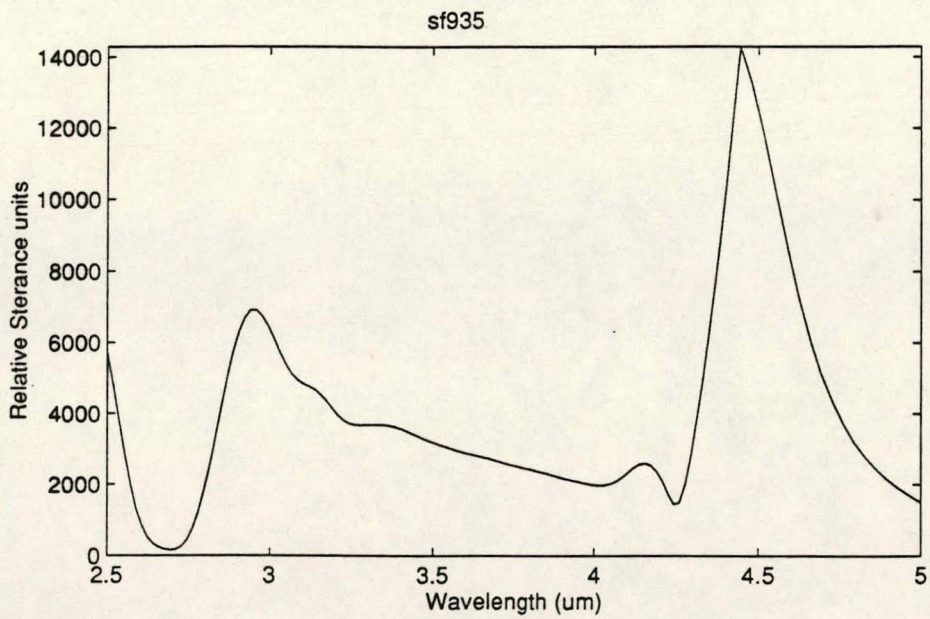
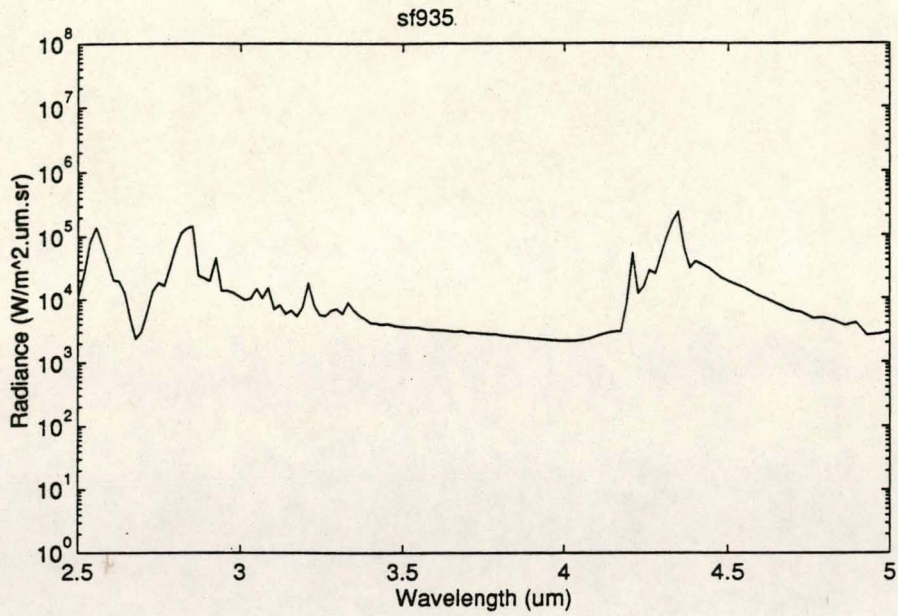


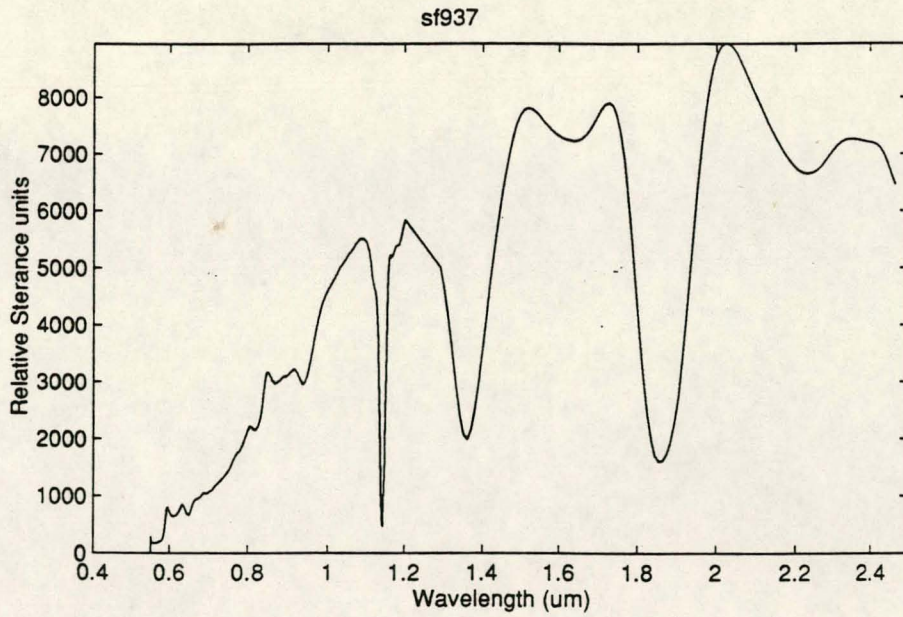
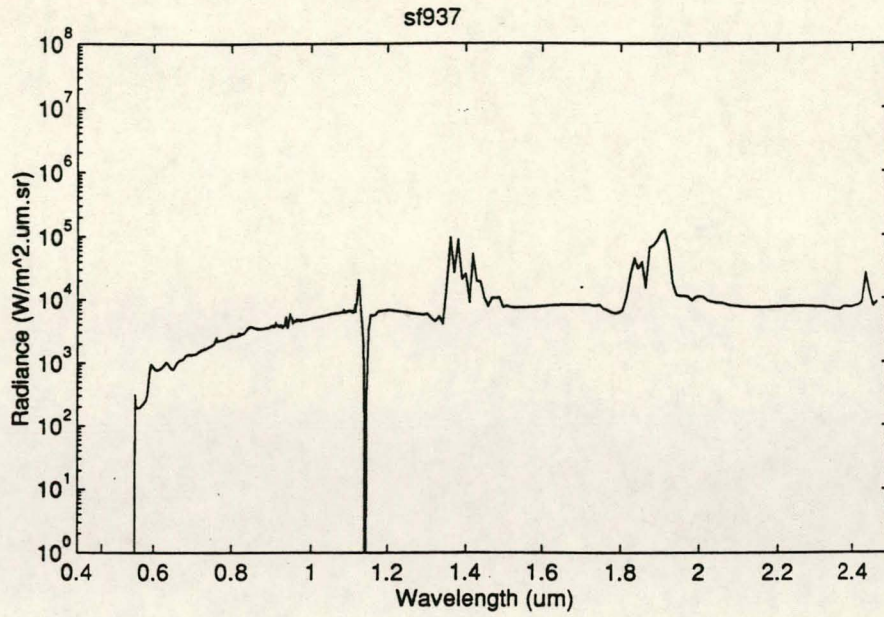


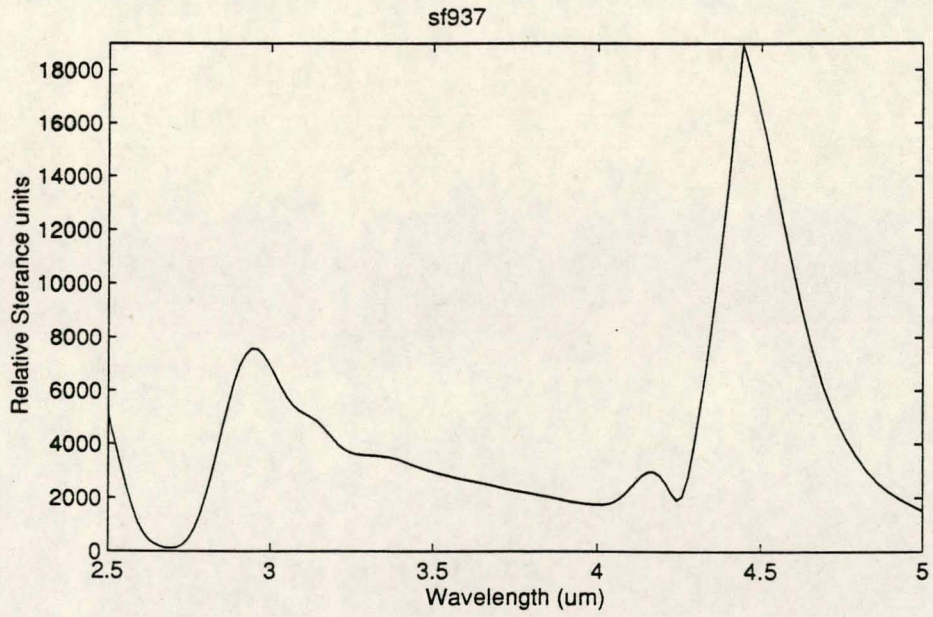
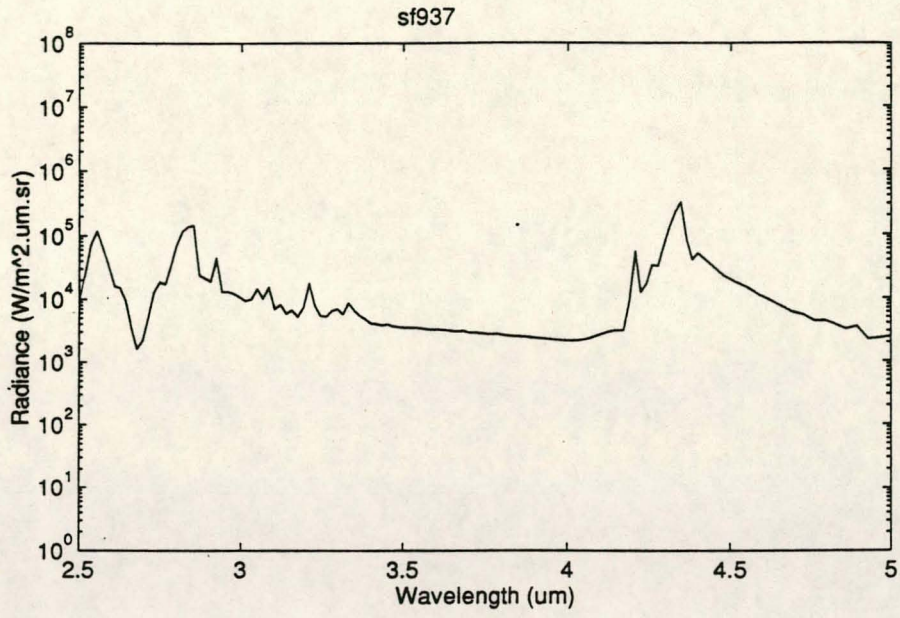


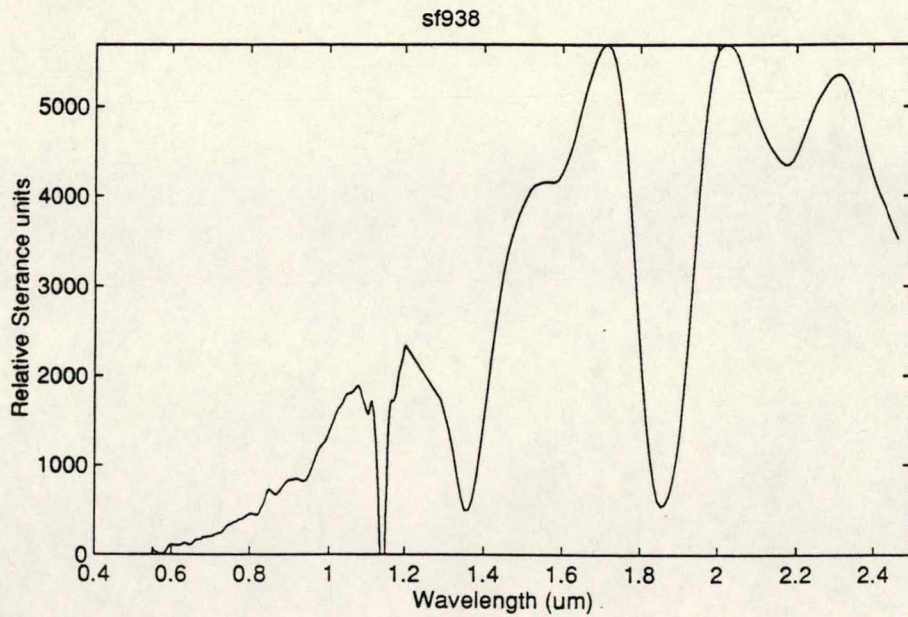
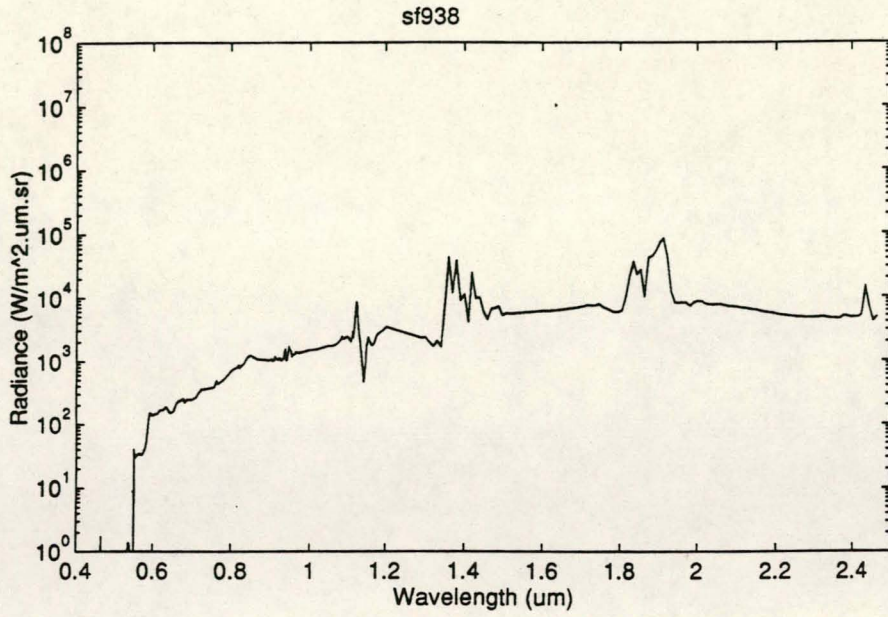


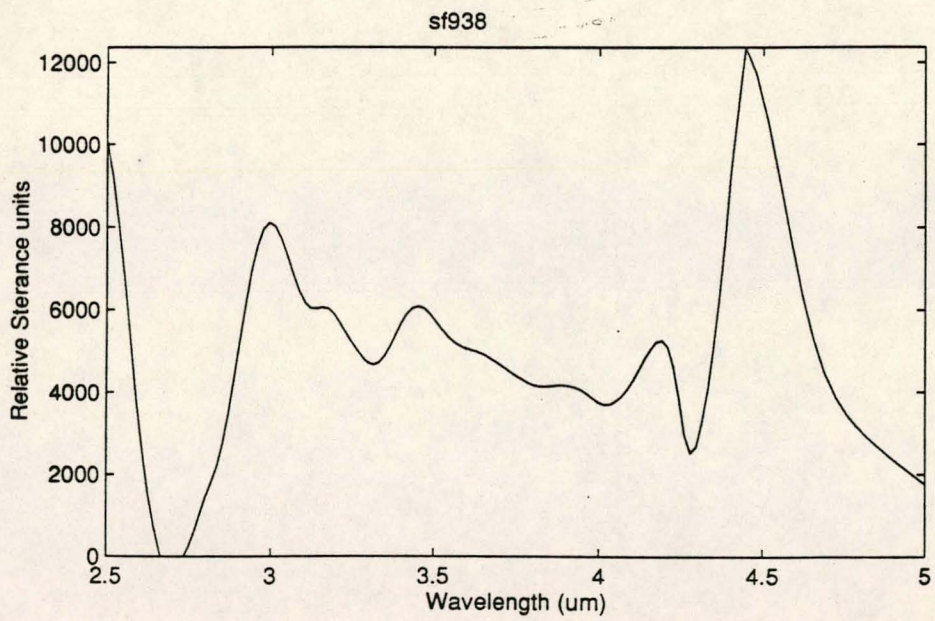
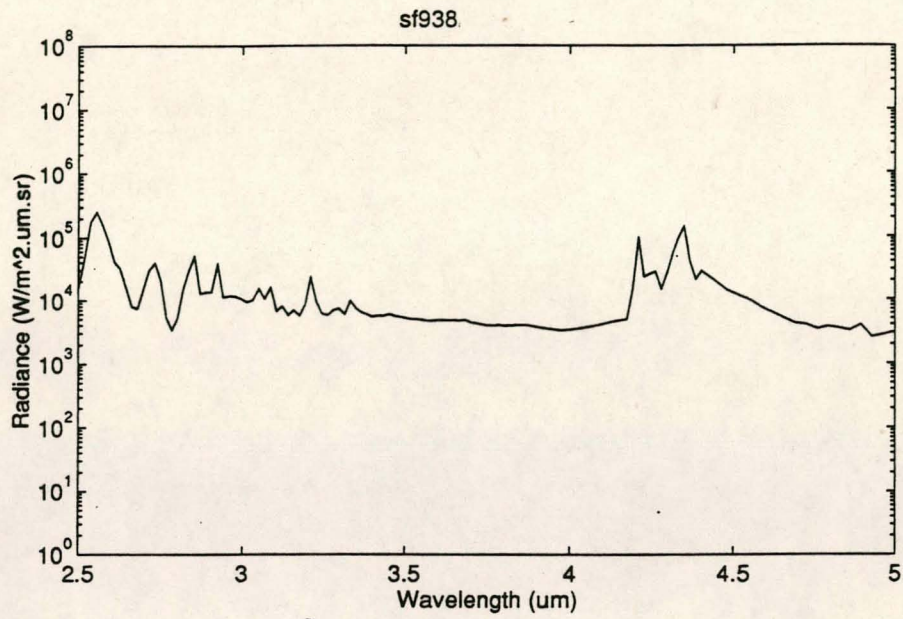


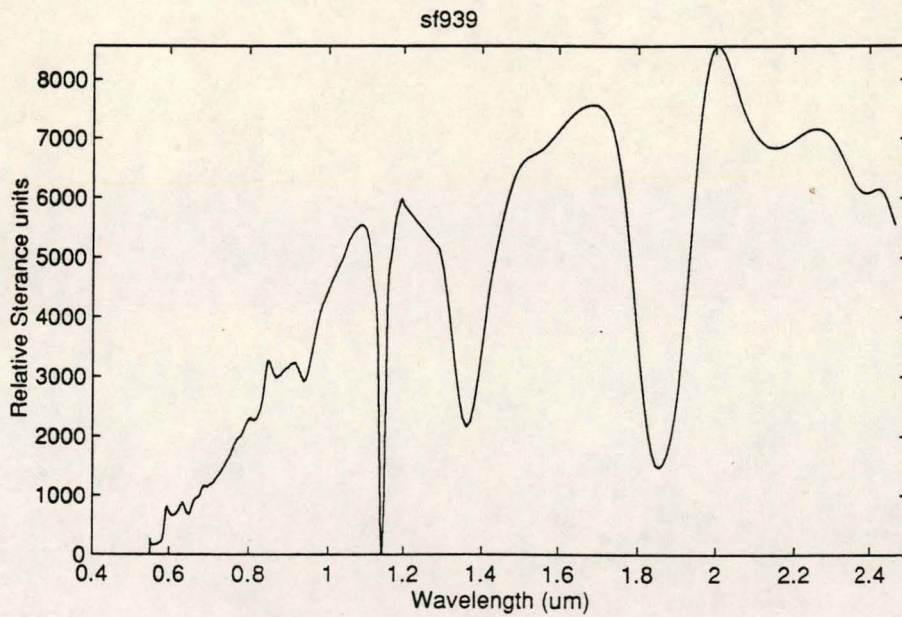
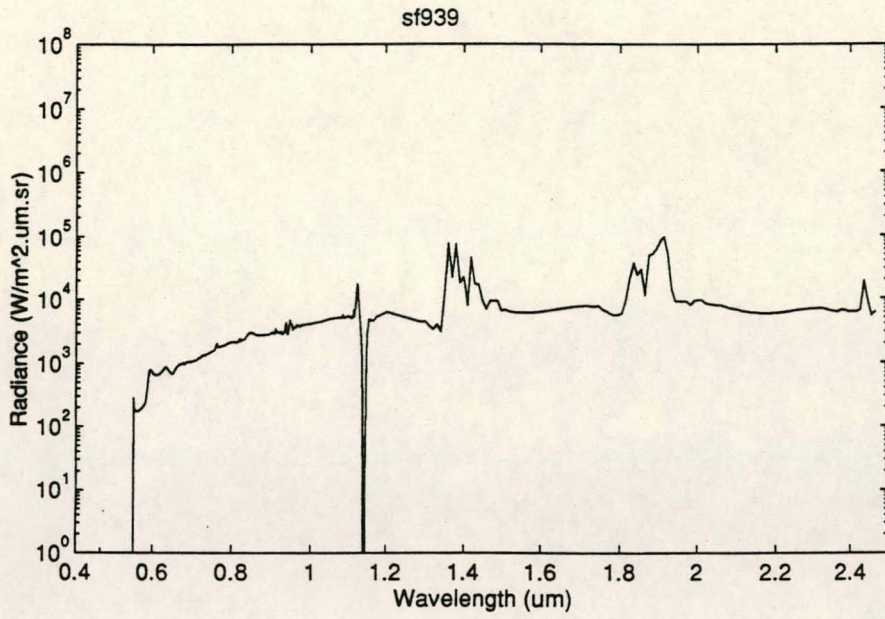


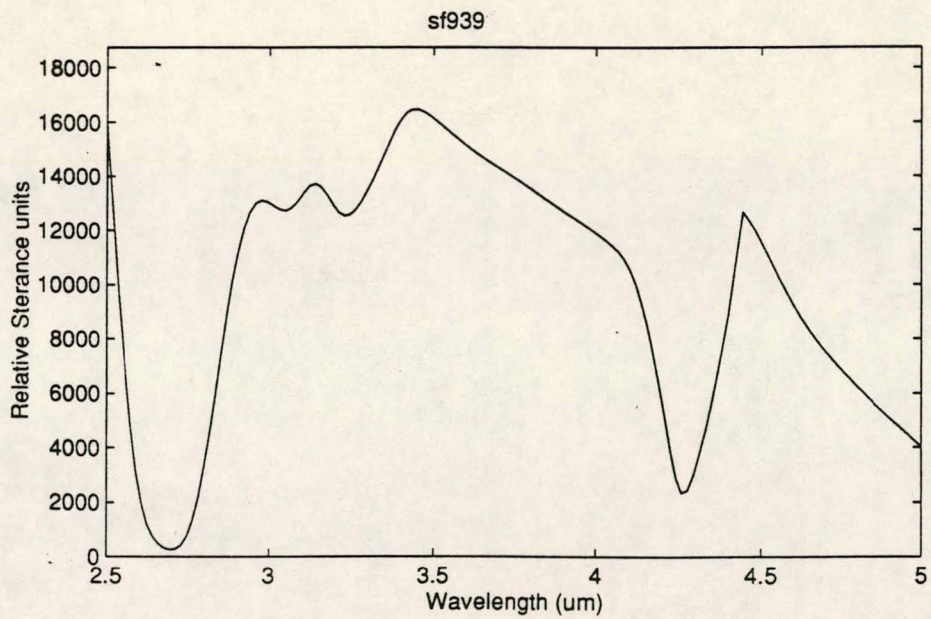
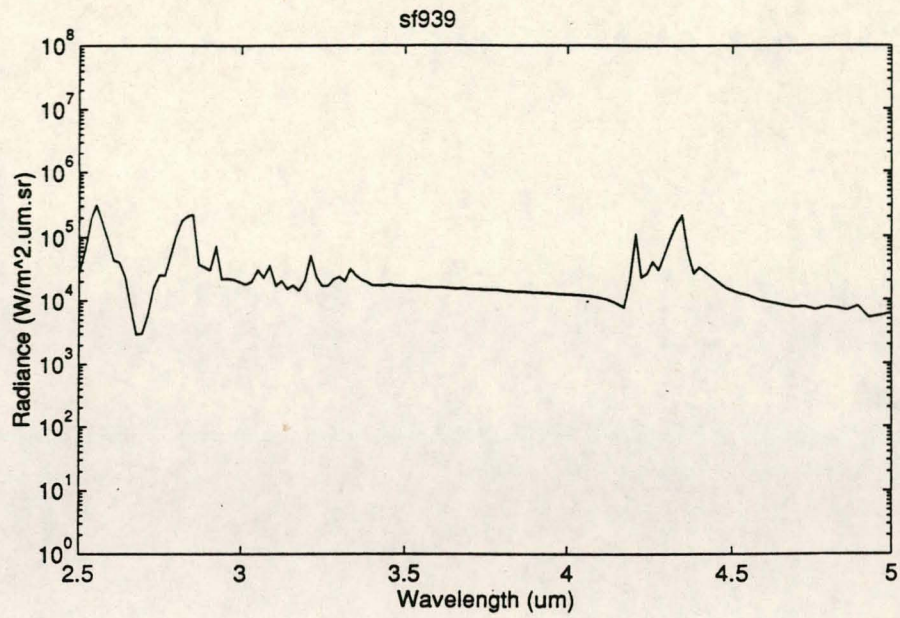


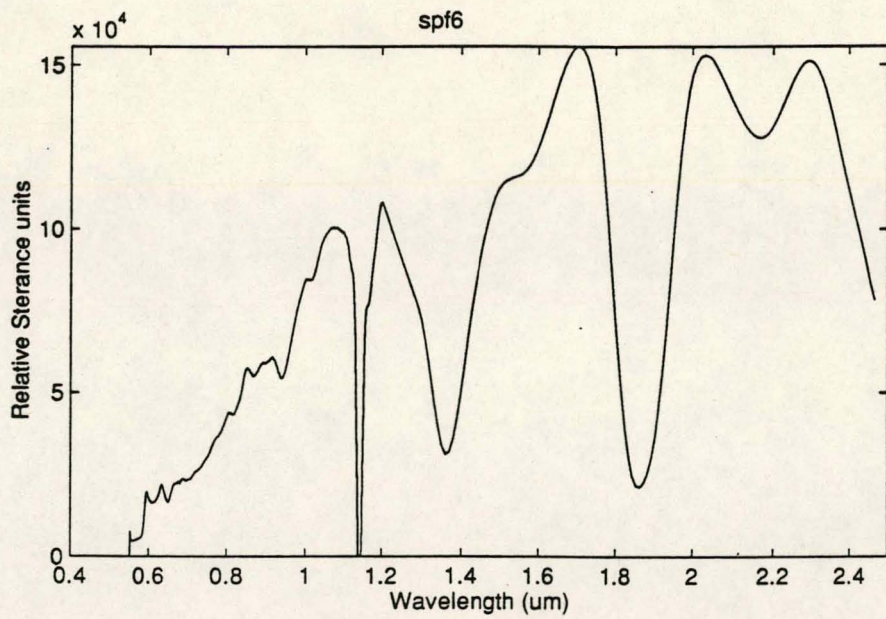
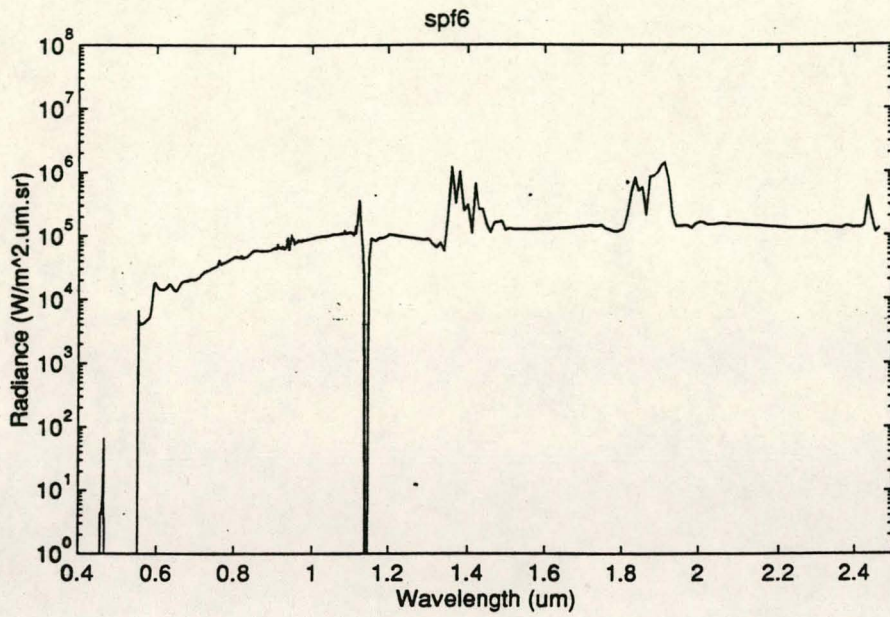


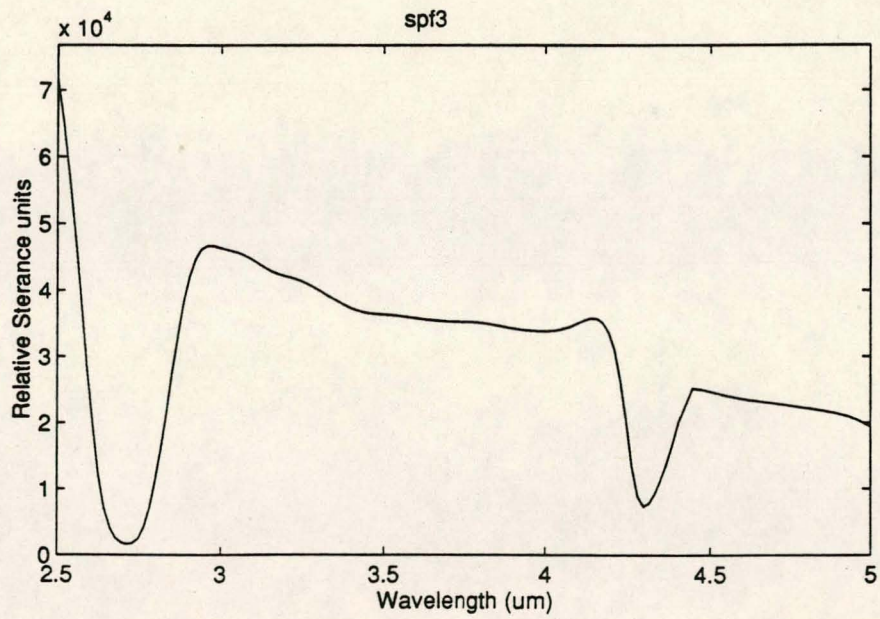
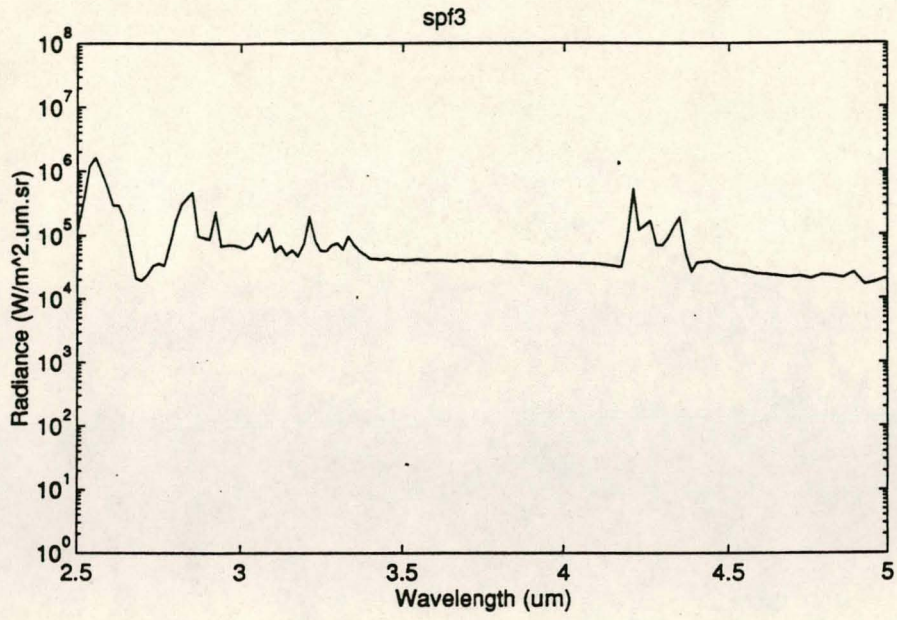




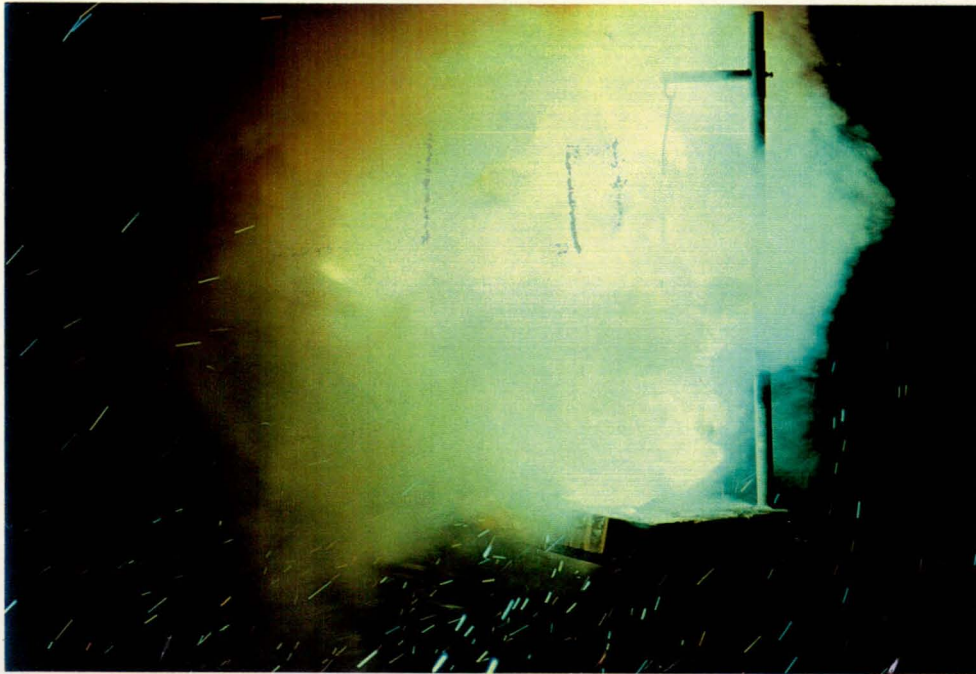




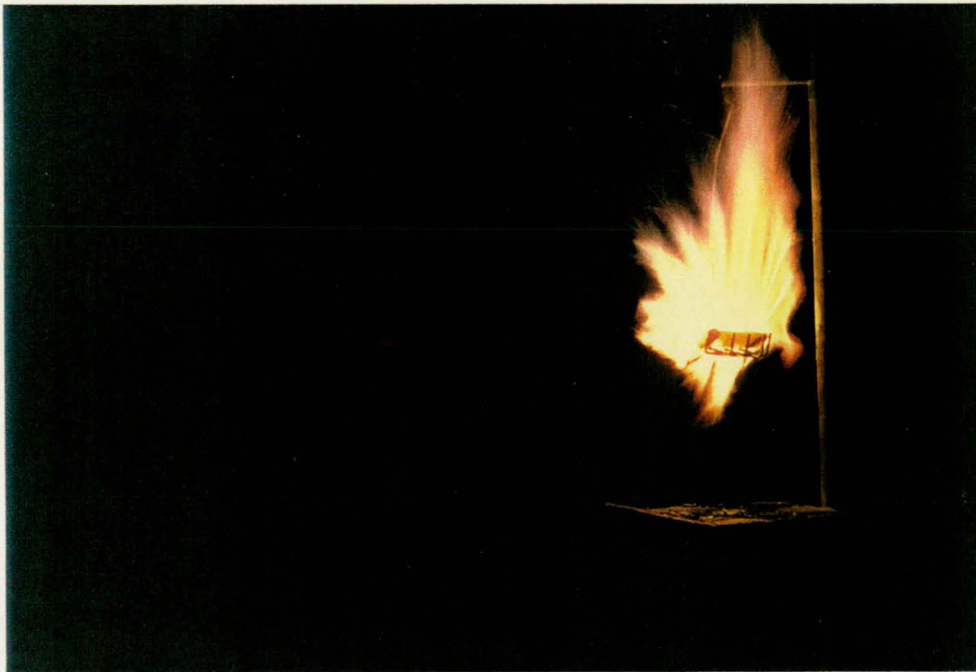




APPENDIX H
PICTORIAL FLARE COMPARISON



Current Std MTV Flare Composition



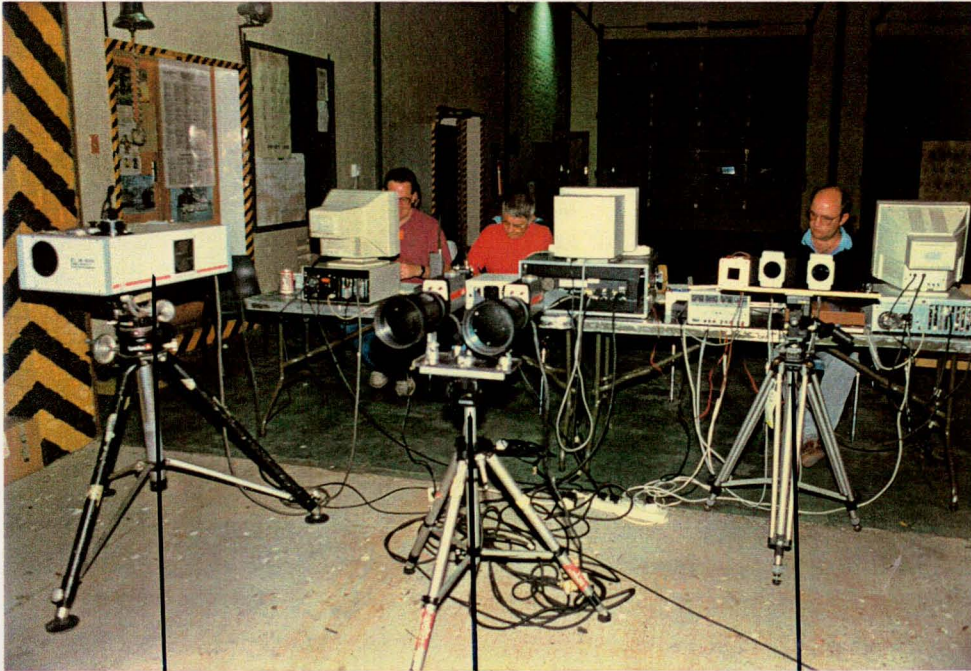
New SF930 Flare Composition

APPENDIX I
CHEMICAL COMPOSITIONS OF THE PLUMES

Input Number	Plume Species	DBR	GDBB	GDBSK	GG	GDBRKN	DBKNKAF	DBNQKN	SF937 1800	SF937 600	V3C	V3F0	V3KS	V4	V4KS	VLAP
1	Al ₂ O ₃	0	0	0	0	0	0.00211	0	0	0	0.07696	0.07798	0.07769	0	0	0.01981
2	C	0	0	0.05056	0.02024	0	0	0	0	0.15666	0	0	0	0	0	0
3	CH ₄	0	0.00029	0.01399	0.07395	0.00002	0	0	0	0.09844	0	0	0	0	0	0
4	CO	0.2532	0.28032	0.30298	0.05652	0.28549	0.23981	0.2282	0.29973	0.00046	0.24063	0.24521	0.24377	0.0993	0.10171	0.12771
5	CO ₂	0.21262	0.1975	0.18366	0.16415	0.19349	0.2233	0.20748	0.03538	0.14561	0.0181	0.01697	0.01736	0.14289	0.14282	0.11803
6	COS	0	0	0	0	0	0	0	0	0	0	0	0.00005	0	0.00008	0
7	Cl	0	0	0	0	0	0	0	0	0	0.0007	0.00065	0.00072	0	0	0.00006
8	Cu	0.00244	0.00302	0	0	0.00276	0.00264	0.0025	0	0	0	0	0	0	0	0
9	Fe	0	0	0	0	0	0	0	0	0	0	0.00011	0	0	0	0
10	FeCl ₂	0	0	0	0	0	0	0	0	0	0	0.00646	0	0	0	0
11	H	0	0	0	0	0	0	0	0.0002	0	0.00194	0.00207	0.00214	0	0	0.00005
12	H ₂	0.14697	0.23053	0.26396	0.27209	0.20571	0.1191	0.14243	0.31521	0.02859	0.31217	0.32264	0.31461	0.10068	0.10031	0.11734
13	H ₂ O	0.20504	0.13198	0.08802	0.21415	0.15622	0.21913	0.21739	0.14132	0.32102	0.11708	0.11197	0.11292	0.36633	0.36521	0.34271
14	H ₂ S	0	0	0	0	0	0	0	0	0	0	0	0.00166	0	0.00249	0
15	HCl	0	0	0	0	0	0	0	0.1261	0.15103	0.15393	0.13862	0.14492	0.189	0.18047	0.18644
16	HF	0	0	0	0	0	0.00103	0	0	0	0	0	0	0	0	0
17	K	0	0	0	0	0	0.00152	0.00038	0	0	0	0	0.00002	0	0	0
18	K ₂ CO ₃	0	0	0	0	0.00552	0.00362	0.00631	0	0	0	0	0	0	0	0
19	K ₂ Cl ₂	0	0	0	0	0	0	0	0	0	0	0	0	0	0.00006	0
20	K ₂ F ₂	0	0	0	0	0	0.00291	0	0	0	0	0	0	0	0	0
21	KCl	0	0	0	0	0	0	0	0	0	0	0	0.00599	0	0.00587	0
22	KF	0	0	0	0	0	0.01077	0	0	0	0	0	0	0	0	0
23	KOH	0	0	0	0	0.00015	0.0091	0.00297	0	0	0	0	0	0	0	0
24	N ₂	0.17501	0.15476	0.09477	0.19875	0.14906	0.15981	0.18748	0.08199	0.09812	0.07836	0.07717	0.07687	0.09534	0.09408	0.09504
25	NH ₃	0	0.00002	0.00004	0.00015	0.00001	0	0	0	0.00008	0	0	0	0	0	0
26	OH	0	0	0	0	0	0	0	0	0	0	0.00009	0.0001	0	0	0
27	Pb	0.00274	0.00157	0.00201	0	0.00155	0.00298	0.00282	0	0	0	0	0	0	0	0
28	S	0	0	0	0	0	0	0	0	0	0	0	0.00009	0	0	0
29	S ₂	0	0	0	0	0	0	0	0	0	0	0	0.00015	0	0.00006	0
30	SH	0	0	0	0	0	0	0	0	0	0	0	0.00065	0	0.00004	0
31	SO	0	0	0	0	0	0	0	0	0	0	0	0.00016	0	0	0
32	SO ₂	0	0	0	0	0	0	0	0	0	0	0	0.00009	0	0.00025	0
33	SiO ₂	0	0	0	0	0	0	0	0	0	0	0	0	0.00644	0.0065	0
34	TiO ₂	0.00197	0	0	0	0	0.00214	0.00202	0	0	0	0	0	0	0	0

Molar Fraction Data of the Species Present in the Different Plumes

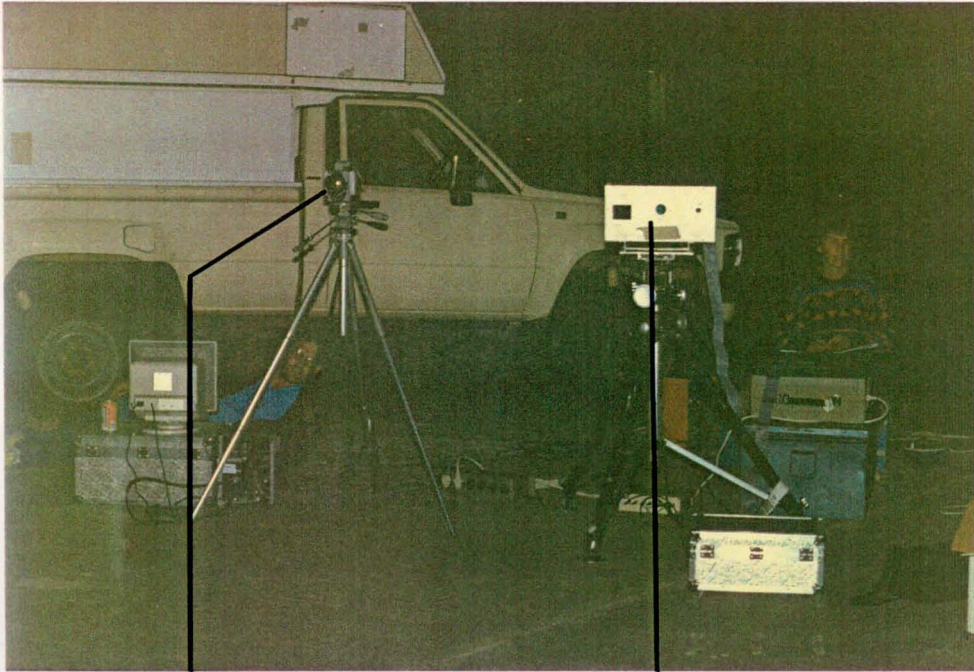
APPENDIX J
APPARATUS USED FOR THE MEASUREMENTS



Sensors 1, 2 & 3 of
UV Radiometer,
Avitronics

Near and Far IR
Thermal Imagers, IMT

SR 5000 IR
Radiometer



AGEMA 900 IR
Thermal Imager,
Aerotek

Channel 0, 1 & 2 UV
Radiometer, Aerotek

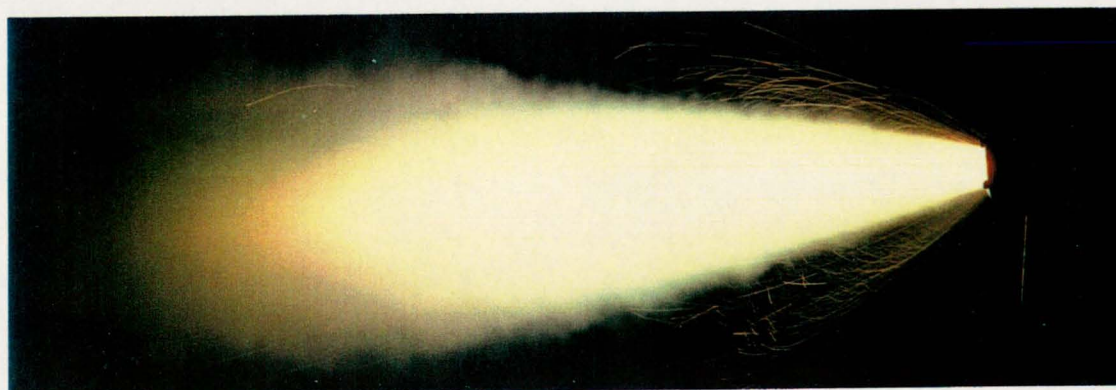
APPENDIX K
PHOTOGRAPHIC MATERIAL OF THE ROCKET MOTOR PLUMES



V3std



V3KS



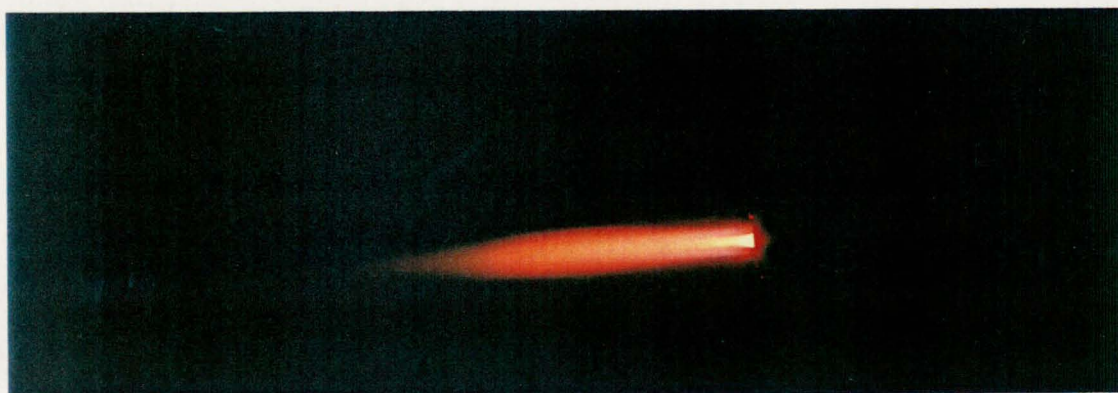
V3FO



V4std



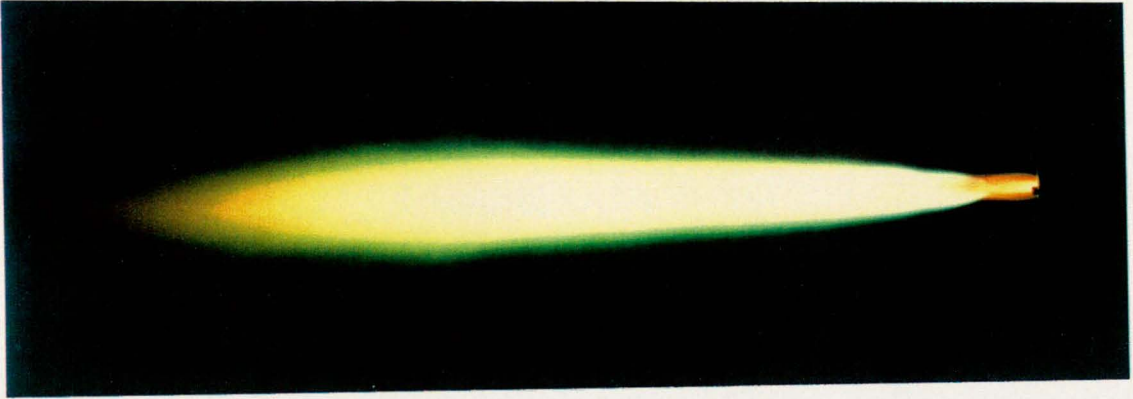
V4KS



V4SC



VLAP



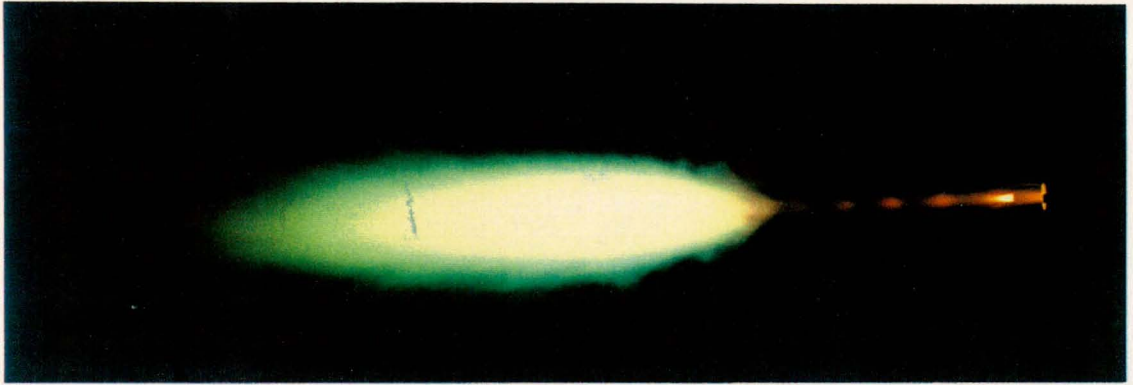
DBR



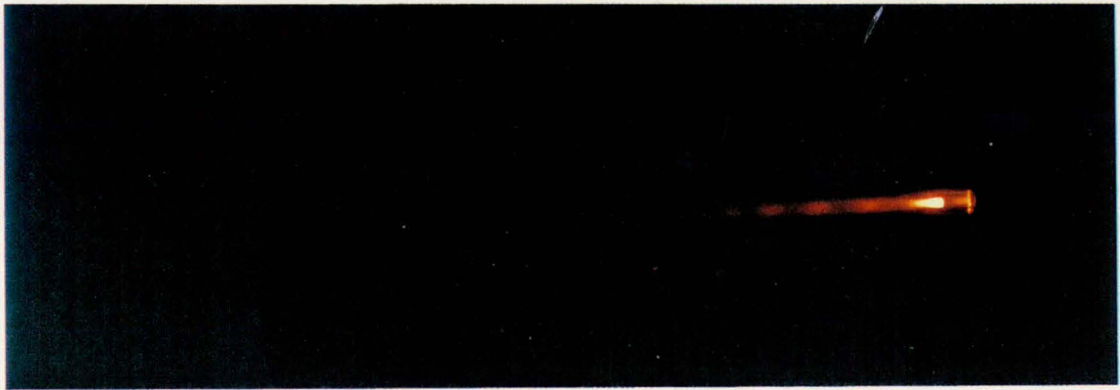
DBKNKAF



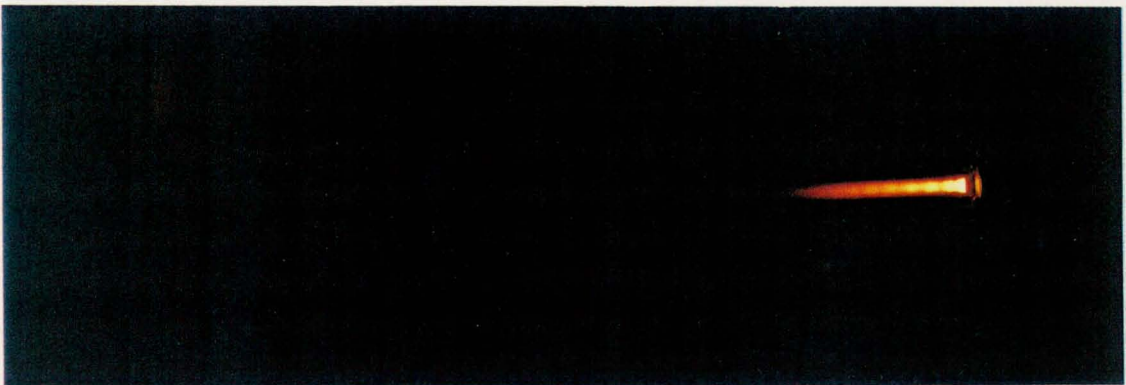
DBNQKN



GDBB (GDBR)

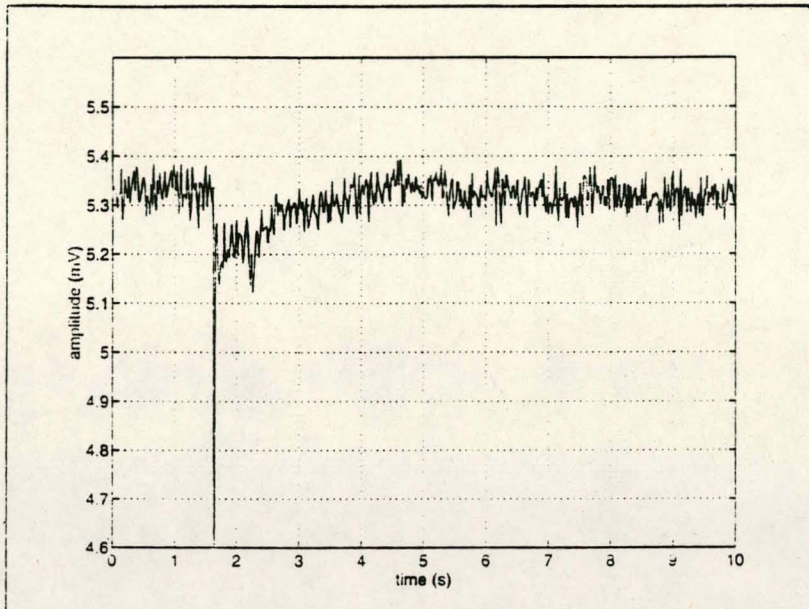


GDBRKN

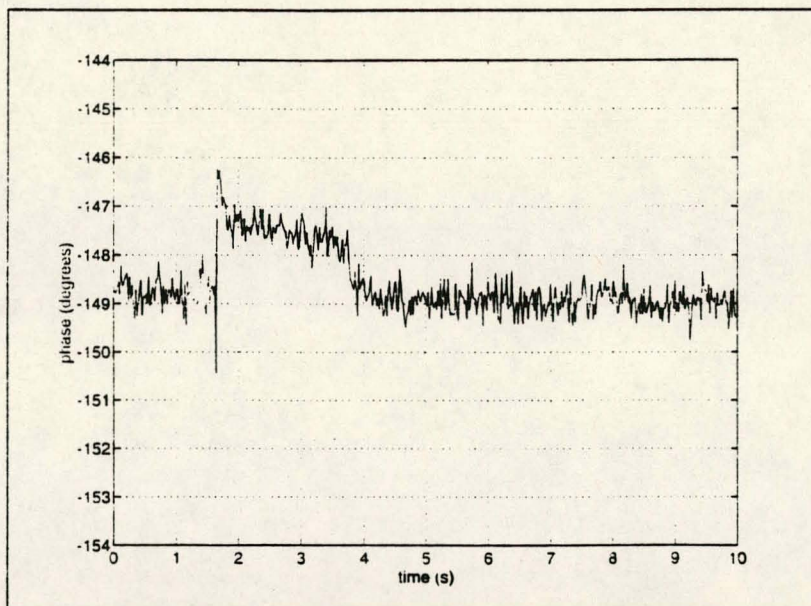


GDBSK

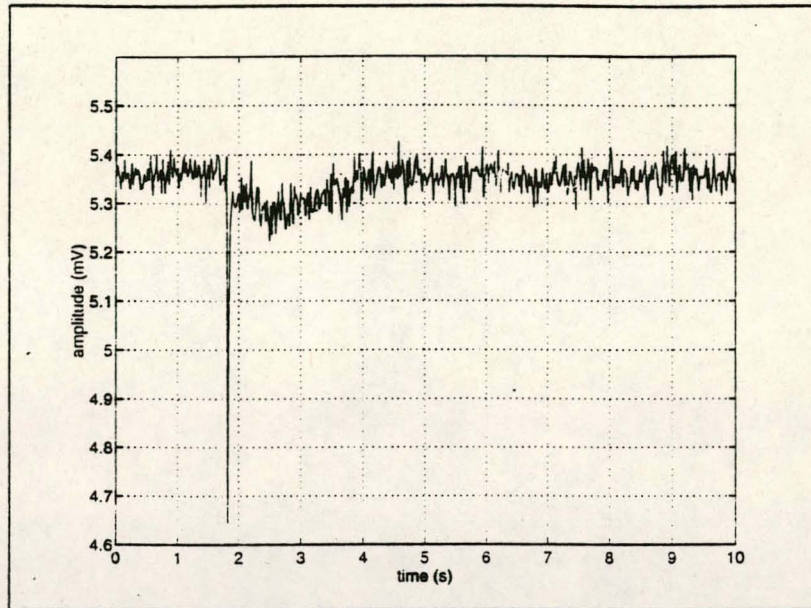
APPENDIX L
RADAR TRANSMISSION DATA



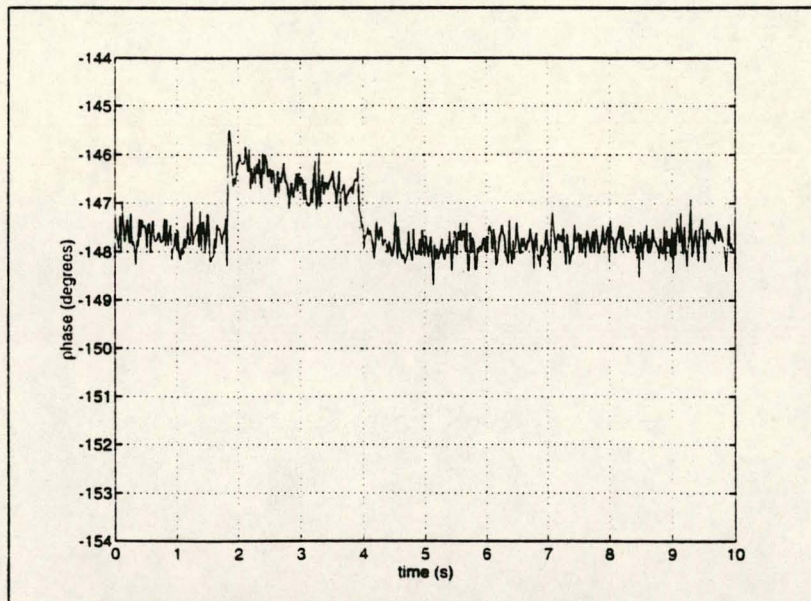
Transmission measured through plume V3STD1.



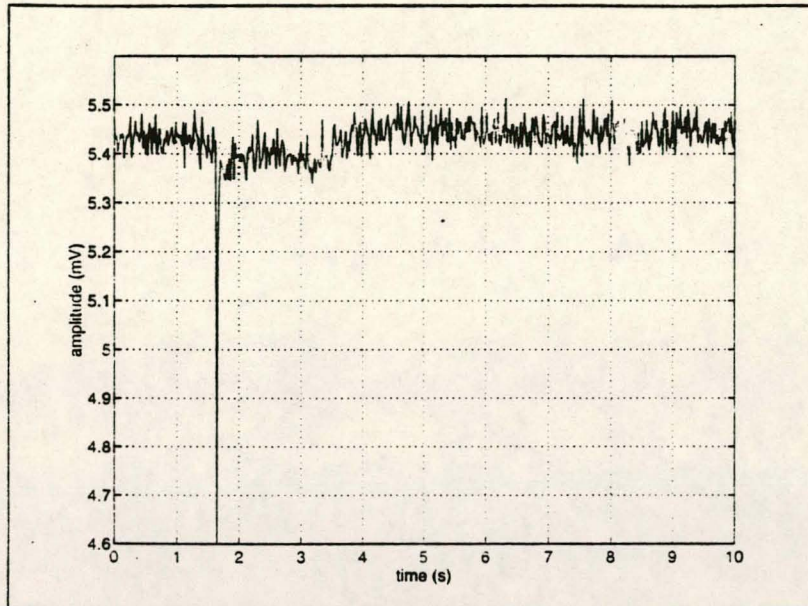
Phase change due to plume V3STD1.



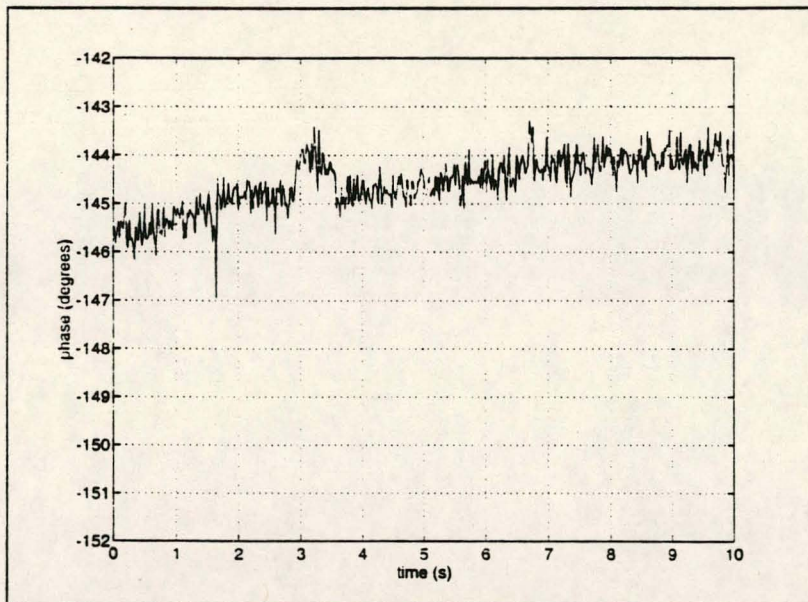
Transmission through piume V3STD2.



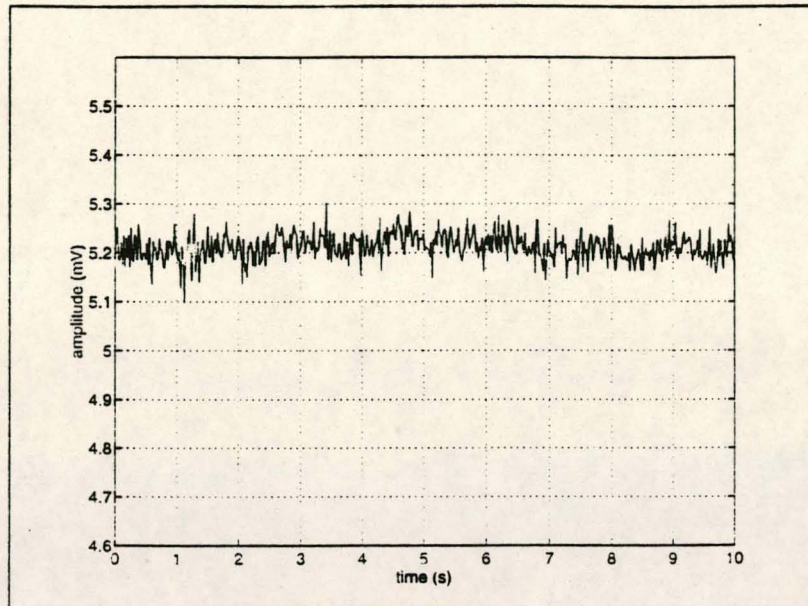
Phase change due to piume V3STD2.



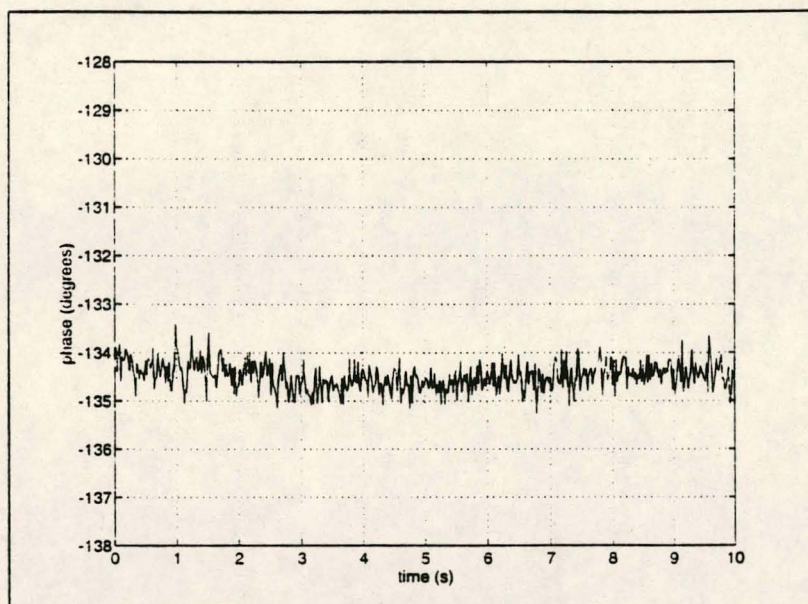
Transmission through plume VLAP.



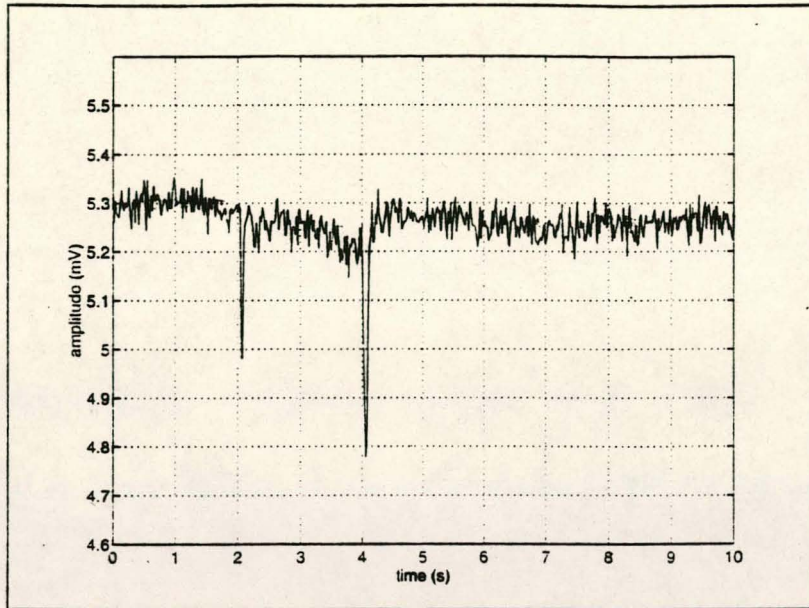
Phase change due to plume VLAP.



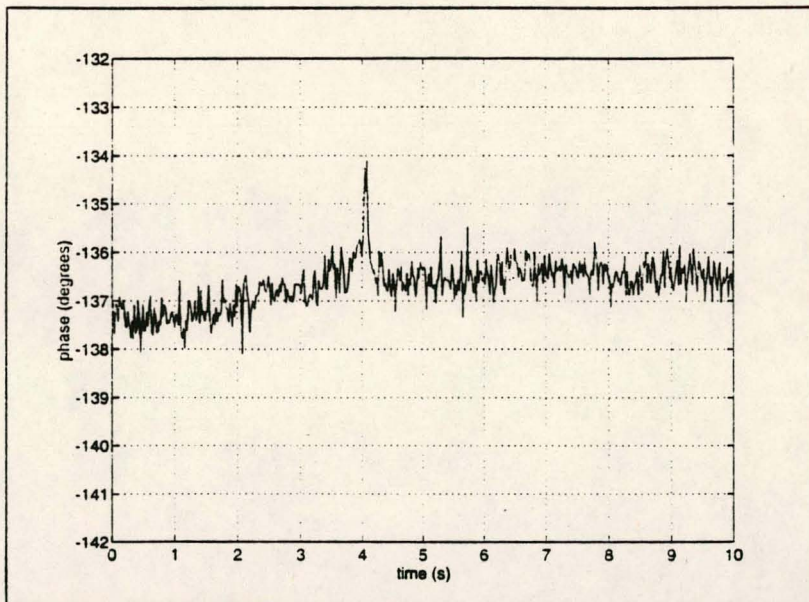
Transmission through plume GG.



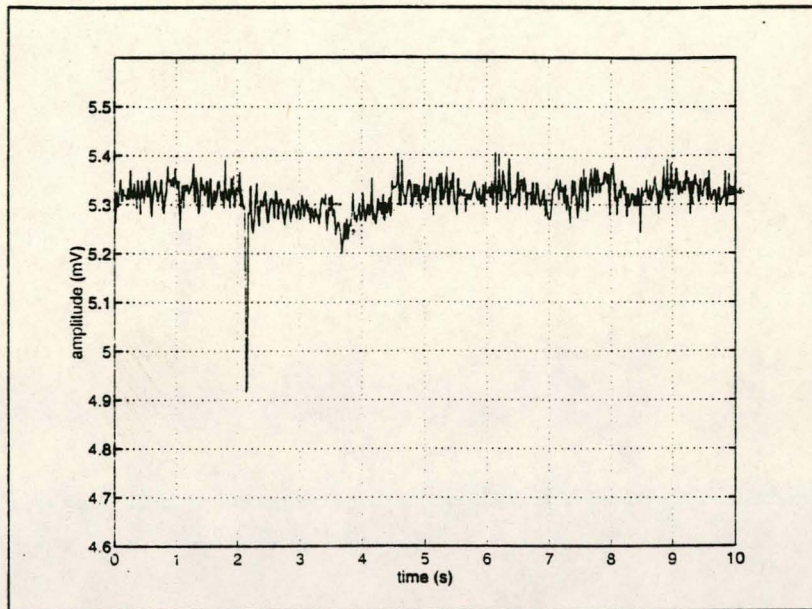
Phase change due to plume GG.



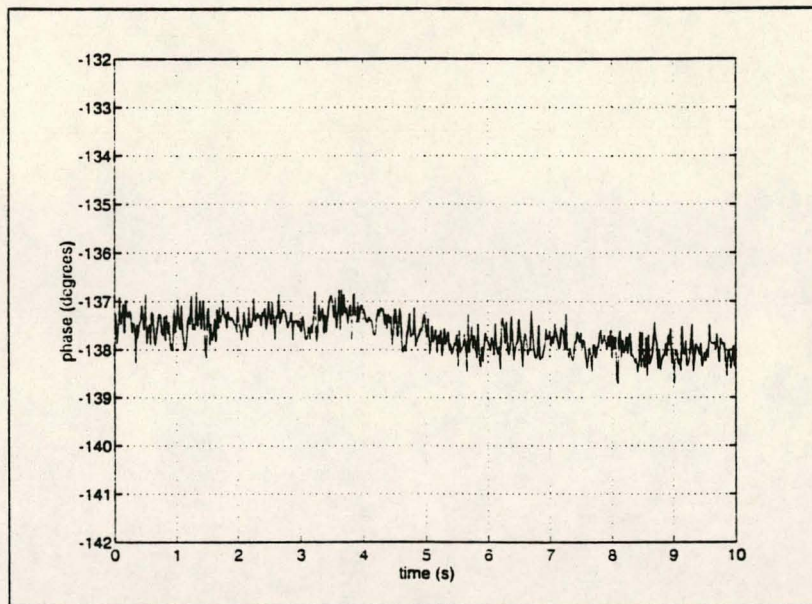
Transmission through plume DBKNKAF.



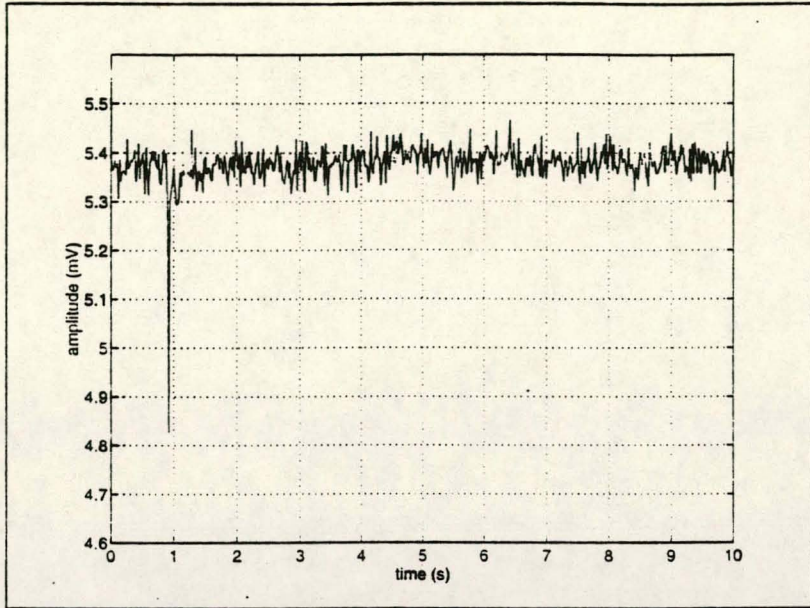
Phase change due to plume DBKNKAF.



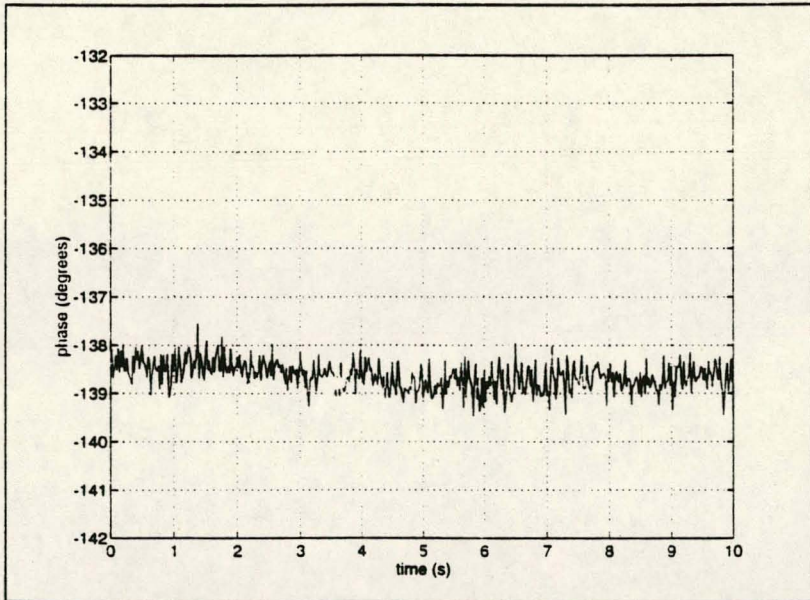
Transmission through plume DBNQKN.



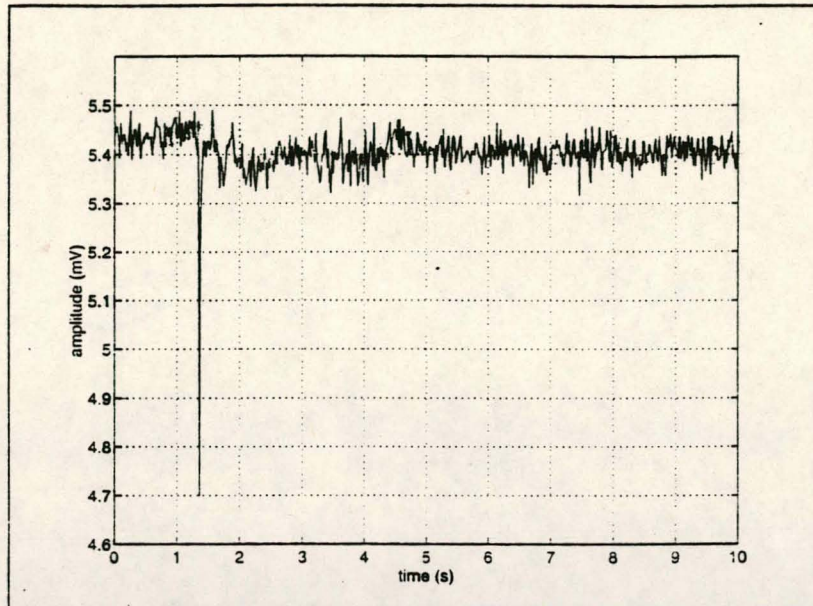
Phase change due to plume DBNQKN.



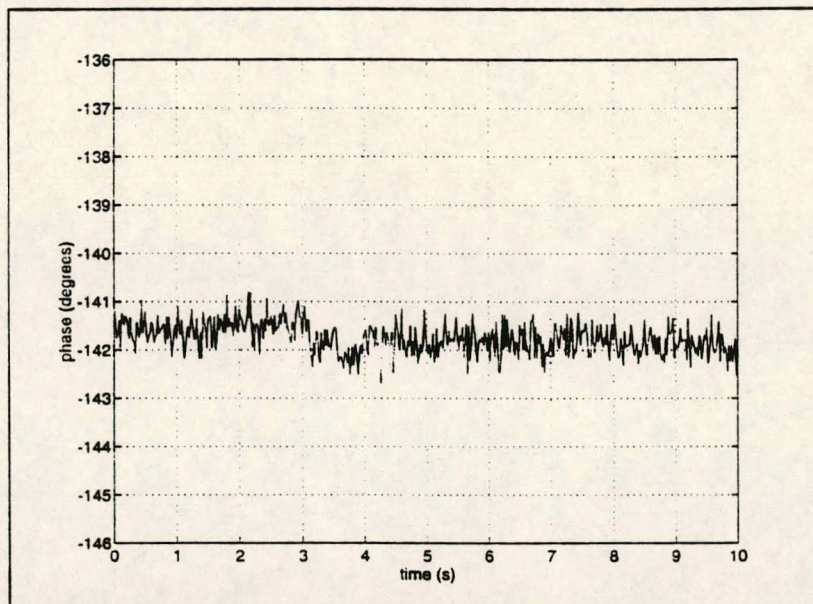
Transmission through plume GDBSK.



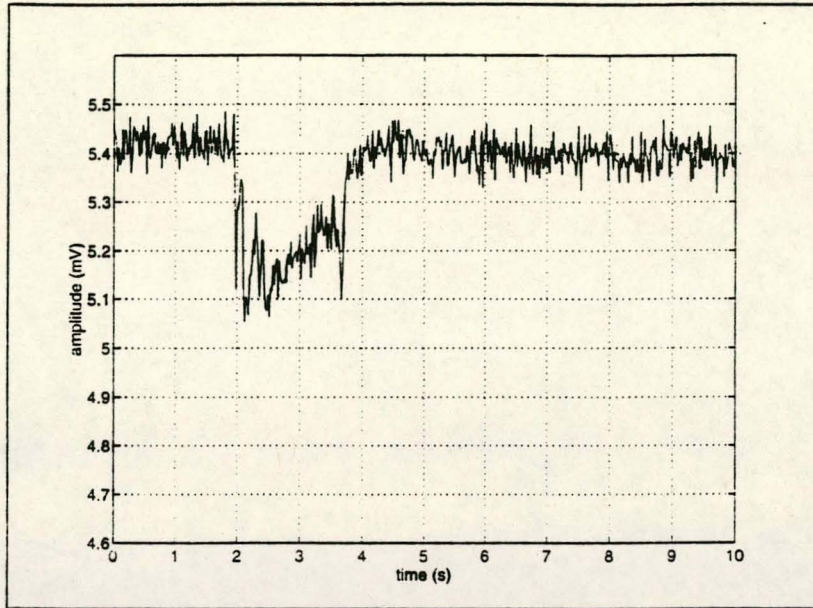
Phase difference due to plume GDBSK.



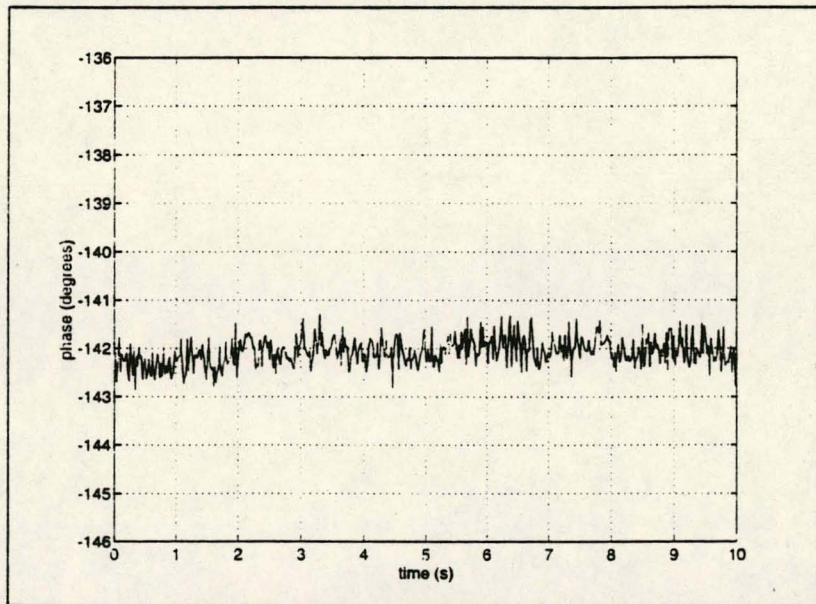
Transmission through plume GDBKN.



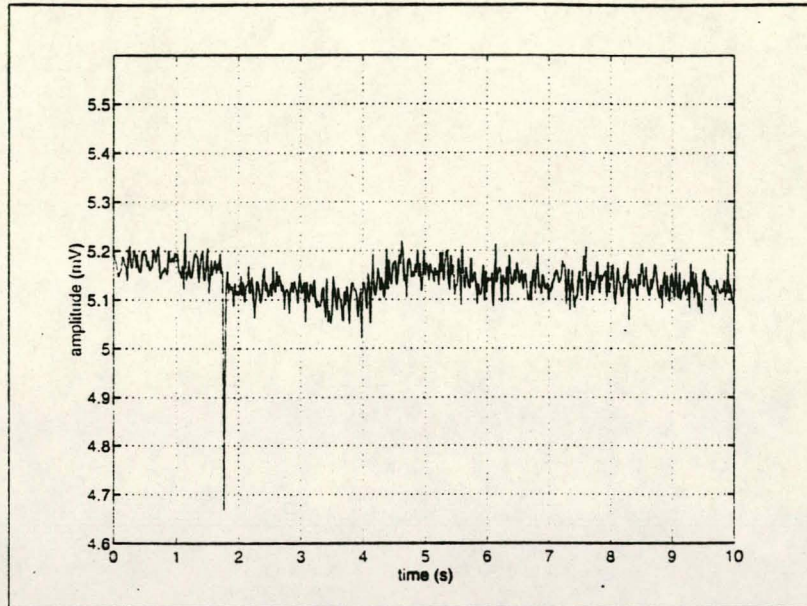
Phase change due to plume GDBKN.



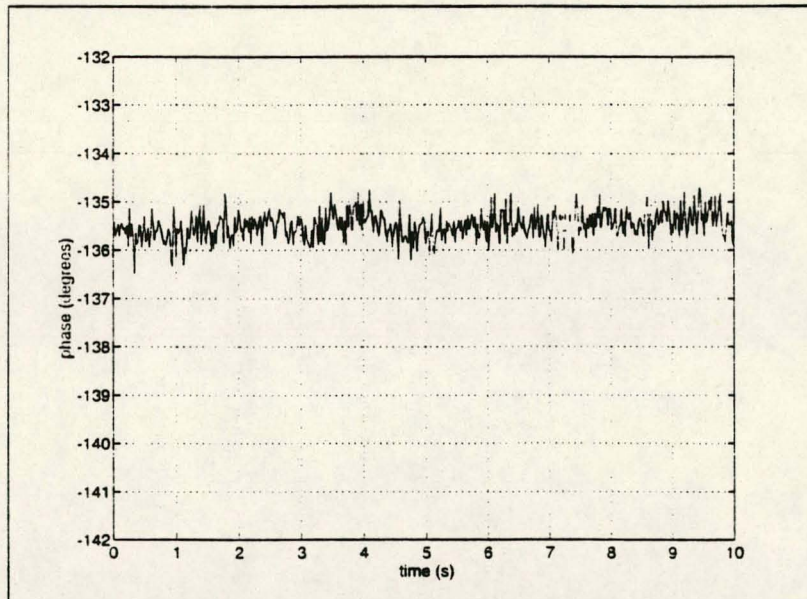
Transmission through plume GDBB.



Phase change due to plume GDBB.

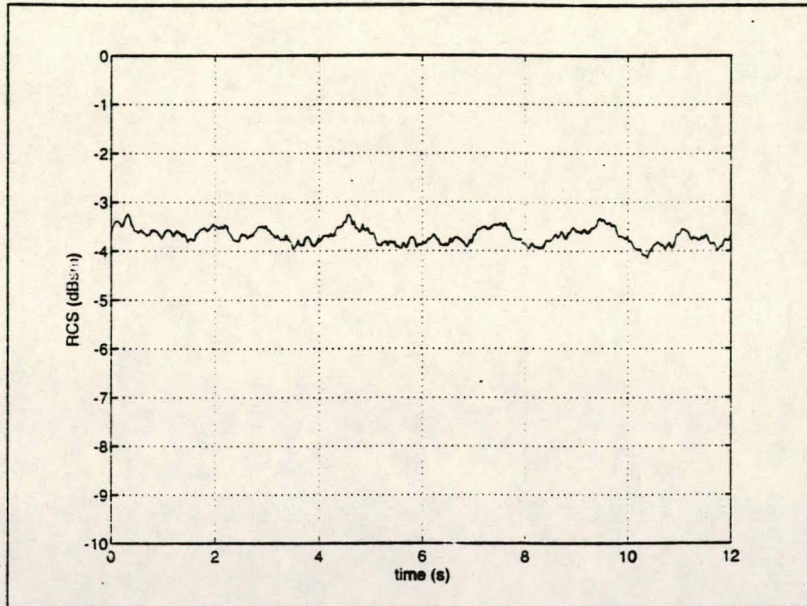


Transmission through plume V4STD1.

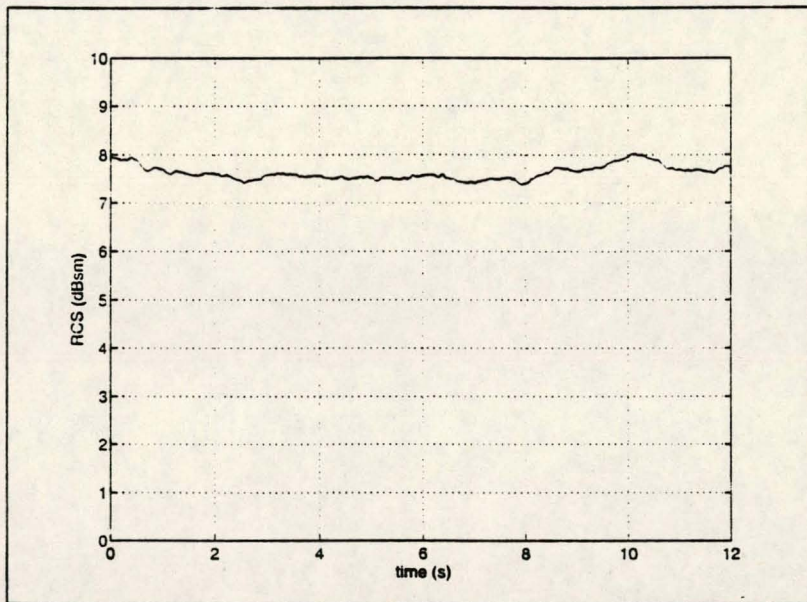


Phase change due to plume V4STD1.

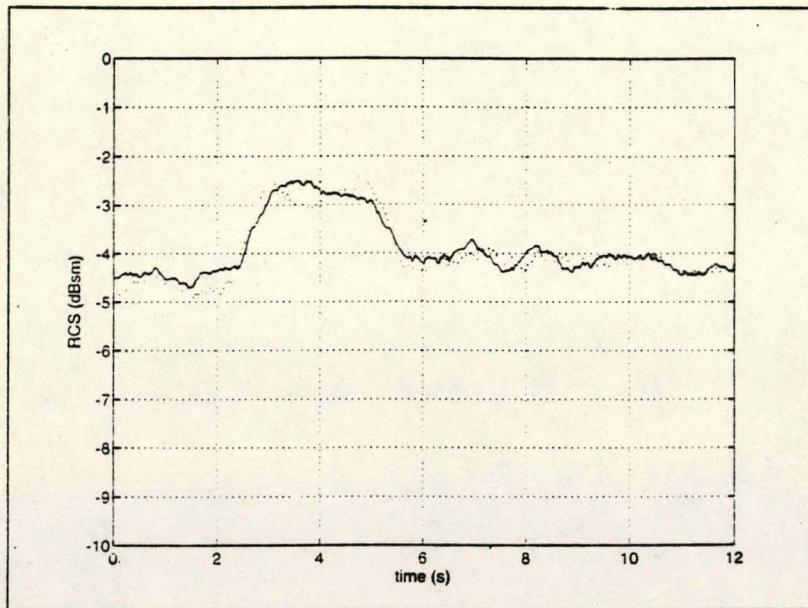
APPENDIX M
RADAR CROSS-SECTION DATA



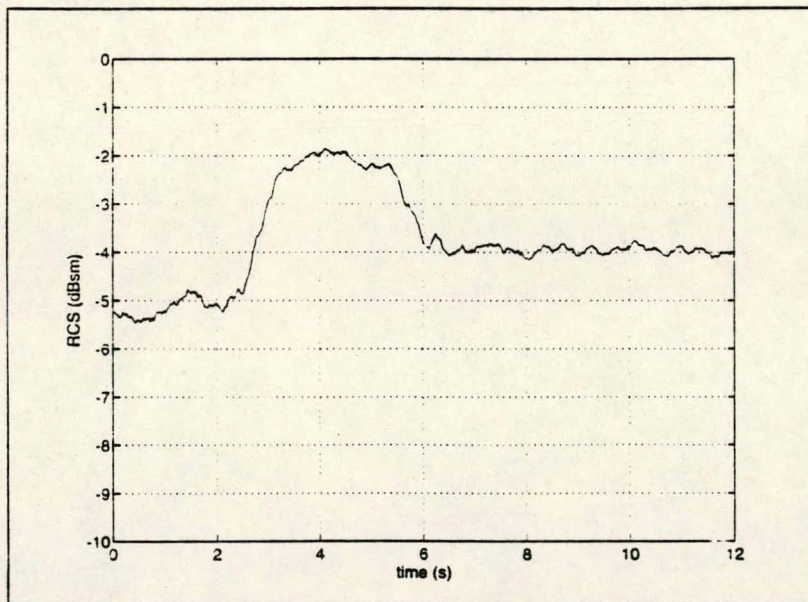
RCS of a 75cm sphere at 3GHz.



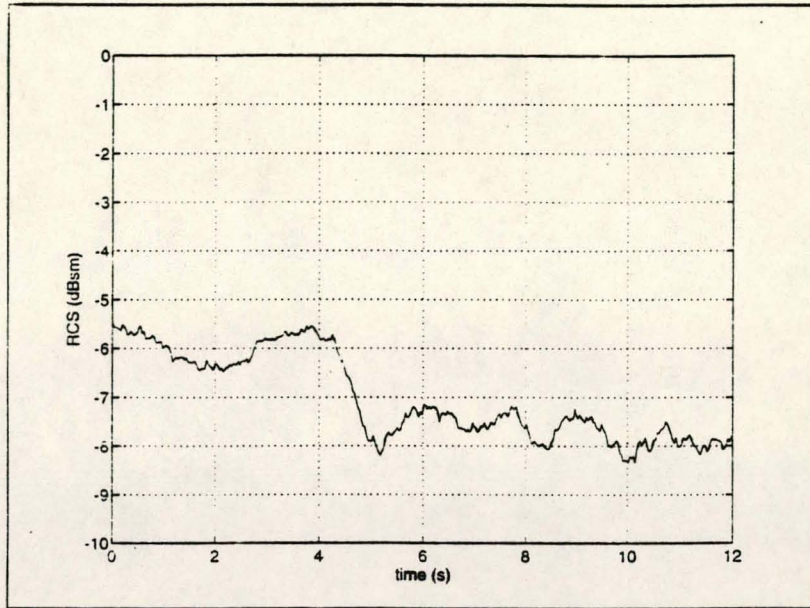
RCS of the corner reflector used to align the antennas and adjust the gate.



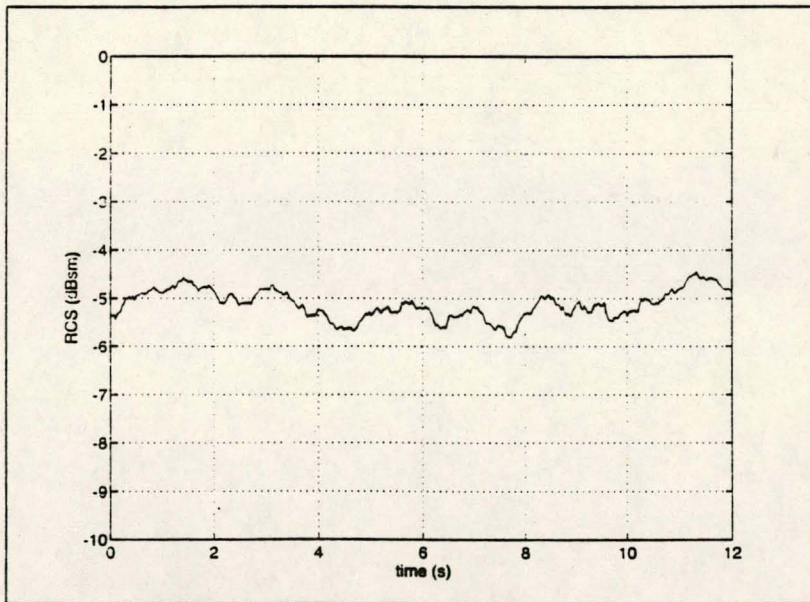
RCS of plumes V3STD#1 and #2 (dotted line) compared.



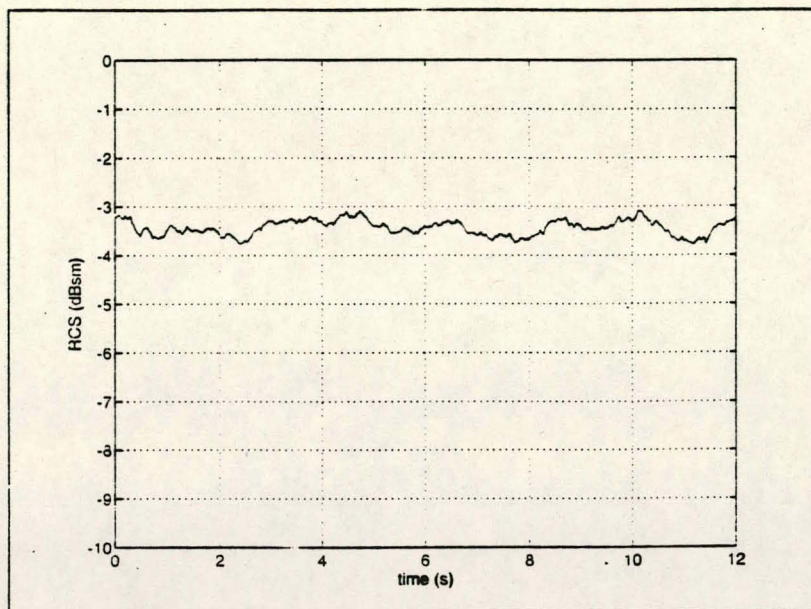
Plume V3KS.



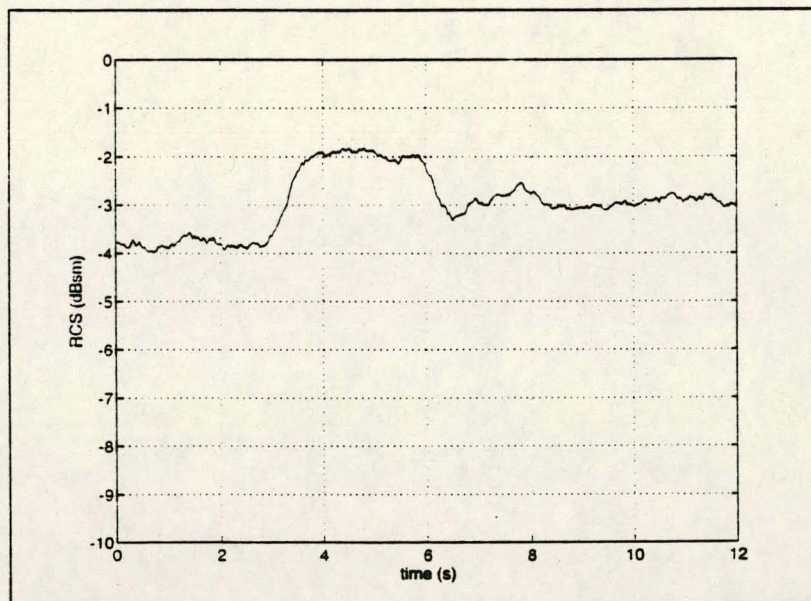
Plume V3FO.



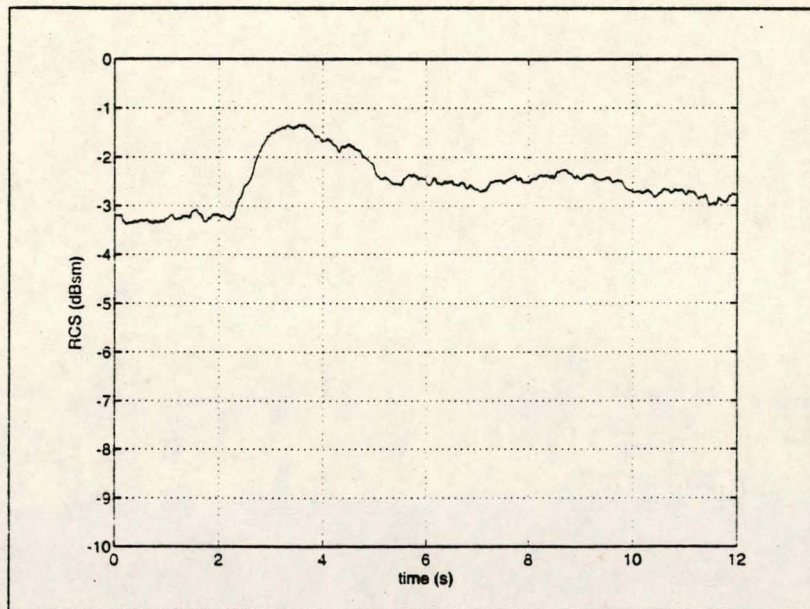
Plume V4STD.



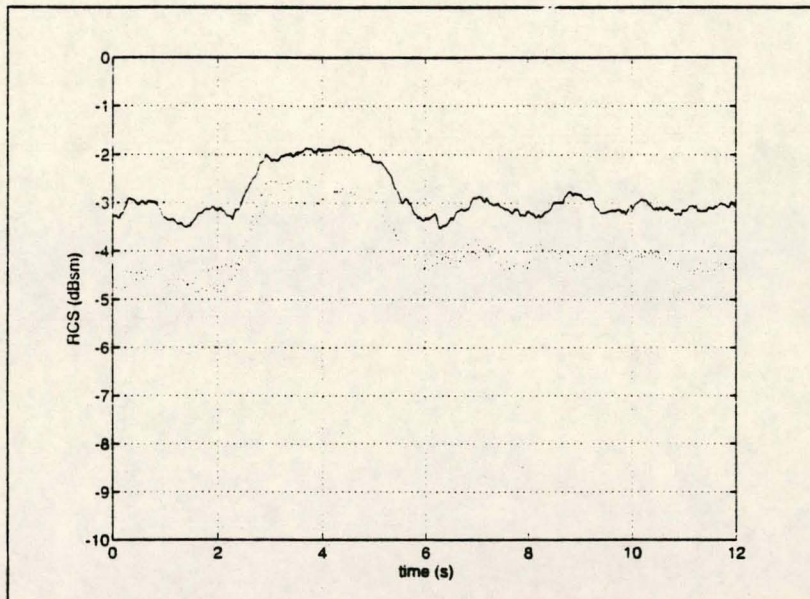
Plume V4KS.



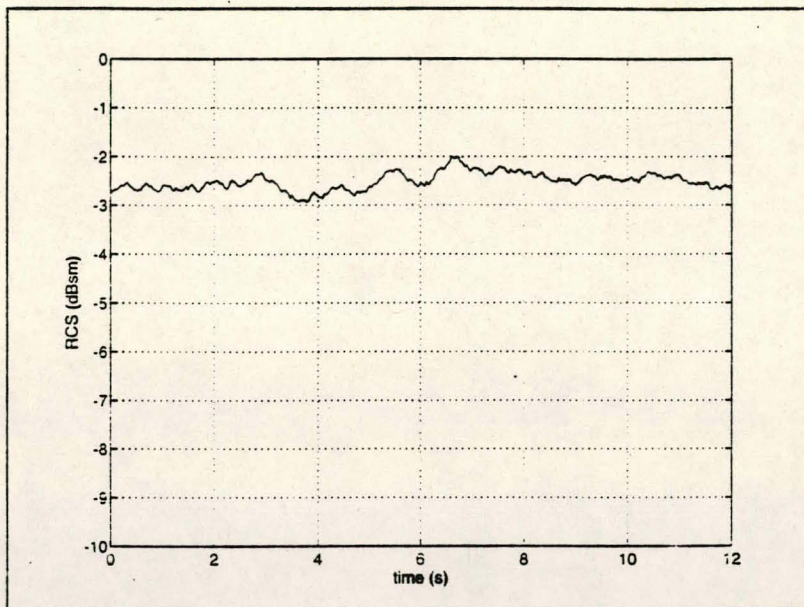
Plume V4F1200.



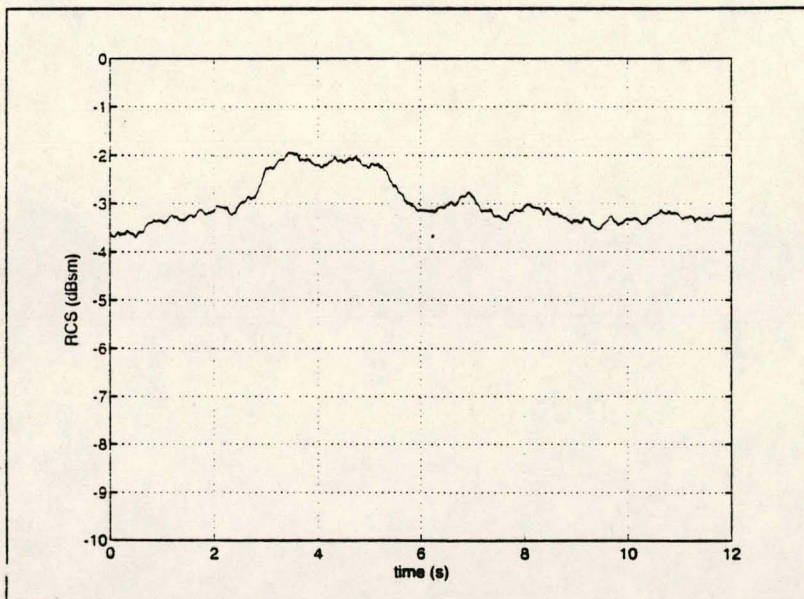
Plume VLAP.



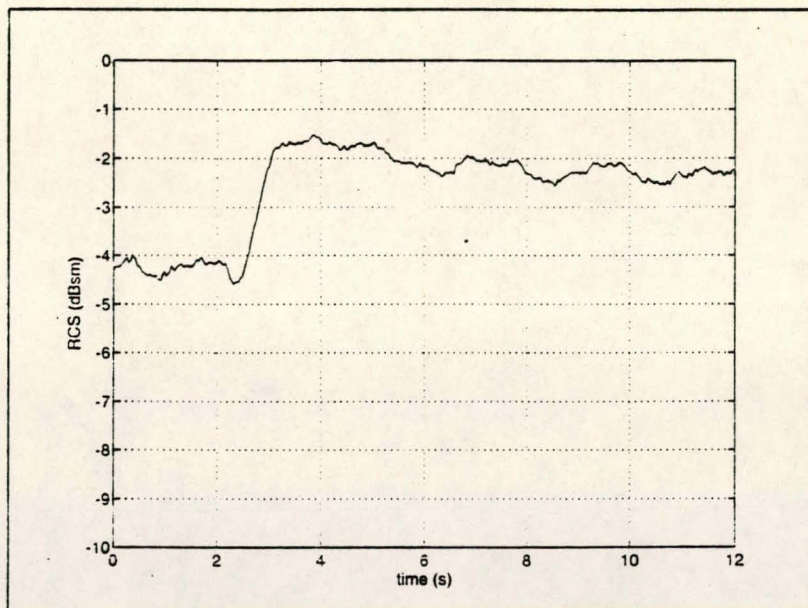
Plume V3STD#3 compared to V3STD#1 and #2.



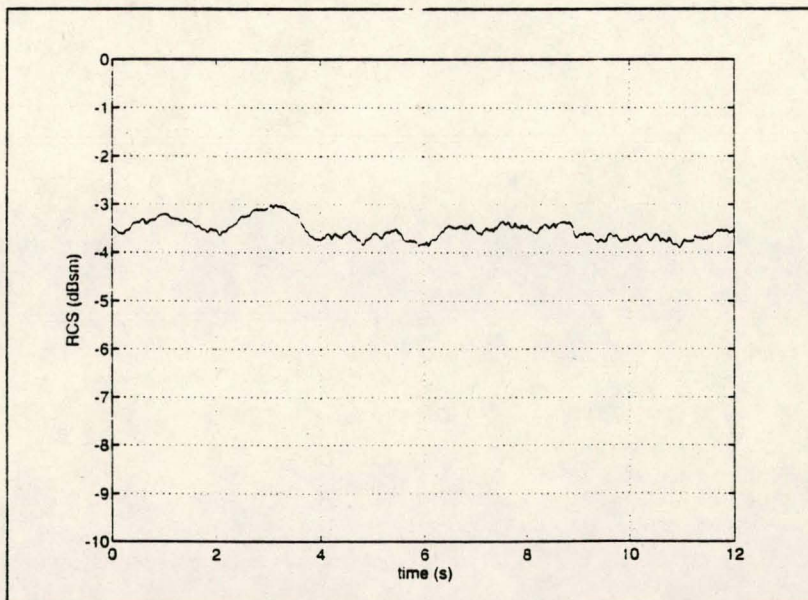
Plume DBR.



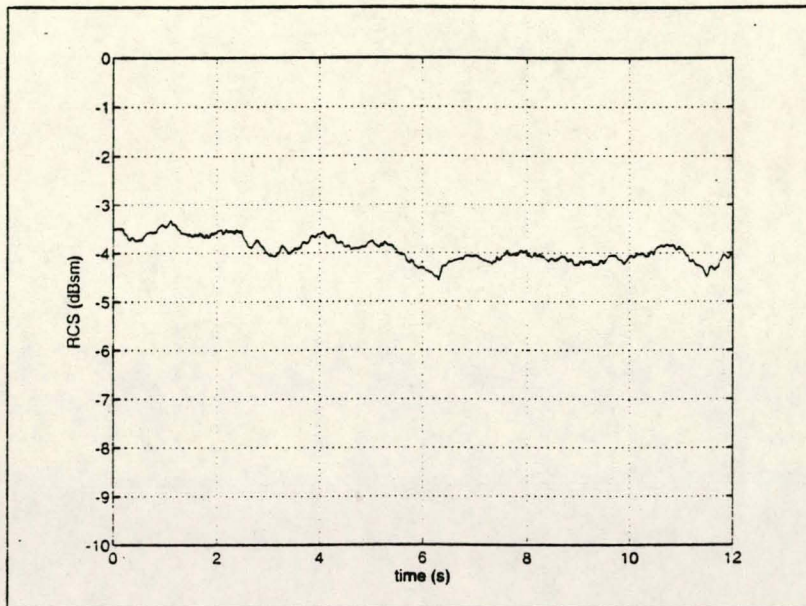
Plume DBKNKAF.



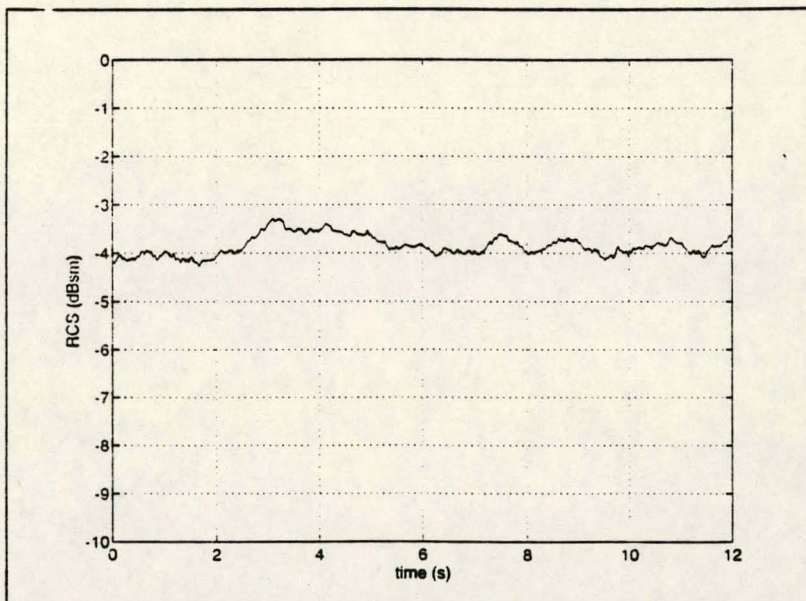
Plume DBNQKN.



Plume GDBSK.



Plume GDBKN.



Plume GDBB.